# Spin-gap Materials from First Principles: Properties and Applications of Half-metallic Ferromagnets

vorgelegt von

Master of Science

## Marjana Ležaić

aus Bor (Serbien und Montenegro)

# Abstract

Half-metallic ferromagnets, discovered in 1983 by de Groot and collaborators, have given a strong boost to the research in the field of spintronics. The main characteristic of these materials is a different behavior in the two spin bands: while the majority spin band shows a typical metallic behavior, the minority spin band is semiconducting. Thus, the spin polarization at the Fermi level is 100%, maximizing the efficiency of magnetoelectronic devices.

In this thesis we address the half-metallicity of materials from the the electronic structure point of view. We focus on the structural, electronic, and magnetic aspects of the half-metallic Heusler alloys and the zincblende compounds. Among the Heusler alloys we focus particularly on NiMnSb. The investigations are based on the Density Functional Theory (DFT), the most successful *ab-initio* theory for real solid state materials. We investigate the bulk properties, the properties of selected low index surfaces and for the case of NiMnSb/InP also a junction with a semiconductor. The importance of the spin-orbit interaction in reducing the polarization at the Fermi energy is considered. The calculations are carried out with the full-potential linearized plane-wave method (FLAPW), one of the most precise density functional methods for multicomponent materials, open structures and surfaces.

A particular effort is made to address the finite temperature properties of half-metals. This is a challenge, as the local-density approximation and the generalized gradient approximation to DFT are theories which address the systems at zero temperature. To bridge the temperature gap, we calculate the interatomic exchange parameters from first principles, using the frozen magnon calculations which employ the spin spiral formalism as implemented in the `FLEUR` code. These parameters are then used in a Heisenberg model which describes the system at finite temperatures. Besides applying the random phase and the mean-field approximation, we seek the finite temperature properties by Monte Carlo simulations. To describe the system NiMnSb properly, we extend the Heisenberg model to include the longitudinal fluctuations in addition to the transverse ones. This leads to the surprising result that, although the magnetic moment of Ni is lost at a temperature around 1/10 of the Curie point, the half-metallicity is preserved. However, the width of the half-metallic gap is reduced and the Fermi level is slightly shifted.

Finally, we present an analysis of possible applications of half-metals in giant magnetoresistance (GMR) and tunneling magnetoresistance (TMR) junctions, concluding that in the TMR case interface states can completely compensate the half-metallic property rendering it useless. A possible application of zincblende half-metals in ideal spin-valves, found to be free of interface states, is described.

*Mojoj porodici*

# Contents

# Chapter 1

# Introduction

In recent years, the field of magnetoelectronics (also referred to as *spintronics*) has become one of the hot topics of solid state physics. Initiated by the discovery of giant magnetoresistance in 1988 by Grünberg and Fert, spintronics aims at exploiting the electronic spin degree of freedom for the fabrication of better nanoelectronic devices. Adding the spin degree of freedom to the conventional electronic devices might have several advantages, like non-volatility, increased data processing speed, decreased electric power consumption and increased integration densities [1].

Half-metallic ferromagnets, first discovered in 1983 by de Groot and collaborators [2], are materials which have given further impetus to the research in the field of spintronics. Due to their specific electronic structure, these materials are very promising candidates for applications in novel spintronics devices [3]. Their main characteristic is a different behavior in the two spin bands. Namely, while the majority spin band shows the typical metallic behavior, the minority spin band is semiconducting. Thus, the spin polarization at the Fermi level is 100%, which maximizes the efficiency of the magnetoelectronic devices [4].

Heusler alloys [5] have attracted during the last century a great interest due to the possibility to study, in the same family of alloys, a series of interesting diverse magnetic phenomena like itinerant and localized magnetism, antiferromagnetism, helimagnetism, Pauli paramagnetism or heavy-fermionic behavior [6, 7, 8, 9]. The first Heusler alloys studied were crystallizing in the $L2_1$ structure which consists of 4 fcc sublattices. Afterwards, it was discovered that some of the alloys adopt the $C1_b$ structure, in which one of the four sublattices remains unoccupied. The latter compounds are often called half- or semi-Heusler alloys, while the $L2_1$ compounds are referred to as full-Heusler alloys. In their pioneering work, de Groot and collaborators [2] discovered, using first-principles electronic structure calculations, that one of the

1

half-Heusler compounds, NiMnSb, is a half-metallic ferromagnet. Since then, various investigations [10, 11, 12, 13] have shown that the half-metallicity also characterizes a number of other half- and full-Heusler alloys. Due to their relatively high Curie temperature, these alloys are good candidates for technical applications like spin-injection devices [14], spin-filters [15], tunnel junctions [16], or giant magnetoresistance devices [17].

New investigations also find half-metallic behavior in some oxides (e.g. $CrO_2$ and $Fe_3O_4$) [18], manganites (e.g. $La_{0.7}Sr_{0.3}MnO_3$) [18], double perovskites (e.g. $Sr_2FeReO_6$) [19], pyrites (e.g. $CoS_2$) [20], transition-metal chalcogenides (e.g. CrAs) and pnictides (e.g. CrSe) in zinc-blende or wurtzite structure [21, 22, 23, 24, 25], and diluted magnetic semiconductors (e.g. Mn doped Si or GaAs) [26, 27].

A proper understanding of the physics of these materials and mechanisms which govern the formation of the gap in the minority spin band is necessary in order to decide which ones of all the candidates would be the most suitable choice in applications and many aspects are being investigated, theoretically and experimentally. As an example, there are numerous investigations of the properties of NiMnSb which developed to a "model system" in this field; experiments on single crystals of NiMnSb by infrared absorption [28] and spin-polarized positron-annihilation [29] gave a spin-polarization of $\sim$100% at the Fermi level. Larson *et al.* [30] showed that the actual structure of NiMnSb is the most stable with respect to an interchange of the atoms. Orgassa *et al.* [31] showed that a few percent of disorder induce states within the gap but do not destroy the half-metallicity. Unfortunately, the thin films of NiMnSb were experimentally found not to be half-metallic [18, 32, 33, 34, 35], and a maximum polarization value obtained by Soulen *et al.* [18] was 58%. Ristoiu *et al.* [36] have studied the surfaces of NiMnSb experimentally and showed that the (001) surface terminated in a MnSb layer presents a spin-polarization of about 67$\pm$9% at room temperature. From *ab-initio* calculations, surface states in the gap of the minority spin band were found for all the possible (001) and (111) terminations of this alloy [37, 38, 39]. In the case of interfaces of NiMnSb with semiconductors, theoretical investigations show that, in certain geometries of the interface, half-metallicity can be preserved [40] while in some other geometries although the half-metallicity is lost, the spin-polarization can remain very high [41].

Though the Curie temperatures of Heusler alloys are high, for practical applications it is important that the half-metallic property remains also at temperatures significantly close to room temperature. Thus it is very important to know how half-metallic materials behave at finite temperatures, i.e. how does the spin polarization at the Fermi level change as a function of temperature. For instance, there is experimental evidence that

the half-metallicity of NiMnSb might be lost at temperatures much lower than the Curie temperature [42, 43]. There are few theoretical works describing the processes which take place in half-metals at finite temperatures [44, 45, 46]. They rely on the determination of the exchange interaction parameters in these materials from *ab-initio* calculations, and then using these in the Heisenberg model to obtain the Curie point. However, the behavior at nonzero temperatures, but below the Curie point, remains an open and nontrivial problem. In particular, questions concerning the half-metallic gap at $T > 0$ have to be explored.

In this thesis we address the half-metallicity of materials from the electronic structure point of view. We focus on the structural, electronic, and magnetic aspects of the half-metallic Heusler alloys and the zinc-blende compounds. Among the Heusler alloys we focus particularly on NiMnSb. The investigations are based on the Density Functional Theory (DFT), the most successful *ab-initio* theory for real solid state materials. We investigate the bulk properties, the properties of selected low index surfaces and for the case of NiMnSb/InP also a junction with a semiconductor. The importance of the spin-orbit interaction in reducing the polarization at the Fermi energy is considered. The calculations are carried out with the full-potential linearized augmented plane-wave method (FLAPW), one of the most precise density functional methods for multicomponent materials, open structures and surfaces.

A particular effort is made to address the finite temperature properties of half-metals. This is a challenge as the local-density approximation (LDA) and the generalized gradient approximation (GGA) to the DFT are theories which address the systems at zero temperature. To bridge the temperature gap we calculated from first principles the interatomic exchange parameters and used these in a Heisenberg model, which is employed to describe the system at finite temperatures. Besides applying the mean-field approximation and the random phase approximation we seek the finite temperature properties by Monte Carlo simulations. To describe the system NiMnSb properly, we had to transcend the Heisenberg model, including longitudinal fluctuations in addition to transverse fluctuations. This leads to the result that the magnetic moment of Ni vanishes at very low temperatures. Surprisingly, the half-metallic gap survives the loss of the Ni moment, though it shifts with respect to the Fermi level and its width is reduced. In order to calculate the exchange parameters using a method with translational symmetry we followed the suggestions of Halilov and co-workers [47] and extended them to multicomponent systems, making use of frozen magnon calculations employing the spin spiral formalism as implemented in the FLEUR code.

The thesis is structured as follows. The idea and formulation of DFT are

presented in Chapter 2. The Full Potential Linearized Augmented Plane-wave (FLAPW) method (as implemented in the FLEUR code) is described in Chapter 3. Special attention is given to the description of non-collinear magnetism within the FLAPW method in Chapter 4. In Chapter 5 we consider the Stoner and Heisenberg models of magnetism in solids. We also describe a way to use the *ab-initio* calculations and determine, from the differences in total energies of different magnetic configurations, the parameters used in the Heisenberg model for the description of magnetic interactions. Analyzing the *ab-initio* results, using the group-theory and simple models, we explain in Chapter 6 the origin of the gap in the half- and full-Heusler alloys and in the half-metallic zinc-blende compounds. Chapter 7 deals with the processes that destroy the half-metallic property, even at low temperatures. As a model system, NiMnSb is investigated in more detail. The discussion in Chapter 8 focuses on the behavior of half-metallic systems at finite temperatures. Finally, in Chapter 9, a possible application of half-metals in ideal spin-valves is described.

# Chapter 2

# Density Functional Theory

Calculating the magnetic properties and the total energy of solids is not a trivial task, given the fact that the atomic nuclei and the electrons constitute a complex many-body problem. Therefore, all theories that deal with these calculations start by adopting the Born-Oppenheimer approximation, which simply neglects the movement of the atomic nuclei and considers them as point charges at fixed positions. This is a pretty good assumption, since the electrons are much lighter than the nuclei and thus move much faster. One can now focus solely on the electrons, which in itself is a formidable problem. The electrons interact with the positive atomic nuclei and with each other via Coulomb forces. Although the former interaction is by no means simple it can be treated, whereas the latter interaction is impossible to calculate and one must resort to approximations.

Attempts to estimate the electron-electron interaction in solids and calculate the electronic dispersion or the total energy of different systems date back to the days of the Thomas-Fermi model [48, 49], the Hartree approximation and to the X-$\alpha$ method of Slater [50]. The extension of these ideas which brought a revolution in the parameter-free *ab-initio* description of complex electronic structure is known as Density Functional Theory (DFT) and was established by Hohenberg and Kohn [51] and Kohn and Sham [52]. This has made it possible to calculate the total energy of solids, using the electron density, $n(\mathbf{r})$, as the key variable ($n(\mathbf{r})=n^{\uparrow}(\mathbf{r})+n^{\downarrow}(\mathbf{r})$, where $n^{\uparrow}(\mathbf{r})$ is the spin up electron density and $n^{\downarrow}(\mathbf{r})$ the spin down electron density). For magnetic systems one has also to consider the magnetization density, $m(\mathbf{r})$, with $m(\mathbf{r})=n^{\uparrow}(\mathbf{r})-n^{\downarrow}(\mathbf{r})$. In this chapter the Density Functional Theory will be described in more detail.

## 2.1 The Hohenberg-Kohn theorem

The basic ideas of DFT will be presented here by considering a non-magnetic system with spin degeneracy, while the spin polarized case will be discussed later. The DFT is based on two theorems.

**Theorem 1** *For a given external potential v, the total energy of a system is a unique functional of the ground state electron density.*

To prove this we consider a Hamiltonian, H=T+V+W, where T represents the kinetic energy of the system, V the interaction of the electrons with an external potential (including the potential coming from the atomic nuclei in the solid) and W the electron-electron interaction. The solution to this Hamiltonian results in a ground state many body wave function $\Psi(\mathbf{r}_1, \mathbf{r}_2, ....\mathbf{r}_N)$ (for N electrons), and we have

$$H\Psi = E_0\Psi. \tag{2.1}$$

The electron density can be calculated from

$$n(\mathbf{r}) = \langle \Psi \mid \sum_{i=1}^{N} \delta(\mathbf{r} - \mathbf{r}_i) \mid \Psi \rangle, \tag{2.2}$$

and the interaction V is written as V=$\int n(\mathbf{r})v(\mathbf{r})d^3r$, where $v(\mathbf{r})$ is the external potential. What follows is the proof that two different external potentials $v(\mathbf{r})$ and $v'(\mathbf{r})$ must give rise to different ground state electron densities. For a system with potential $v'(\mathbf{r})$ we have

$$H'\Psi' = E_0'\Psi'. \tag{2.3}$$

From the variational principle it follows that

$$E_0 = \langle \Psi \mid H \mid \Psi \rangle < \langle \Psi' \mid H \mid \Psi' \rangle. \tag{2.4}$$

By adding and subtracting $v'(r)$ on the rhs. of Eqn. 2.4 we obtain

$$\begin{aligned} \langle \Psi' \mid H \mid \Psi' \rangle &= \langle \Psi' \mid H' + V - V' \mid \Psi' \rangle \\ &= E_0' + \int n'(\mathbf{r})(v(\mathbf{r}) - v'(\mathbf{r}))d^3r. \end{aligned} \tag{2.5}$$

Combining the expressions in Eqns. 2.4 and 2.6 gives

$$E_0 < E_0' + \int n'(\mathbf{r})(v(\mathbf{r}) - v'(\mathbf{r}))d^3r. \tag{2.6}$$

A similar argument, starting from the expression

$$E_0' = \langle \Psi' \mid H' \mid \Psi' \rangle < \langle \Psi \mid H' \mid \Psi \rangle, \tag{2.7}$$

results in

$$E_0' < E_0 + \int n(\mathbf{r})(v'(\mathbf{r}) - v(\mathbf{r}))d^3r. \tag{2.8}$$

Adding Eqn. 2.6 and 2.8 and assuming $n'(\mathbf{r}) = n(\mathbf{r})$ one obtains

$$E_0 + E_0' < E_0' + E_0, \tag{2.9}$$

which is clearly wrong. Hence $n'(\mathbf{r}) \neq n(\mathbf{r})$ and we conclude that two different potentials, $v(\mathbf{r})$ and $v'(\mathbf{r})$ give rise to different densities $n(\mathbf{r})$ and $n'(\mathbf{r})$. Therefore, knowledge of the electron density, $n(\mathbf{r})$, implies that it was calculated from a Hamiltonian with a specified external potential $v(\mathbf{r})$. As the kinetic energy, T, and electron-electron interactions, W, are known and specified one concludes that knowledge of the ground state electron density determines the entire Hamiltonian and hence the ground state energy, which proves Theorem 1. One can thus express a functional relationship between the ground state energy and the corresponding electron density as

$$E[n(\mathbf{r})] = T[n(\mathbf{r})] + V[n(\mathbf{r})] + W[n(\mathbf{r})]. \tag{2.10}$$

The second important theorem of DFT is

**Theorem 2** *The exact ground state density minimizes the energy functional $E[n(\mathbf{r})]$.*

To prove Theorem 2 one starts from Theorem 1 and for a given external potential $v_0(\mathbf{r})$ writes

$$E_{v_0}[n(\mathbf{r})] = \langle \Psi[n(\mathbf{r})] \mid T + W + V_0 \mid \Psi[n(\mathbf{r})] \rangle, \tag{2.11}$$

where the subscript $v_0$ indicates that this is the energy functional for a system with external potential $v_0(\mathbf{r})$. Since the ground state density specifies the Hamiltonian, it also specifies the wave function (of the ground state and of excited states) and hence the notation $\Psi[n(\mathbf{r})]$. If the ground state electron density is denoted by $n_0(\mathbf{r})$, the ground state can be expressed as $\Psi[n_0(\mathbf{r})]$. From the variational principle one again obtains

$$\langle \Psi[n_0(\mathbf{r})] \mid T + W + V_0 \mid \Psi[n_0(\mathbf{r})] \rangle < \langle \Psi[n(\mathbf{r})] \mid T + W + V_0 \mid \Psi[n(\mathbf{r})] \rangle, \tag{2.12}$$

which can also be expressed as

$$E_{v_0}[n_0(\mathbf{r})] < E_{v_0}[n(\mathbf{r})], \tag{2.13}$$

i.e., the ground state density minimizes the energy functional E[$n(\mathbf{r})$], which is what Theorem 2 states. If one would now have an explicit form for E[$n(\mathbf{r})$] he could go ahead and minimize it with respect to the electron density and in this way calculate the ground state energy. Unfortunately, due to the complexity provided by the electron-electron interactions, approximations are necessary to obtain an explicit expression for E[$n(\mathbf{r})$].

**DFT for spin polarized systems**

The reasoning applied to the non-magnetic systems can be extended to the spin polarized ones, and it is shown that the ground state energy is a unique functional of the electron and magnetization density ($n(\mathbf{r})$ and $m(\mathbf{r})$). The proof of this is quite similar to the proof outlined above. One starts by modifying the Hamiltonian to include an external magnetic field, $\mathbf{B}(\mathbf{r})$, so that the Hamiltonian becomes H=T+W+U, where U=$\int v(\mathbf{r})n(\mathbf{r}) - \mathbf{B}(\mathbf{r}) \cdot \mathbf{m}(\mathbf{r})\ d^3r$. Based on the variational principle, similar to the discussion around Eqns. 2.4-2.6, one arrives at

$$E_0 < E_0' + \int n'(\mathbf{r})(v(\mathbf{r}) - v'(\mathbf{r}))d^3r - \int \mathbf{m}'(\mathbf{r})(\mathbf{B}(\mathbf{r}) - \mathbf{B}'(\mathbf{r}))d^3r \quad (2.14)$$

and

$$E_0' < E_0 + \int n(\mathbf{r})(v'(\mathbf{r}) - v(\mathbf{r}))d^3r - \int \mathbf{m}(\mathbf{r})(\mathbf{B}'(\mathbf{r}) - \mathbf{B}(\mathbf{r}))d^3r. \quad (2.15)$$

Assuming that $n(\mathbf{r}) = n'(\mathbf{r})$ and $\mathbf{m}(\mathbf{r}) = \mathbf{m}'(\mathbf{r})$, and adding Eqns. 2.14 and 2.15 the same absurd result as in the discussion of spin degenerate systems, i.e. Eqn. 2.9 follows, and one must draw the conclusion that $n(\mathbf{r}) \neq n'(\mathbf{r})$ and $\mathbf{m}(\mathbf{r}) \neq \mathbf{m}'(\mathbf{r})$. Hence, for magnetic systems the ground state energy is a unique functional of the electron density and the magnetization density.

## 2.2 The Kohn-Sham equations

How do we use DFT now to describe a solid? One starts with a simple non-interacting electron system where the part of the Hamiltonian describing electron-electron interactions, W, is absent. In this case the electrons which move in the field of an external potential which, for reasons that will be obvious below, will be called "effective" potential $V_{eff}$, are solutions to a one-electron Schrödinger equation,

$$[\frac{-\nabla^2}{2} + V_{eff}]\psi_i = \epsilon_i\psi_i. \quad (2.16)$$

There is an infinity of solutions to this equation and to specify a special solution the subscript $i$ is introduced. From Eqn. 2.16 one can calculate an electron density from the lowest lying one-particle ($op$) states. If there are N electron states which are solutions to Eqn. 2.16 one simply calculates the one-particle (a label introduced to show that there are no electron-electron interactions considered) electron density from

$$n_{op}(\mathbf{r}) = \sum_{i=1}^{N/2} 2 \mid \psi_i(\mathbf{r}) \mid^2, \tag{2.17}$$

where the factor 2 comes from spin degeneracy. In this case the energy functional which describes the total energy of the N electrons may be written as,

$$
\begin{aligned}
E_{op}[n_{op}(\mathbf{r})] &\equiv T_{op}[n_{op}] + V_{eff}[n_{op}] \\
&= \sum_{i=1}^{N/2} \langle \psi_i(\mathbf{r}) \mid \frac{-\nabla^2}{2} \mid \psi_i(\mathbf{r}) \rangle + \int n_{op}(\mathbf{r}) V_{eff}(\mathbf{r}) d^3r,
\end{aligned}
\tag{2.18}
$$

and the electron density which minimizes this functional is obtained from the requirement that the energy functional is stationary for small variations of the electron density around the ground state density. This can be written as

$$0 = \delta E_{op} = E_{op}[n_{op}(\mathbf{r}) + \delta n_{op}(\mathbf{r})] - E_{op}[n_{op}(\mathbf{r})], \tag{2.19}$$

which may also be written as

$$0 = \delta T_{op}[n_{op}] + \int \delta n(\mathbf{r}) V_{eff}(\mathbf{r}) d^3r. \tag{2.20}$$

Carrying out the minimization in Eqn. 2.20 leads to Eqn. 2.16. Thus, the independent particles which are the solution to Eqn. 2.16 give rise to a density which minimizes the total energy expression of independent particles in Eqn. 2.19. The reason for introducing Eqns. 2.16 to 2.20 is mainly that they can be solved, at least approximately, to within a desired accuracy. More important, however, is the fact that they can, via the Kohn-Sham approach, be used to actually calculate the ground state energy of a 'real' interacting electron system. The basic principle of the Kohn-Sham approach is now to assume that one can find an effective potential, $V_{eff}$, so that $n_{op}(\mathbf{r}) = n(\mathbf{r})$ where $n(\mathbf{r})$ is the electron density of the fully interacting system. Since we know that the total energy of a system is uniquely determined by the electron density, it seems to be an efficient route to obtain the correct electron density from a one-electron like problem.

The question now is how to determine $V_{eff}$, so that $n_{op}(\mathbf{r})$ becomes equal to $n(\mathbf{r})$. To do this one rewrites the energy functional in Eqn. 2.10 as

$$
\begin{aligned}
E[n(\mathbf{r})] &= T_{op}[n(\mathbf{r})] + \int n(\mathbf{r})v(\mathbf{r})d^3r \\
&+ \frac{1}{2}\int\int e^2 \frac{n(\mathbf{r})\cdot n(\mathbf{r}')}{|\mathbf{r}-\mathbf{r}'|}d^3rd^3r' + E_{xc}[n(\mathbf{r})]
\end{aligned}
\tag{2.21}
$$

(since it is required that $n_{op}(\mathbf{r})$ should be equal to $n(\mathbf{r})$ in the expression above, for simplicity, the subscript *op* on the electron density of the right hand side was skipped). In Eqn. 2.21 the one-particle kinetic energy functional instead of the true kinetic energy functional of Eqn. 2.10 was introduced, as well as the Hartree electrostatic interaction instead of the true electron-electron interaction. Hence in order to make Eqn. 2.21 equal to Eqn. 2.10 one must introduce a term that corrects for these replacements, and this is what the exchange and correlation energy, $E_{xc}[n(\mathbf{r})]$, does. Since the first three terms on the right hand side of eqn.2.21 are possible to calculate numerically, in this way the problem of the complexity of the fully interacting system is mapped into the problem of finding the exchange and correlation functional. So far it has been impossible to find the exact exchange and correlation functional so that Eqn. 2.21 holds for all densities and all systems. However, for a uniform electron gas one can calculate $E_{xc}[n(\mathbf{r})]$[1] for all values of the electron density and parameterized forms of $E_{xc}[n(\mathbf{r})]$ as a function of $n(\mathbf{r})$ are available. The local density approximation (LDA) assumes that these parameterizations work even in cases where the electron gas is not uniform, but varies in space, as it does in a solid, surface or interface. In the frame of this approximation, the expression

$$
E_{xc}[n(\mathbf{r})] = \int \epsilon_{xc}[n(\mathbf{r})]n(\mathbf{r})d^3r,
\tag{2.22}
$$

for the exchange-correlation energy is introduced, where $\epsilon_{xc}[n(\mathbf{r})]$ is named the exchange-correlation energy density. In a parametrized form its dependence on $n(\mathbf{r})$ is relatively simple and may, for example, be found in Ref. [56]. Armed with an (approximate) expression for the ground state energy functional and in analogy with Eqns. 2.19 and 2.20 the ground state density can be determined from this functional by requiring that the functional (Eqn. 2.21)

---

[1]This can be done in the high electron density limit [53] and in the low electron density limit [54]. Interpolation between these two limits gave rise to parametrized forms of the exchange and correlation functional of a uniform electron gas for all values of the density [54]. However, this interpolation is in modern electronic structure calculations replaced by approaches which are based on quantum Monte-Carlo simulations for the intermediate values of the electron gas [55].

is stationary for small variations of the electron density around the ground state density. As a result, an expression which is quite similar to Eqn. 2.20 follows:

$$0 = \delta T_{op}[n] + \int \delta n(\mathbf{r}) \left[ v(\mathbf{r}) + \int e^2 \frac{n(\mathbf{r}')}{|\mathbf{r} - \mathbf{r}'|} d^3 r' + \frac{\partial(\epsilon_{xc}[n(\mathbf{r})]n(\mathbf{r}))}{\partial n(\mathbf{r})} \right]. \quad (2.23)$$

The comparison of Eqns. 2.20 and 2.23 identifies the effective potential which (within the approximations and assumptions introduced) ensures that $n_{op}(\mathbf{r}) = n(\mathbf{r})$, as

$$V_{eff}(\mathbf{r}) = v(\mathbf{r}) + \int e^2 \frac{n(\mathbf{r}')}{|\mathbf{r} - \mathbf{r}'|} d^3 r' + \mu_{xc}(n(\mathbf{r})), \quad (2.24)$$

where

$$\mu_{xc}(n(\mathbf{r})) = \frac{\delta(E_{xc}[n(\mathbf{r})]}{\delta n(\mathbf{r})} = \epsilon_{xc}[n(\mathbf{r})] + n(\mathbf{r}) \frac{\partial(\epsilon_{xc}[n(\mathbf{r})])}{\partial n(\mathbf{r})}. \quad (2.25)$$

Eqn. 2.16 should be solved now with the effective potential specified by Eqn. 2.24. Since the effective potential to be used in Eqn. 2.16 depends on the electron density, the property that should be calculated, one has to perform a self-consistent calculation where an initial electron density is more or less guessed and an effective potential is calculated from Eqn. 2.24. This potential is then used to solve Eqn. 2.16 and a new electron density is calculated from Eqn. 2.17, which is then put back into Eqn. 2.24. This procedure is repeated until convergence is obtained, i.e. until the density does not change appreciably with successive iterations[2]. Once a self consistent electron density has been found one can calculate the ground state energy of the Kohn-Sham (LDA) energy functional (via Eqn. 2.21) and hence one of the main goals in electronic structure calculations has been achieved.

## Kohn-Sham equations for spin-polarized systems

At the end of the previous section it was shown that for magnetic systems the ground state energy may be written as a unique functional of the electron density and of the magnetization density. An alternative way of expressing this is to state that there is an energy functional which depends both on the majority and the minority spin density (since $n(\mathbf{r}) = n^\uparrow(\mathbf{r}) + n^\downarrow(\mathbf{r})$ and $m(\mathbf{r}) =$

---

[2]Normally one mixes the electron density which is the output of Eqn. 2.17 with the electron density which is in input for that particular loop in the self-consistency iterational procedure before one takes this mixed density and puts it in Eqn. 2.24. The whole procedure of mixing is quite complex where many suggestions of how to achieve self consistency with as few iterations as possible have been suggested [57, 58].

$n^\uparrow(\mathbf{r}) - n^\downarrow(\mathbf{r}))^3$ and the energy functional can be written as $\mathrm{E}[n^\uparrow(\mathbf{r}), n^\downarrow(\mathbf{r})]$. Following arguments similar to the ones around Eqn. 2.21, one obtains a Kohn-Sham scheme for spin-polarized systems through

$$
\begin{aligned}
E[n^\uparrow(\mathbf{r}), n^\downarrow(\mathbf{r})] \;=\; & T_{op}[n^\uparrow(\mathbf{r}), n^\downarrow(\mathbf{r})] + \int n(\mathbf{r})v(\mathbf{r})d^3r \\
+\; & \frac{1}{2}\int\int e^2 \frac{n(\mathbf{r})\cdot n(\mathbf{r}')}{\mid \mathbf{r} - \mathbf{r}' \mid}d^3r d^3r' + E_{xc}[n^\uparrow(\mathbf{r}), n^\downarrow(\mathbf{r})].
\end{aligned} \tag{2.26}
$$

In a real solid the preference for occupying one spin channel (to some degree) more than the other is traditionally explained as due to the exchange interaction and the driving force for it is the electron-electron interaction in the Hamiltonian. Hence in the spin-polarized Kohn-Sham scheme this necessarily means that the exchange and correlation potential, which is supposed to absorb all complex electron-electron interactions, must depend both on the charge and the spin (magnetization) density. Turning again to studies on the uniform electron density is useful and parameterizations for $E_{xc}[n^\uparrow(\mathbf{r}), n^\downarrow(\mathbf{r})]$, as a function of $n^\uparrow(\mathbf{r})$ and $n^\downarrow(\mathbf{r})$, have been made. Proceeding analogously to the discussion around 2.16 and 2.17, one analyzes a one-particle Hamiltonian with spin up (down) effective potentials,

$$
[\frac{-\nabla^2}{2} + V_{eff}^{\uparrow(\downarrow)}]\psi_i^{\uparrow(\downarrow)} = \epsilon_i^{\uparrow(\downarrow)}\psi_i^{\uparrow(\downarrow)}, \tag{2.27}
$$

where the electron density for electrons with a given spin is obtained from

$$
n_{op}^{\uparrow(\downarrow)}(\mathbf{r}) = \sum_{i=1} \mid \psi_i^{\uparrow(\downarrow)}(\mathbf{r}) \mid^2 . \tag{2.28}
$$

Repeating the discussion which led to Eqn. 2.24, with the only modification that one now requires the energy functional to be stationary with regard to both the spin up and the spin down density, leads to effective potentials which are different for the two spin directions due to differences in the exchange and correlation potential,

$$
V_{eff}^{\uparrow(\downarrow)}(\mathbf{r}) = v(\mathbf{r}) + \int e^2 \frac{n(\mathbf{r}')}{\mid \mathbf{r} - \mathbf{r}' \mid}d^3r' + \mu_{xc}^{\uparrow(\downarrow)}(n^\uparrow(\mathbf{r}), n^\downarrow(\mathbf{r})), \tag{2.29}
$$

where the exchange-correlation potential is defined similar to Eqn. 2.25 as

$$
\mu_{xc}^{\uparrow(\downarrow)}(n^\uparrow(\mathbf{r}), n^\downarrow(\mathbf{r})) = \frac{\delta E_{xc}[n^\uparrow(\mathbf{r}), n^\downarrow(\mathbf{r})]}{\delta n^{\uparrow(\downarrow)}(\mathbf{r})}. \tag{2.30}
$$

---

[3]This approach, however, simplifies the situation somewhat since the magnetization density is a scalar property with both magnitude and spin. In this analysis it is assumed that the magnetization is pointing only in one direction, the z-direction, of the system.

Hence, the simplest forms of spin polarized calculations treat the spin up and spin down electrons separately and for every iteration in the self consistent loop one solves a Kohn-Sham equation for both spin directions. The spin up and spin down densities are then calculated by occupying the N lowest (spin up or spin down) eigenvalues of the separate two Kohn-Sham equations. Since for a given $V_{eff}^{\uparrow}(\mathbf{r})$ which may be different from $V_{eff}^{\downarrow}(\mathbf{r})$ there may be more spin up states, $\epsilon_i^{\uparrow}$ than spin down states, $\epsilon_i^{\downarrow}$, which have an energy lower than the highest occupied state (the Fermi level, $E_F$) it is clear how spin polarization might occur. With a self consistent spin and magnetization density the magnetic moment is calculated as $\int m(\mathbf{r})d^3r$ (in Bohr magneton units) and the total energy may be calculated from Eqn. 2.26.

## 2.2.1   Solving the Kohn-Sham equations in systems with translational symmetry

In the procedure of solving the Kohn-Sham equations in systems with translational invariance, several simplifications can be used due to this symmetry [59]. The discussion here will concern the bulk calculations, but the conclusions can also be applied to the lower dimensional systems, like thin films or nanowires, in the directions in which the translational symmetry is preserved.

First of all one normally assumes in a bulk material that the potential which enters Eqn. 2.27 is periodic, i.e. $V_{eff}^{\uparrow(\downarrow)}(\mathbf{r}) = V_{eff}^{\uparrow(\downarrow)}(\mathbf{r} + \mathbf{R})$, where $\mathbf{R}$ is a translation vector (a Bravais lattice vector) of the solid. This periodic boundary condition leads to Bloch's theorem [59] which states that as an effect of the periodicity of the bulk material the one-electron wave function must obey the condition

$$\psi_{i,\mathbf{k}}^{\uparrow(\downarrow)}(\mathbf{r} + \mathbf{R}) = e^{i\mathbf{k}\cdot\mathbf{R}}\psi_{i,\mathbf{k}}^{\uparrow(\downarrow)}(\mathbf{r}), \qquad (2.31)$$

where $\mathbf{k}$ is a vector of reciprocal space [4]. Due to the translation symmetry one has only to consider $\mathbf{k}$-vectors which lie inside the first Brillouin zone[5] when looking for solutions to Eqns. 2.27-2.29 [59]. In addition one can solve the Eqns. 2.27-2.29 for each $\mathbf{k}$-vector being separate and independent of the others. However, the dependence of the one-electron wave function on $\mathbf{k}$ makes the calculation of the one-electron density somewhat more complex

---

[4]Reciprocal space is spanned by the vectors $\mathbf{G}_i$, defined as $\mathbf{G}_i \cdot \mathbf{R}_j = 2\pi\delta_{ij}$, where V is the volume of the primitive cell of the Bravais lattice.

[5]Moreover, when the system under consideration additionally possesses a point group symmetry, only the irreducible wedge of the first Brillouin zone (determined by the symmetry) has to be considered.

since a sum over all possible **k**-vectors has to be included, and Eqn. 2.28 is in a crystal replaced by

$$n_{op}^{\uparrow(\downarrow)}(\mathbf{r}) = \sum_i \sum_{\mathbf{k}} \mid \psi_{i,\mathbf{k}}^{\uparrow(\downarrow)}(\mathbf{r}) \mid^2 . \tag{2.32}$$

Similarly, in the calculation of the total energy, Eqn. 2.26, one needs to calculate the sum of Kohn-Sham eigenvalues $\epsilon_i$ (Eqn. 2.16),

$$E_{eig} = \sum_i \sum_{\mathbf{k}} \epsilon_{i,\mathbf{k}}, \tag{2.33}$$

since $T_{op} = E_{eig} - \int v_{eff}(\mathbf{r})n(\mathbf{r})d^3r$. In principle, all **k**-vectors inside the first Brillouin zone (BZ) should be considered in the sums in Eqns. 2.32 and 2.33, but since this number is enormous one would like to replace the sum with an integral. However, if one does not have an analytic dependence of the Kohn-Sham eigenvalues on **k**, a way to approximate Eqn. 2.33 must be found. In order to do this it is useful to introduce the concept of density of states (DOS), which can be calculated from

$$D(E) = \sum_i \frac{1}{8\pi^3} \int_{BZ} \delta(E - \epsilon_{i\mathbf{k}})d^3k. \tag{2.34}$$

With this definition of the DOS one can calculate the eigenvalue sum from

$$E_{eig} = \int_{-\infty}^{E_F} ED(E)dE. \tag{2.35}$$

The expressions 2.34 and 2.35 can be combined into

$$E_{eig} = \sum_i \int_{-\infty}^{\infty} Ef(E)\frac{1}{8\pi^3} \int_{BZ} \delta(E - \epsilon_{i\mathbf{k}})d^3kdE, \tag{2.36}$$

where $f(E)$ is a step function which attains the value one below the Fermi energy and zero above. Finally, the Eq.2.36 is solved on a **k**-points mesh, distributed as to fulfill the symmetry of the space-group. The integral over the Brillouin zone can then be calculated as a weighted sum over the bands, $i$, and the discrete set of sampled **k**-points, $\mathbf{k}_j$, with weight functions, $\mathrm{w}_{ji}$. Several methods can be used for interpolation of the eigenvalues between the **k**-points of the sample, like the linear tetrahedron method [60], the modified tetrahedron method [61], or the Gaussian broadening method [62].

## 2.2.2 Andersen's Force Theorem

It is quite often that one needs to calculate the difference in total energies between an initial and a slightly perturbed state. Andersen's force theorem claims that when the perturbation of the densities $n(\mathbf{r})$, $m(\mathbf{r})$ is small, the difference can be calculated as a difference in the sums of the eigenvalues of the two states (Eqn. 2.33). This can be shown as follows. The total energy can be written as

$$E = \int_{-\infty}^{E_F} E D(E) dE - E_r, \qquad (2.37)$$

where $D(E)$ is the density of states and the first term on the right hand side (called *the band term*) stands for the eigenvalues sum, $E_{eig}$ (Eqn. 2.35). The term $E_r$ includes all the other contributions to the total energy and can be easily explicitly obtained from Eqn. 2.26 with $T_{op} = E_{eig} - \int v_{eff}(\mathbf{r}) n(\mathbf{r}) d^3 r$. The perturbation will cause some changes in the system and we assume these changes to be parametrized by a set of quantities $\{X_i\}$. The total energy is then a function of these parameters and the aim is to calculate

$$\delta E = \sum_i \frac{\delta E}{\delta X_i} \delta X_i. \qquad (2.38)$$

Consider now a perturbation specified by a set of parameters $\{\Delta X_i\}$. The system can be led to self-consistency in two steps. First, the effective potential is held fixed and the Schrödinger equation is solved (for the new set of parameters $\{X_i + \Delta X_i\}$), giving rise to a new density and new energy eigenvalues. This variation we shall denote as $\delta_1$. In the second step the potential is allowed to relax to self-consistency, with the same parameter set $\{X_i + \Delta X_i\}$. Denoting this variational step as $\delta_2$, we can write the complete variation as $\delta = \delta_1 + \delta_2$. Then, the change in the band term in Eqn. 2.37 is

$$\delta E_{eig} = \delta_1 E_{eig} + \delta_2 E_{eig}, \qquad (2.39)$$

and the change of the total energy is

$$\delta E = \delta_1 E_{eig} + \delta_2 E_{eig} - \delta E_r. \qquad (2.40)$$

After writing out the term $\delta E_r$ and applying the first-order perturbation theory for the term $\delta_2 E_{eig}$ [63], one finally obtains

$$\delta E = \delta_1 E_{eig} - \int_{\delta\Omega} n^2 \frac{d\epsilon_{xc}}{dn} \delta\mathbf{S} \cdot d\mathbf{S}, \qquad (2.41)$$

where $d\mathbf{S}$ is the surface element and $\delta\mathbf{S}$ describes the change in the volume $\Omega$ in the sense that a point $\mathbf{S}$ is taken to $\mathbf{S} + \delta\mathbf{S}$ by the perturbation.

The Eqn. 2.41 is known as *Andersen's force theorem* and it's basic message is that in a linear approximation, the interaction drops out of the total energy change. The self-consistency step can therefore be ignored except for the surface term in the case of the volume change. Therefore, we came to a very important conclusion which can save a lot of computational effort: when there is a small perturbation in the system, during which there is no change of the volume, the difference in the total energies of the initial and the perturbed state can be substituted with the difference of the sums of eigenvalues of these two states.

# Chapter 3

# The FLAPW Method

There are several important methods of solving the bandstructure problem (Eqn. 2.27). One approach is to expand the (unknown) one-electron wave function in a set of (known) basis functions. For a system with translational symmetry, a quite general expression for such an expansion would be

$$\psi_{i,\mathbf{k}}(\mathbf{r}) = \sum_j c_{ij\mathbf{k}}\varphi_{j\mathbf{k}}(\mathbf{r}). \tag{3.1}$$

The sum on $j$ is finite in practice and the set of functions $\{\varphi_{j\mathbf{k}}(\mathbf{r})\}$ is in general not orthonormal, while the completeness is another problem. The expansion coefficients $c_{ij\mathbf{k}}$ are, via the Rayleigh-Ritz principle [64], determined from the secular equation

$$\sum_j [H_{jj'}(\mathbf{k}) - \epsilon_{i\mathbf{k}}S_{jj'}(\mathbf{k})]c_{ij\mathbf{k}} = 0, \tag{3.2}$$

where

$$H_{jj'}(\mathbf{k}) = \int_\Omega \varphi_{j\mathbf{k}}(\mathbf{r})[\frac{-\nabla^2}{2} + V_{eff}^{\uparrow(\downarrow)}]\varphi_{j'\mathbf{k}}(\mathbf{r})d^3r \tag{3.3}$$

and

$$S_{jj'}(\mathbf{k}) = \int_\Omega \varphi_{j\mathbf{k}}(\mathbf{r})\varphi_{j'\mathbf{k}}(\mathbf{r})d^3r \tag{3.4}$$

are the so-called overlap matrix elements. The integrals are evaluated over the unit cell ($\Omega$). The detailed solution of the secular equation depends on the type of functions $\{\varphi_{j\mathbf{k}}\}$ chosen (they may or may not be energy-dependent), but the eigenvalues always follow from the condition

$$\det |H_{jj'}(\mathbf{k}) - \epsilon_{i\mathbf{k}}S_{jj'}(\mathbf{k})| = 0. \tag{3.5}$$

A very suitable choice of the basis functions that is already suggested by Bloch's theorem are plane waves. They are orthogonal, diagonal in momentum and any power of momentum and the implementation of planewave
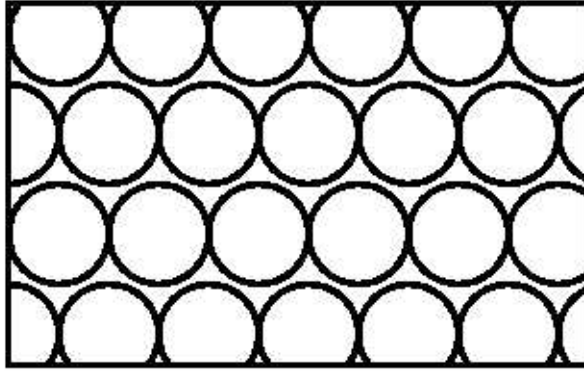
17

Figure 3.1: The division of space in the APW method. The muffin-tin spheres are surrounded by the interstitial region.

based methods is rather straightforward because of their simplicity. However, since the electron wavefunctions are varying very quickly near the core, large wavevectors are needed to represent the wavefunctions accurately. This makes planewaves very inefficient. To overcome this problem one can employ pseudopotential techniques, which allow an accurate description of the wavefunctions between the atoms, but avoid the fast oscillations near the core. Thus, less basis functions are needed. Another way to solve this problem is to use a basis set, which contains radial wavefunctions to describe the oscillations near the core. This has already been suggested by Slater [65]. The corresponding technique is called the augmented planewave method (APW).

## 3.1 The (L)APW Approach

Within the APW approach, space is divided into spheres centered at each atom site, the so-called muffin-tin spheres, and the remaining interstitial region (Fig. 3.1). Inside the muffin-tin spheres the potential is assumed to be spherically symmetric, and in many implementations the interstitial potential is set constant. Since the planewaves solve the Schrödinger equation in a constant potential, while spherical harmonics times a radial function are the solution in a spherical potential, the single particle wavefunctions $\psi_{i,\mathbf{k}}(\mathbf{r})$ are expanded in terms of the following basis functions:

$$\varphi_{\mathbf{G}}(\mathbf{k}, \mathbf{r}) = \begin{cases} e^{i(\mathbf{G}+\mathbf{k})\cdot\mathbf{r}} & \text{interstitial region} \\ \sum_{lm} A_L^{\mu\mathbf{G}}(\mathbf{k}) u_l(r) Y_L(\hat{\mathbf{r}}) & \text{muffin-tin sphere } \mu \end{cases}, \qquad (3.6)$$

where $\mathbf{k}$ is the Bloch vector, $\mathbf{G}$ is a reciprocal lattice vector, $L$ abbreviates the quantum numbers $l$ and $m$ and $u_l$ is the regular solution of the radial Schrödinger equation

$$\left\{-\frac{\hbar^2}{2m}\frac{\partial^2}{\partial r^2} + \frac{\hbar^2}{2m}\frac{l(l+1)}{r^2} + V(r) - E_l\right\} r u_l(r) = 0. \qquad (3.7)$$

Here $E_l$ is an energy parameter and $V(r)$ is the spherical component of the potential. The coefficients $A_L^{\mu\mathbf{G}}(\mathbf{k})$ are determined from the requirement that the wavefunctions have to be continuous at the boundary of the muffin-tin spheres.

Hence, the APW's form a set of continuous basis functions that cover all space, where each function consists of a planewave in the interstitial region plus a sum of functions, which are solutions of the Schrödinger equation to a given set of angular momentum quantum numbers $lm$ and a given parameter $E_l$, inside the muffin-tin spheres.

The described choice of the basis set, however, has several disadvantages.

- If the $E_l$ were kept fixed, used only as a parameter during the construction of the basis, the Hamiltonian could be set up in terms of this basis. This would lead to a standard secular equation for the band energies. Unfortunately, it turns out, that the APW basis does not offer enough variational freedom if the $E_l$ are kept fixed. An accurate description can only be achieved if they are set to the corresponding band energies. However, requiring the $E_l$'s to equal the band energies, the latter can no longer be determined by a simple diagonalization of the Hamiltonian matrix. Since the $u_l$'s depend on the band energies, the solution of the secular equation becomes a nonlinear problem, which is computationally much more demanding than a secular problem.

- It is difficult to extend the APW method beyond the spherically averaged muffin-tin potential approximation, because in the case of a general potential the optimal choice of $E_l$ is no longer the band energy.

- If, for a given choice of $E_l$, the radial functions $u_l$ vanish at the muffin-tin radius, the boundary conditions on the spheres cannot be satisfied, i.e. the planewaves and the radial functions become decoupled. This is called the asymptote problem. It can already cause numerical difficulties if $u_l$ becomes very small at the sphere boundary.

These problems were solved by introducing an additional term in the basis within the muffin-tin spheres and the method is called the linearized augmented planewave method (LAPW) [66]. In this way, extra variational

freedom is added to the basis, so that it is not necessary to set the $E_l$ equal to the band energy. This is done by using not only the radial solution of the Schrödinger equation, but also its derivative with respect to the energy, and the construction can be regarded as a linearization of the APW. To realize this recall that in the APW method the $u_l$'s depend on the band energies and can thus be understood as functions of $r$ and $\epsilon$. Hence, $u_l$ can be expanded into a Taylor-series around $E_l$,

$$u_l(\epsilon, r) = u_l(E_l, r) + \dot{u}_l(E_l, r)(\epsilon - E_l) + O[(\epsilon - E_l)^2]. \qquad (3.8)$$

Here $\dot{u}_l$ denotes the energy derivative of $u_l$, $\partial u_l(\epsilon, r)/\partial \epsilon$, and $O[(\epsilon - E_l)^2]$ denotes errors that are quadratic in the energy difference. Therefore, the LAPW method introduces an error of order $(\epsilon - E_l)^2$ in the wavefunction. Therefore, according to the variational principle the error in the calculated band energies is of the order $(\epsilon - E_l)^4$. Because of this high order, the linearization works very well even over rather broad energy regions. In most cases a single set of energy parameters is sufficient for the whole valence band. However, sometimes the energy region has to be split up in two (very rarely more) windows with separate sets of energy parameters.

The LAPW basis functions are of the form

$$\varphi_\mathbf{G}(\mathbf{k}, \mathbf{r}) = \begin{cases} e^{i(\mathbf{G}+\mathbf{k})\cdot\mathbf{r}} & \text{interstitial region} \\ \sum_L A_L^{\mu\mathbf{G}}(\mathbf{k})u_l(r)Y_L(\hat{\mathbf{r}}) + B_L^{\mu\mathbf{G}}(\mathbf{k})\dot{u}_l(r)Y_L(\hat{\mathbf{r}}) & \text{muffin-tin sphere } \mu \end{cases}$$

$$(3.9)$$

with the extra term $B_L^\mathbf{k}\dot{u}_l(r)Y_L(\hat{\mathbf{r}})$ compared to the APW method. The additional coefficient is determined by requiring that not only the basis functions, but also their derivatives with respect to $r$ are continuous at the sphere boundaries. It is useful to require the normalization

$$\langle u|u \rangle = \int_0^{R_{MT}} u_l^2(r)r^2 dr = 1. \qquad (3.10)$$

Here $R_{MT}$ is the muffin-tin sphere radius. Taking the derivative of (3.10) with respect to the energy it can easily be shown, that $u_l$ and $\dot{u}_l$ are orthogonal. $\dot{u}_l$ is calculated from a Schrödinger-like equation, derived by taking the energy derivative of (3.7),

$$\left\{ -\frac{\hbar^2}{2m}\frac{\partial^2}{\partial r^2} + \frac{\hbar^2}{2m}\frac{l(l+1)}{r^2} + V(r) - E_l \right\} r\dot{u}_l(r) = ru_l(r). \qquad (3.11)$$

Still the solution of this equation has to be made orthogonal to $u_l$, since any linear combination of $\dot{u}_l$ and $u_l$ also solves the equation. Once the $u_l$

and $\dot{u}_l$ are made orthogonal the basis functions inside the spheres form a completely orthogonal basis set, since the angular functions $Y_{lm}(\hat{\mathbf{r}})$ are also orthogonal. However, the LAPW functions are in general not orthogonal to the core states, which are treated separately in the LAPW method. This fact can cause problems in the presence of high lying core states. A detailed discussion of these problems and strategies to circumvent them can be found in the book by Singh [67], which includes a very comprehensive review of many aspects of the LAPW method.

With the construction of the LAPW basis the main problems of the APW method are solved:

- Since it is no longer necessary to set the energy parameters equal the band energies, the later can be determined by a single diagonalization of the Hamiltonian matrix.

- The LAPW method can be extended to nonspherical muffin tin potentials with little difficulty, because the basis offers enough variational freedom. This leads then to the full-potential linearized augmented planewave method (FLAPW).

- If $u_l$ is zero at the sphere boundary, its radial derivative and $\dot{u}_l$ are in general nonzero. Hence, the boundary conditions can always be satisfied and there is no asymptote problem.

The nonlinearity inherent to the APW method can only be circumvented at the expense of a larger eigenvalue problem. Within LAPW (and also within APW) the basis functions are represented by planewaves. The functions inside the muffin tins are coupled to the planewaves via the boundary conditions, and can only be varied indirectly by a variation of the planewave coefficients. Clearly, with a finite number of planewaves, at maximum the same number of functions inside the spheres can be varied independently. Hence, to make use of the of the extra variational freedom, that the LAPW basis set allows compared to the APW basis, i.e. to vary the $u_l$'s and the $\dot{u}_l$'s independently, more planewaves have to be used.

## 3.2   The Full-Potential Description

In the past, in the majority of applications of APW and LAPW methods, the potential in the unit cell $V(\mathbf{r})$ was typically approximated by

$$V(\mathbf{r}) = \begin{cases} V_I^0 = const. & \text{interstitial region} \\ \\ V_{MT}^0(r) & \text{muffin-tin spheres,} \end{cases} \tag{3.12}$$

using a constant potential in the interstitial region and a spherically symmetric potential inside each sphere. While the LAPW method yields accurate results for close-packed metal systems the restrictions to the potential (so-called shape-approximations) become difficult to justify for crystals with open structures such as silizides, perovskides, surfaces or clusters.

In the full-potential LAPW method (FLAPW) [68, 69] there are no shape-approximations in the interstitial region and inside the muffin-tin spheres. The constant interstitial potential $V_I^0$ is replaced by the warped potential $\sum V_I^{\mathbf{G}} e^{i\mathbf{G}\cdot\mathbf{r}}$ and to the spherical muffin-tin potential the non-spherical term is added,

$$V(\mathbf{r}) = \begin{cases} \displaystyle\sum_{\mathbf{G}} V_I^{\mathbf{G}} e^{i\mathbf{G}\cdot\mathbf{r}} & \text{interstitial region} \\ \displaystyle\sum_{L} V_{MT}^{L}(r) Y_L(\hat{\mathbf{r}}) & \text{muffin-tin spheres.} \end{cases} \tag{3.13}$$

The charge density, $\rho(\mathbf{r})$, is represented in the same way as the potential:

$$\rho(\mathbf{r}) = \begin{cases} \displaystyle\sum_{\mathbf{G}} \rho_I^{\mathbf{G}} e^{i\mathbf{G}\cdot\mathbf{r}} & \text{interstitial region} \\ \displaystyle\sum_{L} \rho_{MT}^{L}(r) Y_L(\hat{\mathbf{r}}) & \text{muffin-tin spheres.} \end{cases} \tag{3.14}$$

### 3.2.1 The Muffin-Tin A- and B-Coefficients

Within FLAPW the electron wavefunctions are expanded differently in the interstitial region and the muffin-tins. Each basis function consists of a planewave in the interstitial, which is matched to the radial functions and spherical harmonics in the muffin-tins. The coefficients of the function inside the spheres are determined from the requirement, that the basis functions and their derivatives are continuous at the sphere boundaries. These coefficients play an important role. In this section we will therefore discuss how the matching conditions can be solved and what properties they induce.

In many systems where the FLAPW method can be applied, some atoms are symmetry equivalent, i.e. these atoms can be mapped onto each other by a space group operation $\{\mathbf{R}|\boldsymbol{\tau}\}$. Such a group of atoms is called an atom type, represented by one of the atoms. Let $\{\mathbf{R}^\mu|\boldsymbol{\tau}^\mu\}$ be the operation that maps the atom $\mu$ onto its representative. This atom can now be assigned a local coordinate frame $S^\mu$, where the origin of $S^\mu$ is at the atoms position $\mathbf{p}^\mu$.

The local frame is chosen such that the unit vectors of the local frame $S^\mu$ are mapped onto those of the global frame by $\mathbf{R}^g$ ($\mathbf{R}^\mu S^\mu = S^g$). The local frame of the representative atom $S^\alpha$ is only translated with respect to

the global frame, i.e. the same rotation $\mathbf{R}^\mu$ maps $S^\mu$ onto $S^\alpha$. The potential (and other quantities) inside the muffin-tins can now be written in terms of the local coordinate system. Due to the symmetry we find $V_{MT^\alpha}(\mathbf{r}^\alpha) = V_{MT^\mu}(\mathbf{r}^\mu)$, where $\mathbf{r}^\alpha$ and $\mathbf{r}^\mu$ are expanded in terms of the local frames $S^\alpha$ and $S^\mu$ respectively. As a consequence the radial functions $u_l(r)$ and the Hamiltonian matrices are the same for all atoms of the same type. This way symmetry is exploited to save memory and computing time (during the calculation of the t-matrices).

Any planewave can be expanded into spherical harmonics via the Rayleigh expansion,

$$e^{i\mathbf{Kr}} = 4\pi \sum_L i^l \, j_l(rK) \, Y_L^*(\hat{\mathbf{K}}) \, Y_L(\hat{\mathbf{r}}), \tag{3.15}$$

where $r = |\mathbf{r}|$, $K = |\mathbf{K}|$ and $\mathbf{K}$ abbreviates $(\mathbf{G} + \mathbf{k})$. Looked at from the local frame $\mathbf{K}$ and $\mathbf{p}^\mu$ appear rotated, besides the origin of the local frame is shifted. Therefore, the planewave has the following form in the local frame:

$$e^{i(\mathbf{R}^\mu\mathbf{K})(\mathbf{r}+\mathbf{R}^\mu\mathbf{p}^\mu)} \tag{3.16}$$

Thus, the Rayleigh expansion of the planewave in the local frame is given by:

$$e^{i\mathbf{Kp}^\mu} \, 4\pi \sum_L i^l \, j_l(rK) \, Y_L^*(\mathbf{R}^\mu\hat{\mathbf{K}}) \, Y_L(\hat{\mathbf{r}}) \tag{3.17}$$

The requirement of continuity of the wavefunctions at the sphere boundary leads to the equation

$$\sum_L A_L^{\mu\mathbf{G}}(\mathbf{k}) \, u_l(R_{MT^\alpha})Y_L(\hat{\mathbf{r}}) + B_L^{\mu\mathbf{G}}(\mathbf{k}) \, \dot{u}_l(R_{MT^\alpha})Y_L(\hat{\mathbf{r}})$$
$$= e^{i\mathbf{Kp}^\mu} \, 4\pi \sum_L i^l \, j_l(rK) \, Y_L^*(\mathbf{R}^\mu\hat{\mathbf{K}}) \, Y_L(\hat{\mathbf{r}}), \tag{3.18}$$

where $R_{MT^\alpha}$ is the muffin-tin radius of the atom type $\alpha$. The second requirement is, that the derivative with respect to $r$, denoted by $\partial/\partial r = '$, is also continuous

$$\sum_L A_L^{\mu\mathbf{G}}(\mathbf{k}) \, u_l'(R_{MT^\alpha})Y_L(\hat{\mathbf{r}}) + B_L^{\mu\mathbf{G}}(\mathbf{k}) \, \dot{u}_l'(R_{MT^\alpha})Y_L(\hat{\mathbf{r}})$$
$$= e^{i\mathbf{Kp}^\mu} \, 4\pi \sum_L i^l \, Kj_l'(rK) \, Y_L^*(\mathbf{R}^\mu\hat{\mathbf{K}}) \, Y_L(\hat{\mathbf{r}}). \tag{3.19}$$

These conditions can only be satisfied, if the coefficients of each spherical harmonic $Y_L(\hat{\mathbf{r}})$ are equal. Solving the resulting equations for $A_L^{\mu\mathbf{G}}(\mathbf{k})$ and

$B_L^{\mu\mathbf{G}}(\mathbf{k})$ yields:

$$
\begin{aligned}
A_L^{\mu\mathbf{G}}(\mathbf{k}) &= e^{i\mathbf{K}\mathbf{p}^\mu}4\pi\frac{1}{W}i^l\,Y_L^*(\mathbf{R}^\mu\hat{\mathbf{K}}) \\
&\quad [\dot{u}_l(R_{MT^\alpha})Kj_l'(R_{MT^\alpha}K) - \dot{u}_l'(R_{MT^\alpha})j_l(R_{MT^\alpha}K)] \\
B_L^{\mu\mathbf{G}}(\mathbf{k}) &= e^{i\mathbf{K}\mathbf{p}^\mu}4\pi\frac{1}{W}i^l\,Y_L^*(\mathbf{R}^\mu\hat{\mathbf{K}}) \\
&\quad [u_l'(R_{MT^\alpha})j_l(R_{MT^\alpha}K) - u_l(R_{MT^\alpha})Kj_l'(R_{MT^\alpha}K)]
\end{aligned}
\tag{3.20}
$$

The Wronskian $W$ is given by:

$$
W = [\dot{u}_l(R_{MT^\alpha})u_l'(R_{MT^\alpha}) - u_l(R_{MT^\alpha})\dot{u}_l'(R_{MT^\alpha})]
\tag{3.21}
$$

**Transformation of the FLAPW basis functions in systems that possess inversion symmetry**

Planewaves transform in a very simple way under the operation $\mathbf{r} \to -\mathbf{r}$. Let $\mathcal{I}$ be the inversion operator:

$$
\mathcal{I}e^{i\mathbf{K}\mathbf{r}} = e^{-i\mathbf{K}\mathbf{r}} = \left(e^{i\mathbf{K}\mathbf{r}}\right)^*
\tag{3.22}
$$

The FLAPW basis functions still have this property, i.e. $\varphi_{\mathbf{G}}(\mathbf{k}, -\mathbf{r}) = \varphi_{\mathbf{G}}^*(\mathbf{k}, \mathbf{r})$. Clearly, the system must possess inversion symmetry, because only if there is an equivalent atom at the position $-\mathbf{p}^\mu$ to each atom $\mu$ at position $\mathbf{p}^\mu$, the basis functions inside the corresponding spheres can be complex conjugates. The value of the basis function $\varphi_{\mathbf{G}}(\mathbf{k}, \mathbf{r})$ inside the muffin-tin $\mu$ is give by:

$$
\varphi_{\mathbf{G}}(\mathbf{k}, \mathbf{r}) = \sum_L A_L^{\mu\mathbf{G}}(\mathbf{k})\,u_l(r)Y_L(\hat{\mathbf{r}}) + B_L^{\mu\mathbf{G}}(\mathbf{k})\,\dot{u}_l(r)Y_L(\hat{\mathbf{r}})
\tag{3.23}
$$

The vector $-\mathbf{r}$ lies in the opposite muffin-tin at the position $-\mathbf{p}^\mu$. Let's denote this atom by $-\mu$. Thus, we find:

$$
\varphi_{\mathbf{G}}(\mathbf{k}, -\mathbf{r}) = \sum_L A_L^{-\mu\mathbf{G}}(\mathbf{k})\,u_l(r)Y_L(\hat{\mathbf{r}}) + B_L^{-\mu\mathbf{G}}(\mathbf{k})\,\dot{u}_l(r)Y_L(\hat{\mathbf{r}})
\tag{3.24}
$$

The argument of the spherical harmonic is $\hat{\mathbf{r}}$ rather than $-\hat{\mathbf{r}}$, because the vector is expanded in the local frame of the atom $-\mu$. Substituting the explicit form of $A_L^{-\mu\mathbf{G}}(\mathbf{k})$ and $B_L^{-\mu\mathbf{G}}(\mathbf{k})$ from (3.20), yields:

$$
\varphi_{\mathbf{G}}(\mathbf{k}, -\mathbf{r}) = \sum_L e^{i\mathbf{K}(-\mathbf{p}^\mu)}\,i^l\,Y_L^*(-\mathbf{R}^\mu\hat{\mathbf{K}})\,Y_L(\hat{\mathbf{r}})\{Au_l(r) + B\dot{u}_l(r)\}
\tag{3.25}
$$

where it has been used, that $\mathbf{p}^{-\mu} = -\mathbf{p}^\mu$ and $\mathbf{R}^{-\mu} = -\mathbf{R}^\mu$, $A$ and $B$ abbreviates all terms in (3.20) that are real and do not depend on $r$ or $\hat{\mathbf{r}}$. Using that $Y_L(\hat{\mathbf{r}}) = (-1)^l\, Y_L(\hat{\mathbf{r}})$ (3.25) becomes:

$$\varphi_{\mathbf{G}}(\mathbf{k}, -\mathbf{r}) = \sum_L e^{-i\mathbf{K}(\mathbf{p}^\mu)}\, (-i)^l\, Y_L^*(\mathbf{R}^\mu \hat{\mathbf{K}})\, Y_L(\hat{\mathbf{r}})\{Au_l(r) + B\dot{u}_l(r)\} \quad (3.26)$$

In the last step it can be exploited that $Y_{l-m}(\hat{\mathbf{r}}) = (-1)^m\, Y_{lm}^*(\hat{\mathbf{r}})$. Substituting $m' = -m$ (3.26) becomes:

$$\varphi_{\mathbf{G}}(\mathbf{k}, -\mathbf{r}) = \sum_{lm'} e^{-i\mathbf{K}(\mathbf{p}^\mu)}\, (-i)^l\, Y_{lm'}(\mathbf{R}^\mu \hat{\mathbf{K}})\, Y_{lm'}^*(\hat{\mathbf{r}})\{Au_l(r) + B\dot{u}_l(r)\} \quad (3.27)$$

Hence, we have shown, that the FLAPW basis functions transform according to

$$\varphi_{\mathbf{G}}(\mathbf{k}, -\mathbf{r}) = \varphi_{\mathbf{G}}^*(\mathbf{k}, \mathbf{r}) \tag{3.28}$$

in the interstitial region and the muffin-tins, if the system possesses inversion symmetry.

## The Hamiltonian Matrix of Systems with Inversion Symmetry

The property of the FLAPW basis functions derived in the previous section leads to property of the Hamiltonian and overlap matrix. In systems that possess inversion symmetry these two matrices are real symmetric rather than complex hermitian. The Hamiltonian depends explicitly on $\mathbf{r}$ via the potential. The matrix elements are given by:

$$H^{\mathbf{G'G}}(\mathbf{k}) = \int \varphi_{\mathbf{G'}}^*(\mathbf{k}, \mathbf{r})\mathcal{H}(\mathbf{r})\varphi_{\mathbf{G}}(\mathbf{k}, \mathbf{r}d^3 r \tag{3.29}$$

Substituting $\mathbf{r'} = -\mathbf{r}$ yields:

$$H^{\mathbf{G'G}}(\mathbf{k}) = \int \varphi_{\mathbf{G'}}(\mathbf{k}, \mathbf{r'})\mathcal{H}(\mathbf{r'})\varphi_{\mathbf{G}}^*(\mathbf{k}, \mathbf{r'})d^3 r \tag{3.30}$$

where (3.28) and $\mathcal{H}(\mathbf{r}) = \mathcal{H}(-\mathbf{r})$ have been used. In addition the Hamiltonian operator is real, i.e. $\mathcal{H}(\mathbf{r}) = \mathcal{H}^*(\mathbf{r})$. Thus, we finally obtain:

$$\begin{aligned} H^{\mathbf{G'G}}(\mathbf{k}) &= \int \varphi_{\mathbf{G'}}(\mathbf{k}, \mathbf{r'})\mathcal{H}^*(\mathbf{r'})\varphi_{\mathbf{G}}^*(\mathbf{k}, \mathbf{r'}d^3 r \\ &= \left(H^{\mathbf{G'G}}(\mathbf{k})\right)^*. \end{aligned} \tag{3.31}$$

Apparently, the same relation holds for the overlap matrix. The fact that the two matrices are real means a great simplification in actual calculation.

In principle, the diagonalization of a hermitian matrix is no more difficult than in the real case. However, one complex multiplication contains four real multiplication, and therefore the complex problem is far more "expensive" than the real, and the diagonalization needs the biggest part of the computing time in each iteration.

## 3.2.2   The Generalized Eigenvalue Problem

The solution of the eigenvalue problem has to be carried out separately for every Bloch vector, using the basis set and the Hamiltonian matrix set up for this Bloch vector. Having this established, the index $\mathbf{k}$ to the basis functions and the Hamiltonian matrix will here be omitted for simplicity.

It should be noted that the FLAPW basis functions do not form an orthogonal basis set, although in general the planewaves do. The reason is that the muffin-tin spheres are cut out from the integration region in which the orthogonality is defined (the unit cell). An additional contribution comes from the muffin-tin. Even though the $u_l(r)Y_L$ and $\dot{u}_l(r)Y_L$ are mutually orthogonal, in general each planewave couples to all functions in the spheres. Due to the non-orthogonality of the basis functions, the overlap matrix $\mathbf{S}$ is not a diagonal, but a hermitian matrix, with elements

$$S_{\mathbf{G'G}} = \int \varphi_{\mathbf{G'}}^*(\mathbf{r})\varphi_{\mathbf{G}}(\mathbf{r})d^3r. \tag{3.32}$$

The secular equation (3.4), in the matrix form written as

$$\{\mathbf{H} - \epsilon_i\mathbf{S}\}\,\mathbf{c}_i = 0, \tag{3.33}$$

where the eigenvector $\mathbf{c}_i$ is the coefficient vector corresponding to the $\mathrm{i}^{th}$ eigenvalue, is called a generalized eigenvalue problem.

However, this problem can be reduced to a standard eigenvalue problem using the Cholesky decomposition. It can be shown [70] that any hermitian and positive definite matrix can be decomposed into a matrix product of a lower triangular with only positive diagonal elements matrix and its transposed. Clearly, the overlap matrix satisfies these conditions and can be written

$$\mathbf{S} = \mathbf{LL}^{tr} \tag{3.34}$$

Therefore (3.33) becomes

$$\mathbf{Hc}_i = \epsilon_i\mathbf{LL}^{tr}\mathbf{c}_i \tag{3.35}$$

multiplying from the left with $\mathbf{L}^{-1}$ and introducing a unit matrix we get

$$\mathbf{L}^{-1}\mathbf{H}(\mathbf{L}^{-1})^{tr}\mathbf{L}^{tr}\mathbf{c}_i = \epsilon_i\mathbf{L}^{tr}\mathbf{c}_i \tag{3.36}$$

defining

$$\mathbf{P} = \mathbf{L}^{-1}\mathbf{H}(\mathbf{L}^{-1})^{tr}, \quad \mathbf{x}_i = \mathbf{L}^{tr}\mathbf{c}_i \tag{3.37}$$

we finally have

$$\mathbf{P}\mathbf{x}_i = \epsilon_i\mathbf{x}_i \tag{3.38}$$

Thus the generalized eigenvalue problem has been reduced to a simple eigenvalue problem. The eigenvectors $\mathbf{c}_i$ can be obtained by the back-transformation

$$\mathbf{c}_i = (\mathbf{L}^{tr})^{-1}\mathbf{x}_i \tag{3.39}$$

## 3.3   Film Calculations within FLAPW

The ability to treat surfaces has become very important nowadays with the growing number of investigations in this area. It is necessary in this case to make some adjustments to the basis set, since the translation symmetry in the direction perpendicular to the surface is broken, and only the 2-dimensional symmetry parallel to the surface is left to be used to reduce the problem. In our approach surfaces are approximated by thin films, typically 10–15 atomic layers thick. Obviously, this approximation, which is called the thin-slab approximation, can only yield good results if the interaction between the two surfaces of the film is week enough, so that each of them shows the properties of the surfaces of an ideal semi-infinite crystal. In the case of film calculations space is divided into three distinct regions, the muffin-tins, the interstitial and the vacuum region (Fig. 3.2). The interstitial region now stretches from $-D/2$ to $D/2$ in z-direction, which is defined to be the direction perpendicular to the film. The representation of the wavefunctions inside the muffin-tin spheres remains exactly the same as in the bulk case. Since the periodicity along the z-direction is lost, the unit cell extends principally from $-\infty$ to $\infty$ in z-direction. Still the wavefunctions can be expanded in terms of planewaves. However, the wavevectors perpendicular to the film are not defined in terms of $D$, but in terms of $\tilde{D}$, which is chosen larger than $D$ to gain greater variational freedom. Therefore, the planewaves have the form

$$\varphi_{\mathbf{G}_\parallel G_\perp}(\mathbf{k}_\parallel, \mathbf{r}) = e^{i(\mathbf{G}_\parallel + \mathbf{k}_\parallel)\cdot\mathbf{r}_\parallel} \, e^{iG_\perp z} \tag{3.40}$$

with

$$G_\perp = \frac{2\pi n}{\tilde{D}} \tag{3.41}$$

where $\mathbf{G}_\parallel$ and $\mathbf{k}_\parallel$ are the 2-dimensional wave- and Bloch vectors, $\mathbf{r}_\parallel$ is the parallel component of $\mathbf{r}$ and $G_\perp$ is the wavevector perpendicular to the film. The basis functions in the vacuum region are constructed in the same spirit
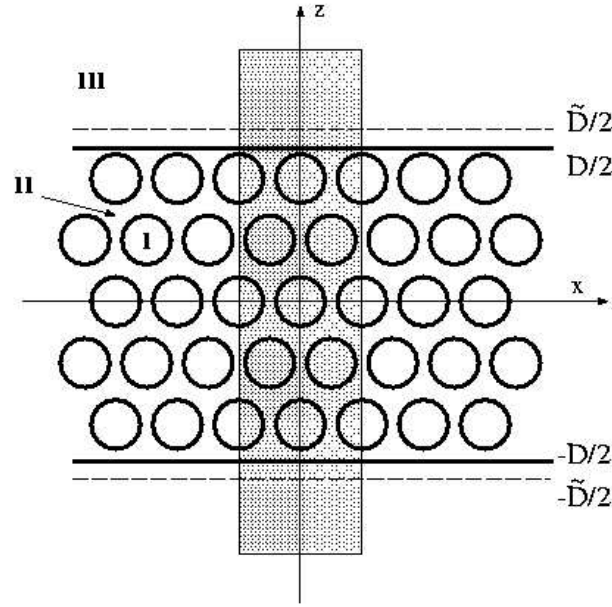
Figure 3.2: The unit cell in film calculations: (I) the muffin-tin spheres; (II) the interstitial region; the film is delimited on both sides by vacuum (III)

as the functions in the muffin-tins [71]. They consist of planewaves parallel to the film, and a z-dependent function $u_{\mathbf{G}_\parallel}(\mathbf{k}_\parallel, z)$, which solves the corresponding 1-dimensional Schrödinger equation (3.42), plus its energy derivative $\dot{u}_{\mathbf{G}_\parallel}(\mathbf{k}_\parallel, z)$.

$$\left\{ -\frac{\hbar^2}{2m}\frac{\partial^2}{\partial z^2} + V_0(z) - E_{vac} + \frac{\hbar^2}{2m}(\mathbf{G}_\parallel + \mathbf{k}_\parallel)^2 \right\} u_{\mathbf{G}_\parallel}(\mathbf{k}_\parallel, z) = 0 \qquad (3.42)$$

$E_{vac}$ is the vacuum energy parameter and $V_0(z)$ is the planar averaged part of the vacuum potential. As in the case of $\dot{u}_l$ in the muffin-tins, the function $\dot{u}_{\mathbf{G}_\parallel}(\mathbf{k}_\parallel, z)$ is calculated from a Schrödinger-like equation, which can be obtained by deriving (3.42) with respect to the energy.

$$\left\{ -\frac{\hbar^2}{2m}\frac{\partial^2}{\partial z^2} + V_0(z) - E_{vac} + \frac{\hbar^2}{2m}(\mathbf{G}_\parallel + \mathbf{k}_\parallel)^2 \right\} \dot{u}_{\mathbf{G}_\parallel}(\mathbf{k}_\parallel, z) = u_{\mathbf{G}_\parallel}(\mathbf{k}_\parallel, z)$$
$$(3.43)$$

The resulting basis functions have the form

$$\varphi_{\mathbf{G}_\parallel G_\perp}(\mathbf{k}_\parallel, \mathbf{r}) = \left\{ A_{\mathbf{G}_\parallel G_\perp}(\mathbf{k}_\parallel) u_{\mathbf{G}_\parallel}(\mathbf{k}_\parallel, z) + B_{\mathbf{G}_\parallel G_\perp}(\mathbf{k}_\parallel)\dot{u}_{\mathbf{G}_\parallel}(\mathbf{k}_\parallel, z) \right\} \, e^{i(\mathbf{G}_\parallel + \mathbf{k}_\parallel)\mathbf{r}_\parallel}$$
$$(3.44)$$

The coefficients $A_{\mathbf{G}_{\parallel}G_{\perp}}(\mathbf{k}_{\parallel})$ and $B_{\mathbf{G}_{\parallel}G_{\perp}}(\mathbf{k}_{\parallel})$ are determined in exactly the same way as it is done for the muffin-tins (MT) by requiring that the functions are continuous and differentiable at the vacuum boundary. To increase the variational freedom in the vacuum basis functions, instead of the energy parameter $E_{vac}$ a whole series of $G_{\perp}$-dependent energy parameters, $E_{vac}^{i} = E_{vac}^{G_{\perp}} = E_{vac} - \frac{\hbar^2}{2m}G_{\perp}^2$ can be used [72]. In general this is not necessary, since the energy spectrum of the electrons in the vacuum region is small.

Summarizing, the basis set used for thin film calculations with the FLAPW method is

$$
\varphi_{\mathbf{G}_{\parallel}G_{\perp}}(\mathbf{k}_{\parallel},\mathbf{r}) = 
\begin{cases}
e^{i(\mathbf{G}_{\parallel}+\mathbf{k}_{\parallel})\mathbf{r}_{\parallel}}\ e^{iG_{\perp}z} & \text{Int.} \\[2ex]
\begin{aligned}
&\Big\{A_{\mathbf{G}_{\parallel}G_{\perp}}(\mathbf{k}_{\parallel})u_{\mathbf{G}_{\parallel}}(\mathbf{k}_{\parallel},z)\\
&+B_{\mathbf{G}_{\parallel}G_{\perp}}(\mathbf{k}_{\parallel})\dot{u}_{\mathbf{G}_{\parallel}}(\mathbf{k}_{\parallel},z)\Big\}\,e^{i(\mathbf{G}_{\parallel}+\mathbf{k}_{\parallel})\mathbf{r}_{\parallel}}
\end{aligned} & \text{Vac.} \\[2ex]
\sum_{L} A_{L}^{\mu\mathbf{G}}(\mathbf{k})u_l(r)Y_L(\hat{\mathbf{r}}) + B_{L}^{\mu\mathbf{G}}(\mathbf{k})\dot{u}_l(r)Y_L(\hat{\mathbf{r}}) & \text{MT } \mu.
\end{cases}
$$
$$(3.45)$$

# 3.4 Relativity in Valence Electron Calculations

Relativistic effects are important for the correct numerical description of core or valence electrons. Both core and valence electrons have finite wavefunctions near the nucleus, where the kinetic energy is large. This kinetic energy enhancement becomes more significant for heavier elements and compounds. Additionally, only relativistic effects, in particular the spin-orbit-coupling, introduce a link between spatial and spin coordinates. Thus, information about the orientation of spins relative to the lattice can only be gained if relativity is taken into account. For fully relativistic description of the electronic structure all relativistic effects (mass-velocity, Darwin-term, spin-orbit coupling) have to be taken into account [73]. However, in many applications an approximation is used, where the spin-orbit interaction is neglected. This approximation is called the scalar relativistic approximation. The spin-orbit interaction can be then additionally included, either self-consistently or, with the use of Andersen's force theorem, in a second variational scheme.

### 3.4.1 The Kohn-Sham-Dirac Equation

In a relativistic density functional theory the Kohn-Sham equation has the form of a single particle Dirac equation

$$\left\{ c\boldsymbol{\alpha} \cdot \mathbf{p} + (\beta - 1)\mathrm{mc}^2 + \mathrm{V}^{\mathrm{eff}}(\mathbf{r}) \right\} \boldsymbol{\Psi} = \mathrm{E}\boldsymbol{\Psi} \tag{3.46}$$

$$\boldsymbol{\alpha} = \left( \begin{pmatrix} 0 & \sigma_x \\ \sigma_x & 0 \end{pmatrix}, \begin{pmatrix} 0 & \sigma_y \\ \sigma_y & 0 \end{pmatrix}, \begin{pmatrix} 0 & \sigma_z \\ \sigma_z & 0 \end{pmatrix} \right)^{\mathrm{tr}} = \begin{pmatrix} 0 & \boldsymbol{\sigma} \\ \boldsymbol{\sigma} & 0 \end{pmatrix} \tag{3.47}$$

$$\beta = \begin{pmatrix} \mathbf{I}_2 & 0 \\ 0 & -\mathbf{I}_2 \end{pmatrix} \tag{3.48}$$

Here, $\sigma_x$ $\sigma_y$ $\sigma_z$ are the Pauli matrices and $\boldsymbol{\sigma}$ is the vector of Pauli matrices, $\mathbf{p}$ is the momentum operator, and $I_n$ denotes an $(n \times n)$ unit matrix. $V^{eff}$ is the effective potential, that contains electron-nucleon Coulomb potential, Hartree potential and exchange-correlation potential. In the case of non-zero spin-polarization, $V^{eff}$ becomes spin-dependent. Finally, $\boldsymbol{\Psi}$ is the relativistic four component wavefunction.

The straightforward way to solve this problem would be to expand each of the four components of $\boldsymbol{\Psi}$ in terms of the FLAPW basis. However, if all four components were treated with the same accuracy, this would result in a basis set which contains four times as many functions as in the non-relativistic (non-magnetic) case. Since the numerical effort of the Hamiltonian diagonalization scales with the dimension of the matrix to the power of three, this would increase the computing time needed for the diagonalization by a factor of 64.

The FLAPW implementation we use introduces some approximations to make relativistic calculations more efficient. One of these approximations is the scalar relativistic approximations, which has been suggested by D.D. Koelling and B.N. Harmon [74], where the spin-orbit term is neglected, and spin and spatial coordinates become decoupled. Hence, the Hamiltonian matrix reduces to two matrices of half the size, which can be diagonalized separately. This saves a factor of four in computing time. The scalar relativistic approximation will be discussed more detailed in the next section. It should be noted, that relativistic effects are only significant close to the nucleus, where the kinetic energy is large. It is therefore reasonable to treat the interstitial region and the vacuum non-relativistically. Thus, merely within the muffin-tins the electrons are treated relativistically. And only the large component of $\boldsymbol{\Psi}$ is matched to the non-relativistic wavefunctions at the boundary

between the muffin-tins and the interstitial region, because the small component is already negligible at this distance from the nucleus. The small component is attached to the large component, and cannot be varied independently. However, this is a sensible approximation for two reasons: Firstly even inside the muffin-tin sphere the large component is still much bigger than the small component, and plays the more important role, and secondly the two components are determined by solving the scalar relativistic equations for the spherically averaged potential. Therefore, they are very well suited to describe the wavefunctions.

Hence, the size of the basis set and the Hamiltonian matrix remains the same as in non-relativistic calculations, but the problem has to be solved twice, once for each direction of spin. This amounts to a numerical effort, that is equal to that needed in spin-polarized non-relativistic calculations.

## 3.4.2 The Scalar Relativistic Approximation

As it was pointed out in the previous section, the electrons are only treated relativistically inside the muffin-tin spheres. Thus, the first problem that has to be addressed is the construction of the relativistic radial function. This is done by solving the scalar relativistic equation, including only the spherically averaged part of the potential. The starting point is the following Dirac equation.

$$\left\{ c\boldsymbol{\alpha} \cdot \mathbf{p} + (\beta - 1)\mathrm{mc}^2 + \mathrm{V(r)} \right\} \boldsymbol{\Psi} = \mathrm{E}\boldsymbol{\Psi} \tag{3.49}$$

The solution of (3.49) is discussed in many textbooks, e.g. E.M. Rose [75]. Due to spin-orbit coupling $m$ and $m_s$ are not good quantum numbers any more, and they have to be replaced by the quantum numbers $\kappa$ and $\mu$ (or $j$ and $\mu$), which are eigenvalues of the operators $K$ and the z-component of the total angular momentum $j_z$ (or the total angular momentum $\mathbf{j}$ and $j_z$) respectively. $K$ is defined by

$$K = \beta(\boldsymbol{\sigma} \cdot \mathbf{l} + 1) \tag{3.50}$$

The solutions of (3.49) have the form

$$\boldsymbol{\Psi} = \boldsymbol{\Psi}_{\kappa\mu} = \begin{pmatrix} g_\kappa(r)\chi_{\kappa\mu} \\ if_\kappa(r)\chi_{-\kappa\mu} \end{pmatrix}, \tag{3.51}$$

where $g_\kappa(r)$ is the large component, $f_\kappa(r)$ is the small component, $\chi_{\kappa\mu}$ and $\chi_{-\kappa\mu}$ are spin angular functions, which are eigenfunctions of $\mathbf{j}$, $j_z$, $K$ and $\mathbf{s}^2$

with eigenvalues $j$, $\mu$, $\kappa$ (-$\kappa$) and $s = 1/2$ respectively. The spin angular functions can be expanded into a sum of products of spherical harmonics and Pauli spinors, where the expansion coefficients are the Clebsch-Gordon coefficients. The radial functions have to satisfy the following set of coupled equations.

$$\begin{pmatrix} -\dfrac{\kappa+1}{r} - \dfrac{\partial}{\partial r} & 2Mc \\ \dfrac{1}{c}(V(r) - E) & \dfrac{\kappa - 1}{r} - \dfrac{\partial}{\partial r} \end{pmatrix} \begin{pmatrix} g_\kappa(r) \\ f_\kappa(r) \end{pmatrix} = 0 \qquad (3.52)$$

with

$$M = m + \frac{1}{2c^2}(E - V(r)). \qquad (3.53)$$

To derive the scalar relativistic approximation D.D. Koelling and B.N. Harmon [74] introduce the following transformation.

$$\begin{pmatrix} g_\kappa(r) \\ \phi_\kappa(r) \end{pmatrix} = \begin{pmatrix} 1 & 0 \\ \dfrac{1}{2Mc}\dfrac{\kappa+1}{r} & 1 \end{pmatrix} \begin{pmatrix} g_\kappa(r) \\ f_\kappa(r) \end{pmatrix} \qquad (3.54)$$

Using this transformation (3.52) becomes

$$\begin{pmatrix} -\dfrac{\partial}{\partial r} & 2Mc \\ \dfrac{1}{2Mc}\dfrac{l(l+1)}{r^2} + \dfrac{1}{c}(V(r) - E) + \dfrac{\kappa+1}{r}\dfrac{M'}{2M^2 c} & -\dfrac{2}{r} - \dfrac{\partial}{\partial r} \end{pmatrix} \begin{pmatrix} g_\kappa(r) \\ \phi_\kappa(r) \end{pmatrix} = 0,$$
$$(3.55)$$

where $M'$ denotes the derivative of $M$ with respect to $r$ ($\partial M/\partial r$), and the identity $\kappa(\kappa+1) = l(l+1)$ has been used. Recalling, that $\kappa$ is the eigenvalue of $K = \beta(\boldsymbol{\sigma} \cdot \mathbf{l} + 1)$ the term $(\kappa + 1)M'/2M^2 cr$ can be identified as the spin-orbit term. This term is dropped in the scalar relativistic approximation, because it is the only one, that causes coupling of spin up and spin down contributions. The radial functions $g_l(r)$ and $\phi_l(r)$ (the index $\kappa$ has been replaced by $l$) can now be calculated from the following set of differential equations.

$$\frac{\partial}{\partial r} g_l(r) = 2Mc\phi_l(r) \qquad (3.56)$$

$$\frac{\partial}{\partial r}\phi_l(r) = \left( \frac{1}{2Mc}\frac{l(l+1)}{r^2} + \frac{1}{c}(V(r) - E) \right) g_l(r) - \frac{2}{r}\phi_l(r) \quad (3.57)$$

The energy derivative of these yields straightforwardly a set of equations for $\dot{g}_l(r)$ and $\dot{\phi}_l(r)$, which are the relativistic analog of $\dot{u}_l(r)$. For numerical

reasons the functions $g_l(r)$ and $\phi_l(r)$ are replaced by $p_l(r) = rg_l(r)$ and $q_l(r) = cr\phi_l(r)$. In our implementation of FLAPW the radial wavefunctions are normalized according to

$$\left\langle \begin{pmatrix} g_l \\ \phi_l \end{pmatrix} \middle| \begin{pmatrix} g_l \\ \phi_l \end{pmatrix} \right\rangle = \int_0^{R_{MT}} (g_l^2(r) + \phi_l^2(r)) r^2 dr = 1 \qquad (3.58)$$

The energy derivatives of the radial functions have to be made orthogonal to the radial functions.

$$\left\langle \begin{pmatrix} g_l \\ \phi_l \end{pmatrix} \middle| \begin{pmatrix} \dot{g}_l \\ \dot{\phi}_l \end{pmatrix} \right\rangle = 0 \qquad (3.59)$$

Thus, the scalar relativistic FLAPW basis set is

$$\varphi_{\mathbf{G}_\parallel G_\perp}(\mathbf{r}) = \begin{cases} \dfrac{1}{\sqrt{\Omega}} \, e^{i(\mathbf{G}_\parallel + \mathbf{k}_\parallel)\mathbf{r}_\parallel} \, e^{iG_\perp z} & Int. \\[2ex] \left\{ A_{\mathbf{G}_\parallel G_\perp} u_{\mathbf{G}_\parallel}(z) + B_{\mathbf{G}_\parallel G_\perp} \dot{u}_{\mathbf{G}_\parallel}(z) \right\} \, e^{i(\mathbf{G}_\parallel + \mathbf{k}_\parallel)\mathbf{r}_\parallel} & Vac. \\[2ex] \displaystyle\sum_{\substack{\alpha \\ lm}} A_{lm}^{\alpha\mathbf{Gk}} \begin{pmatrix} g_l(r) \\ \phi_l(r) \end{pmatrix} Y_{lm}(\hat{\mathbf{r}}) + B_{lm}^{\alpha\mathbf{Gk}} \begin{pmatrix} \dot{g}_l(r) \\ \dot{\phi}_l(r) \end{pmatrix} Y_{lm}(\hat{\mathbf{r}}) & MT \end{cases}$$

$$(3.60)$$

Note that the Pauli-spinors have been omitted, since the spin up and down problems are solved independently within the scalar relativistic approximation. Rewriting (3.55)

$$\mathcal{H}_{SP} \begin{pmatrix} g_l(r) \\ \phi_l(r) \end{pmatrix} = E \begin{pmatrix} g_l(r) \\ \phi_l(r) \end{pmatrix} \qquad (3.61)$$

with

$$\mathcal{H}_{SP} = \begin{pmatrix} \dfrac{1}{2M} \dfrac{l(l+1)}{r^2} + V(r) & -\dfrac{2c}{r} - c\dfrac{\partial}{\partial r} \\[2ex] c\dfrac{\partial}{\partial r} & -2mc^2 + V(r) \end{pmatrix} \qquad (3.62)$$

a matrix expression for the scalar relativistic Hamiltonian including only the spherically averaged part of the potential can be obtained. For completeness, the radial charge density is defined by

$$\rho_l(r) = \left\langle \begin{pmatrix} g_l \\ f_l \end{pmatrix} \middle| \begin{pmatrix} g_l \\ f_l \end{pmatrix} \right\rangle = \int_0^{R_{MT}} (g_l^2(r) + f_l^2(r)) r^2 dr. \qquad (3.63)$$

# Chapter 4

# Non-Collinear Magnetism

The energy functional of a general magnetic system can be expressed in two ways, as a functional of the charge density $n$ and the magnetization density vector field $\mathbf{m}$, or as a functional of the hermitian $2\times 2$ density matrix $\boldsymbol{\rho}$. The two formulations are completely equivalent. The density matrix is defined by the following equation:

$$\boldsymbol{\rho} = \frac{1}{2}\, n\, \mathbf{I}_2 + \boldsymbol{\sigma}\cdot\mathbf{m} = \frac{1}{2}\left(\begin{array}{cc} n + m_z & m_x - im_y \\ m_x + im_y & n - m_z \end{array}\right). \tag{4.1}$$

The potential matrix can be defined in the same way,

$$\mathbf{V} = V\,\mathbf{I}_2 + \mu_B\,\boldsymbol{\sigma}\cdot\mathbf{B} = \left(\begin{array}{cc} V + \mu_B B_z & \mu_B(B_x - iB_y) \\ \mu_B(B_x + iB_y) & V - \mu_B B_z \end{array}\right). \tag{4.2}$$

The components of the density matrix are given in terms of the solutions of the Kohn-Sham equation:

$$\rho_{\alpha\beta} = \sum_{i=1}^{N} \psi_{i,\alpha}^* \psi_{i,\beta}. \tag{4.3}$$

In an actual implementation of non-collinear magnetism in a computer program these matrix quantities are very useful, though they are less intuitive than the "physical" quantities $n$, $\mathbf{m}$, $V$, and $\mathbf{B}$.

Using the potential matrix (4.2), the Kohn-Sham equation becomes

$$\left\{-\frac{\hbar^2}{2m}\nabla^2\,\mathbf{I}_2 + \mathbf{V}\right\}\boldsymbol{\psi}_i = \epsilon_i\boldsymbol{\psi}_i. \tag{4.4}$$

The kinetic energy part of the Hamiltonian is diagonal in the two spin directions. It is only the off-diagonal part of the hermitian $2 \times 2$ potential

matrix, e.g. $V_{21} = \mu_B(B_x + iB_y)$, that couples the two components of the Pauli spinor $\psi_i$. If the $B$-field is collinear, the spin coordinate frame can always be chosen such that the $B$-field points in the spin z-direction. In this case $V_{21}$, and thus the off-diagonal part of the Hamiltonian, becomes zero, because $B_x$ and $B_y$ are zero. The notation $V_\uparrow = V + \mu_B B_z$, $V_\downarrow = V - \mu_B B_z$ is commonly used for the diagonal elements of $\mathbf{V}$ in the collinear case. Since the two spin directions become completely independent, the spin-up and down problem can be solved separately in two steps. Each step can be treated like the non-magnetic problem with the appropriate potential $V_\uparrow$ or $V_\downarrow$. In practice this means that extending a non-magnetic ab-initio program to collinear magnetism is rather straight forward. In addition collinear calculations are by far less costly. Since the effort required to diagonalize the Hamiltonian matrix scales with the number of basis functions to the third power, diagonalizing two small matrices for each spin is much faster than diagonalizing one matrix of twice the size. It also requires only 1/4 of the memory to store the matrix. Another advantage arises when the system has inversion symmetry. In that case the Hamiltonian and the overlap matrix become real symmetric rather than complex hermitian (cf. Sec. 3.2.1, p. 24). In a general non-collinear calculation the Hamiltonian matrix is always complex, due to the complex Pauli matrix $\sigma_y$, i.e. the term $i\mu_B B_y$ in $V_{21}$. A third point is, that in most cases non-collinearity reduces the symmetry. The consequence is, that the area of the irreducible part of the Brillouin zone increases. The computational effort increases linearly with the number of $k$-points that have to be taken into account for the Brillouin zone integration. So far most magnetic calculations have been performed for collinear systems, because such calculations are more simple and significantly less time consuming.

## 4.1 The Spin Space Groups

The spin-orbit coupling and the dipole interaction, which is usually treated classically, are the only terms in the Hamiltonian that couple real space and spin space. Only these parts of the Hamiltonian create a relation between the spin and the spatial coordinates. When the spin-orbit coupling and the dipole interaction (both terms are of similar size in the systems under consideration) are neglected, real space and spin space can be regarded as completely independent. For this purpose generalized groups, the spin space groups (SSG)[76], have been introduced [77, 78]. The action of a SSG operator $\{\alpha_S | \alpha_R | \mathbf{t}\}$ on a two-component spinor can be defined by

$$\{\alpha_S | \alpha_R | \mathbf{t}\} \boldsymbol{\psi}(\mathbf{r}) = \mathbf{U}(\alpha_S) \boldsymbol{\psi}(\{\alpha_R | \mathbf{t}\}^{-1} \mathbf{r}) = \mathbf{U}(\alpha_S) \boldsymbol{\psi}(\alpha_R^{-1} \mathbf{r} - \alpha_R^{-1} \mathbf{t}), \quad (4.5)$$

where $\boldsymbol{\psi}$ is a two-component spinor, $\alpha_S$ and $\alpha_R$ are the spin and space rotation, respectively, $\mathbf{t}$ is a space translation and $\mathbf{U}$ is the spin $1/2$ rotation matrix (with $\alpha, \beta, \gamma$ Euler angles),

$$\mathbf{U}(\alpha, \beta, \gamma) = \begin{pmatrix} e^{-i\frac{\alpha+\gamma}{2}}\cos(\frac{\beta}{2}) & -e^{-i\frac{\alpha-\gamma}{2}}\sin(\frac{\beta}{2}) \\ e^{i\frac{\alpha-\gamma}{2}}\sin(\frac{\beta}{2}) & e^{i\frac{\alpha+\gamma}{2}}\cos(\frac{\beta}{2}) \end{pmatrix}. \tag{4.6}$$

Under the restriction $\alpha_S = \alpha_R$ we return to the definition of the operations of the usual space group. The operators of the space group are thus a subset of the SSG operators. The condition $\alpha_S = \alpha_R$ implies that the spin and the space coordinates are transformed in the same way. This property is required for operations that leave the Hamiltonian invariant when SOC is taken into account. The relative angle between the lattice and the spin is important in this case. However, when SOC is neglected $\alpha_S$ and $\alpha_R$ can be different. This is a very important feature of the SSG and it is a prerequisite for the treatment of incommensurate spin-spirals within an ab-initio calculation.

## 4.2  Spin-Spirals

A magnetic structure with moments that are rotated by a constant angle from atom to atom along a certain direction of the crystal is called a spin-spiral. This can be described by a reciprocal lattice vector, the spin-spiral vector $\mathbf{q}$. The rotation angle of the magnetic moment of an atom at the position $\mathbf{R}_n$ is then given by $\varphi = \mathbf{q} \cdot \mathbf{R}_n$. The magnetic moment of an atom at the position $\mathbf{R}_n$ is given by

$$\mathbf{M}^n = M(\cos(\mathbf{q} \cdot \mathbf{R}_n + \phi)\sin\theta, \sin(\mathbf{q} \cdot \mathbf{R}_n + \phi)\sin\theta, \cos\theta), \tag{4.7}$$

where $\theta$ is the so-called *cone angle*, a relative angle between the magnetic moment and the rotation axis, and $\phi$ an eventual phase factor, also called *phase angle*. Fig. 4.1 shows four examples of spin-spirals with spin-rotation axis perpendicular (upper two) and parallel (lower two) to the spin-spiral vector $\mathbf{q}$ and different angles between the spin-rotation axis and the magnetic moment. The spin-spiral vector $\mathbf{q}$ is a vector in the real space coordinate frame, while the spin-rotation axis is a direction (vector) in the spin-coordinate frame. Since these two coordinate frames become totally independent when spin-orbit coupling is neglected, the angle between the spin-spiral vector $\mathbf{q}$ and the spin-rotation axis becomes meaningless. In that case the two spirals at the top and the two spirals at the bottom of Fig. 4.1 become completely equivalent. However, the spin spirals with different $\theta$ do not become equivalent. $\theta$ is still a well defined quantity, if SOC is neglected, because the rotation axis is a vector (direction) in spin space.
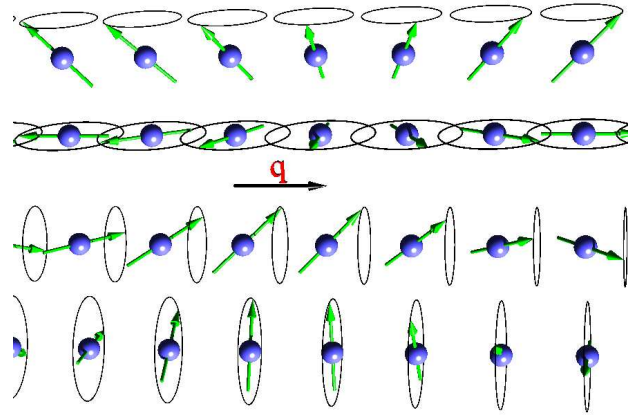
Figure 4.1: Four examples of spin-spirals with spin-rotation axis perpendicular (upper two) and parallel (lower two) to the spin-spiral vector $\mathbf{q}$. For each case two spirals with cone angles of $\theta = \pi/2$ and $\theta = \pi/4$ between the magnetic moment and the rotation axes are shown.

Spin-spirals are frequently called spin density wave, or more specific spiral spin density wave (to distinguish from the longitudinal spin density waves) or frozen magnons. The origin of the last term is that a spin-spiral looks like a "snap shot" of a single magnon at a fixed time. Spin spiral calculations can therefore be used to simulate the effect of temperature on a magnetic system (Sec. 5.3). Another possible application of spin-spirals is the simulation of domain walls including the calculation of the formation energy.

Though there are many possible applications for spin-spiral calculations, it was the discovery of a spiral ground state structure in fcc iron [79] and $4f$ and $5f$ metals [80] that gave rise to many theoretical studies [81, 82]. A very important theorem, which allows the treatment of the spin-spirals in the first-principles calculations without the use of large super-cells, is the generalized Bloch theorem [83, 84]. This theorem, however, can only be proved when SOC is neglected. For this reason the spin-rotation axis will always be considered as parallel to the z-axis of the spin-coordinate frame. Thus, only the $m_x$ and $m_y$ components are rotated, while $m_z$ does not change.

## 4.3   Generalized Bloch Theorem

In the case of an incommensurate spin-spiral the periodicity with respect to lattice translations along the direction of $\mathbf{q}$ is lost. This is a major problem for ab-initio methods that rely on the translational periodicity. However, when spin-orbit coupling is neglected all atoms of the spiral structure are

equivalent. The magnitude of the magnetic moment of each atom is the same and they all "see" the same local environment, i.e. the relative angles between the local moment and the moments of the neighbors are equal. Only the angle between the local moment and the lattice changes from site to site, but that is only significant in the presence of SOC. This leads to a generalization of the Bloch Theorem[83, 84].

Let us consider a spin-spiral structure in a crystal without an external magnetic field and take the rotation angle $\varphi = \mathbf{q} \cdot \mathbf{R}_n$ to be counterclockwise. The only term of the Hamiltonian that changes from site to site is the exchange correlation $B$-field $\mathbf{B}_{xc}$, i.e. the matrix potential $\mathbf{V} = V\mathbf{I}_2 + \mu_B \boldsymbol{\sigma} \cdot \mathbf{B}_{xc}$. Hence, the Hamiltonian satisfies the relation

$$\mathcal{H}(\mathbf{r} + \mathbf{R}_n) = \mathbf{U}(\mathbf{q}\mathbf{R}_n)\mathcal{H}(\mathbf{r})\mathbf{U}^\dagger(\mathbf{q}\mathbf{R}_n). \tag{4.8}$$

As pointed out in the previous section the rotation axis can always be taken to be along the spin z-axis. Thus, the spin 1/2 rotation matrix (Eq.4.6 ) has the form

$$\mathbf{U}(\mathbf{q}\mathbf{R}_n) = \begin{pmatrix} e^{-i\varphi/2} & 0 \\ 0 & e^{i\varphi/2} \end{pmatrix}, \quad \varphi = \mathbf{q} \cdot \mathbf{R}_n. \tag{4.9}$$

Keeping these properties of the Hamiltonian in mind we can define a generalized translation, $\mathcal{T}_n = \{-\mathbf{q}\mathbf{R}_n | \epsilon | \mathbf{R}_n\}$, that combines a lattice translation and a spin rotation. Here $\epsilon$ denotes the identity operation. These translations are members of the SSG but not of the usual space group, since the rotation in spin space differs from the rotation in real space. Applying a generalized translation to $\mathcal{H}\psi$ yields

$$\begin{aligned} \mathcal{T}_n \mathcal{H}(\mathbf{r})\psi(\mathbf{r}) &= \mathbf{U}(-\mathbf{q}\mathbf{R}_n)\mathcal{H}(\mathbf{r} + \mathbf{R}_n)\mathbf{U}^\dagger(-\mathbf{q}\mathbf{R}_n)\mathbf{U}(-\mathbf{q}\mathbf{R}_n)\psi(\mathbf{r} + \mathbf{R}_n) \\ &= \mathcal{H}(\mathbf{r})\mathbf{U}(-\mathbf{q}\mathbf{R}_n)\psi(\mathbf{r} + \mathbf{R}_n). \end{aligned} \tag{4.10}$$

Thus, the generalized translation commutes with the Hamiltonian:

$$\mathcal{T}_n \mathcal{H} = \mathcal{H}\mathcal{T}_n \tag{4.11}$$

It can be shown that the generalized translation operations satisfy the relation

$$\mathcal{T}_n \mathcal{T}_m = \mathcal{T}_m \mathcal{T}_n = \mathcal{T}_{n+m} \tag{4.12}$$

In analogy with the proof of Bloch's theorem[59] it follows that the eigenstates can be chosen such that

$$\mathcal{T}_n \psi(\mathbf{k}, \mathbf{r}) = \mathbf{U}(-\mathbf{q}\mathbf{R}_n)\psi(\mathbf{k}, \mathbf{r} + \mathbf{R}_n) = e^{i\mathbf{k} \cdot \mathbf{R}_n}\psi(\mathbf{k}, \mathbf{r}). \tag{4.13}$$

This formulation of the generalized Bloch Theorem is equivalent to the statement that the eigenstates of the Hamiltonian can be written in the form

$$\boldsymbol{\psi}(\mathbf{k}, \mathbf{r}) = e^{i\mathbf{k}\cdot\mathbf{r}} \begin{pmatrix} e^{-i\mathbf{q}\cdot\mathbf{r}/2}\alpha(\mathbf{k}, \mathbf{r}) \\ e^{+i\mathbf{q}\cdot\mathbf{r}/2}\beta(\mathbf{k}, \mathbf{r}) \end{pmatrix}, \tag{4.14}$$

where $\alpha(\mathbf{k}, \mathbf{r})$ and $\beta(\mathbf{k}, \mathbf{r})$ are functions with translational periodicity, e.g. $\alpha(\mathbf{k}, \mathbf{r}) = \alpha(\mathbf{k}, \mathbf{r} + \mathbf{R}_n)$. We will prove the equivalence of (4.13) and (4.14) in two steps.

(i) $(4.14) \Rightarrow (4.13)$

$$\begin{aligned} \mathcal{T}_n \boldsymbol{\psi}(\mathbf{k}, \mathbf{r}) &= \begin{pmatrix} e^{i\mathbf{q}\cdot\mathbf{R}_n/2} & 0 \\ 0 & e^{-i\mathbf{q}\cdot\mathbf{R}_n/2} \end{pmatrix} e^{i\mathbf{k}\cdot(\mathbf{r}+\mathbf{R}_n)} \begin{pmatrix} e^{-i\mathbf{q}\cdot(\mathbf{r}+\mathbf{R}_n)/2}\alpha(\mathbf{k}, \mathbf{r} + \mathbf{R}_n) \\ e^{+i\mathbf{q}\cdot(\mathbf{r}+\mathbf{R}_n)/2}\beta(\mathbf{k}, \mathbf{r} + \mathbf{R}_n) \end{pmatrix} \\ &= e^{i\mathbf{k}\cdot\mathbf{R}_n}\boldsymbol{\psi}(\mathbf{k}, \mathbf{r}) \end{aligned} \tag{4.15}$$

(ii) $(4.13) \Rightarrow (4.14)$ $\alpha$ and $\beta$ can always be defined to be

$$\alpha(\mathbf{k}, \mathbf{r}) = \frac{\psi_1(\mathbf{k}, \mathbf{r})}{e^{i(\mathbf{k}-\mathbf{q}/2)\mathbf{r}}}, \quad \beta(\mathbf{k}, \mathbf{r}) = \frac{\psi_2(\mathbf{k}, \mathbf{r})}{e^{i(\mathbf{k}+\mathbf{q}/2)\mathbf{r}}}, \tag{4.16}$$

where $\psi_1$ and $\psi_1$ are the two components of the spinor $\boldsymbol{\psi}$. Now it remains to be proved that $\alpha$ and $\beta$ are periodic. Starting from (4.13) we find

$$\begin{pmatrix} e^{i\mathbf{q}\cdot\mathbf{R}_n/2} & 0 \\ 0 & e^{-i\mathbf{q}\cdot\mathbf{R}_n/2} \end{pmatrix} \begin{pmatrix} e^{i(\mathbf{k}-\mathbf{q}/2)(\mathbf{r}+\mathbf{R}_n)}\alpha(\mathbf{k}, \mathbf{r} + \mathbf{R}_n) \\ e^{i(\mathbf{k}+\mathbf{q}/2)(\mathbf{r}+\mathbf{R}_n)}\beta(\mathbf{k}, \mathbf{r} + \mathbf{R}_n) \end{pmatrix} =$$

$$e^{i\mathbf{k}\cdot\mathbf{R}_n} \begin{pmatrix} e^{i(\mathbf{k}-\mathbf{q}/2)\mathbf{r}}\alpha(\mathbf{k}, \mathbf{r} + \mathbf{R}_n) \\ e^{i(\mathbf{k}+\mathbf{q}/2)\mathbf{r}}\beta(\mathbf{k}, \mathbf{r} + \mathbf{R}_n) \end{pmatrix} \tag{4.17}$$

$$\Rightarrow \quad e^{i\mathbf{k}\cdot\mathbf{R}_n} \begin{pmatrix} e^{i(\mathbf{k}-\mathbf{q}/2)\mathbf{r}}\alpha(\mathbf{k}, \mathbf{r} + \mathbf{R}_n) \\ e^{i(\mathbf{k}+\mathbf{q}/2)\mathbf{r}}\beta(\mathbf{k}, \mathbf{r} + \mathbf{R}_n) \end{pmatrix} = e^{i\mathbf{k}\cdot\mathbf{R}_n} \begin{pmatrix} e^{i(\mathbf{k}-\mathbf{q}/2)\mathbf{r}}\alpha(\mathbf{k}, \mathbf{r}) \\ e^{i(\mathbf{k}+\mathbf{q}/2)\mathbf{r}}\beta(\mathbf{k}, \mathbf{r}) \end{pmatrix}$$

$$\Rightarrow \quad \alpha(\mathbf{k}, \mathbf{r} + \mathbf{R}_n) = \alpha(\mathbf{k}, \mathbf{r}), \quad \beta(\mathbf{k}, \mathbf{r} + \mathbf{R}_n) = \beta(\mathbf{k}, \mathbf{r}). \tag{4.18}$$

The fact that $\alpha$ and $\beta$ are periodic functions is very important for the implementation of the spin-spiral into the FLAPW method.

## 4.4  Non-Collinear Magnetism in FLAPW

The implementation of non-collinear magnetism in the first non-collinear ab-initio calculations [85, 86, 87, 88, 89, 81, 90], allows only one direction of

magnetization per atom, i.e. the direction of the magnetization density $\mathbf{m}$ is not allowed to change within one sphere[1], but varies only from sphere to sphere (the atomic sphere approximation for the direction of magnetization). This agrees with the intuitive picture that each atom carries a magnetic moment and these moments differ between the atoms. Such methods describe only the inter-atomic non-collinearity. However, in general the direction of the magnetization changes continuously from site to site, though, in many cases, the deviations from the main atomic direction are only significant in a region between the atom, where the magnitude of the magnetization is rather small. The first calculation that treated the magnetization as a continuous vector quantity was published by Nordström et al. [91]. They followed the most general approach allowing the magnetization to change magnitude and direction continuously, i.e. even within an atom. Thus, their implementation, that is based on the FLAPW method, allows them to also investigate the intra-atomic non-collinearity.

Our method uses a "hybrid" approach (Fig.4.2) where the magnetization is treated as a continuous vector field in the interstitial and in the vacuum regions, while inside each muffin-tin sphere we only allow for one direction of magnetization. Like in the collinear case, it is still possible to work with $V_\uparrow$ and $V_\downarrow$ in the non-collinear case, since we restrict the magnetization to the local quantization quantization axis. Therefore, a local spin-space coordinate-frame is introduced with the z-axis parallel to the local quantization axis. $V_\uparrow$ and $V_\downarrow$ are now spin-up and -down with respect to the local axis. Since both, the potential and the basis functions, are set up in terms of the local spin-coordinate frame, the determination of the basis functions and calculation of the integrals of these functions with the Hamiltonian inside the muffin-tins is completely unchanged. The changes come in, when the basis functions inside the muffin-tins are matched to the plane waves in the interstitial region, because the local spin-coordinate frame $S^\alpha$ is rotated with respect to the global frame $S^g$.

The FLAPW method uses augmented plane waves as basis functions. Therefore, each basis function can be uniquely identified by is wave vector $\mathbf{G}$ and the spin direction. The basis functions in the interstitial region are:

$$e^{i(\mathbf{k}+\mathbf{G})\mathbf{r}}\chi_\sigma^g \tag{4.19}$$

$\chi_\sigma^g$ is a two component spinor. The index $g$ has been added to notify that $\chi_\sigma^g$ is the representation of this spinor in the global spin frame. This representation of the basis functions is used for both collinear and non-collinear calculations. However, the potential matrix $\mathbf{V}$, and thus the Hamiltonian, is diagonal in

---

[1]Within the muffin-tin spheres, however, magnetization can vary in magnitude
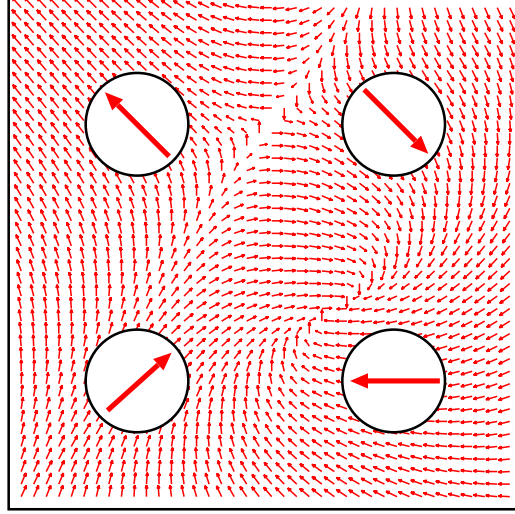
Figure 4.2: Schematic illustration of the representation of the non-collinear magnetization density within the present approach. The magnetization is treated as a continuous vector field in the interstitial region and in the vacuum. Within each muffin-tin the magnetization has a fixed direction and can only vary in magnitude.

the two spin directions in the collinear case. Therefore, the Hamiltonian can be set up and solved separately for the two spin directions. In the non-collinear case the off-diagonal part of $\mathbf{V}$ is not zero anymore. Hence, the full Hamiltonian for both spin directions has to be set up and solved in a single step. In the vacuum we also use the global spin frame for the representation of the basis functions. The basis set is only changed in the muffin-tins, because we use a local spin coordinate frame, which is rotated with respect to the global frame. The consequence is that, when the plane waves are matched to the functions in the muffin tin spheres, each spin direction in the interstitial region has to be matched to both, the spin-up and -down basis functions, in the sphere. Thus, the basis set has the following form.

$$
\varphi_{\mathbf{G},\sigma}(\mathbf{k},\mathbf{r}) = \begin{cases} e^{i(\mathbf{G}+\mathbf{k})\mathbf{r}} \ \chi_\sigma^g & \text{Int.} \\[2mm] \left( A_\sigma^{\mathbf{G}}(\mathbf{k}_\parallel) u_\sigma^{\mathbf{G}_\parallel}(\mathbf{k}_\parallel,z) + B_\sigma^{\mathbf{G}}(\mathbf{k}_\parallel) \dot{u}_\sigma^{\mathbf{G}_\parallel}(\mathbf{k}_\parallel,z) \right) e^{i(\mathbf{G}_\parallel+\mathbf{k}_\parallel)\mathbf{r}_\parallel} \ \chi_\sigma^g & \text{Vac.} \\[2mm] \displaystyle\sum_{\sigma^\alpha} \sum_L \left( A_{L\sigma\sigma^\alpha}^{\mu\mathbf{G}}(\mathbf{k}) u_l(r) + B_{L\sigma\sigma^\alpha}^{\mu\mathbf{G}}(\mathbf{k}) \dot{u}_l(r) \right) Y_L(\hat{\mathbf{r}}) \ \chi_{\sigma^\alpha} & \text{MT}\mu \end{cases}
$$

(4.20)

The sum in the muffin-tins is over the local spin directions and $L$ abbreviates $lm$. The $A$- and $B$-coefficients depend on the local and the global spin and

are obtained from the boundary conditions

$$
e^{i(\mathbf{k}+\mathbf{G})\mathbf{r}}\chi_\sigma = \sum_{\sigma\alpha}\sum_{L}\left(A_{L\sigma\sigma^\alpha}^{\mu\mathbf{G}}(\mathbf{k})u_{l\sigma^\alpha}^\alpha(r) + B_{L\sigma\sigma^\alpha}^{\mu\mathbf{G}}(\mathbf{k})\dot{u}_{l\sigma^\alpha}^\alpha(r)\right)Y_L(\hat{\mathbf{r}})\chi_{\sigma^\alpha}^{\alpha g}.
$$

(4.21)

The global spin-coordinate frame $S^g$ can be transformed into the local frame by a rotation, given by the Euler angles $(\alpha, \beta, 0)$. In this case, the Euler angles are equivalent to the polar angles of the local quantization axis in the global frame, $\alpha = \varphi$, $\beta = \theta$. The magnetization density and the magnetic field, seen from the global frame, $\mathbf{m}^{\alpha g}(\mathbf{r})$ and $\mathbf{B}^{\alpha g}(\mathbf{r})$, are related to the same quantities seen from the local frame by

$$
\begin{aligned}
\mathbf{m}^{\alpha g}(\mathbf{r}) &= \mathbf{R}^{\alpha gl}\,\mathbf{m}^{\alpha l}(\mathbf{r}) \\
\mathbf{B}^{\alpha g}(\mathbf{r}) &= \mathbf{R}^{\alpha gl}\,\mathbf{B}^{\alpha l}(\mathbf{r}).
\end{aligned}
$$

(4.22)

where the index $\alpha$ indicates, that this corresponds to quantities inside the muffin-tin of atom type $\alpha$. The Pauli spinors transform according to

$$
\chi^{\alpha g} = \mathbf{U}^{\alpha gl}\,\chi^{\alpha l},
$$

(4.23)

where

$$
\chi_\uparrow^{\alpha l} = \begin{pmatrix} 1 \\ 0 \end{pmatrix}, \quad \chi_\downarrow^{\alpha l} = \begin{pmatrix} 0 \\ 1 \end{pmatrix}
$$

(4.24)

is their representation in the local spin frame. The matrices $\mathbf{R}^{\alpha gl}$ and $\mathbf{U}^{\alpha gl}$ are given with

$$
\mathbf{R}^{\alpha gl} = \begin{pmatrix} \cos\varphi\cos\theta & -\sin\varphi & \cos\varphi\sin\theta \\ \sin\varphi\cos\theta & \cos\varphi & \sin\varphi\sin\theta \\ -\sin\theta & 0 & \cos\theta \end{pmatrix},
$$

(4.25)

$$
\mathbf{U}^{\alpha gl} = \begin{pmatrix} e^{-i\frac{\varphi}{2}}\cos(\frac{\theta}{2}) & -e^{-i\frac{\varphi}{2}}\sin(\frac{\theta}{2}) \\ e^{i\frac{\varphi}{2}}\sin(\frac{\theta}{2}) & e^{i\frac{\varphi}{2}}\cos(\frac{\theta}{2}) \end{pmatrix}.
$$

(4.26)

# Chapter 5

# Describing Magnetic Systems

In the following chapters we will be dealing with magnetic systems. There-fore, we shortly present here two models describing the magnetic interactions, namely the Stoner and the Heisenberg model. In Sec. 5.3 we will give a description of a method of calculating the Heisenberg exchange interaction parameters from the first principles.

## 5.1 Stoner Model

The one–particle nature of the Kohn–Sham equation makes it possible to derive a Stoner like theory for ferromagnetism [92, 93, 94, 95], which includes correlation effects and provides explicit expressions for the Stoner parameter. Starting point is the assumption, that within the spin-density functional theory the magnetization density $m(\mathbf{r}) = |\mathbf{m}(\mathbf{r})|$ of solids is usually small compared to the electron density $n(\mathbf{r})$. Expanding the exchange correlation energy $\epsilon_{\mathrm{xc}}(n(\mathbf{r}), m(\mathbf{r}))$ into a Taylor series in terms of the parameter $\xi = m/n$ yields

$$\epsilon_{\mathrm{xc}}(n, \xi) = \epsilon_{\mathrm{xc}}(n, 0) + \frac{1}{2}\epsilon_{\mathrm{xc}}''(n, 0)\xi^2 + \cdots \qquad (5.1)$$

On taking the derivative of the exchange-correlation energy with respect to spin-up and spin-down densities,

$$\begin{aligned} n^{\uparrow} &= (n+m)/2 \simeq n(1+\xi)/2 \\ n^{\downarrow} &= (n-m)/2 \simeq n(1-\xi)/2, \end{aligned}$$

$$(5.2)$$

the exchange and correlation potential for the two spin directions becomes

$$\mu_{xc}^{\uparrow(\downarrow)}(\mathbf{r}) = V_{\mathrm{xc}}^{\pm}(\mathbf{r}) = V_{\mathrm{xc}}^{0}(\mathbf{r}) \mp \tilde{V}_{\mathrm{xc}}(\mathbf{r})m(\mathbf{r}) \qquad (5.3)$$
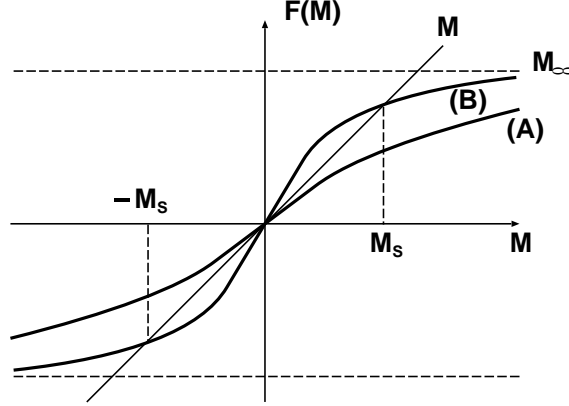
45

Figure 5.1: Graphical solution of (5.10).

(with $(+)$ for $\uparrow$ and $(-)$ for $\downarrow$), where

$$
\begin{aligned}
V_{\text{xc}}^0 &= \epsilon_{\text{xc}}(n,0) + n\frac{\partial \epsilon_{\text{xc}}(n,0)}{\partial n} \\
\tilde{V}_{\text{xc}} &= \frac{1}{n^2}\epsilon_{\text{xc}}''(n,0)m.
\end{aligned}
\tag{5.4}
$$

In the Stoner model this potential shift is expressed in terms of a constant:

$$
V_{\text{xc}}^{\pm}(\mathbf{r}) = V_{\text{xc}}^0(\mathbf{r}) \mp \frac{1}{2}IM \qquad M = \int_{V_{\text{atom}}} m(\mathbf{r})d\mathbf{r} .
\tag{5.5}
$$

$M$ is the total magnetic moment per atom, and $I$ is the exchange integral (Stoner parameter). Because of this constant shift the spatial shape of the potential remains the same as in the nonmagnetic case. Consequently, the solutions of the Kohn-Sham equations also remain unchanged, only the single particle energies $\epsilon_i$ are shifted by the same amount $\mp IM/2$,

$$
\psi_i^{\pm}(\mathbf{r}) = \psi_i^0(\mathbf{r}), \qquad \epsilon_i^{\pm} = \epsilon_i^0 \mp \frac{1}{2}IM
\tag{5.6}
$$

Hence, the whole band structure is spin-split, and the shape of the bands remains unaltered. As a result, the local densities of states (LDOS) projected on an atom for the spin-directions $\pm$, $n^{\pm}(\epsilon)$, are also shifted by $\pm IM/2$.

$$
n^{\pm}(\epsilon) = n(\epsilon \pm \frac{1}{2}IM) .
\tag{5.7}
$$

From this property of the DOS a criterion for the existence of ferromagnetism can be derived. Integrating the density of states up to the Fermi energy $E_{\text{F}}$

| Metal | Na | Al | Cr | Mn | Fe | Co | Ni | Cu | Pd | Pt |
|---|---|---|---|---|---|---|---|---|---|---|
| $n(E_F)$ [(eV)$^{-1}$] | 0.23 | 0.21 | 0.35 | 0.77 | 1.54 | 1.72 | 2.02 | 0.14 | 1.14 | 0.79 |
| $I$ [eV] | 1.82 | 1.22 | 0.76 | 0.82 | 0.93 | 0.99 | 1.01 | 0.73 | 0.68 | 0.63 |
| $In(E_F)$ [eV] | 0.41 | 0.25 | 0.27 | 0.63 | 1.43 | 1.70 | 2.04 | 0.11 | 0.78 | 0.50 |

Table 5.1: Bulk DOS $n(E_F)$ at the Fermi energy ($E_F$) as calculated from nonmagnetic calculations, the Stoner parameter $I$, and the product of both, $In(E_F)$. All results are obtained with the density functional theory in the local density approximation [93, 94].

yields the number of electrons $N$ and the total magnetic moment per atom $M$.

$$N = \int_{\epsilon < E_F} \left[ n(\epsilon + \frac{1}{2}IM) + n(\epsilon - \frac{1}{2}IM) \right] d\epsilon \qquad (5.8)$$

$$M = \int_{\epsilon < E_F} \left[ n(\epsilon + \frac{1}{2}IM) - n(\epsilon - \frac{1}{2}IM) \right] d\epsilon . \qquad (5.9)$$

The self consistency requirement embodied in (5.9) determines the unknown Fermi energy and magnetic moment. Requiring charge neutrality the first equation can be used to obtain the Fermi energy as a function of the magnetization $E_F = E_F(M)$. Substituting this into the second equation leads to a self consistency problem for $M$.

$$M = F(M), \qquad \text{with}$$
$$F(M) = \int_{\epsilon < E_F(M)} \left[ n(\epsilon + \frac{1}{2}IM) - n(\epsilon - \frac{1}{2}IM) \right] d\epsilon . \qquad (5.10)$$

The function $F(M)$ is odd in $M$, $F(0) = 0$, and $F(M) = -F(-M)$, it is a monotonically increasing function, i.e. $F'(0) > 0$, and saturates at the largest possible magnetization $\pm M_\infty = F(\pm\infty)$. A graphical solution of (5.10) is illustrated in Fig. 5.1. Two functions $F(M)$, consistent with the above properties, are plotted. In case A only the trivial nonmagnetic solution $M = 0$ is present, whereas in case B three solutions exist, two of which have non-zero magnetization. From the properties of $F(M)$ follows that (5.10) always has solutions with non-zero magnetization, if the slope of $F'(0) = I\,n(E_F) > 1$. This is finally the Stoner criterion for ferromagnetism:

$$I\,n(E_F) > 1 . \qquad (5.11)$$

The Stoner criterion is an instability condition which expresses the competition between the exchange interaction in terms of the exchange integral $I$ which drives the system into ferromagnetism for large $I$ and the kinetic energy in terms of the DOS which increases in the magnetic states, the more the wider the band width or the lower the density of states, respectively. A big exchange integral and a large nonmagnetic DOS at the Fermi energy favors ferromagnetism. Table 5.1 lists the exchange integral $I$, the local DOS at the Fermi energy $n(E_\mathrm{F})$ derived from nonmagnetic calculations and the product $In(E_\mathrm{F})$ for a number of elemental metals. It shows, that the Stoner condition for ferromagnetism is only fulfilled for Fe, Co, and Ni, precisely those metals that show itinerant ferromagnetism.

## 5.2   Heisenberg Model and Beyond

To predict the magnetic ground state of a magnetic system can be a highly nontrivial problem. In cases, for example, where competing exchange interactions between neighboring atoms cannot be satisfied, the exchange interaction is frustrated which gives rise to a multitude of possible spin-structures. In the past, the magnetism of complex spin structures of itinerant magnets has been almost exclusively discussed within the framework of model Hamiltonians, e.g. the classical Heisenberg Hamiltonian,

$$H_{2\text{-spin}} = -\sum_{\substack{i,j \\ i>j}} J_{ij}\, \mathbf{M}_i \cdot \mathbf{M}_j \;. \tag{5.12}$$

The magnetic moments (usually referred to as spins) localized on the lattice sites $i, j$ are considered as classical vectors $\mathbf{M}$, with the assumption that their magnitudes $M$ are constant. The exchange interaction between the magnetic moments is described by the pair interaction $J_{ij}$. In localized spin systems the $J_{ij}$ can be safely restricted to the ferromagnetic ($J_1 > 0$) or antiferromagnetic ($J_1 < 0$) nearest-neighbor (n.n.) interaction, i.e. $J_{ij} = 0$ for all $i$, $j$, except for $J_{n.n.} = J_1$. Also in itinerant magnets $J_1$ often dominates over the rest of the further distant pairs. However, an attempt to reproduce $T_C$ solely from $J_1$ produces results of limited validity.

Exchange interactions beyond the classical Heisenberg model can be motivated from a perturbation expansion of the Hubbard model [96]. Expanding the Hubbard model into a spin model, replacing the spin operators by classical spin vectors, a second order perturbation expansion reproduces the classical Heisenberg model. The fourth order perturbation treatment (the third order is zero in the absence of spin-orbit interaction) yields two additional terms of different form. One is the four-spin exchange interaction

(4-spin):

$$H_{\text{4-spin}} = -\sum_{ijkl} K_{ijkl}\big[(\mathbf{M}_i\mathbf{M}_j)(\mathbf{M}_k\mathbf{M}_l)+(\mathbf{M}_j\mathbf{M}_k)(\mathbf{M}_l\mathbf{M}_i)-(\mathbf{M}_i\mathbf{M}_k)(\mathbf{M}_j\mathbf{M}_l)\big].$$

The 4-spin interaction arises from the hopping of electrons over four sites, i.e. the process $1 \rightarrow 2 \rightarrow 3 \rightarrow 4 \rightarrow 1$, the other term, resulting from the hopping $1 \rightarrow 2 \rightarrow 1 \rightarrow 2 \rightarrow 1$, is the bi-quadratic exchange:

$$H_{\text{biquadr}} = -\sum_{ij} B_{ij}(\mathbf{M}_i \cdot \mathbf{M}_j)^2. \tag{5.13}$$

The exchange parameters $J_{ij}$, $K_{ijkl}$, and $B_{ij}$ depend on the details of the electronic structure and it is known [97] that for transition-metals the sign and magnitude are rapidly varying functions of the $d$-band filling. In thin films, $M^4 K_1$ and $M^4 B_1$ are about one order of magnitude smaller than $M^2 J_1$, which is for example for Mn/Cu(111) about 30 meV. The higher order spin interactions have then the effect, depending on the sign and value, of splitting the magnetic states which are degenerate when described by the 2-spin Heisenberg model.

In itinerant magnets, the electrons that are responsible for the formation of the magnetic state do participate in the formation of the Fermi-surface and hop across the lattice. Thus, it is by no means clear how far a short-ranged n.n. interaction or even how far the Heisenberg model, and models beyond that, can go in giving a sufficiently good description of the physics of itinerant magnets at surfaces and films. We believe that the combination of ab-initio calculations and the study of model Hamiltonians provides a powerful approach to investigate the magnetic structures of complex magnetic systems.

## 5.3 *Ab-initio* Calculation of Heisenberg Exchange Parameters

Magnetic excitations in itinerant ferromagnets are basically of two different types. One type are the Stoner excitations, in which an electron is excited from an occupied state of the majority-spin band to an empty state of the minority-spin band and creates an electron-hole pair. The Stoner excitations are associated with longitudinal fluctuations of the magnetization. The other type are the spin-waves (magnons) which correspond to collective transverse fluctuations of the magnetization direction. Near the bottom of the excitation spectrum, the density of states of magnons is considerably higher
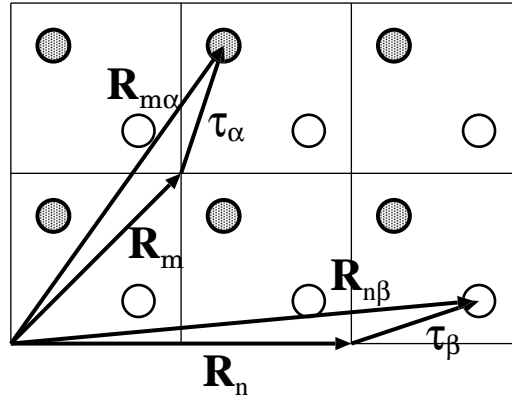
Figure 5.2: A two-dimensional lattice with a two-atoms basis. $\mathbf{R}_{m(n)}$ are the lattice translation vectors, while $\boldsymbol{\tau}_{\alpha(\beta)}$ specify the positions of the atoms $\alpha, \beta$ within the unit cell.

than that of corresponding Stoner excitations, so that the thermodynamics in the low-temperature regime is completely dominated by magnons and Stoner excitations can be neglected. Therefore, it seems reasonable to extend this approximation up to the Curie temperature and to derive an *ab initio* technique of finite-temperature magnetism by neglecting systematically the Stoner excitations.

The time scale of the magnetic moment dynamics is much larger than the time scale of electrons orbiting around an atom and the time scale of the interatomic hopping of electrons. Typical magnon energies for a transition metal are a few tenths of an eV, while the $d$-band width is a few eV. For this reason, we adopt the so-called adiabatic approximation (or the *frozen magnon approximation*), in which we assume that when the system is evolving from a state with a certain configuration of the magnetic moments to an other state with a different moment configuration, the relaxation time of the electronic processes is simply zero. In other words, we can imagine the evolution of the system as a series of "snapshots" of different intermediate configurations (hence the term *frozen* magnon approximation).

In the attempt to describe the finite temperature effects on the magnetic structure, we simulate the thermal excitations with spin-spirals, applying a classical Heisenberg Hamiltonian (Eqn.5.12) to model the magnetic interactions. The part of the total energy (per unit cell) due to these interactions is then obtained from the expression

$$E_M = -\frac{1}{2N} \sum_{\substack{n,m \\ \alpha,\beta \\ (\mathbf{R}_{m\alpha} \neq \mathbf{R}_{n\beta})}} \mathbf{M}_{m\alpha} \mathbf{M}_{n\beta}\, J(\mathbf{R}_{m\alpha}, \mathbf{R}_{n\beta}), \qquad (5.14)$$

where $\mathbf{R}_{m\alpha(n\beta)} \equiv \mathbf{R}_{m(n)} + \boldsymbol{\tau}_{\alpha(\beta)}$. Here, $\mathbf{R}_{m(n)}$ are the lattice translation vectors and $\boldsymbol{\tau}_{\alpha(\beta)}$ are the vectors specifying the positions of the atoms within the unit cell (Fig. 5.2). $\mathbf{M}_{m\alpha(n\beta)}$ are the magnetic moments localized at the sites $\mathbf{R}_{m\alpha(n\beta)}$, while $J(\mathbf{R}_{m\alpha}, \mathbf{R}_{n\beta})$ is the exchange coupling constant for the pair of atoms situated at these sites. The summations using indices $n, m$ are carried out over all unit cells, and the ones using indices $\alpha, \beta$, over all the atoms in the unit cell. The factor $1/2$ takes care of the double counting and the on-site term $(\mathbf{R}_{m\alpha} = \mathbf{R}_{n\beta})$ is left out.

The constants $J(\mathbf{R}_{m\alpha}, \mathbf{R}_{n\beta})$ contain the information about the inter-cite interaction due to the exchange coupling. The knowledge of these exchange interactions is essential for the description of thermal excitations in magnetic solids and their deriving from *ab-initio* calculations is the core problem in the attempt to describe the system with the Heisenberg Hamiltonian. One popular approach employs the Lichtenstein formula [98], which can be easily used in case of a Green functions method. We present here an alternative approach which employs the spin spirals implemented in the `FLEUR` program, and goes back to Halilov *et al.* [47]. In the case of a spin-spiral with the wave vector $\mathbf{q}$, the magnetic moments are described by Eqn. 4.7. Using this equation and defining $\mathbf{R} \equiv \mathbf{R}_n - \mathbf{R}_m$ and $\boldsymbol{\tau}_{\alpha\beta} \equiv \boldsymbol{\tau}_\alpha - \boldsymbol{\tau}_\beta$, equation 5.14 becomes

$$E_M(\mathbf{q};\Theta;\Phi) = -\frac{1}{2}\sum_{\substack{\alpha,\beta \\ \mathbf{R} \\ (\mathbf{R} \neq \boldsymbol{\tau}_{\alpha\beta})}} M_\alpha M_\beta J(\boldsymbol{\tau}_\alpha, \boldsymbol{\tau}_\beta - \mathbf{R})\{\sin\theta_\alpha \sin\theta_\beta \cos[\mathbf{q}\cdot(\boldsymbol{\tau}_{\alpha\beta} - \mathbf{R}) + \phi_\alpha - \phi_\beta]$$

$$+ \cos\theta_\alpha \cos\theta_\beta\}. \tag{5.15}$$

Here, the energy $E_M$ is a function of the spin-spiral vector $\mathbf{q}$, as well as of the cone and phase angles of the spin vectors on all the atoms of the unit cell. The dependence on these angles is in the argument of $E_M$ expressed with $\Theta$, for the set of all cone angles $\{\theta_\alpha\}$ (we remind that the cone angles $\theta_\alpha$ are defined as the angle between the magnetic moment and the rotation axis) and by $\Phi$ for the set of all phase angles $\{\phi_\alpha\}$. To account for the condition $\mathbf{R} \neq \boldsymbol{\tau}_{\alpha\beta}$ under which the sum in Eqn. 5.15 is conducted, from now on we set $J(\boldsymbol{\tau}_\alpha, \boldsymbol{\tau}_\alpha) \equiv 0$, for all the atoms $\alpha$ in the unit cell.

With the aim to obtain the exchange interaction constants $J(\boldsymbol{\tau}_\alpha, \boldsymbol{\tau}_\beta - \mathbf{R})$ at the minimum of computational expense, we define in the following a set of expressions which are evaluated computationally. We first define the Fourier transform

$$J_{\alpha\beta}(\mathbf{q}) = \sum_{\mathbf{R}} J(\boldsymbol{\tau}_\alpha, \boldsymbol{\tau}_\beta - \mathbf{R})e^{i\mathbf{q}\cdot(\boldsymbol{\tau}_{\alpha,\beta} - \mathbf{R})}. \tag{5.16}$$

It is straightforward to show that with the use of this Fourier transform, Eqn. 5.15 becomes

$$E_M(\mathbf{q};\Theta;\Phi) = -\frac{1}{2}\sum_{\alpha,\beta} M_\alpha M_\beta \left\{ \sin\theta_\alpha \sin\theta_\beta \mathcal{R}e\left[J_{\alpha\beta}(\mathbf{q})e^{i(\phi_\alpha-\phi_\beta)}\right] \right.$$
$$\left. +\cos\theta_\alpha \cos\theta_\beta J_{\alpha\beta}(\mathbf{0})\right\}. \tag{5.17}$$

**Symmetry Relations**

Starting from the condition that $J(\mathbf{R}_{m\alpha}, \mathbf{R}_{n\beta})$ are real and symmetric and the definition of the Fourier transform $J_{\alpha\beta}(\mathbf{q})$ (Eqn 5.16), several useful symmetry properties of $J_{\alpha\beta}(\mathbf{q})$ can be derived (valid for each $\mathbf{q}$ vector):

1. $J_{\alpha\beta}(\mathbf{q}) = J_{\beta\alpha}(-\mathbf{q})$

2. $\mathcal{R}e\left[J_{\alpha\beta}(\mathbf{q})\right] = \mathcal{R}e\left[J_{\alpha\beta}(-\mathbf{q})\right]$

3. $\mathcal{I}m\left[J_{\alpha\beta}(\mathbf{q})\right] = -\mathcal{I}m\left[J_{\alpha\beta}(-\mathbf{q})\right]$

   (3a) $\mathcal{I}m\left[J_{\alpha\beta}(\mathbf{0})\right] = 0$

   (3b) $\mathcal{I}m\left[J_{\alpha\alpha}(\mathbf{q})\right] = 0$

4. $J_{\alpha\beta}(\mathbf{q}) = J_{\alpha\beta}(\hat{C}^{-1}\mathbf{q})$, $\hat{C}$ crystal point group symmetry element.

A very important consequence of the relation 4 is that the $\mathbf{q}$ vectors can be sampled from the irreducible wedge of the Brillouin zone and with the symmetry transformations $J_{\alpha,\beta}(\mathbf{q})$ in the rest of the Brillouin zone can be obtained. Moreover, due to the relation 1, even if the system does not possess the inversion symmetry it is not necessary to make two separate calculations for $\mathbf{q}$ and $-\mathbf{q}$. Finally, if the system does possess the inversion symmetry, due to the relations 3 and 4, all the coefficients $J_{\alpha,\beta}(\mathbf{q})$ are real.

## 5.3.1   The Calculational Scheme

To develop a scheme for the calculation of the Fourier transforms $J_{\alpha,\beta}(\mathbf{q})$, we distinguish three different cases.

- <u>**Case 1: $\theta_\lambda = 0$, $\forall\lambda$**</u>  $\boxed{\uparrow\uparrow\uparrow\uparrow\uparrow\uparrow\uparrow}$

  This is the ferromagnetic case. The magnetic moments of all the atoms

in the unit cell are pointing in the same direction. In this case the spin-spiral vector has no meaning and the same total energy is obtained for any **q**:

$$E_M^0 \equiv E_M(\mathbf{q}; 0, ..., 0; 0, ..., 0) = -\frac{1}{2} \sum_{\alpha, \beta} M_\alpha M_\beta J_{\alpha\beta}(\mathbf{0}). \qquad (5.18)$$

- **Case 2: $\theta_\lambda = 0, \; \forall \lambda \neq \mu; \; \theta_\mu \neq 0$** $\boxed{\uparrow\uparrow\uparrow \nearrow \uparrow\uparrow\uparrow}$

In this case all the atoms in the unit cell are ordered ferromagnetically, except for atom $\mu$. Its magnetic moment is tilted by angle $\theta_\mu$ and the spin-spiral running through the system will move only the magnetic moments situated on the atoms of the same kind as $\mu$. With the use of the symmetry relations for the coefficients $J_{\alpha,\beta}(\mathbf{q})$ and Eqn. 5.18, the total energy for this case is found to be

$$E_M^\mu(\mathbf{q}) \equiv E_M(\mathbf{q}; 0, ..., \theta_\mu, ..., 0; 0, ..., 0) =$$

$$= E_M^0 + (1 - \cos\theta_\mu) M_\mu \sum_{\substack{\lambda \\ (\lambda \neq \mu)}} M_\lambda J_{\lambda\mu}(\mathbf{0}) - \frac{1}{2} M_\mu^2 sin^2\theta_\mu \left[ J_{\mu\mu}(\mathbf{q}) - J_{\mu\mu}(\mathbf{0}) \right].$$

$$(5.19)$$

Taking $\mathbf{q} = \mathbf{0}$, we obtain

$$E_M^\mu(\mathbf{0}) - E_M^0 = (1 - \cos\theta_\mu) M_\mu \sum_{\substack{\lambda \\ (\lambda \neq \mu)}} M_\lambda J_{\lambda\mu}(\mathbf{0}), \qquad (5.20)$$

and finally, from Eqns. 5.19 and 5.20,

$$J_{\mu\mu}(\mathbf{q}) - J_{\mu\mu}(\mathbf{0}) = -2\frac{E_M^\mu(\mathbf{q}) - E_M^\mu(\mathbf{0})}{M_\mu^2 \sin^2\theta_\mu}. \qquad (5.21)$$

- **Case 3: $\theta_\lambda = 0, \; \forall \lambda \neq \mu, \nu; \; \theta_\mu, \theta_\nu \neq 0$** $\boxed{\uparrow\nwarrow\uparrow \nearrow\uparrow\uparrow\uparrow}$

This case will appear only if there are two or more magnetic atoms in the unit cell. Keeping the rest of the magnetic moments parallel, the magnetic moments on atoms $\mu$ and $\nu$ are tilted by angles $\theta_\mu$ and

$\theta_\nu$, respectively, so the spin-spiral running through the system changes the orientation of magnetic moments on both of these atoms. Defining $\phi_{\mu\nu} \equiv \phi_\mu - \phi_\nu$, using Eqns. 5.18, 5.19 and the symmetry relations for $J_{\alpha\beta}(\mathbf{q})$, we obtain the total energy as

$$E_M^{\mu\nu}(\mathbf{q}, \phi_{\mu\nu}) \equiv E_M(\mathbf{q}; 0, ..., \theta_\mu, ..., \theta_\nu, ..., 0; 0, ..., \phi_\mu, ..., \phi_\nu, ..., 0) =$$

$$= E_M^\mu(\mathbf{q}) + E_M^\nu(\mathbf{q}) - E_M^0 - M_\mu M_\nu \left\{ sin\theta_\mu sin\theta_\nu \mathcal{R}e\left[ J_{\mu\nu}(\mathbf{q})e^{i\phi_{\mu\nu}} \right] \right.$$

$$\left. + (1 - \cos\theta_\mu)(1 - \cos\theta_\nu) J_{\mu\nu}(\mathbf{0}) \right\}.$$
(5.22)

As we have seen, if the system does not possess inversion symmetry, the coefficients $J_{\mu\nu}(\mathbf{q})$ are complex for $\mu \neq \nu$. Their imaginary part can be obtained as

$$\mathcal{I}m\left[ J_{\mu\nu}(\mathbf{q}) \right] = -\mathcal{R}e\left[ J_{\mu\nu}(\mathbf{q})e^{i\frac{\pi}{2}} \right].$$
(5.23)

For $\mathbf{q} = \mathbf{0}$, from Eqn. 5.23 and symmetry relation $(3a)$, we obtain

$$\mathcal{R}e\left[ J_{\mu\nu}(\mathbf{0})e^{i\frac{\pi}{2}} \right] = -\mathcal{I}m\left[ J_{\mu\nu}(\mathbf{0}) \right] = 0,$$
(5.24)

which together with Eqn. 5.22 yields

$$E_M^{\mu\nu}(\mathbf{0}, \frac{\pi}{2}) - E_M^\mu(\mathbf{0}) - E_M^\nu(\mathbf{0}) + E_M^0 = -M_\mu M_\nu (1 - \cos\theta_\mu)(1 - \cos\theta_\nu) J_{\mu\nu}(\mathbf{0}).$$
(5.25)

Putting this result back into Eqn. 5.22, for a configuration of spins in which $\phi_{\mu\nu} = 0$ we obtain the expression for the real part of $J_{\mu\nu}(\mathbf{q})$,

$$\mathcal{R}e[J_{\mu\nu}(\mathbf{q})] = \frac{E_M^{\mu\nu}(\mathbf{0}, \frac{\pi}{2}) - E_M^{\mu\nu}(\mathbf{q}, 0) + [E_M^\mu(\mathbf{q}) - E_M^\mu(\mathbf{0})] + [E_M^\nu(\mathbf{q}) - E_M^\nu(\mathbf{0})]}{M_\mu M_\nu \sin\theta_\mu \sin\theta_\nu},$$
(5.26)

while for a configuration of spins in which $\phi_{\mu\nu} = \pi/2$, the expression for the imaginary part emerges:

$$\mathcal{I}m[J_{\mu\nu}(\mathbf{q})] = \frac{E_M^{\mu\nu}(\mathbf{q}, \frac{\pi}{2}) - E_M^{\mu\nu}(\mathbf{q}, 0)}{M_\mu M_\nu \sin\theta_\mu \sin\theta_\nu} - \mathcal{R}e[J_{\mu\nu}(\mathbf{q})].$$
(5.27)

## 5.3.2   The Brillouin Zone Integration

We have established now that the Fourier transforms $J_{\mu\nu}(\mathbf{q})$ can be obtained from the differences in total energy between the states having specified magnetic configurations. Armed with Eqns. 5.21, 5.26 and 5.27 we are now ready to calculate the Heisenberg exchange coupling constants, $J(\boldsymbol{\tau}_\mu, \boldsymbol{\tau}_\nu - \mathbf{R})$. First, however, one has to take into account that from the Eqn. 5.21 it is only possible to calculate the difference $J_{\mu\mu}(\mathbf{q}) - J_{\mu\mu}(\mathbf{0})$, but not the coefficient $J_{\mu\mu}(\mathbf{q})$ alone. This problem can be easily bridged by introducing the coefficients $\tilde{J}_{\mu\nu}(\mathbf{q})$, defined as

$$\tilde{J}_{\mu\nu}(\mathbf{q}) \equiv J_{\mu\nu}(\mathbf{q}) - \delta_{\mu\nu} J_{\mu\nu}(\mathbf{0}). \tag{5.28}$$

Also, for simplicity, the non-zero cone angles can in all calculations be taken to have the same value $\theta$. The Eqns. 5.21, 5.26 and 5.27 can now be re-written as

$$\tilde{J}_{\mu\mu}(\mathbf{q}) = -2\frac{E_M^\mu(\mathbf{q}) - E_M^\mu(\mathbf{0})}{M_\mu^2 \sin^2\theta} \tag{5.29}$$

$$\mathcal{R}e\left[\tilde{J}_{\mu\nu}(\mathbf{q})\right] = \frac{E_M^{\mu\nu}(\mathbf{0}, \pi/2) - E_M^{\mu\nu}(\mathbf{q}, 0)}{M_\mu M_\nu \sin^2\theta} - \frac{1}{2}\frac{M_\mu}{M_\nu}\tilde{J}_{\mu\mu} - \frac{1}{2}\frac{M_\nu}{M_\mu}\tilde{J}_{\nu\nu} \tag{5.30}$$

$$\mathcal{I}m\left[\tilde{J}_{\mu\nu}(\mathbf{q})\right] = \frac{E_M^{\mu\nu}(\mathbf{q}, \frac{\pi}{2}) - E_M^{\mu\nu}(\mathbf{q}, 0)}{M_\mu M_\nu \sin^2\theta} - \mathcal{R}e\left[\tilde{J}_{\mu\nu}(\mathbf{q})\right]. \tag{5.31}$$

All one has to do now to obtain the exchange coupling constants in the real space is integrate. With the use of the relation ($V_{BZ}$ is the volume of the first Brillouin zone)

$$\int_{V_{BZ}} e^{i\mathbf{q}\cdot\mathbf{r}} d^3q = \begin{cases} 0, & \text{for } \mathbf{r} \neq \mathbf{0} \\ V_{BZ}, & \text{for } \mathbf{r} = \mathbf{0} \end{cases}, \tag{5.32}$$

along with the Eqns. 5.16 and 5.28 it is easy to see that

$$J(\boldsymbol{\tau}_\mu, \boldsymbol{\tau}_\nu - \mathbf{R}) = \frac{1}{V_{BZ}}\int_{V_{BZ}} \tilde{J}_{\mu\nu}(\mathbf{q})\, e^{-i\mathbf{q}\cdot(\boldsymbol{\tau}_{\mu\nu}-\mathbf{R})} d^3q. \tag{5.33}$$

Finally, from the definition 5.28 it is clear that $\tilde{J}_{\mu\nu}(\mathbf{q})$ satisfies the same symmetry relations as the coefficients $J_{\mu\nu}(\mathbf{q})$, so that $\tilde{J}_{\mu\nu}(\mathbf{q}) = \left[\tilde{J}_{\mu\nu}(-\mathbf{q})\right]^*$ and the integral 5.33 becomes

$$J(\boldsymbol{\tau}_\mu, \boldsymbol{\tau}_\nu - \mathbf{R}) = \frac{2}{V_{BZ}}\int_{\frac{V_{BZ}}{2}} \left\{\mathcal{R}e\left[\tilde{J}_{\mu\nu}(\mathbf{q})\right]\cos[\mathbf{q}\cdot(\boldsymbol{\tau}_{\mu\nu}-\mathbf{R})]\right.$$
$$\left. + \mathcal{I}m\left[\tilde{J}_{\mu\nu}(\mathbf{q})\right]sin[\mathbf{q}\cdot(\boldsymbol{\tau}_{\mu\nu}-\mathbf{R})]\right\} d^3q, \tag{5.34}$$

where the integration is conducted only over one half of the Brillouin zone.

To estimate the computational effort needed to obtain the exchange interaction constants, we will consider the following cases:

- Let us first assume that there is only one magnetic atom in the unit cell. In this case, the difference of the total energies in Eqn. 5.29 is essentially just the difference between the spin-spiral with the wave vector $\mathbf{q}$ and the ferromagnetic state (i.e. the magnon energy). To calculate the exchange interaction constants $J(\boldsymbol{\tau}_\mu, \boldsymbol{\tau}_\mu - \mathbf{R})$ we need, besides the energy of the ferromagnetic state, only one calculation per $\mathbf{q}$ point, i.e. in total $(1 + N_\mathbf{q})$ calculations, where $N_\mathbf{q}$ is the number of $\mathbf{q}$ points for which the calculations are performed.

- Now let us consider a system with more than one magnetic atom in the unit cell, but which possesses inversion symmetry. In the case of two or more magnetic atoms per unit cell, the energy $E_M^\mu(\mathbf{0})$ in the Eqn. 5.29 is no longer equal to the energy of the ferromagnetic state. In this case we will have to calculate this energy once for each magnetic atom. Also for each $\mathbf{q}$ point then we calculate the energy $E_M^\mu(\mathbf{q})$ for each magnetic atom. If there are $N_m$ magnetic atoms in the unit cell and the calculations are performed on $N_\mathbf{q}$ $\mathbf{q}$-points, this makes $(1 + N_\mathbf{q})N_m$ calculations. Now we have the constants $\tilde{J}_{\mu\mu}(\mathbf{q})$. In the systems with inversion symmetry, we will additionally have to calculate only the real part of $\tilde{J}_{\mu\nu}(\mathbf{q})$ (Eqn. 5.30), since the imaginary part is zero. To do this we will also need one calculation per pair of magnetic atoms to calculate the energies $E_M^{\mu\nu}(\mathbf{0}, \pi/2)$, plus one calculation per pair of magnetic atoms for each $\mathbf{q}$-point to determine the energies $E_M^{\mu\nu}(\mathbf{q}, 0)$, which makes $(1 + N_\mathbf{q})(N_m - 1)N_m/2$ additional calculations. In total, for the systems with inversion symmetry this gives $(1 + N_\mathbf{q})N_m + (1 + N_\mathbf{q})(N_m - 1)N_m/2 = (1 + N_\mathbf{q})(1 + N_m)N_m/2$ calculations.

- If the system does not possess inversion symmetry, in addition to the previous calculations one has to perform an additional calculation per pair of magnetic atoms for each $\mathbf{q}$ point to determine the energy $E_M^{\mu\nu}(\mathbf{q}, \pi/2)$. This means we have to perform additional $N_\mathbf{q}N_m(N_m - 1)/2$ calculations. Therefore, for the systems without inversion symmetry this makes $N_\mathbf{q}N_m(N_m - 1)/2 + (1 + N_\mathbf{q})(1 + N_m)N_m/2 = N_m(1 + N_m + 2N_mN_\mathbf{q})/2$ calculations in total.

The described calculations can be very time consuming, since they involve the determination of energies differences which are in general quite small (typically of the order of a few mRy), which means that a sufficient accuracy has

to be achieved requiring bigger basis sets and finer **k** point meshes. The size of the **q** point set one should use depends on the chosen distance between the two atoms for which the interaction constant is being calculated. If the energies needed here would be calculated self-consistently, this would mean that to get a reliable result one would have to spend months on these calculations! Fortunately, in most of the cases of interest the spin-spiral can be considered a small perturbation and Andersen's force theorem (Subsection 2.2.2) can be used to calculate the energy differences.

# Chapter 6

# Half-Metallic Ferromagnets

The origin of the term *half-metallic ferromagnets* lies in the specific electronic structure of these materials. Its main characteristic is that the two spin bands have a completely different behavior. While the majority spin band (referred to also as spin-up band) shows the typical metallic behavior, the minority spin band (spin-down band) is semiconducting (Fig. 6.1). Therefore, the spin-polarization at the Fermi level is 100%! This property has brought the half-metallic ferromagnets into the focus of many investigations, since they are the ideal candidates for applications in spin-electronic devices [4].

In this chapter some characteristics and the mechanism which opens the gap in the minority spin band will be discussed in more detail for the classes of half- and full-Heusler alloys, and the zinc-blende compounds of the transition metals with group V and VI elements. The structures which are adopted by these compounds are shown in Fig. 6.2. Commonly, their lattices can be seen as 4 intersecting fcc lattices. In the full-Heusler alloys, all 4 sublattices are occupied. This is known as $L2_1$ structure, described by the formula
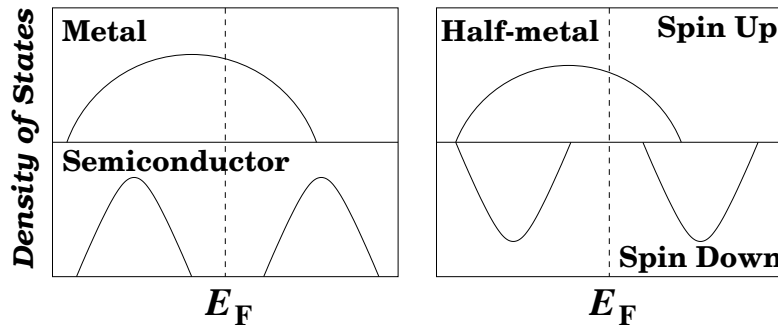
Figure 6.1: Schematic representation of the density of states for a half-metal with respect to normal metals and semiconductors.
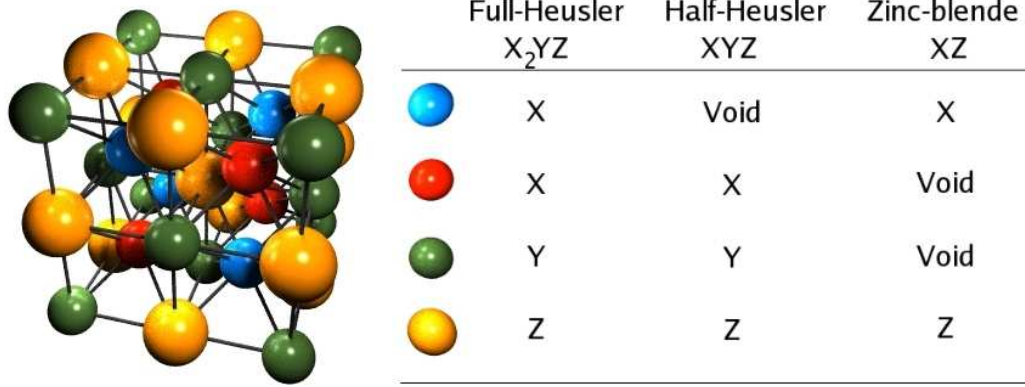
| | Full-Heusler $X_2YZ$ | Half-Heusler XYZ | Zinc-blende XZ |
|---|---|---|---|
| ● (blue) | X | Void | X |
| ● (red) | X | X | Void |
| ● (green) | Y | Y | Void |
| ● (orange) | Z | Z | Z |

Figure 6.2: $L2_1$, $C1_b$ and zinc-blende structure. The lattice is consisted of 4 intersecting fcc. lattices. The unit cell is that of a fcc lattice with four atoms as basis at the positions: X at $a(\frac{1}{4}\frac{1}{4}\frac{1}{4})$ and $a(\frac{3}{4}\frac{3}{4}\frac{3}{4})$, Y at $a(0\,0\,0)$ , and Z at $a(\frac{1}{2}\frac{1}{2}\frac{1}{2})$ in Cartesian coordinates, $a$ being the lattice parameter of the cubic unit cell. In the case of the full Heusler alloys ($L2_1$ structure) all the sites are occupied, in half-Heusler alloys ($C1_b$ structure) one of the X-sites is unoccupied, while in zinc-blende structure one of the X-sites and the Y-site are unoccupied (note that this is equivalent to the case when the other one of the two X-sites and the Z-site are unoccupied). If all atoms were identical, the lattice would be simply the bcc.

$X_2YZ$. A material which adopts this structure is for instance $Co_2MnSi$. The half-Heusler alloys crystallize in $C1_b$ structure in which three of the four sublattices are occupied (formula XYZ). An example is the aforementioned alloy NiMnSb. Finally, the zinc-blende structure, which is adopted by many semiconductors (e.g. GaAs), is the one in which two of the sublattices are occupied (i.e. the formula is XZ), and this is the structure of the half-metallic CrTe.

Due to the spin-down gap around Fermi energy ($E_F$), half metallic ferromagnets present in principle a number of exotic properties such as:

- DC conductance of only the spin-up electrons, since conductance is a Fermi level property

- Integer spin moment per unit formula

- Zero longitudinal spin susceptibility, since a band shift by a magnetic field will not alter the occupation of spin-up and -down states.

- Exponential decay with distance of the Heisenberg exchange constants $J_ij(\mathbf{R}_i - \mathbf{R}_j)$.

# 6.1 Half-Heusler Alloys

## 6.1.1 Electronic Structure and Origin of the Gap

In the following, a few examples of the half-Heusler alloys will be presented and their electronic structure examined in order to get a deeper insight into the processes which govern the opening and the size of the gap in the minority spin direction. The calculations were done with the use of the generalized gradient approximation (GGA) for the exchange correlation potential, as
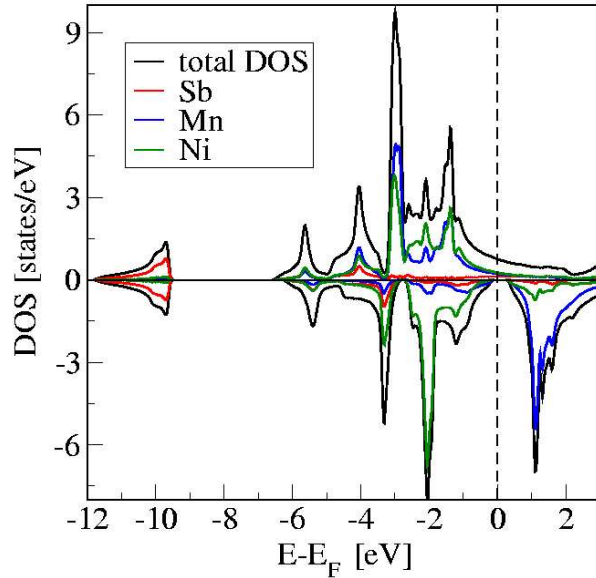


Figure 6.3: Atom-resolved density of states (DOS) of NiMnSb. The zero energy value corresponds to the Fermi level $E_{\mathrm{F}}$

given by Perdew *et al.* [99] With the use of GGA, the equilibrium lattice constants obtained for these compounds (Table 6.1) are usually up to 1% higher than the experimental ones.

A typical density of states (DOS) for a half-metallic half-Heusler compound is shown in figure 6.3. This is the DOS of NiMnSb, the half-metal discovered in 1983 by de Groot [2]. The total DOS is shown in black lines, and separately are given the local contributions to the density of states (LDOS) on the Ni-site (green), the Mn-site (blue) and the Sb-site (red). The positive part of the abscissa stands for the spin-up DOS, while the negative one shows the DOS of the spin-down band. The DOS of NiMnSb has contributions from 4 different bands: Each Sb atom with the atomic configuration $5s^2 5p^3$ introduces a deep lying $s$ band, located at about $-12$eV, and three $p$-bands in the
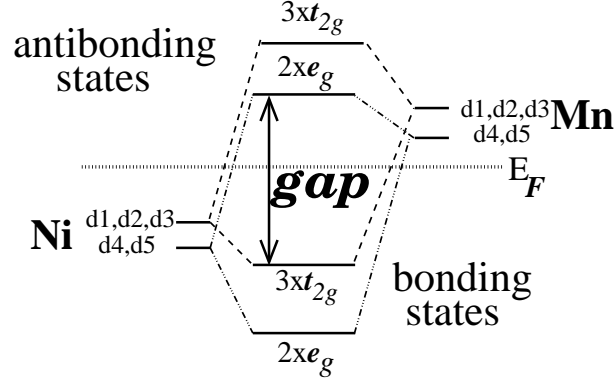
Figure 6.4: Schematic illustration of the origin of the gap in the minority band of the half-Heusler alloys. The energy levels $E_b$ of the energetically lower lying bonding hybrids are separated by the levels $E_{ab}$ of the antibonding hybrids by a gap, such that only the bonding states are occupied.

region between $-6$ and $-3$eV. The main characteristic of the LDOS of Mn $d$ electrons is a large exchange splitting, which pushes the majority and the minority spin bands apart. The majority Mn states lie at the lower energies, where they hybridize with the $sp$ orbitals of Sb and the $d$ orbitals of Ni. In the minority band, the lower lying $d$ states of Ni hybridize with the Mn $d$ spin-down states of higher energy, forming hybrids of bonding type under the Fermi level, with a peak at $-2$ eV, and the antibonding ones above it, with a peak at 1.1 eV. The bonding hybrids are of mostly Ni character with a small Mn admixture, while the the antibonding empty ones have mostly Mn character with a small admixture of Ni states. This small Ni DOS above the Fermi level in the minority spin band is responsible for the magnetic moment situated on Ni atom. Between these bonding and antibonding hybrid states, the gap opens [10]. The described hybridization in the minority band is schematically illustrated in Fig. 6.4.

From the first-principles calculations, the gap in the minority band of NiMnSb of approximately 0.4 eV is obtained. This value is in good agreement with the experiments of Kirillova and collaborators [28], who estimated the same value from the analysis of their infrared spectra. Although the local density approximation (LDA) and the generalized gradient approximation (GGA) strongly underestimate the values of the gaps in semiconductors, the minority gap in the half-metallic systems is much better described by the LDA and GGA since in these systems the screening is metallic.

The gap in the half-metallic $C1_b$ compounds is normally an indirect gap, with the maximum of the valence band at the $\Gamma$ point and the minimum
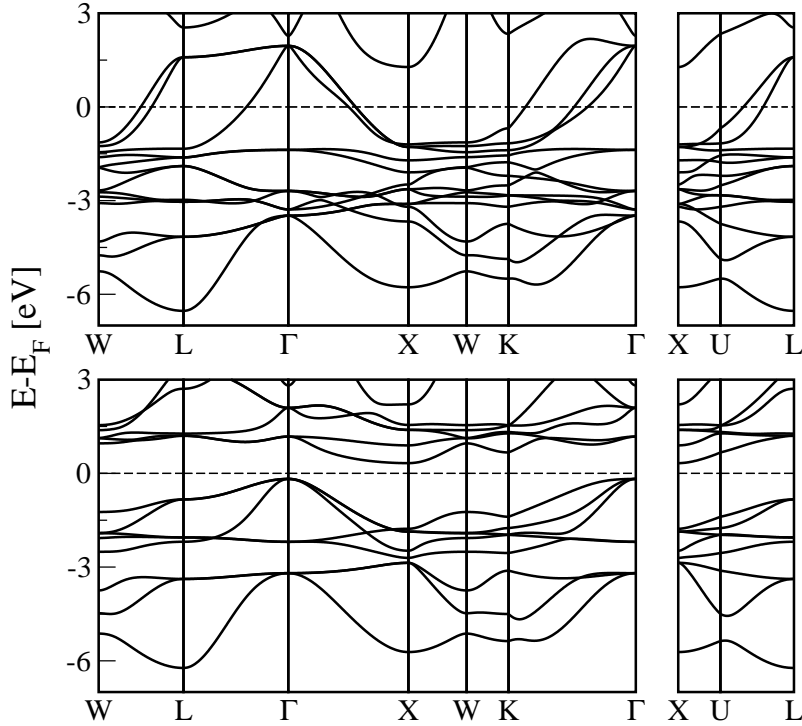
Figure 6.5: The bulk bandstructure of NiMnSb, along the high symmetry lines of the first Brillouin zone of an fcc lattice. The upper panel presents the bandstructure in the majority spin direction, while the lower one presents the bandstructure in the minority spin direction, with the (indirect) gap at the Fermi level ($E_F$).

of the conduction band at the $X$-point. The bandstructure of NiMnSb is presented in the Fig. 6.5.

In the Fig. 6.6, atom-resolved densities of states of the half-Heusler alloys with formula XYSb are shown, where X stands for Ni, Pd, or Pt (green lines) and Y stands for V, Cr or Mn (blue lines). The LDOS of Sb is plotted with red lines, and the total DOS with the black ones. All the calculations were performed at the equilibrium lattice constants of each material (Table 6.1). The comparison of the densities of states provides information about the chemical trends. First, all of them present a larger or smaller gap in the minority spin band, although this gap is not at the Fermi level in all the cases. All compounds present a very high spin-polarization at the Fermi energy, but the truly half-metallic ones are only three: NiVSb, PtVSb and NiMnSb.

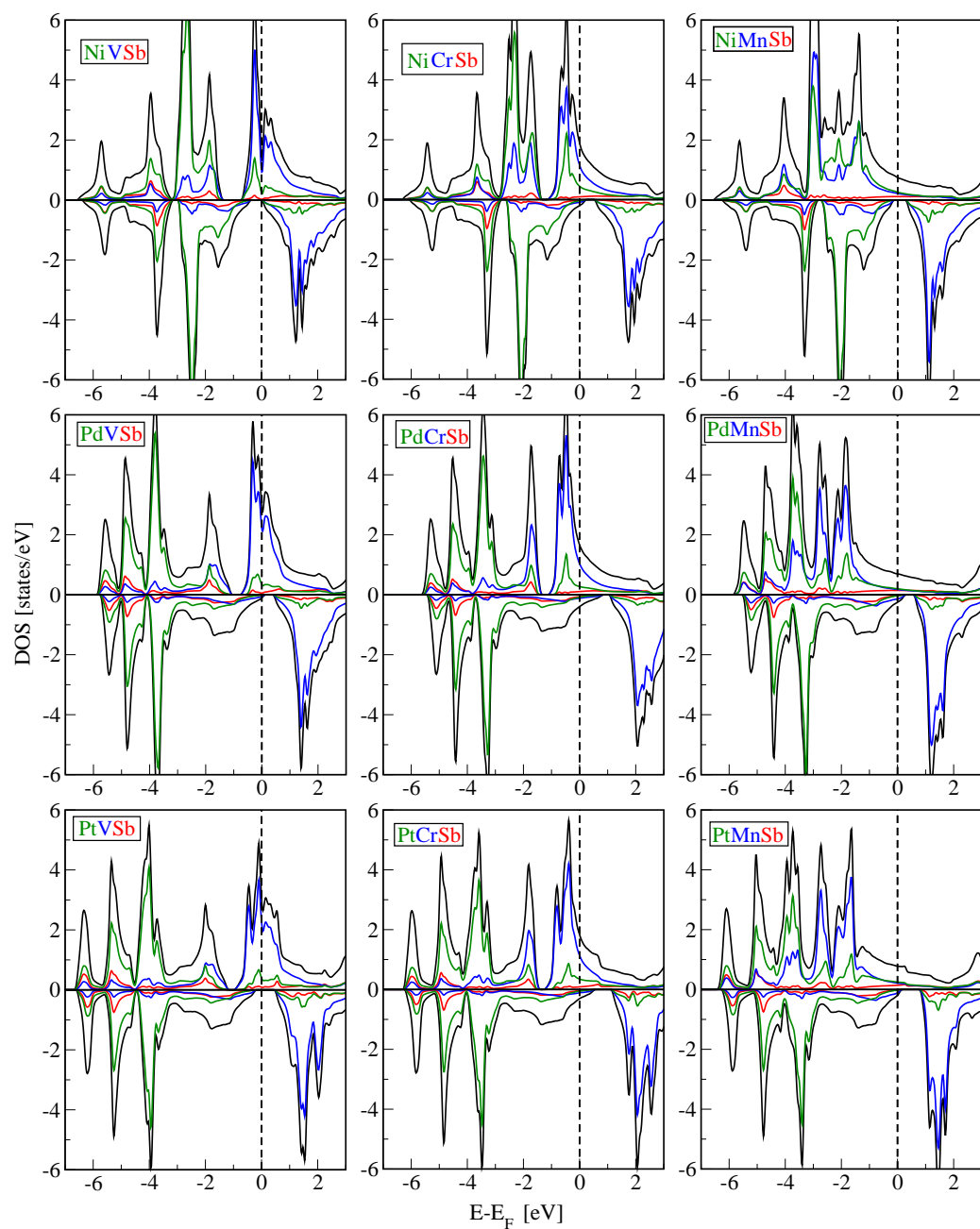When changing the Y-atom from V to Cr and then to Mn, the ex-

Figure 6.6: Atom-resolved densities of states of the half-Heusler alloys with formula XYSb, X=Ni, Pd, Pt, Y=V, Cr, Mn. With red lines, LDOS of Sb is plotted, blue lines stand for V, Cr, or Mn LDOS, while the green lines present the LDOS of Ni, Pd and Pt. The black lines stand for the total DOS.
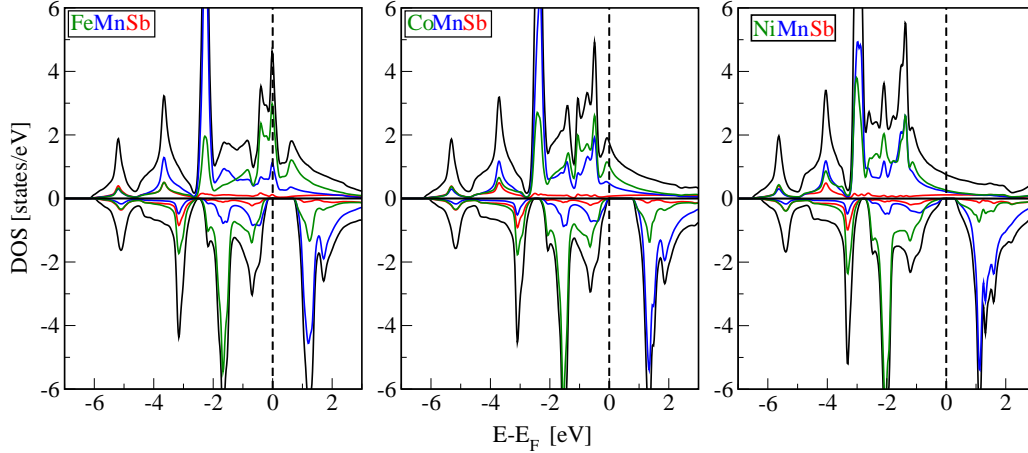
Figure 6.7: Atom-resolved densities of states of the half-Heusler alloys with formula XMnSb, X=Fe, Co, Ni. LDOS of Sb - red lines, LDOS of Mn - blue lines, LDOS of Fe, Co, Ni - green lines. The black lines stand for the total DOS.

change splitting becomes larger, and the majority states of these atoms shift lower, accommodating more electrons in the majority band, and hybridizing stronger with the lower lying states of X-atom. The minority states of Y atom remain unoccupied, so the magnetic moment rises by approximately $1 \ \mu_B$ (Table 6.1) when Y is changing to the next element to the right.

When the X-atom is changing from Ni to Pd and then to Pt, there are two counteracting mechanisms influencing the size of the gap. First, the lattice constant is becoming bigger, which takes the X and Y atoms further apart and reduces the hybridization between them. A weaker hybridization means a smaller gap. On the other hand, the $4d$ orbitals of Pd are more extended than the $3d$ of Ni, and the $5d$ of Pt are more extended than the $4d$ of Pd. The more extended orbitals hybridize stronger and this means a larger gap. In the Fig. 6.6 we see that the difference in the size of the gap is noticeable when switching from PdYSb to PtYSb compounds, while it remains approximately the same for NiYSb and PdYSb. It is easy to understand this if we notice that the difference in the lattice constant between NiYSb and PdYSb compounds is typically around 5% (Table 6.1), while this difference for PdYSb and PtYSb compounds is just around 0.5%. Therefore, the effect of the stronger hybridization because of the stronger delocalization of the $d$ orbitals of higher shells is totally compensated by the larger lattice constant in PdYSb compounds, while in the PtYSb compounds the former prevails.

The effect of the change of X-atom from Fe to Co to Ni in the XMnSb

compounds is shown in Fig. 6.7. This change has a similar result like the change of the Y-atom in XYSb compounds (Fig. 6.6), namely, when switching from an X-atom to the next one on its right, the Fermi level shifts, allowing for the accommodation of one more electron in the majority band of the compound, while the antibonding states in the minority band remain unoccupied, giving rise to a change of the magnetic moment by 1 $\mu_B$. Since the lattice constant of NiMnSb is somewhat bigger than that of FeMnSb and CoMnSb, which themselves differ very little (Table 6.1), the gap in the minority band of NiMnSb is smaller then in the latter two compounds, due to the weaker hybridization.

### The Role of the $sp$-Element

While the $sp$-elements are not responsible for the existence of the minority gap, they are nevertheless very important for the physical properties of the Heusler alloys and the structural stability of the $C1_b$ structure. A careful discussion of the bonding in these compounds has been recently published by Nanda and Dasgupta [100] using the crystal orbital Hamiltonian population (COHP). For the semiconductor FeVSb they find that while the largest contribution to the bonding arises from the V-$d$ – Fe-$d$ hybridization, contributions of similar size arise also from the Fe-$d$ – Sb-$p$ and the V-$d$ – Sb-$p$ hybridization. Similar results are also valid for NiMnSb. Since the majority $d$-band is completely filled, the major part of the bonding arises from the minority band.

The Sb atom has 5 valence electrons ($5s^2$, $5p^3$), and in the half-Heusler compounds it introduces a deep lying $s$-band (in NiMnSb, Fig. 6.3, at about $-12$ eV) and three $p$-bands below the center of the $d$-bands. These bands accommodate a total of 8 electrons per unit cell, so that formally Sb acts as a triple charged $Sb^{-3}$ ion. Analogously, a Te-atom behaves in these compounds as a $Te^{-2}$ ion and an Sn-atom as an $Sn^{-4}$ ion. This does not mean, that locally such a large charge transfer exists. In fact, the $s$- and $p$-states strongly hybridize with the transition metal $d$-states and the charge in these bands is delocalized. What counts is that the $s$- and $p$-bands accommodate 8 electrons per unit cell, thus effectively acting as reservoir and reducing the $d$-charge of the transition metal atoms.

In the Fig. 6.8, the change in XVSb (X=Ni, Pd, Pt) compounds made by substituting the (group V) Sb atom by the (group VI) Te atom is investigated. The first observation is that not much has changed around Fermi level, except, of course, for a small shift to accommodate the additional electron. The change appears mostly in the lower lying bands, which are hybrids of the transition metals' $d$-states and the $p$-states of Sb (Te), lying at the energies
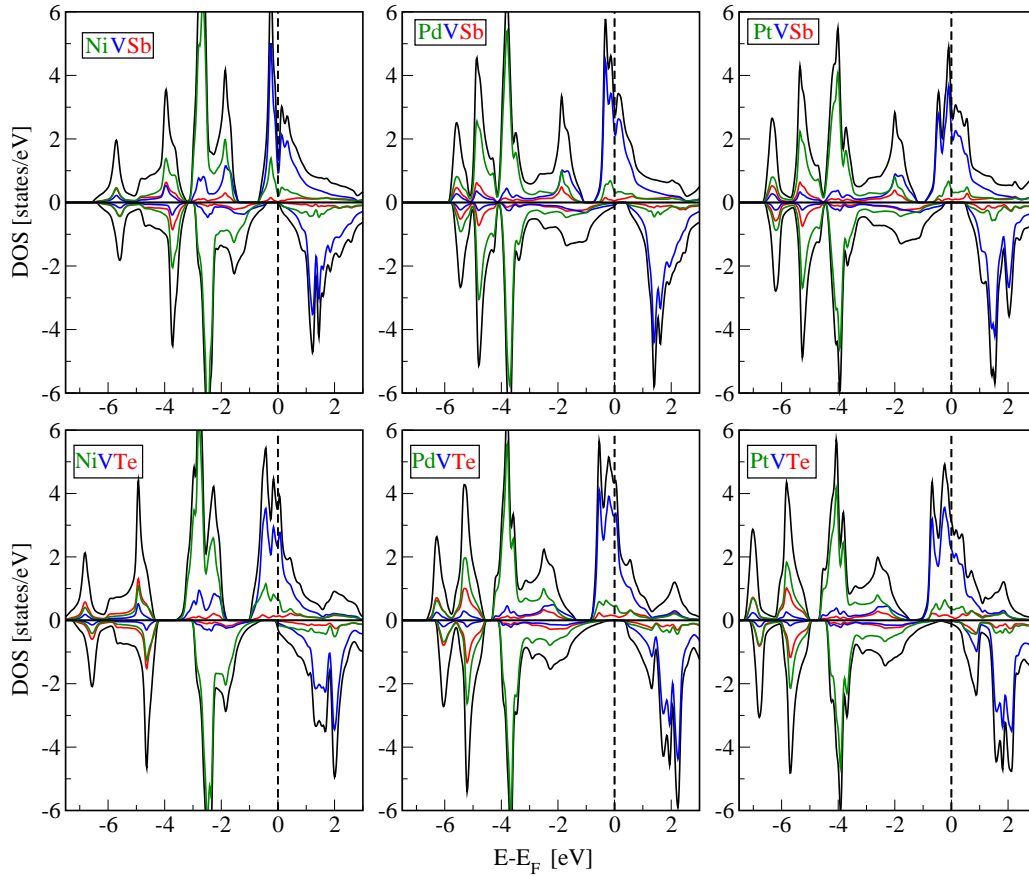
Figure 6.8: The comparison of DOS of XVSb and XVTe half-Heusler compounds, with X=Ni, Pd, Pt (green lines). LDOS of V is presented with blue and the one of *sp* atom (Sb, Te) with red lines. The total DOS is plotted in black lines.

of 6-4 eV under the Fermi level. The atom of Te is more electronegative than the Sb one, so its *p*-states lie lower in energy. Since the mentioned states have the highest admixture of the *sp* atom states they will be the ones strongly affected by the change of this atom, and will shift lower in Te-compounds.

The size of the gap in the minority band can be influenced by the *sp* atom indirectly. This is shown in Fig. 6.9, where the DOS of the compounds CoCrP and CoCrSb is depicted. Both P and Sb are group V elements, P being a much smaller atom, with considerably larger electronegativity. The effect of the electronegativity is, as in the previous case, reflected in the shift of the bands to the lower energies, but the most striking difference in the two densities of states is the size of the gap, which is almost twice larger in the P-compound. The reason for this is just the very simple one, namely,
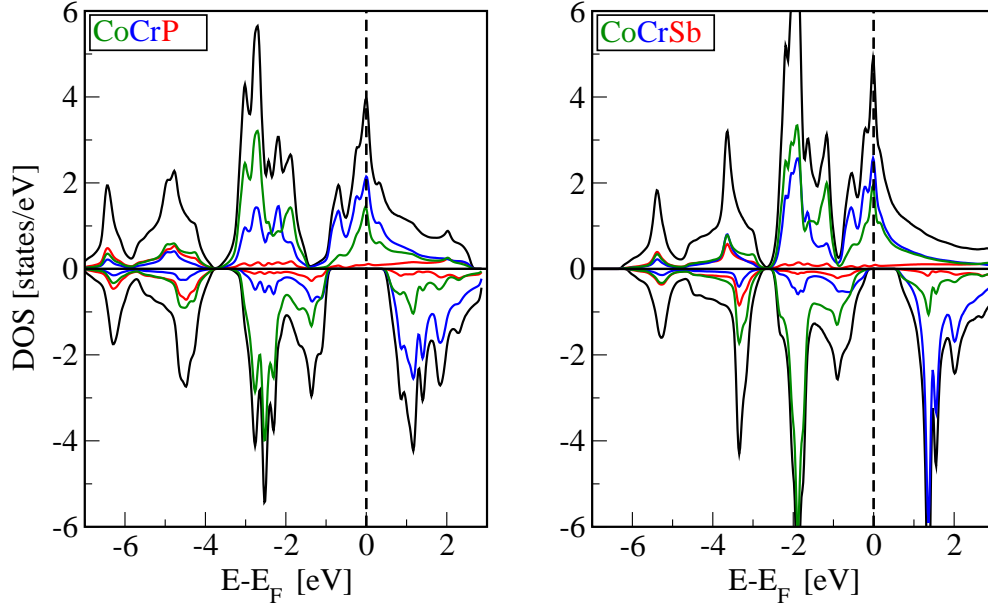
Figure 6.9: The comparison of DOS of CoCrP and CoCrSb half-Heusler compounds. With green lines - LDOS of Co, blue lines - LDOS of Cr, red lines - LDOS of the $sp$ atom (P, Sb), black lines - the total DOS.

since the P-atom is much smaller than the Sb atom, the lattice parameter of the P-compound is much smaller that that of the Sb-compound (Table 6.1). The consequence of the smaller lattice parameter is a stronger hybridization of the $d$-states of Co and Cr and, therefore, a larger gap.

## 6.1.2 The magnetic moment of the half-Heusler compounds

The total number of valence electrons, $Z$, is given by the sum of the number of spin-up ($N_\uparrow$) and spin-down ($N_\downarrow$) electrons, while the total moment, $M_t$, is given by their difference:

$$Z = N_\uparrow + N_\downarrow \quad , \quad M_t = N_\uparrow - N_\downarrow \quad \rightarrow \quad M_t = Z - 2N_\downarrow. \qquad (6.1)$$

Consider the case of NiMnSb, which has 22 valence electrons per unit cell, 10 from Ni, 7 from Mn and 5 from Sb. Since, due to the gap at $E_F$, in the minority band exactly 9 bands are fully occupied (1 Sb-like $s$ band, 3 Sb-like p bands and 5 Ni-like $d$ bands) accommodating 9 electrons per unit cell, the majority band contains $22 - 9 = 13$ electrons, resulting in a moment of exactly 4 $\mu_B$ per unit cell. Since in all the half-metallic half-Heusler compounds 9 minority bands are fully occupied, we obtain the simple
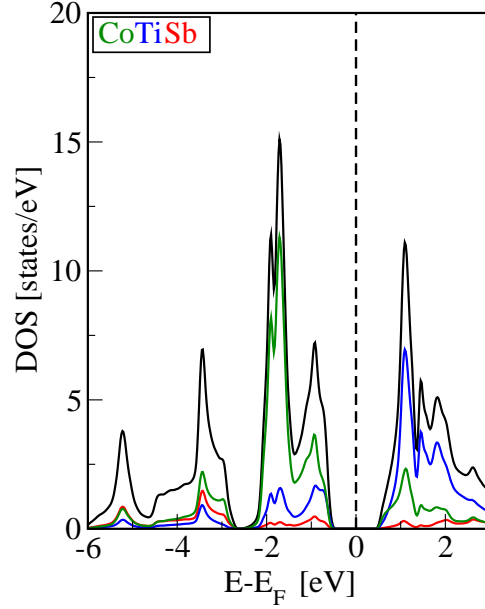
Figure 6.10: The DOS of the semiconductor CoTiSb. With green lines - LDOS of Co, blue lines - LDOS of Ti, red lines - LDOS of Sb, black lines - the total DOS.

*rule of 18* [10]:

$$M_t = Z - 18. \tag{6.2}$$

Equation 6.2 suggests that among the half-Heusler alloys there are also some non-magnetic semiconductors, with 18 valence electrons. Such semiconductors do exist, and the DOS of one of them, CoTiSb, is depicted in Fig. 6.10. Semiconducting are also CoZrSb, FeVSb and NiTiSn. The gaps of these semiconductors are approximately 0.8 eV in CoTiSb and CoZrSb, 0.36 eV in FeVSb and 0.14 eV in NiTiSn [9].

It is obvious that if the compound is half-metallic, its total magnetic moment should be integer. For the compounds in which the Fermi level is at the edge of the gap, with some small DOS at the Fermi level, we expect the relation 6.2 to be valid only approximately. In the table 6.1, the total magnetic moments of some half-Heusler compounds are shown. The rule of 18, Eqn. 6.2, is reproduced for all the half-metallic compounds, namely NiVSb, PtVSb, FeMnSb, CoCrSb, CoCrP with the total magnetic moment of 2 $\mu_B$, CoMnSb, PdVTe with the total magnetic moment of 3 $\mu_B$, NiMnSb with the total magnetic moment of 4 $\mu_B$ and for the semiconducting non-magnetic CoTiSb. We will see in the next two sections that similar rules can be deduced also for other half-metallic compounds.

| | alloy (XYZ) | $a_{\mathrm{opt}}$ (Å) | $M_X$ ($\mu_B$) | $M_Y$ ($\mu_B$) | $M_Z$ ($\mu_B$) | $M_t$ ($\mu_B$) |
|---|---|---|---|---|---|---|
| $Z=18$ | CoTiSb | 5.894 | 0 | 0 | 0 | 0 |
| $Z=20$ | NiVSb | 5.903 | 0.096 | 1.783 | −0.061 | 2.000 |
| | PdVSb | 6.205 | −0.010 | 2.010 | −0.113 | 2.015 |
| | PtVSb | 6.238 | −0.017 | 1.955 | −0.070 | 2.000 |
| | FeMnSb | 5.844 | −1.023 | 3.021 | −0.029 | 2.000 |
| | CoCrSb | 5.820 | −0.394 | 2.372 | −0.081 | 2.000 |
| | CoCrP | 5.345 | −0.020 | 1.940 | −0.064 | 2.000 |
| $Z=21$ | NiCrSb | 5.896 | 0.012 | 2.997 | −0.119 | 3.061 |
| | PdCrSb | 6.193 | −0.023 | 3.317 | −0.150 | 3.328 |
| | PtCrSb | 6.226 | −0.062 | 3.200 | −0.116 | 3.196 |
| | CoMnSb | 5.820 | −0.129 | 3.215 | −0.086 | 3.000 |
| | NiVTe | 5.988 | 0.205 | 2.367 | −0.023 | 2.968 |
| | PdVTe | 6.314 | 0.043 | 2.658 | −0.069 | 3.000 |
| | PtVTe | 6.341 | 0.048 | 2.514 | −0.004 | 2.952 |
| $Z=22$ | NiMnSb | 5.914 | 0.262 | 3.703 | −0.063 | 4.000 |
| | PdMnSb | 6.229 | 0.095 | 4.021 | −0.097 | 4.080 |
| | PtMnSb | 6.240 | 0.111 | 3.918 | −0.074 | 4.012 |

Table 6.1: The (GGA) optimized lattice constants $a_{\mathrm{opt}}$, the magnetic moments in the muffin-tin spheres of atoms X, Y, Z ($M_{X,Y,Z}$), and the total magnetic moment per unit cell, $M_t$, of several half-Heusler compounds (XYZ), with $Z$ valent electrons in the unit cell.

## 6.2 Full Heusler Alloys

The second family of Heusler alloys are the full-Heusler alloys. Here, in particular compounds containing Co and Mn will be presented, as these are the full-Heusler alloys that have attracted most of the attention. They are all strong ferromagnets with high Curie temperatures (above 600 K) and, with exception of $Co_2MnAl$, they show very little disorder [6]. They adopt the $L2_1$ structure shown in figure 6.2. Each Mn or $sp$ atom has eight Co atoms as first neighbors, sitting at the octahedral symmetry positions, while each Co atom has four Mn and four $sp$ atoms as first neighbors and thus the symmetry of the crystal is reduced to the tetrahedral one. The Co atoms occupying two different sublattices are equivalent, as the environment of one sublattice is the same as the environment of the second one but rotated by 90$^o$. The occupancy of two fcc sublattices by Co (or in general by X)
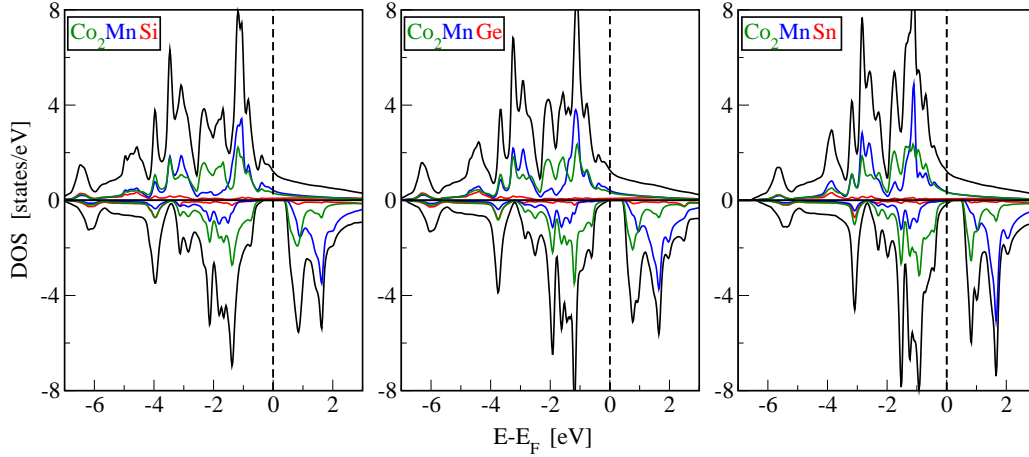
Figure 6.11: Atom-resolved densities of states of the full-Heusler alloys with formula Co$_2$MnZ, Z=Si, Ge, Sn. LDOS of Si, Ge, Sn - red lines, LDOS of Mn - blue lines, LDOS of Co - green lines. The black lines stand for the total DOS.

atoms distinguish the full-Heusler alloys with the $L2_1$ structure from the half-Heusler compounds with the $C1_b$ structure, like e.g. CoMnSb, where only one sublattice is occupied by Co atoms and the other one is empty. Although in the $L2_1$ structure the Co atoms are sitting on second neighbor positions, their interaction is important for the magnetic properties of these compounds.

In figure 6.11 the densities of states of the full-Heusler compounds Co$_2$MnSi, Co$_2$MnGe, and Co$_2$MnSn are shown (all the calculations were done at the (GGA) optimized lattice constants of the compounds, Table 6.2). The valence band extends up to around 7 eV below the Fermi level and the spin-up DOS shows a large peak just below the Fermi level for these compounds. This picture was also verified in the photoemission experiments on Co$_2$MnSn by Brown *et al.* [101]. The gap in the minority band is indirect, with the maximum of the valence band at $\Gamma$ and the minimum of the conduction band at the $X$-point (Fig 6.12), like in the case of half-Heusler alloys.

## 6.2.1  Origin of the Gap and Magnetism of Full-Heusler Alloys

In the full-Heusler alloys, like in the half-Heusler alloys, the four *sp*-bands are located far below the Fermi level, and play no role in forming the gap. As an example, we discuss here the alloy Co$_2$MnGe. The states responsible for the gap are the $d$ states of the Mn atom and of the two Co atoms. In
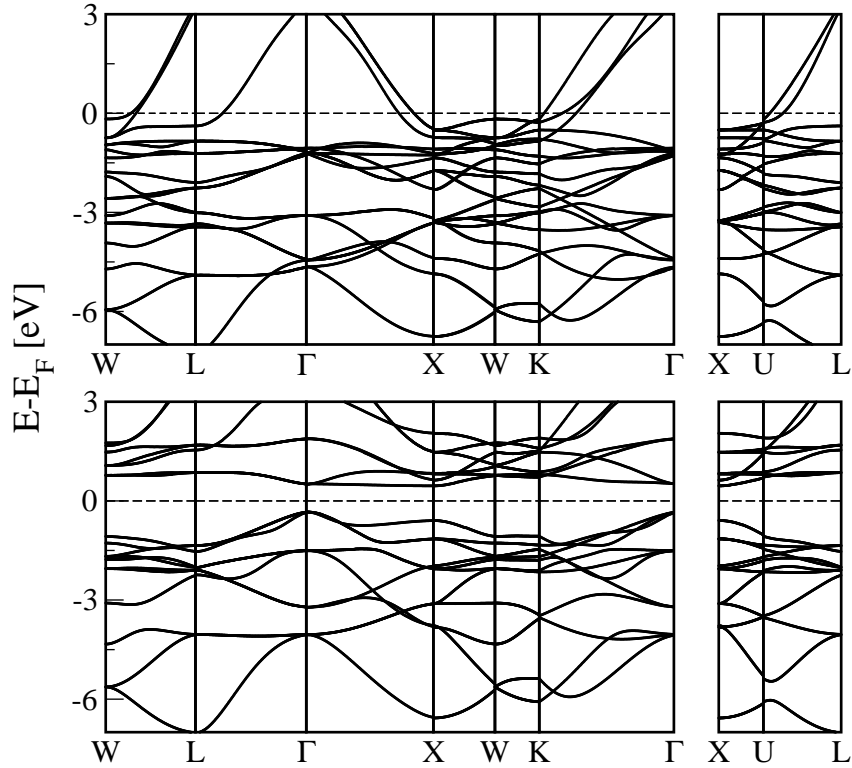
Figure 6.12: The bulk bandstructure of $Co_2MnSi$, along the high symmetry lines of the first Brillouin zone of an fcc lattice. The upper panel presents the bandstructure in the majority spin direction, while the lower one presents the bandstructure in the minority spin direction, with the (indirect) gap at the Fermi level ($E_F$).

order to obtain a simple picture of the mechanisms involved, only the $d$-states at the $\Gamma$ point, which show the full structural symmetry, are considered. A thorough analysis, relaying on the group theory, can be found in the work of Galanakis *et al.* [11]. The Co atoms form a simple cubic lattice and the Mn atoms (also the *sp* atoms) occupy the body centered sites of this lattice and have 8 Co atoms at the nearest neighboring sites. The hybridization which takes place is sketched in figure 6.13. It can, for a better understanding, be divided into two contributions.

- **<u>Co-Co</u>**
  Although the distance between the Co atoms is a second neighbor distance, the hybridization between these atoms is qualitatively very important. The 5 $d$ orbitals are divided into the twofold degenerate $d_4$, $d_5$ ($z^2$, $x^2 - y^2$) and the threefold degenerate $d_1$, $d_2$, $d_3$ ($xy, yz, zx$) states
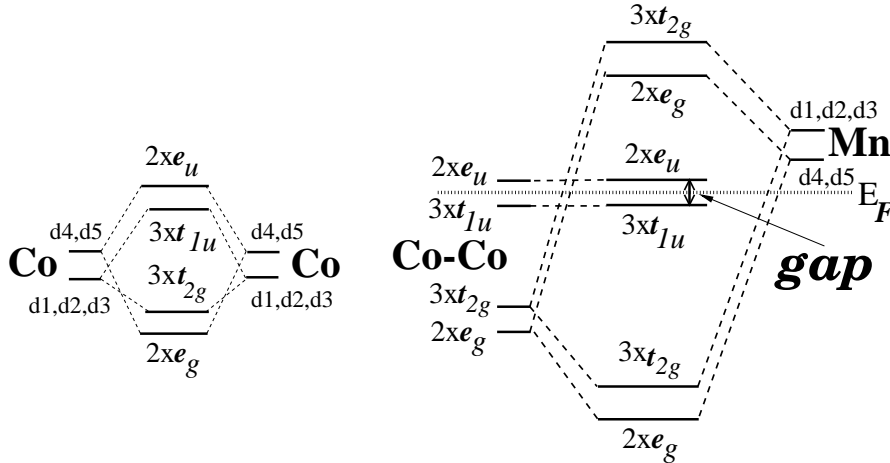
Figure 6.13: Schematic illustration of the origin of the gap in the minority band in full-Heusler alloys.

(Fig. 6.13 left). The $e_g$ orbitals ($t_{2g}$ orbitals) can only couple with the $e_g$ orbitals ($t_{2g}$ orbitals) of the other Co atom forming bonding hybrids, denoted by $e_g$ (or $t_{2g}$) and antibonding orbitals, denoted by $e_u$ (or $t_{1u}$). The coefficients in front of the orbitals give the degeneracy.

- **Co-Co-Mn**
  In a second step we consider the hybridization of the Co-Co orbitals with the Mn $d$-orbitals (Fig 6.13 right). The doubly degenerated $e_g$ orbitals hybridize with the $d_4$ and $d_5$ of the Mn, which transform according to the same irreducible representation of the symmetry group. They create a double degenerated bonding $e_g$ state that is very low in energy and an antibonding one that is unoccupied and above the Fermi level. The $3 \times t_{2g}$ Co orbitals couple to the $d_{1,2,3}$ of the Mn and create 6 new orbitals, 3 of which are bonding and are occupied and the other three are antibonding and high in energy. Finally the $2 \times e_u$ and $3 \times t_{1u}$ Co orbitals cannot couple with any of the Mn $d$ orbitals as these are not transforming with the $u$ representations and are orthogonal to the Co $e_u$ and $t_{1u}$ states. With respect to the Mn and the Ge atoms these states are therefore non-bonding. The $t_{1u}$ states are below the Fermi level and they are occupied while the $e_u$ are just above the Fermi level.Thus in total 8 minority $d$ bands are filled and 7 are empty.

To summarize, among the minority-spin states all 5 Co-Mn bonding bands are occupied and all 5 Co-Mn antibonding bands are empty, and the Fermi level falls in between the 5 non-bonding Co bands, such that the three $t_{1u}$

| alloy (Co₂MnZ) | $a_{\mathrm{opt}}$ (Å) | $M_{Co}$ ($\mu_B$) | $M_{Mn}$ ($\mu_B$) | $M_Z$ ($\mu_B$) | $M_t$ ($\mu_B$) |
|---|---|---|---|---|---|
| Co2MnAl | 5.688 | 0.784 | 2.664 | −0.092 | 4.024 |
| Co₂MnGa | 5.715 | 0.765 | 2.742 | −0.076 | 4.115 |
| Co2MnSi | 5.627 | 1.058 | 2.975 | −0.061 | 5.000 |
| Co₂MnGe | 5.732 | 1.014 | 3.057 | −0.048 | 5.000 |
| Co₂MnSn | 5.994 | 0.981 | 3.210 | −0.057 | 5.038 |

(The first two rows are labelled $N=28$; the last three rows are labelled $N=29$.)

Table 6.2: The (GGA) optimized lattice constants $a_{\mathrm{opt}}$, the magnetic moments in the muffin-tin spheres of atoms Co, Mn, Z=Al, Ga, Si, Ge, Sn ($M_{Co,Mn,Z}$), and the total magnetic moment per unit cell, $M_t$, of several full-Heusler compounds of type Co₂MnZ (Z=Al, Ga, Si, Ge, Sn), with $Z$ valent electrons in the unit cell.

bands are occupied and the two $e_u$ bands are empty. The maximal moment of the full Heusler alloys is therefore 7 $\mu_B$ per unit cell, which is achieved, if all majority $d$-states are occupied.

It should be also mentioned that the LDOS of Mn clearly shows a much bigger gap at $E_F$ (Figs. 6.11, 6.14) than the one of the whole compound. The real gap is determined by the Co-Co interaction or, more precisely, by the $t_{1u} - e_u$ splitting.

In the previous section it was shown that the moment of the half-metallic half-Heusler compounds follows the rule of 18. A similar rule can be deduced for the full-Heusler alloys. In the Table 6.2, the calculated magnetic moments of several full-Heusler alloys of the type Co2MnZ (Z=Al, Ga, Si, Ge, Sn) are given. The compounds containing Al and Ga (Fig 6.14) have 28 valence electrons and the ones containing Si, Ge and Sn 29 valence electrons. The first compounds have a total spin moment close to $4\mu_B$ and the second ones close to 5 $\mu_B$ which agrees with the experimentally deduced moments of these compounds [102]. The total spin moment, $M_t$, is related to the total number of valence electrons, $Z$, by a simple relation (*the rule of 24*) [11],

$$M_t = Z - 24. \tag{6.3}$$

This rule arises from the fact that the minority band contains 12 electrons per unit cell: 4 are occupying the low lying $s$ and $p$ bands of the $sp$ element and 8 the Co-like minority $d$ bands ($2 \times e_g$, $3 \times t_{2g}$ and $3 \times t_{1u}$), as explained above (Fig. 6.13). Since 7 minority bands are unoccupied, the largest possible moment per unit cell is 7 $\mu_B$ and occurs when all majority $d$-states are occupied.
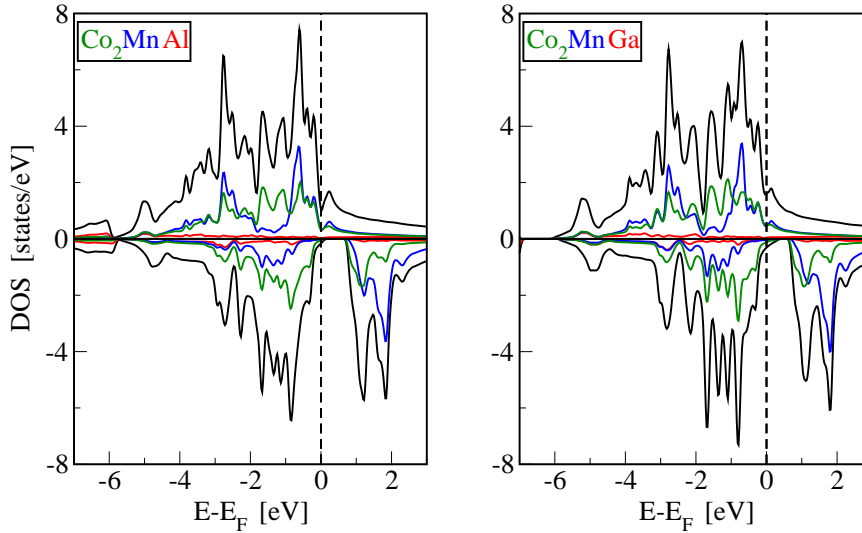
Figure 6.14: Atom-resolved densities of states of the full-Heusler alloys with formula Co2MnZ, Z=Al, Ga. LDOS of Al, Ga - red lines, LDOS of Mn - blue lines, LDOS of Co - green lines, total DOS - black lines

## 6.3   Zinc-blende Half-metallic Compounds

Compounds consisting of $3d$ and $sp$ elements, though unstable (or metastable) in zinc-blende (zb) structure, are lately being successfully grown on zb semi-conductors. For instance, binary CrAs in the zinc-blende (zb) structure was grown epitaxially on GaAs; this compound was found to be half metallic, both by experiment and by relevant calculations [24]. It has also the ad-vantage of a Curie temperature $T_C$, higher than room temperature, at least 400 K [103]. Similar is the case for ferromagnetic zb CrSb [104]. Moreover, the growth of nanoscale zb MnAs dots on GaAs substrates [105] has been achieved and CrAs/GaAs multilayers have been fabricated [106]. In Fig. 6.15 the densities of states of a few zb half-metals are presented. The compounds on the left, VTe and CrAs, possess 11 valent electrons and a magnetic mo-ment of 3 $\mu_B$, while the ones on the right, MnSb and CrTe, have 12 valent electrons and a magnetic moment of 4 $\mu_B$ per unit cell. Like in the case of the full- and half-Heusler alloys, all the calculations were performed at the (GGA) equilibrium lattice constant of the compounds (Table 6.3).
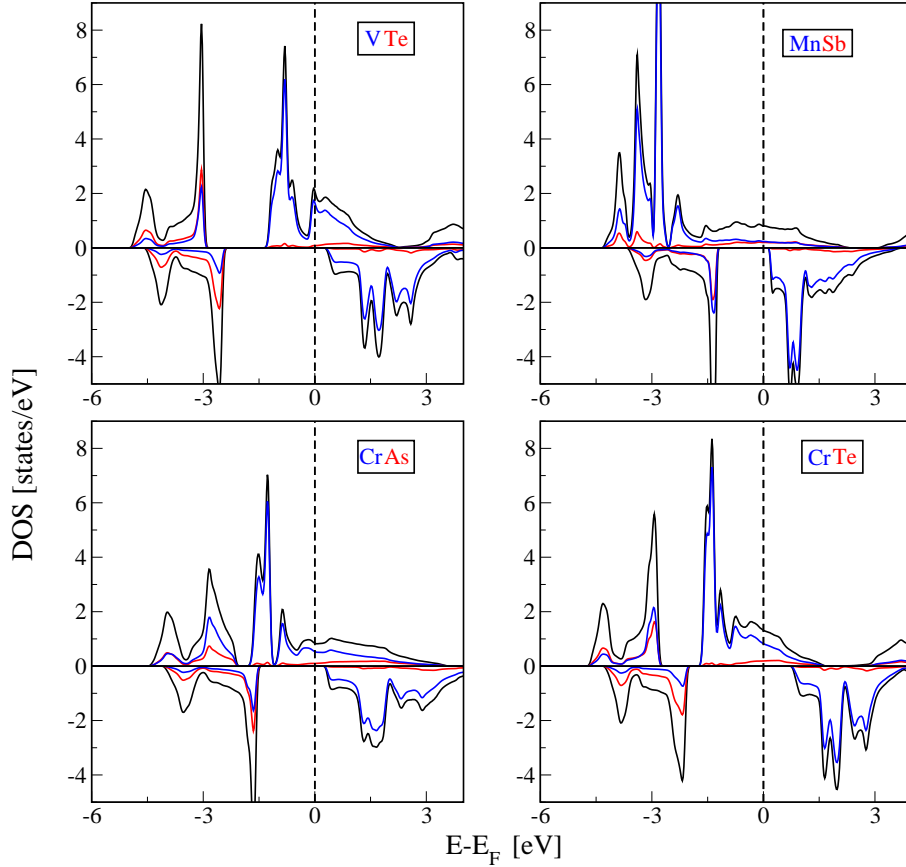
Figure 6.15: Atom-resolved densities of states of some of the zb compounds with formula YZ, where Y=V, Mn, Cr and Z=As, Sb, Te. LDOS of the Y-atom is shown in blue lines, LDOS of Z-atom in red lines and the black lines show the total DOS.

## 6.3.1 Origin of the gap and Magnetism of Zinc-blende Half-metallic Compounds

In the description of the origin of the gap in the minority band of the zb compounds, it is convenient, like in the case of the full-Heusler alloys, to concentrate on the states at the $\Gamma$ point ($\mathbf{k} = 0$), since they possess the full crystal symmetry.[1] In the zb structure, the tetrahedral environment allows the $t_{2g}$ states ($d_{xy}$, $d_{yz}$, and $d_{xz}$) of the 3$d$ atom to hybridize with the $p$ states of the four first neighbors (the $sp$ atoms), since in the tetrahedral geome-

---

[1]Although for arbitrary $\mathbf{k}$ the wavefunctions do not belong exclusively to a single irreducible representation such as $t_{2g}$ or $e_g$, it is convenient to retain this terminology for the bands formed by originally $t_{2g}$ or $e_g$ orbitals since they are energetically rather separated.

$[t_{2g}]$

$d_{xy}$ $d_{yz}$ $d_{xz}$

Antibonding

Cr

As

$d_{z^2}$ $d_{x^2-y^2}$
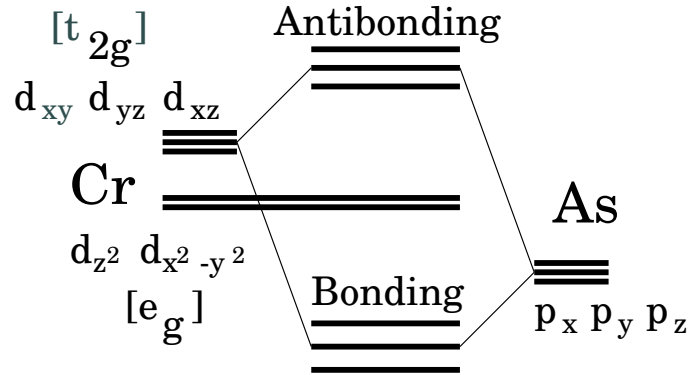
$[e_g]$

Bonding

$p_x$ $p_y$ $p_z$

Figure 6.16: Schematic illustration of the origin of the gap in the minority band of the zinc-blende compounds. The energy levels $E_b$ of the energetically lower lying bonding hybrids are separated by the levels $E_{ab}$ of the antibonding hybrids by a gap, such that only the bonding states are occupied.

try the $p$ orbitals of the four neighboring sites transform according to the same irreducible representation as the $t_{2g}$ orbitals when analyzed around the central site. This creates a large bonding-antibonding splitting (Fig. 6.16), with the low-lying bonding states being more of $p$ character around the $sp$ neighbors, and the antibonding being rather of $d$ character around the $3d$ atom. The gap formed in between is partly filled by the $e_g$ states of the $3d$ atom ($d_{z^2}$ and $d_{x^2-y^2}$); these have a non-bonding character, forming narrow bands. The position of the bands will be different for majority and minority electrons, due to the exchange splitting.

Such a symmetry-induced $p$-$d$ hybridization and bonding-antibonding splitting is also taking place in transition metal doped zinc-blende semiconductors [107, 108]. The case of the zb compounds studied here may be seen as the limit of the full substitution of the semiconductor cation by the transition metal. It is important to note that the tetrahedral coordination, characteristic of zb geometry, is necessary for the formation of the bonding-antibonding gap, since, as it has been reported [109, 110, 111], in the hexagonal NiAs geometry MnP, MnAs and MnSb show no gap.

Figure 6.17 shows the bandstructure of CrTe. The $s$ states of Te are very low in energy and omitted in the figure. Around $-4$ eV, the $p$-bands can be seen. In the majority band, the states formed by the Cr $e_g$ orbitals are found at about 1.5 eV under the Fermi level, while in the minority band these states are at about 1.5 eV above the Fermi level. They are narrow, reflecting the fact that their hybridization with the states of Te neighbors is weak (or even zero, at $\mathbf{k} = 0$, due to symmetry). These bands can accommodate two electrons per
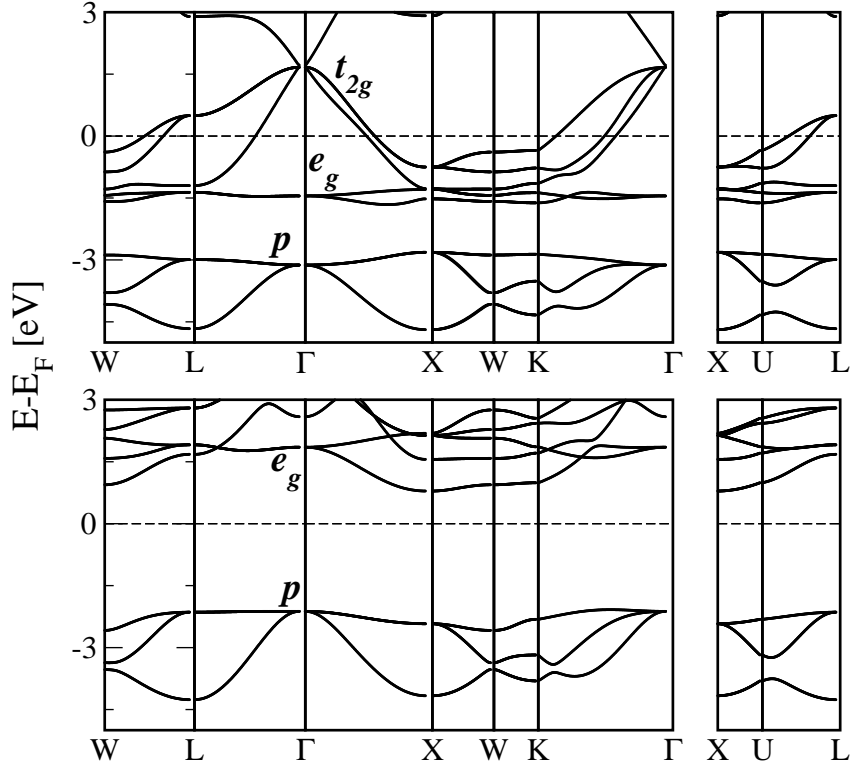
Figure 6.17: The bulk bandstructure of CrTe, along the high symmetry lines of the first Brillouin zone of an fcc lattice. The upper panel presents the bandstructure in the majority spin direction, while the lower one presents the bandstructure in the minority spin direction.

spin. Above them, the substantially wider antibonding $p$-$t_{2g}$ hybrids appear, starting from $-1.5$ eV for majority and from $+1$ eV for minority. Their large bandwidth can be attributed to the strong hybridization and to their high energy position. The bonding-antibonding splitting is also contributing to the fact that they are pushed up beyond the narrow $e_g$ states. As a result, the three families of bands do not intermix, but are rather energetically separate. In the majority-spin direction the bonding-antibonding splitting is smaller, because Cr $3d$ states are originally lower in energy, closer to the $p$ states of the Te atom. In the minority spin direction the states are higher due to the exchange splitting and the gap is positioned around $E_F$. Band counting gives an integer total magnetic moment of 4 $\mu_B$.

An additional note can be made here. Looking at the Fig. 6.15, one notices that in the case of the compounds containing group-V $sp$ element (As, Sb), the low lying states in the majority band have more of the transition

| | compound (YZ) | $a_{\mathrm{opt}}$ (Å) | $M_Y$ ($\mu_B$) | $M_Z$ ($\mu_B$) | $M_t$ ($\mu_B$) |
|---|---|---|---|---|---|
| $Z=10$ | VAs | 5.694 | 1.885 | −0.156 | 2.000 |
| $Z=11$ | CrAs | 5.652 | 2.958 | −0.240 | 3.000 |
| | VTe | 6.250 | 2.630 | −0.123 | 3.000 |
| $Z=12$ | CrTe | 6.257 | 3.705 | −0.151 | 4.000 |
| | MnSb | 6.182 | 3.907 | −0.155 | 4.000 |

Table 6.3: The (GGA) optimized lattice constants $a_{\mathrm{opt}}$, the magnetic moments in the muffin-tin spheres of atoms Y= V, Cr, Mn ($M_Y$), Z=As, Sb, Te ($M_Z$) and the total magnetic moment per unit cell, $M_t$, of several zinc-blende half-metallic compounds of type YZ, with $Z$ valent electrons in the unit cell.

metal character, as opposed to the case of the compounds with group-VI $sp$ element (Te). The reason is that the $p$ states of the group-VI elements lie lower in energy than the $p$ states of the group-V elements which in turn lie at approximately the same energy as the majority $d$ states of the transition metal (or even higher). On the other hand, in the minority band the $d$ states are, due to the exchange splitting, shifted to higher energies and the low lying states are here rather of the character of the $sp$ atom. In the case of MnSb for instance, the exchange splitting of Mn is very large and the $p$-$t_{2g}$ hybridization which opens the gap in the minority band is not visible in the majority band (Fig. 6.15). The lower lying $p$ states of group-VI elements are the reason why the gap in the compounds containing these elements is bigger than in the compounds with group-V elements.

Finally, like in the case of half- and full-Heusler alloys, for the zb half-metallic compounds it is also possible to define a rule which determines the total magnetic moment from the number of the valence electrons. One can see this from simple electron counting. The bonding $p - d$ bands can accommodate 6 electrons (3 per spin), and since they lie low in energy they must be filled up. In addition, there is yet another band lower in energy, consisting of the $s$ states of the $sp$ atom, which has space for two electrons (one per spin). Once these 8 bands are filled by 8 of the valence electrons, the remaining electrons will fill part of majority $d$ states, first the lower-lying $e_g$ and then the $t_{2g}$, creating the magnetic moment. This electron counting gives then for the magnetic moment the *rule of 8* [21],

$$M_t = (Z - 8), \tag{6.4}$$

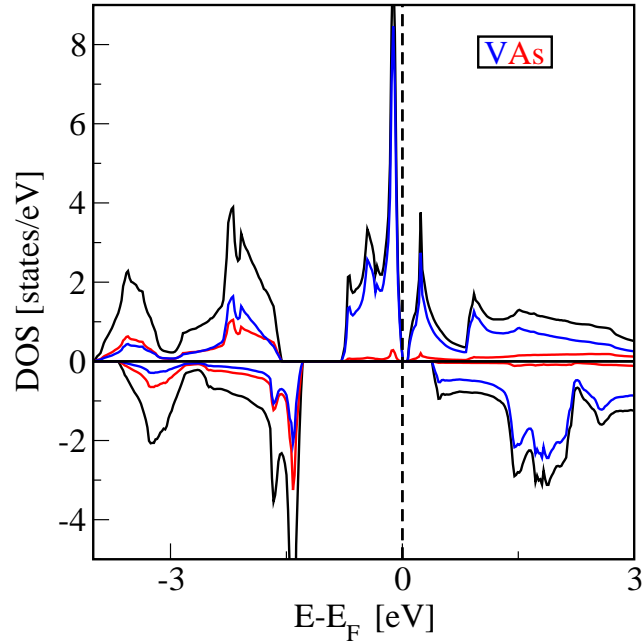where $Z$ is the total number of valence electrons in the unit cell. As an

Figure 6.18: Atom-resolved density of states of the zinc-blende ferromagnetic semiconductor VAs. LDOS of V - blue lines, LDOS of As - red lines. The total DOS is shown with the black lines

illustration of this rule, in the Table 6.3 the magnetic moments of some of the half-metallic zb compounds are given. The case of VAs is interesting, because it turns out that it is a (very) narrow gap semiconductor (Fig. 6.18). It has in total ten valence electrons, eight of which are accommodated in the low lying $s$ and $p$ bands. The majority $e_g$ band accommodates the remaining two. Since the $e_g$ are energetically separated from the higher lying $t_{2g}$ states by a small gap in the majority band, the Fermi energy lies in this small gap.

# Chapter 7

# Half-metallicity made difficult

The emergence of the field of magnetoelectronics during the last decade has given birth to a new series of challenges in materials science [3, 4]. A central problem remains the the spin-injection from a ferromagnet into a semiconductor [112, 113]. Its successful realization would lead to the creation of a series of novel devices such as spin-filters [15], tunnel junctions [16] or GMR devices for spin injection [17]. The use of half-metallic ferromagnets as electrodes was proposed to maximize the efficiency of such spintronic devices and for this reason a great amount of work is being done on investigation of stability of the gap in the minority spin band.

Experiments seem to well establish the half-metallicity in the case of NiMnSb single crystals [28, 29] or away from the surface in the case of thick films [35]. On the other hand, the surface states will destroy the gap in the first several layers (see Section 7.2). Another problem one encounters when trying to form an interface of a half-metal with a semiconductor are the possible interface states which might appear in the gap. Interfaces of NiMnSb with InP are investigated in Section 7.3.

Several studies were performed on NiMnSb in which the gap was found to be stable under hydrostatic pressure and tetragonalization [114] or a small disorder [31] but the exchange of the atoms occupying the different sublattices completely destroys the gap [30]. A study of antisite defects and their screening mechanisms in $Co_2MnGe$ and $Co_2MnSi$ can be found in Ref. [115]. In general, impurities in half-metals can be a serious source of problems. An isolated point defect cannot change the band gap nor the Fermi level, since these are bulk properties. Also the number of minority states cannot be changed, except when the defect introduces additional resonances in the minority band, or takes out weight from this band by splitting-off states into the gap. As a result, in the dilute limit the band gap and half-metallicity is preserved, but states in the gap, either occupied or empty ones, can occur.

An exception occurs if a multifold degenerate gap-state is partially occupied and thus fixed at the Fermi level. Then a symmetry lowering Jahn-Teller splitting of the level is expected to occur. For finite concentrations, impurity states in the gap overlap and fast broaden to form impurity bands. If the impurities are randomly distributed, one can show by applying the coherent potential approximation (CPA) [27], that the band width scales as $\sqrt{c}$, where $c$ is the impurity concentration. For instance, this means, that the bandwidth is for a concentration of 1 % only a factor 3 smaller than for 10 %. Therefore the impurity bands broaden very fast with concentration and can soon fill up the band gap, in particular, if the band gap is small and the impurity states are rather extended.

The control of defects and disorder is an important problem for the application of Heusler alloys in spin electronics, but even in an ideally prepared single crystal the spin-orbit coupling will introduce states in the half-metallic gap of the minority states (for the spin-down electrons), which are produced by spin-flip scattering of the majority states (with spin-up direction). The effect of spin-orbit coupling is investigated in Section 7.1.

Finally, one of the most serious enemies of half-metallicity, thermal excitations, will not only introduce states within the gap, but at sufficiently high temperature they will totally destroy the magnetism of a ferromagnet. Since we would like to have devices which function at the temperature range in which we function (i.e. around 290 K), it is important for the applications of half-metals to know how they behave at this temperature. A study of the finite temperature behavior of half-metals will be presented in the next chapter.

## 7.1   Effect of Spin-orbit Coupling

In half-metals, spin-orbit coupling (SOC) can introduce states in the gap in the minority spin band and so reduce the spin polarization at the Fermi level. This effect is expected to be stronger for the compounds which contain heavy elements. For instance in MnBi, theoretically predicted half-metallic zb compound, Mavropoulos and coworkers [116] found that DOS in the gap of the minority spin band introduced by SOC is of the order of 13 % of the DOS in the majority band at the Fermi level.

The spin-orbit coupling of the two spin channels is related to the unperturbed potential $V(r)$ around each atom via the angular momentum operator $\vec{L}$ and the Pauli spin matrix $\vec{\sigma}$:

$$V_{\mathrm{so}}(r) = \frac{1}{2m^2c^2}\frac{\hbar}{2}\frac{1}{r}\frac{dV}{dr}\,\vec{L}\cdot\vec{\sigma} = \begin{pmatrix} V_{\mathrm{so}}^{\uparrow\uparrow} & V_{\mathrm{so}}^{\uparrow\downarrow} \\ V_{\mathrm{so}}^{\downarrow\uparrow} & V_{\mathrm{so}}^{\downarrow\downarrow} \end{pmatrix} \qquad (7.1)$$
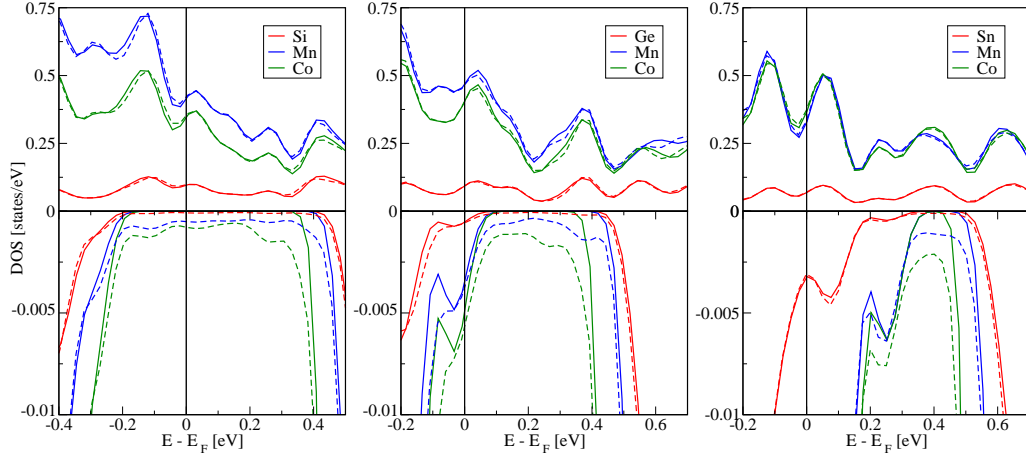
Figure 7.1: Atom-resolved densities of states of the full-Heusler alloys with formula $Co_2MnZ$, Z=Si, Ge, Sn, with (dashed lines) and without (solid lines) spin-orbit coupling. LDOS of Si, Ge, Sn - red lines, LDOS of Mn - blue lines, LDOS of Co - green lines.

The $2 \times 2$ matrix form is written in spinor basis. The two spin directions are denoted with $\uparrow$ and $\downarrow$. The unperturbed crystal Hamiltonian eigenvalues for the two spin directions are $E^{0\uparrow}_{n\vec{k}}$ and $E^{0\downarrow}_{n\vec{k}}$, and the unperturbed Bloch eigenfunctions as $\Psi^{0\uparrow}_{n\vec{k}}$ and $\Psi^{0\downarrow}_{n\vec{k}}$. Then, noting that within the spin-down gap there exist no unperturbed solutions $\Psi^{0\downarrow}_{n\vec{k}}$ and $E^{0\downarrow}_{n\vec{k}}$, the first order solution of Schrödinger equation for the perturbed wavefunction $\Psi^{\downarrow}_{n\vec{k}}$ reads for states in the gap:

$$\Psi^{(1)\downarrow}_{n\vec{k}}(\vec{r}) = \sum_{n'} \frac{\langle \Psi^{0\downarrow}_{n'\vec{k}} | V^{\downarrow\uparrow}_{so} | \Psi^{0\uparrow}_{n\vec{k}} \rangle}{E^{0\uparrow}_{n\vec{k}} - E^{0\downarrow}_{n'\vec{k}}} \Psi^{0\downarrow}_{n'\vec{k}}(\vec{r}). \tag{7.2}$$

Here, the summation runs only over the band index $n'$ and not over the Bloch vectors $\vec{k}'$, because Bloch functions with $\vec{k}' \neq \vec{k}$ are mutually orthogonal. Close to the crossing point $E^{0\uparrow}_{n\vec{k}} = E^{0\downarrow}_{n'\vec{k}}$ the denominator becomes small and the bands couple strongly. Then one should also consider higher orders in the perturbation expansion. Since at the gap edges there exist spin-down bands of the unperturbed Hamiltonian, this effect can become important near the gap edges. Apart from that, the important result is that in the gap region the spin-down spectral intensity is a weak image of the spin-up one. Since the spin-down DOS is related to $|\Psi^{(1)\downarrow}_{n\vec{k}}|^2$, it is expected that within the gap the DOS has a quadratic dependence on the spin-orbit coupling strength: $n_\downarrow(E) \sim (V^{\downarrow\uparrow}_{so})^2$.
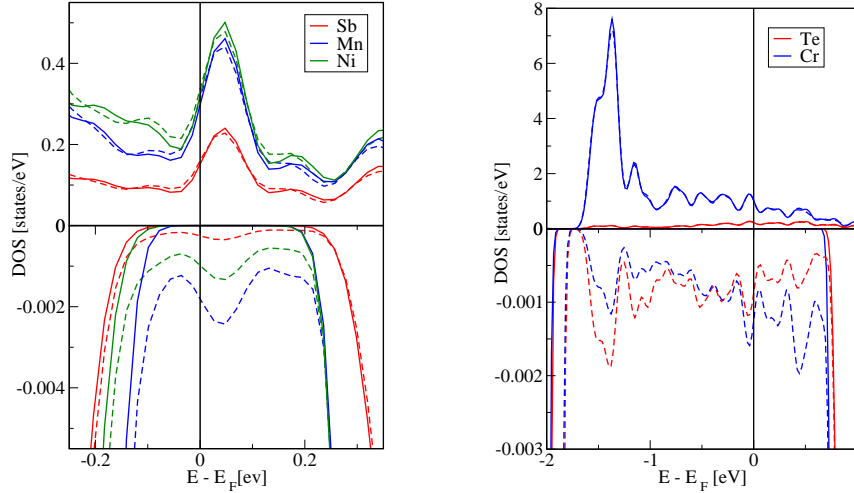
Figure 7.2: Atom-resolved densities of states of the half-Heusler alloy NiMnSb (left) and zb half-metal CrTe (right), with (dashed lines) and without (solid lines) spin-orbit coupling. LDOS of Sb, Te - red lines, LDOS of Mn, Cr - blue lines, LDOS of Ni - green lines.

In Fig. 7.1, densities of states of full-Heusler compounds $Co_2MnSi$, $Co_2MnGe$ and $Co_2MnSn$ with (dashed lines) and without (solid linew) SOC are shown. Although both $Co_2MnGe$ and $Co_2MnSn$ present a small DOS in the minority band at the Fermi level ($E_F$ enters slightly into the valence band), it is instructive to examine the DOS in the gap region and see how the spinpolarization decreases as one changes to heavier elements (Si→Ge→Sn). Spin-polarization at the energy $E$, $P(E)$, is defined by the ratio

$$P(E) = \frac{n^{\uparrow}(E) - n^{\downarrow}(E)}{n^{\uparrow}(E) + n^{\downarrow}(E)}. \tag{7.3}$$

In the Table 7.1 two quantities are shown: the spin polarization at $E_F$, $P(E_F)$, and in the middle of the gap, $P(E_M)$. The latter reflects the strength of the spin-orbit induced spin flip scattering, while the former is relevant only when $E_F$ is well within the gap. For the two half-metals shown in the Fig. 7.2, NiMnSb and zb CrTe, also high values of polarization at the Fermi level (which in both cases lies in the gap) are obtained: 99.3% for NiMnSb and 99.6% for CrTe.

Comparing the results gathered in the Table 7.1, one can notice a slight lowering of the polarization with a change to the heavier *sp*. Mavropoulos *et al.* have investigated the behavior of the spin polarization in half-Heusler alloys of the type XMnSb, taking for the X-element Ni, Pd and Pt [117]. They found a much more drastic decrease of the spin polarization in the middle of

| Alloy | Co$_2$MnSi | Co$_2$MnGe | Co$_2$MnSn | NiMnSb | PdMnSb* | PtMnSb* |
|---|---|---|---|---|---|---|
| $P(E_F)$ | 99.7% | 97.9% | 81.5% | 99.3% | 40.0% | 66.5% |
| $P(E_M)$ | 99.7% | 99.4% | 99.0% | 99.3% | 66.5% | 94.5% |

Table 7.1: Calculated spin polarization at the Fermi level $[P(E_F)]$ and in the middle of the spin-down gap $[P(E_M)]$, for several Heusler alloys. ($*$):Reference [117]

the gap, namely 99.3% for NiMnSb (the same value is also obtained from a calculation presented here, Fig. 7.2 left), 98.5% for PdMnSb, and 94.5% for PtMnSb. A possible reason for this difference is that in the cases of Co$_2$MnSi, Co$_2$MnGe, and Co$_2$MnSn, the *sp* atom, whose states are far away from the gap was changed, while in the case they studied one of the *d* atoms, whose states hybridize and open the gap, was changed.

## 7.2   Surfaces of NiMnSb

Recently, high quality films of NiMnSb alloys have been grown [118, 119, 120], but they were found not to be half-metallic [18, 121]. A maximum value of 58% for the spin polarization of NiMnSb was obtained by Soulen *et al.* [18]. These polarization values are consistent with a small perpendicular magnetoresistance measured for NiMnSb in a spin-valve structure [122] and superconducting tunnel junction or a tunnel magnetoresistive junction [16]. Ristoiu *et al.* showed that during the growth of the NiMnSb thin films, first Sb and then Mn atoms segregate to the surface, which is far from being perfect, thus decreasing the obtained spin polarization [36]. After removing the excess of Sb by a flash annealing, they managed to get a nearly stoichiometric ordered alloy surface being terminated by a MnSb layer, which presented a spin polarization of about 67±9% at room temperature [36].

   First-principles calculations have been also employed to study the surfaces of NiMnSb. Jenkins and King were the first to study by a pseudopotential technique (CASTEP) the MnSb terminated (001) surface of NiMnSb and showed that there are two surface states at the Fermi level, which are well localized at the surface layer [37]. They have also shown that there is a small reconstruction of the surface with the Mn atoms moving slightly inwards and the Sb outwards and this small $c(1 \times 1)$ relaxation is energetically more favorable than the creation of Mn or Sb dimers. The unrelaxed (001) surfaces were also studied by Galanakis, using the full-potential version of the Korringa-Kohn-Rostoker Green function method [38] and a large spin polar-

ization at the MnSb-terminated surface in agreement with the experiments of Ristoiu *et al.* [36] was found. A study of the (111) surfaces by Jenkins [39] has shown that the Sb-terminated (111) surfaces are more stable than the Mn- and Ni-terminated ones [39].

In this section, ab-initio calculations of the (001) and (111) surfaces of NiMnSb obtained with FLAPW method are presented. All possible terminations are taken into account. The atomic positions of the atoms near the surface are relaxed and the influence of these relaxations on the properties of the surfaces is studied.

Prior to presenting the results, an important note should be made. Based on the experience from ferromagnets and semiconductors, two effects should be particularly relevant for the surfaces of half-metals:

- In ferro- and antiferromagnets, the moments of the surface atoms are strongly enhanced due to the missing hybridization with the cut-off neighbors

- In semiconductors, surface states can appear in the gap, such that the surface often becomes metallic. Also this is a consequence of the reduced hybridization, leading to dangling bond states in the gap.

## 7.2.1   Structure of the surfaces

In this section, a short description of the unit cells used for the surface calculations is given. It is convenient to view the crystal as a set of successive atomic planes, with a relevant in-plane unit cell, corresponding to the surface unit cell. In Fig. 7.3, two of many possible choices of unit cells of $C1_b$ structure (see Fig. 6.2) are shown. The (001) in-plane unit cell (upper panel) is quadratic. Its in-plane lattice parameter is $a/\sqrt{2}$, $a$ being the lattice parameter of the cubic unit cell. The bulk unit cell is built by four equidistant layers, and the interlayer distance is $a/4$. For the calculation of (001) surfaces, the the number of layers will, of course, depend on the selected thickness of the film. There are two different possible terminations in the case of the (001) surfaces, one containing the Mn and Sb atoms while the other contains the Ni atom. In the present study, 9 atomic layers were used for the calculations of (001) surfaces. This means that the two surfaces are equivalent, but rotated by 90°.

The bulk unit cell shown in the lower panel of the Fig. 7.3 corresponds to the hexagonal (111) in-plane lattice for $C1_b$ structure. Along the [111] direction, the unit cell consists of alternating layers containing only one chemical element. There are 12 equidistant layers in the bulk unit cell (the stacking

## (001)

$\alpha_1$

| 1 | (0, 0) | 3 | (0, 0.5) |
|---|--------|---|----------|
| 2 | (0.5, 0.5) | 4 | (0.5, 0) |

$a/\sqrt{2}$

| layer | atom 1 | atom 2 | atom 3 | atom 4 |
|-------|--------|--------|--------|--------|
| 1 | Mn | Sb | | |
| 2 | | | Ni | |
| 3 | Sb | Mn | | |
| 4 | | | | Ni |

$\alpha_2$

## (111)

| 1 | (0, 0) | 3 | (2/3, 2/3) |
|---|--------|---|------------|
| 2 | (1/3, 1/3) | | |

$\alpha_1$

$a/\sqrt{2}$

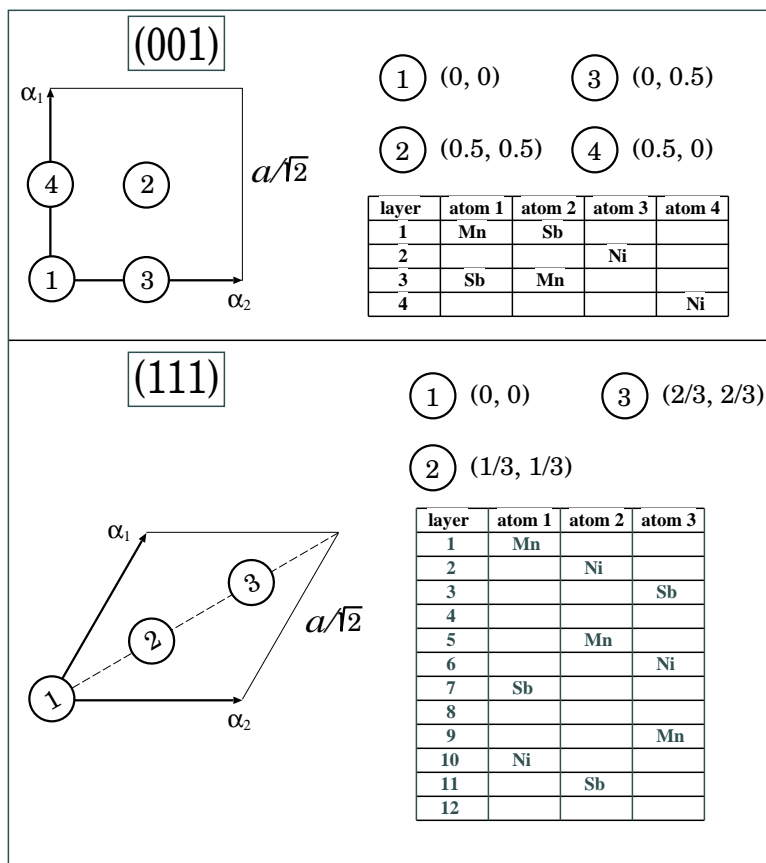| layer | atom 1 | atom 2 | atom 3 |
|-------|--------|--------|--------|
| 1 | Mn | | |
| 2 | | Ni | |
| 3 | | | Sb |
| 4 | | | |
| 5 | | Mn | |
| 6 | | | Ni |
| 7 | Sb | | |
| 8 | | | |
| 9 | | | Mn |
| 10 | Ni | | |
| 11 | | Sb | |
| 12 | | | |

$\alpha_2$

Figure 7.3: Two choices of bulk unit cells, the one consisting of (001) layers (upper panel) and the other consisting of (111) layers (lower panel). On the left, the in-plane unit cells are drawn. In the tables, the atoms which occupy the positions 1, 2, 3 (and 4 in the case of (001) surface) in each layer of the unit cell are listed. The positions of the atoms are given in units of the in-plane lattice constant.

along the [111] direction is given in the corresponding table in Fig. 7.3), 3 of which are empty, and the total hight of the cell is $a\sqrt{3}$. The lattice parameter of the in-plane unit cell is $a/\sqrt{2}$. This in-plane unit cell was used for the calculation of the (111) surfaces. In the case of a Ni-terminated surface, for example, there are two different possibilities: either to have a Mn subsurface layer or an Sb one. The films used here for calculations of (111) surfaces consisted of 13 atomic layers. This means that the two sides of the films were giving the two possible terminations for each of the three constituents (Ni, Mn and Sb).

## 7.2.2 (001) surfaces

As mentioned above, there are two different possible terminations for the (001) surfaces, either the Ni one or the MnSb one. In both cases, the three top layers were geometrically relaxed. In the case of Ni termination, the Mn and Sb atoms at the subsurface layer did almost not move, while the distance between the Ni layer and the MnSb subsurface layer was reduced by around 10%. In the case of MnSb termination the Mn atom at the surface layer moves inwards and the Sb atom outwards. The distance between the Mn surface atom and the Ni subsurface layer is contracted by 3.5 % and the distance between the Sb surface atom and the Ni subsurface layer is expanded by 7.3 %. These results agree nicely with the results obtained for the same termination of the (001) surface by Jenkins and King [37].

### Density of states

In the left panel of figure 7.4, we present atom- and spin-projected densities of states (DOS) for the Ni atom at the surface and the Mn and Sb atoms in the subsurface layer for the case of the Ni-terminated surface. The right panel contains the analogous results for the MnSb terminated NiMnSb(001) surface. For both possible terminations, the surface DOS of both the relaxed and non-relaxed calculations together with the bulk results (grey region) are gathered. Relaxation has a very small effect on the DOS, even around the
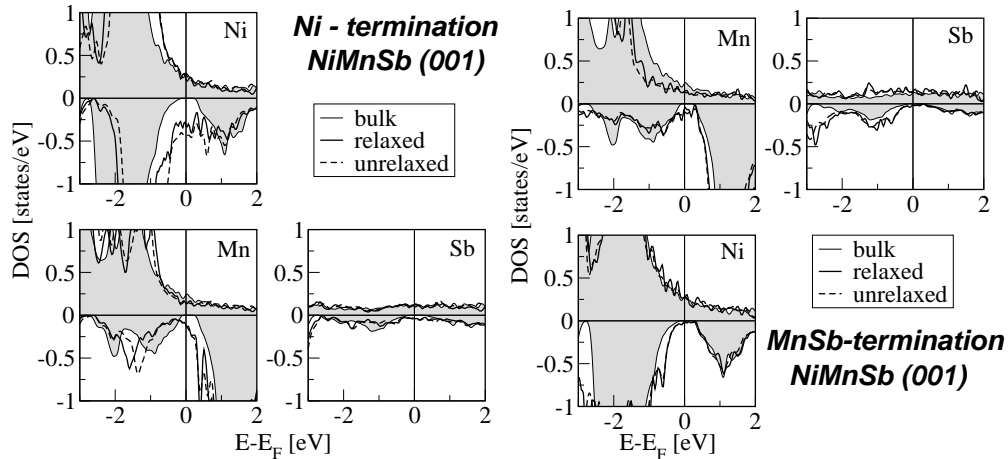
Figure 7.4: Local DOS for the atoms at the surface and subsurface layers for both Ni- and MnSb- terminated NiMnSb(001) surfaces. With the thick solid line the results for the relaxed surface and with the dashed line for the non-relaxed case. Grey represents the bulk results.
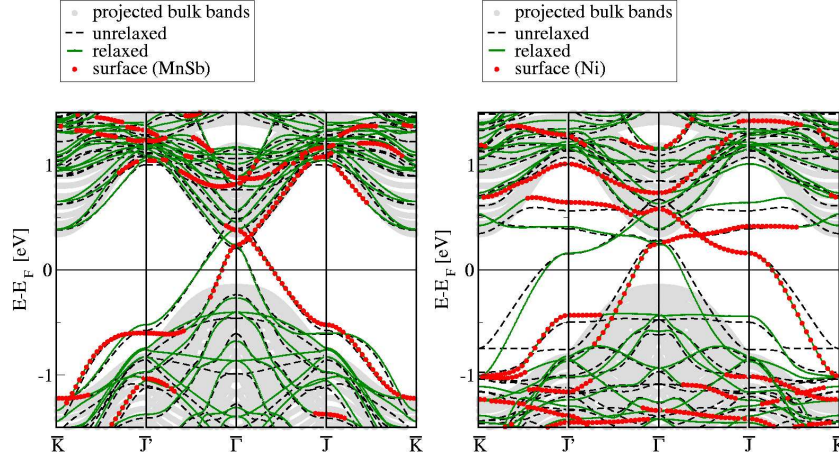
Figure 7.5: Minority-spin surface-bandstructure for the two different (001) surfaces. With grey the projection of the bulk bands on the surface is plotted, with dashed lines the band structure of the non-relaxed surface and with green line of the relaxed one. The red circles represent the surface states for just one of the two equivalent surfaces of the slab, having more than 50% of their weight located at the first two layers of one of the surfaces.

Fermi level.

In the case of the MnSb terminated surface the DOS, with the exception of the gap region, is very similar to the bulk calculations. The Ni atom in the subsurface layer presents practically a half-ferromagnetic character with an almost zero minority-spin DOS, while for the bulk there is an absolute gap. The Mn and Sb atoms in the surface layer show more pronounced differences with respect to the bulk, and within the gap there is a very small Mn-$d$ and Sb-$p$ DOS, due to the surface states. These states are strongly



Figure 7.6: Two-dimensional (001) surface Brillouin zone

localized at the surface layer as at the subsurface layer there are practically no states inside the gap. This is in agreement with previous first principles calculations by Galanakis [38], as well as with the experiments of Ristoiu *et al.* [36] who in the case of a well ordered MnSb-terminated (001) surface measured a high spin polarization.

In order to show the origin of the surface states, the minority-spin surface-bandstructures for the two terminations are drawn in figure 7.5. The two-
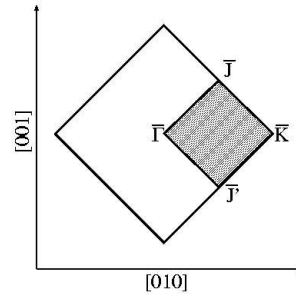
dimensional Brillouin zone (also called *surface Brillouin zone*, SBZ) is a simple square (Fig. 7.6). The bandstructure of the relaxed system (green lines) has little difference with respect to the unrelaxed one (dashed lines). As it was pointed out earlier, since the slab used in the calculations consists of 9 atomic layers, the two opposite sides of the film are equivalent, but rotated by 90º. This implies that what is $[\bar{\Gamma} \to \bar{J}]$ direction for one of the surfaces, is $[\bar{\Gamma} \to \bar{J}']$ for the other and vice versa. Since the bandstructure in the Fig. 7.5 presents all the states of the electronic system of the slab, these states (green lines) appear to be the same along these two directions. To distinguish between the states coming from the two different surfaces, the red circles show the states that have more than 50% of their weight located at the first two layers at one of the surfaces. The presented results agree with the ones of Jenkins and King who for the same surface have shown that there are two surface states [37]. The results for the MnSb terminated surface are presented in the left panel. The lower lying state (at 0.20 eV at the $\bar{\Gamma}$ point) is due to the interaction between $e_g$-like dangling bond states located at the Mn atoms. The second surface state, which is higher in energy ($\sim$0.3 eV at the $\bar{\Gamma}$ point) arises from the hybridization between $t_{2g}$-like orbitals of Mn with $p$-type orbitals of Sb. The first surface state disperses downwards along the $[\bar{\Gamma} \to \bar{J}']$ direction while the second surface state disperses upwards along the same direction. Their behavior is inversed along the $[\Gamma \to \bar{J}]$ direction. The two surface states cross along the $[\Gamma \to \bar{J}]$ direction bridging the minority gap between the valence and the conduction band. Along the other directions anticrossing occurs leading to band-gaps. Of interest are also the saddle-like structures around the zone center which manifest as van Hove singularities in the DOS.

For the Ni-terminated surface the DOS shown in Fig. 7.4 reveals that the surface states are much more pronounced (i.e. the spin polarization at the Fermi energy is lowered). The surface bands, as shown in Fig. 7.5, are flat in the region of the bulk gap in the minority spin-band, leading to the increased DOS at these energies.

### Spin polarization

The spin polarization at the Fermi level is of primary importance, since the electrons near the Fermi level are most relevant for transport properties. In Fig. 7.7, the angular-momentum-, spin-, and layer-projected DOS at the Fermi level ($n^{\uparrow}(E_F)$ or $n^{\downarrow}(E_F)$) for all the calculated slabs are shown. The layers near the edges of the each figure represent the two equivalent surfaces while the layers in the middle can be considered as "bulk". In the case of the unrelaxed surfaces (upper panels) the DOS intensity of the layers at the
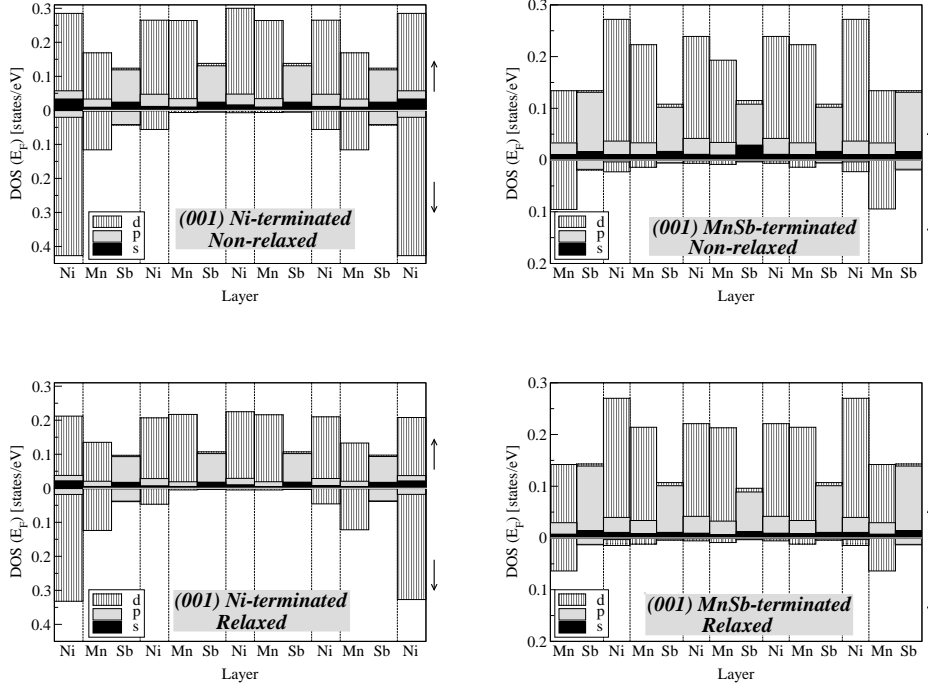
Figure 7.7: Angular momentum-projected DOS at the Fermi level along the whole slab used in the calculations. Note that the slabs in the case of the (001) surfaces have the same terminations from both sides.

middle of the slab is almost zero and thus the dimensions of the slab used in the calculation are sufficient to realistically represent the real surface. Only in the case of the relaxations for the MnSb-termination, the Mn atom in the middle layer presents a very small DOS. As expected, the states at the Fermi level are mainly of $d$ character for Mn and Ni and of $p$ character for Sb.

In Table 7.2, the spin polarization data for both (001) surfaces are gathered. The spin polarization was calculated at the Fermi level, either taking into account only the first two surface layers ($P_1$), or the first four surface layers ($P_2$). $P_2$ represents quite well the experimental situation, as the spin polarization in the case of films is usually measured by inverse photoemission which probes only the 3-4 atomic layers of the sample that are closest to the surface[123]. As it is expected, the inclusion of more layers increases the spin polarization since the deeper layers are more bulk-like. Relaxation in the case of the Ni-terminated surface decreases the spin polarization while in the case of the MnSb-terminated surface the spin polarization is increased by the

| Spin Polarisation | | (001) Ni unrelaxed | (001) Ni relaxed | (001) MnSb non-relaxed | (001) MnSb relaxed |
|---|---|---|---|---|---|
| Layers S, S-1 | $n^\uparrow(E_F)$ | 0.855 | 0.641 | 0.777 | 0.796 |
| | $n^\downarrow(E_F)$ | 0.655 | 0.556 | 0.161 | 0.107 |
| | $P_1$ | 13% | 7% | 66% | 76% |
| Layers S, S-1 S-2, S-3 | $n^\uparrow(E_F)$ | 1.781 | 1.352 | 1.573 | 1.543 |
| | $n^\downarrow(E_F)$ | 0.730 | 0.618 | 0.194 | 0.135 |
| | $P_2$ | 42% | 37% | 78% | 84% |

Table 7.2: Spin-projected DOS at the Fermi level ($n^\uparrow(E_F)$ or $n^\downarrow(E_F)$) for different (001) surfaces taking into account either the top two layers, S and S-1 (upper panel), or the top four layers (lower panel). The spin polarization is defined by the Eqn. 7.3

relaxation of the atomic positions.

In the case of the Ni terminated surface, the minority-spin DOS at the Fermi level is quite large with respect to the majority DOS and net polarization $P_2$ is 42% for the unrelaxed case and slightly decreases to 37% by the structural optimization. In the case of the MnSb terminated surface, the spin polarization is much larger and now $P_2$ reaches a value of 84% for the relaxed structure, which means that more than 90% of electrons at the Fermi level are of majority-spin character. As can be seen from the Fig. 7.7, the main difference between the two different terminations is the contribution of the Ni spin-down states. In the case of the MnSb surface, Ni in the subsurface layer has a negligible spin-down DOS at the Fermi level with respect to the Ni-terminated surface; in the latter case, the spin polarization of the surface Ni layer is even reversed!

It is also interesting to note that for both terminations the net Mn spin polarization is close to zero while Sb atoms in both cases show a large spin polarization. The calculated $P_2$ value of 84% for the MnSb terminated surface is larger than the experimental value of 67% obtained by Ristoiu and collaborators [36] for a thin-film terminated with a MnSb stoichiometric alloy surface layer, but experimentally no exact details of the structure of the film are known and the comparison between experiment and theory is not straightforward.

## Magnetic moments

The spin magnetic moments in the muffin-tin spheres of the atoms in the surface and subsurface layers are shown in Table 7.3. We should firstly notice

| (001) Ni-terminated | | | (001) MnSb-terminated | | |
|---|---|---|---|---|---|
| $m_{spin}$ | unrelaxed | relaxed | $m_{spin}$ | unrelaxed | relaxed |
| Ni(S) | 0.435 | 0.377 | Mn(S) | 3.937 | 3.925 |
| Mn(S-1) | 3.792 | 3.642 | Sb(S) | −0.101 | −0.102 |
| Sb(S-1) | −0.043 | −0.044 | Ni(S-1) | 0.211 | 0.242 |
| Ni(S-2) | 0.273 | 0.278 | Mn(S-2) | 3.661 | 3.690 |
| Mn(S-3) | 3.707 | 3.585 | Sb(S-2) | −0.065 | −0.067 |
| Sb(S-3) | −0.055 | −0.054 | Ni(S-3) | 0.269 | 0.243 |

Table 7.3: Atom-projected spin magnetic moments ($m_{spin}$) in $\mu_B$ for the atoms at the top four layers for both Ni- and MnSb-terminated (001) surfaces, for relaxed and unrelaxed cases.

that relaxation has a very small effect on the spin moments. Even for the surface layer which shows the largest relaxation effects, spin moments change only marginally.

In the case of the MnSb terminated NiMnSb(001) surface, the Ni spin moment is comparable to the bulk situation (see Table 6.1). The Mn in the surface layer loses $\sim 0.3 e^-$ more than the bulk Mn due to the spilling of charge out into the vacuum. This charge is mainly of minority-spin character and Mn's spin moment increases with respect to the bulk and is slightly more than $\sim 3.9 \mu_B$. This behavior arises from the reduced symmetry of the surroundings of the Mn atom in the surface, where it loses two of the four neighboring Ni atoms. In the majority band, this leads to a narrowing of the $d$-DOS and a slight increase of the $d$ count by 0.10 $e^-$, while in the minority valence band the Mn $d$ contribution decreases by 0.20 $e^-$. Moreover, the splitting between the unoccupied Mn states above $E_F$ and the center of the occupied Mn states decreases and at $E_F$ a surface state appears. It should also be mentioned here that since the half-metallic character is lost, an increase of the total spin moment is observed, which is no more an integer.

In the case of the Ni terminated surface, the changes in the DOS compared to the bulk are more pronounced. The Ni atom in the surface instead of gaining $\sim 0.5 e^-$ as in the bulk now even loses some charge. As was the case for the Mn surface atom in the MnSb terminated surface, the Ni spin magnetic moment is increased. (see Table 7.3). The Mn and Sb atoms in the subsurface layer present a charge transfer comparable to the bulk compound and also a comparable spin moment.

### 7.2.3 (111) surfaces

We now turn to the study of NiMnSb (111) surfaces. Relaxations in the case of the (111) surfaces, which were allowed for the first three surface layers, are considerably larger than for the (001) surfaces. In Table 7.4, the change in the distance between two successive layers with respect to the unrelaxed cases is shown. Along the [111] direction the layers consist of only one chemical element. In the unrelaxed cases the distance between Sb and Mn successive layers is twice the distance between a Ni and a Mn or Sb layer (see Fig. 7.3 for the stacking). As can be easily seen, for a Ni termination there can be either a Mn or a Sb layer as subsurface layers, and similarly for Mn and Sb terminations.

When the (111) surface is Ni-terminated, the Ni atoms at the surface layer move closer to the subsurface layer and the contraction is 23% and 18% for Sb and Mn as subsurface layers, respectively. Relaxations are much less important from the subsurface layer and on. When the surface is a Mn-Ni-Sb-... one, the Mn atoms move closer to Ni ones due to the lower coordination. In the case of the Mn-Sb-Ni-... the relaxation of the Mn surface layer is much more important since the Mn-Sb distance is twice the Mn-Ni one and the Mn atoms at the surface layer and the Sb atoms at the subsurface layer have to account for more empty space. Similarly, relaxations are much more important in the case of the Sb-Mn-Ni-... surface than the Sb-Ni-Mn-... termination.

| Relaxations (111) | $\Delta d_{12}$ | $\Delta d_{23}$ | $\Delta d_{34}$ |
|---|---|---|---|
| Ni-Sb-Mn-Ni-... | $-23\%$ | $2\%$ | $<1\%$ |
| Ni-Mn-Sb-Ni-... | $-18\%$ | $4\%$ | $-3\%$ |
| Mn-Ni-Sb-Mn-... | $-13\%$ | $-5\%$ | $2\%$ |
| Mn-Sb-Ni-Mn-... | $-16\%$ | $18\%$ | $\sim 0\%$ |
| Sb-Ni-Mn-Sb-... | $2\%$ | $-11\%$ | $4\%$ |
| Sb-Mn-Ni-Sb-... | $-16\%$ | $32\%$ | $-7\%$ |

Table 7.4: Change in the distance ($\Delta d_{ij}$) between successive layers ($i$ and $j$) when the atomic positions were relaxed for the (111) surfaces with respect to the unrelaxed cases. Negative values correspond to contraction and positive to expansion. Notice also that in the unrelaxed cases the distance between Sb and Mn successive layers is twice the distance between a Ni and a Mn or Sb layer.

### Ni-terminated surfaces

As it was already mentioned there are two different possible configurations of a Ni-terminated surface:

1. When the subsurface layer is the Mn one, the sequence of the layers under it is Ni - Mn - Sb - Ni - Mn - ...

2. When the subsurface layer is the Sb one, the sequence of the layers under it is Ni - Sb - Mn - Ni - Sb - ...

In bulk, Ni has four Mn and four Sb atoms as the first neighbors. When it is at the (111) surface, the Ni atom loses four out of its eight first neighbors.

| (111) Ni-Mn-Sb-... | | | (111) Ni-Sb-Mn-... | | |
|---|---|---|---|---|---|
| $m_{spin}$ | unrelaxed | relaxed | $m_{spin}$ | unrelaxed | relaxed |
| Ni(S) | 0.536 | 0.470 | Ni(S) | 0.295 | 0.300 |
| Mn(S−1) | 3.892 | 3.774 | Sb(S−1) | −0.042 | −0.042 |
| Sb(S−2) | −0.050 | −0.049 | Mn(S-2) | 3.714 | 3.541 |
| Ni(S−3) | 0.272 | 0.265 | Ni(S−3) | 0.234 | 0.214 |
| Mn(S−4) | 3.700 | 3.567 | Sb(S−4) | −0.069 | −0.070 |
| Sb(S−5) | −0.052 | −0.050 | Mn(S−5) | 3.679 | 3.557 |
| (111) Mn-Ni-Sb-... | | | (111) Mn-Sb-Ni-... | | |
| $m_{spin}$ | unrelaxed | relaxed | $m_{spin}$ | unrelaxed | relaxed |
| Mn(S) | 3.902 | 3.731 | Mn(S) | 4.164 | 3.892 |
| Ni(S−1) | 0.229 | 0.280 | Sb(S−1) | −0.041 | −0.047 |
| Sb(S−2) | −0.074 | −0.071 | Ni(S−2) | 0.299 | 0.331 |
| Mn(S−3) | 3.628 | 3.564 | Mn(S−3) | 3.700 | 3.659 |
| Ni(S−4) | 0.239 | 0.247 | Sb(S−4) | −0.060 | −0.066 |
| Sb(S−5) | −0.069 | −0.076 | Ni(S−5) | 0.273 | 0.268 |
| (111) Sb-Mn-Ni-... | | | (111) Sb-Ni-Mn-... | | |
| $m_{spin}$ | unrelaxed | relaxed | $m_{spin}$ | unrelaxed | relaxed |
| Sb(S) | −0.186 | −0.208 | Sb(S) | −0.118 | −0.120 |
| Mn(S−1) | 3.616 | 3.564 | Ni(S−1) | 0.133 | 0.146 |
| Ni(S−2) | 0.189 | 0.092 | Mn(S−2) | 3.521 | 3.500 |
| Sb(S−3) | −0.073 | −0.074 | Sb(S−3) | −0.064 | −0.067 |
| Mn(S−4) | 3.646 | 3.593 | Ni(S−4) | 0.256 | 0.235 |
| Ni(S−5) | 0.260 | 0.244 | Mn(S−5) | 3.698 | 3.689 |

Table 7.5: Atom-projected spin magnetic moments ($m_{spin}$) in $\mu_B$ for the atoms at the top six layers for all Ni-, Mn- and Sb-terminated (111) surfaces and for both relaxed and unrelaxed cases.
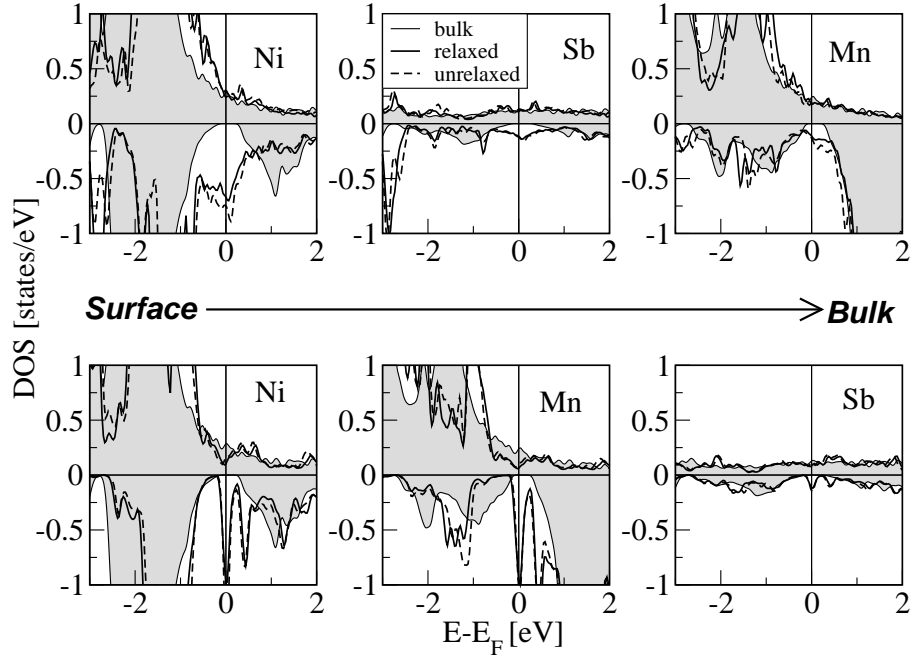
Figure 7.8: Same as Figure 7.4 for the Ni-terminated (111) surfaces. There are two different Ni terminations, either with a Sb or a Mn subsurface layer.

In the case of Ni-Mn-Sb-... termination it loses three Sb atoms and one Mn atom while in the Ni-Sb-Mn-... case one Sb and three Mn atoms.

In Table 7.5 the spin moments are presented for the first six layers of all surfaces under study. Relaxations only slightly change the spin moments. In the case of Ni-Mn-Sb-... both Ni and Mn atoms at the surface have very large moments with respect to both the bulk values and the Ni-Sb-Mn-... case. Especially the Ni moment is almost doubled ($0.47\ \mu_B$) with respect to the bulk value of $0.26\ \mu_B$. In the case of the bulk NiMnSb, the minority gap is created by the hybridization between the $d$-orbitals of the Ni and Mn atoms, but the Sb atom plays also a crucial role since it provides states lower in energy than the $d$ bands which accommodate electrons of the transition metal atoms (see Section 6.1). At the surface terminated at Ni-Mn-Sb-..., each Ni surface atom loses three out of the four Sb first neighbors and regains most of the charge accommodated in the $p$ bands of Sb. These extra electrons fill up mostly majority states increasing the Ni spin moment. The Mn spin moment is also increased since Mn and Ni majority $d$ states strongly hybridize forming a common majority band. Thus, the spin moment
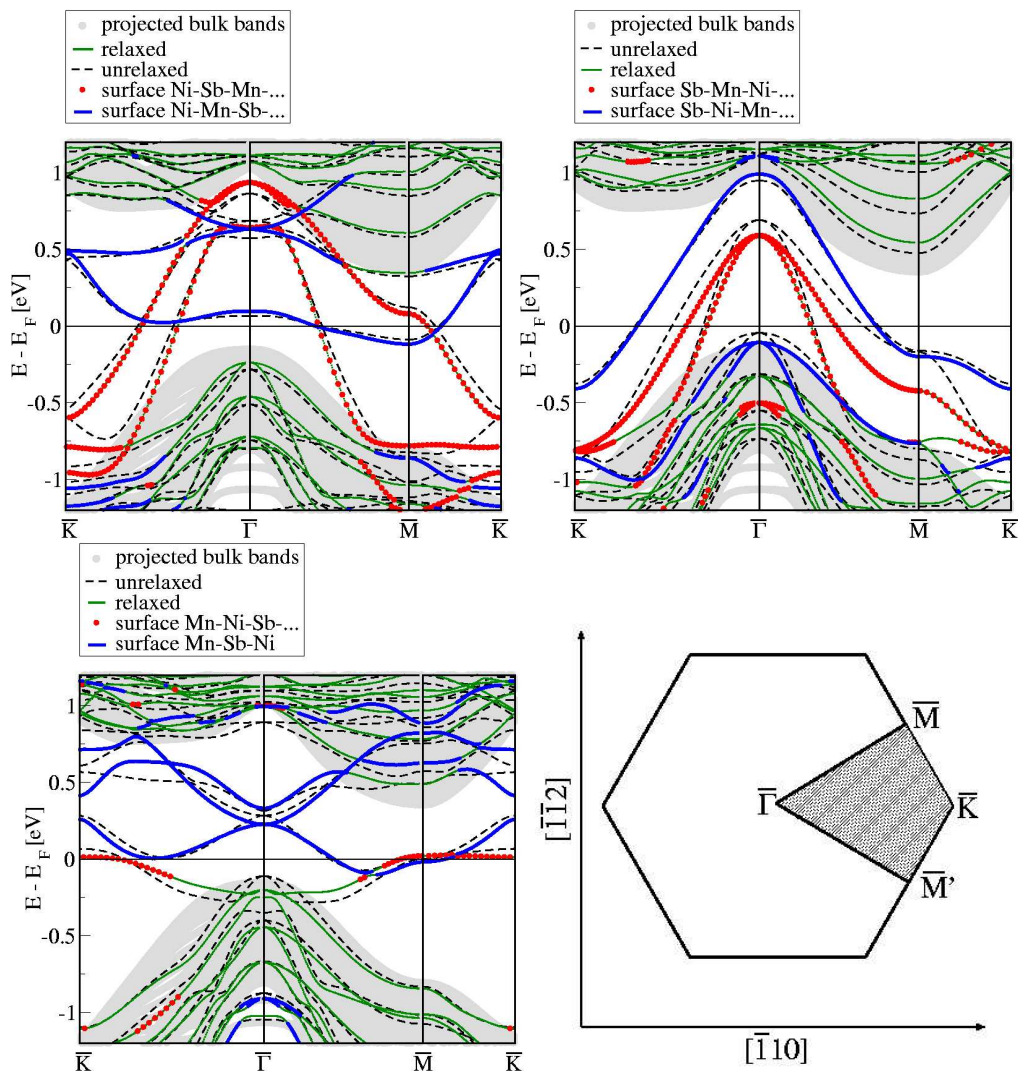
Figure 7.9: Same as Figure 7.5. The red filled spheres denote the surface states for the relaxed Ni-Sb-Mn-... surface and the blue for the Ni-Mn-Sb-... terminated surface. Similar at the left panel for the Sb terminated surfaces and at the bottom panel for the Mn-terminated surfaces. In the right lower corner, (111) two-dimensional first Brillouin zone is drawn.

of Mn at the subsurface layer increases reaching the $3.77\mu_B$ with respect to the bulk value of $3.7\mu_B$. If one goes further away from the surface, the atoms have a bulk-like environment and their spin moments are similar to the bulk case. In the Ni-Sb-Mn-... surface, Ni at the surface loses only one Sb first neighbor and the effect of the cut-off neighbors is much smaller. The moment is slightly smaller than the bulk one, mainly due to a surface state in the minority band shown in Figure 7.9. Already at the Sb subsurface atom the atoms regain a bulk-like behavior for the spin moment.

In Figure 7.8 the spin-resolved density of states (DOS) is shown, for the three layers closest to the surface, for both types of Ni termination. For the Ni-Mn-Sb-... termination, there is a minority surface state pinned exactly at the Fermi level which completely destroys the half-metallicity. As mentioned above the population of the majority states increases and due to the exchange splitting the minority states are pushed higher in energy and this results to a very sharp shape of the surface state. Actually, there are two surface states as will be discuss later. This phenomenon is more pronounced for the Mn atom at the subsurface layer, which presents a much larger exchange splitting (since it scales with the spin magnetic moment). This surface state gradually decays with the distance from the surface and for the Ni atom at the $S-3$ position (not shown here) it practically vanishes. We can see these surface states also in the surface-bandstructure presented in Fig. 7.9. With the blue lines the surface states for this termination are plotted. In reality there are two surface states similarly to the (001) surfaces, which are now very narrow-spread in energy resulting in the very sharp peak, around the Fermi level.

In the case of the Ni-Sb-Mn-... surface, the Ni spin moment is much smaller and the Mn atom is deep in the substrate. Ni bands even move slightly higher in energy and thus the surface states are now much more extended in the energy axis and cannot be well separated from the rest of the DOS as shown in Fig. 7.8. This situation is similar to the Ni terminated (001) surface. These surfaces states are presented in Figure 7.9 with the red dots. They are clearly much broader in energy than the states in the case of the Ni-Mn-Sb-... termination resulting in a very extended peak at the Fermi level which is not easily distinguished in the DOS. The band-structures presented here are similar to the ones calculated by Jenkins [39].

## Mn and Sb-terminated surfaces

Finally, here the Mn and Sb terminated surfaces will be discussed. As it was the case for the Ni terminated ones, there are again two different possible terminations. In Table 7.5 the atomic spin moments are gathered for all the
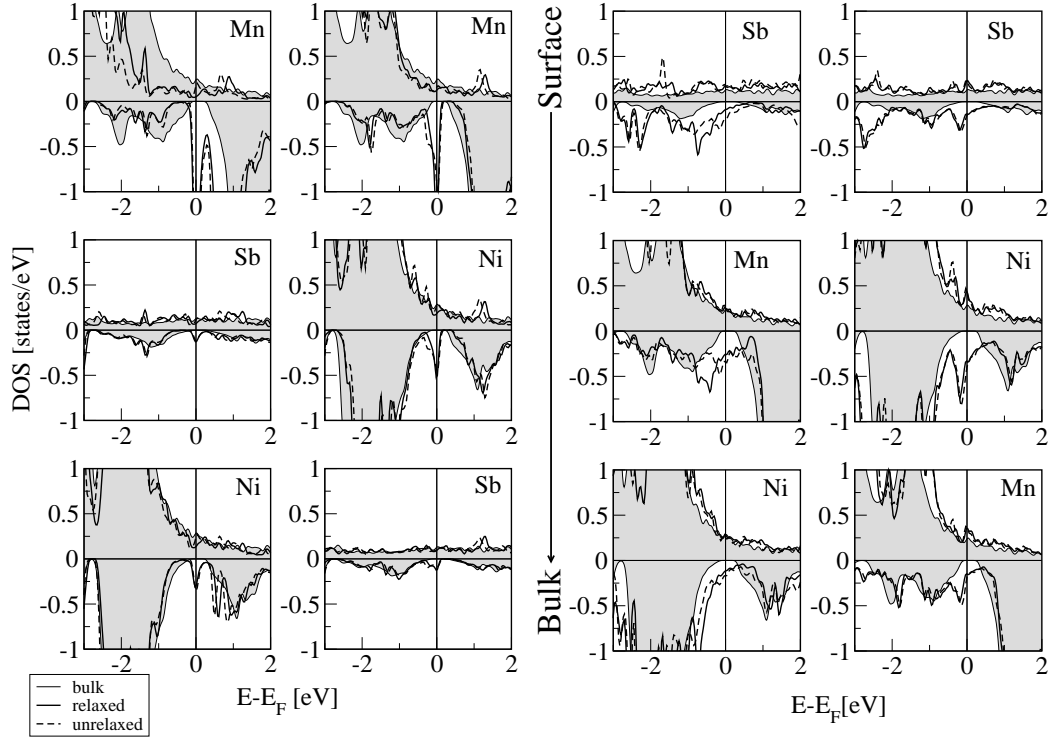
Figure 7.10: Same as figure 7.8 for the Mn- and Sb-terminated (111) surfaces. Each column represents a different surface termination. The top panels represent the surface layers, the middle ones the subsurface layers and the bottom panels the subsubsurface ones.

possible cases.

In the case of the Mn surfaces, Mn at the surface layer loses half of its Sb second neighbors and, similarly to what happened in the case of the Ni-Mn-Sb-... surface, its spin moment is strongly enhanced reaching 3.9 $\mu_B$ for the Mn-Ni-Sb-... and the 4.2 $\mu_B$ for the Mn-Sb-Ni-... case. In the latter case, between the Mn surface and Sb subsurface layers the distance is twice as large as between the other layers. Thus, the hybridization between the Mn $d$-orbitals and the Sb $p$- and Ni $d$-orbitals is strongly reduced, leading to an increase of the spin moment with respect to the Mn-Ni-Sb-... case. The atoms deeper in the surface quickly reach a bulk-like behavior.

Following the same arguments as for Mn, one can understand also the behavior of the spin moments for the Sb terminated surfaces presented in Table 7.5. The absolute value of the Sb spin moment at the surface layer increases with respect to the bulk. When the subsurface layer is a Mn layer (Sb-Mn-Ni-.. case), the hybridization effects are less important (since these

layers are further apart) and the Sb spin moment can reach a value of -0.2 $\mu_B$, almost triple the bulk value (-0.06 $\mu_B$) and double the value for the (001) surface ($-0.1\ \mu_B$). The change in the Sb $p$-bands influences also through hybridization the bands of the transition metal atoms for which now the minority bands population increases leading to smaller spin moments of the Ni and Mn atoms at the subsurface layers. The phenomenon is more intense in the case of Sb-Ni-Mn-... where the Ni layer is just below the Sb surface layer and the reduction in the spin moments of Ni and Sb is much larger than the Sb-Mn-Ni-... case.

Figure 7.10 presents the DOS for the first three layers for all Mn and Sb surfaces. In the case of the Mn-terminated surfaces, there is a minority surface state pinned exactly at the Fermi level which destroys the half-metallicity and which survives also in the Ni subsurface layer, and vanishes in the next Mn layer (not shown here). The surface states in the reciprocal space are similar to the ones of the Ni-Mn-Sb-... surface (Figure 7.9). In the case of the Mn-Sb-Ni-... surface there are three surface states with very flat dispersion while in the case of the Mn-Ni-Sb-... (111) surface there is just one very flat surface state along the $\bar{M} - \bar{K}$ line, leading to the very sharp peak shown in Figure 7.10 and leaving a band gap just above the Fermi level. The charge densities of the surface states for the two Mn-terminated surfaces, which lie just at the Fermi level at the point $\bar{M}$ of the (111) SBZ, are shown in Fig. 7.11. It can be seen that these states decay with the distance from the surface, but also that they are weakly coupled to each other, since they are at the same energy. For a more accurate description of the surface states a thicker slab can be used, which would decouple the states originating at the opposite surfaces.

Finally, also in the case of both Sb terminated surfaces there is a minority surface state bridging the gap and thus destroying the half-metallicity at the surface. Its intensity is large also in the subsurface layers, but already in the third layer it starts to decay. These surface states can be also found in the two-dimensional reciprocal space picture, as shown in the right panel of Fig. 7.9. They are very wide in energy and thus can not be well separated from the rest of the DOS.

To sum up, of all the investigated surfaces, the MnSb terminated (001) one presents electronic and magnetic properties most similar to the bulk compound. There is however a small finite Mn-$d$ and Sb-$p$ DOS within the bulk spin-down gap. The spin polarization at the Fermi level for this termination reaches the 84%. The (001) surfaces terminated with Ni present a quite large density of states at the Fermi level and properties considerably different from the bulk and the MnSb terminated surfaces. In both terminations, there are two distinct surface states as seen in the surface-bandstructure but with dif-
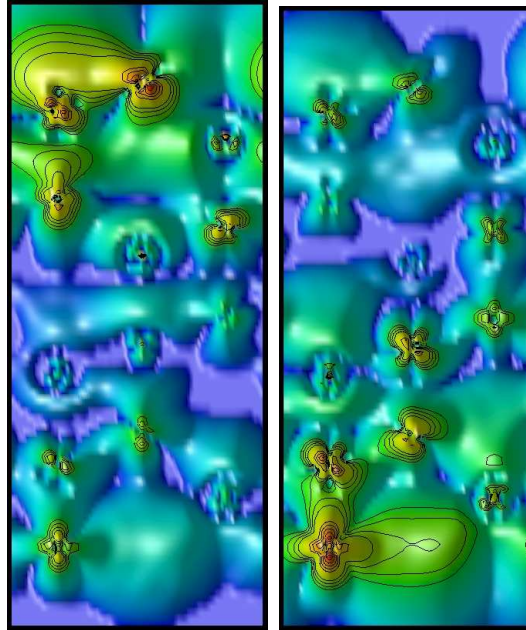
Figure 7.11: The charge densities of the surface states of the two (relaxed) Mn-terminated surfaces at the Fermi level, at the point M̄ (see Fig. 7). On the left, the surface state of the Mn-Ni-Sb-... terminated surface, and on the right the surface state of the Mn-Sb-Ni-... terminated surface is shown. The slab used for the calculation is terminated with Mn-Ni-Sb-... sequence on the top, and with Mn-Sb-Ni-... sequence on the bottom. The logarithmic scale was used.

ferent extension. In all (111) surfaces minority-spin surface states kill the half-metallicity at the surface. The highest DOS of these surface states is just at the Fermi level for the Ni and Mn terminated surfaces, and slightly below the Fermi level for the Sb one. The characteristic of all the surface states is that they are localized close to the surface region and normally vanish within few atomic layers.

## 7.3   Interfaces of NiMnSb with InP

In this section, a study of the electronic and magnetic properties of the interfaces between the half-metallic Heusler alloy NiMnSb and the binary (zb) semiconductor InP is presented. Theoretical calculations for the interfaces of Heusler alloys with semiconductors are few and all results agree that in general the half-metallicity is lost at the interface between the Heusler alloy and the semiconductor [40, 124, 125, 126, 127]. Wijs and de Groot have

argued than in the case of the NiMnSb/CdS (111) contacts the Sb/S interface keeps half-metallicity when the S atoms sit exactly on top of Sb. [40]. It will be shown later on that an interface of NiMnSb and InP with similar geometry also remains half-metallic.

### 7.3.1 Structure of the interfaces

InP is a zinc-blende semiconductor, and since NiMnSb crystallizes in $C_{1b}$ structure (see Fig. 6.2), one can imagine that InP continues the growth of NiMnSb just replacing the atom of Ni with the atom of P and the atom of Sb with the atom of In (or vice versa) and leaving the Mn site unoccupied (though in reality usually half-metals are grown on semiconductors and not the other way around). Thus, making the described substitutions, with the use of Fig. 7.3, one can easily imagine how the (ideal) interfaces look like. Within 1% accuracy, NiMnSb (5.91Å) has the same experimental lattice constant as InP (5.87Å) and epitaxial growth of NiMnSb on top of InP has been already achieved experimentally by molecular beam epitaxy [120, 128]. Since the lattice parameters of the two compounds are so close, in the calculations perfect epitaxy can be assumed.

To simulate the (001) interfaces, a repeated slab made up of 8 layers of NiMnSb and 8 layers of the semiconductor was used. There are several combinations at the interface, e.g. at the NiMnSb/InP contact the interface can be either a Ni/In one, Ni/P, MnSb/In or MnSb/P. Since 8 layers of NiMnSb and 8 layers of InP were used in the supercell, this means that if one of the contacts is Ni/P the other one is MnSb/In (see Fig. 7.3). For the (111) interfaces, the supercells consisted of 16 layers of NiMnSb and 12 layers of InP. All the calculations were performed at the experimental lattice constant of InP (5.87 Å), except for these cases, where the relaxation effects at the interfaces have been checked. There, the theoretically optimized lattice constant of InP (5.94 Å) has been used.

Compared to simple surfaces, interfaces are more complex systems due the hybridization between the orbitals of the atoms of the metallic alloy and the semiconductor at the interface. Thus, results obtained for the surfaces in the previous section cannot be easily generalized for interfaces since for different semiconductors different phenomena can occur.

### 7.3.2 NiMnSb(001)/InP(001) contacts

First we examine the four possible (001) interfaces. In Table 7.6 the spin moments for the case of the MnSb/In and MnSb/P interfaces are gathered. "I" stands for the interface layers, +1 means moving one layer deeper in the

|  | MnSb/In | MnSb/P | MnSb surf. | bulk |
|---|---|---|---|---|
| I−3 | Ni: 0.307 | Ni: 0.297 | Ni: 0.269 | Ni: 0.262 |
| I−2 | Mn: 3.679 | Mn: 3.706 | Mn: 3.661 | Mn: 3.703 |
| I−2 | Sb:−0.051 | Sb:−0.042 | Sb:−0.065 | Sb:−0.063 |
| I−1 | Ni: 0.303 | Ni: 0.312 | Ni: 0.211 | Ni: 0.264 |
| I | Mn: 3.371 | Mn: 3.646 | Mn: 3.937 | Mn: 3.705 |
| I | Sb:−0.031 | Sb:−0.050 | Sb:−0.101 | Sb:−0.062 |
| I | In:−0.048 | P : 0.017 |  |  |
| I+1 | P :−0.026 | In:−0.017 |  |  |
| I+2 | In:−0.012 | P :−0.010 |  |  |
| I+3 | P :−0.013 | In: 0.001 |  |  |

Table 7.6: Atomic spin moments given in $\mu_B$ for the interface between the MnSb-terminated (001) NiMnSb and the In or the P terminated InP. Last columns are the moments for the MnSb-terminated NiMnSb(001) surface and the bulk NiMnSb. "I" denotes the interface layers and $\pm$ means one layer deeper in the half-metal or the semiconductor.

semiconductor and $-1$ one layer deeper in the half-metallic spacer. In the case of the MnSb terminated half-metallic film there is a difference depending on the semiconductor termination. In the case of the In termination the Mn spin moment decreases considerably and is now 3.4 $\mu_B$ compared to the bulk value of 3.7 $\mu_B$. For the P terminated InP film the spin moment of Mn at the interface is very close to the bulk value. At the In interface, the Mn minority $d$-states hybridize strongly with the In states and thus the Mn spin moment is severely reduced and it shows a negative induced spin moment. In the case of P, the situation is reversed and P has a positive induced spin moment. The Mn-$d$ - P-$p$ hybridization is not as strong as the Mn-$d$ - In-$p$ one and the Mn spin moment at the interface is close to the bulk value. If we move deeper into the half-metallic film, the spin moments regain their bulk-like behavior while, if we move deeper in the semiconductor film, the induced spin moments quickly vanish.

Compared to the MnSb-terminated surface for which in the previous section a spin polarization as high as 84% was found, for the interfaces between MnSb-terminated NiMnSb and InP the situation is completely different. The hybridization between the $d$-states of Mn and $p$-states of Sb with the $p$-states of either the In or the P atom at the interface is such that the net polarization at the interface is almost zero. This is clearly seen in Fig. 7.12, where with the red line the spin and atom resolved density of states (DOS) of the atoms at the interface for MnSb/P (up) and MnSb/In (down) contacts is presented. At the MnSb/P interface, there is a minority interface state
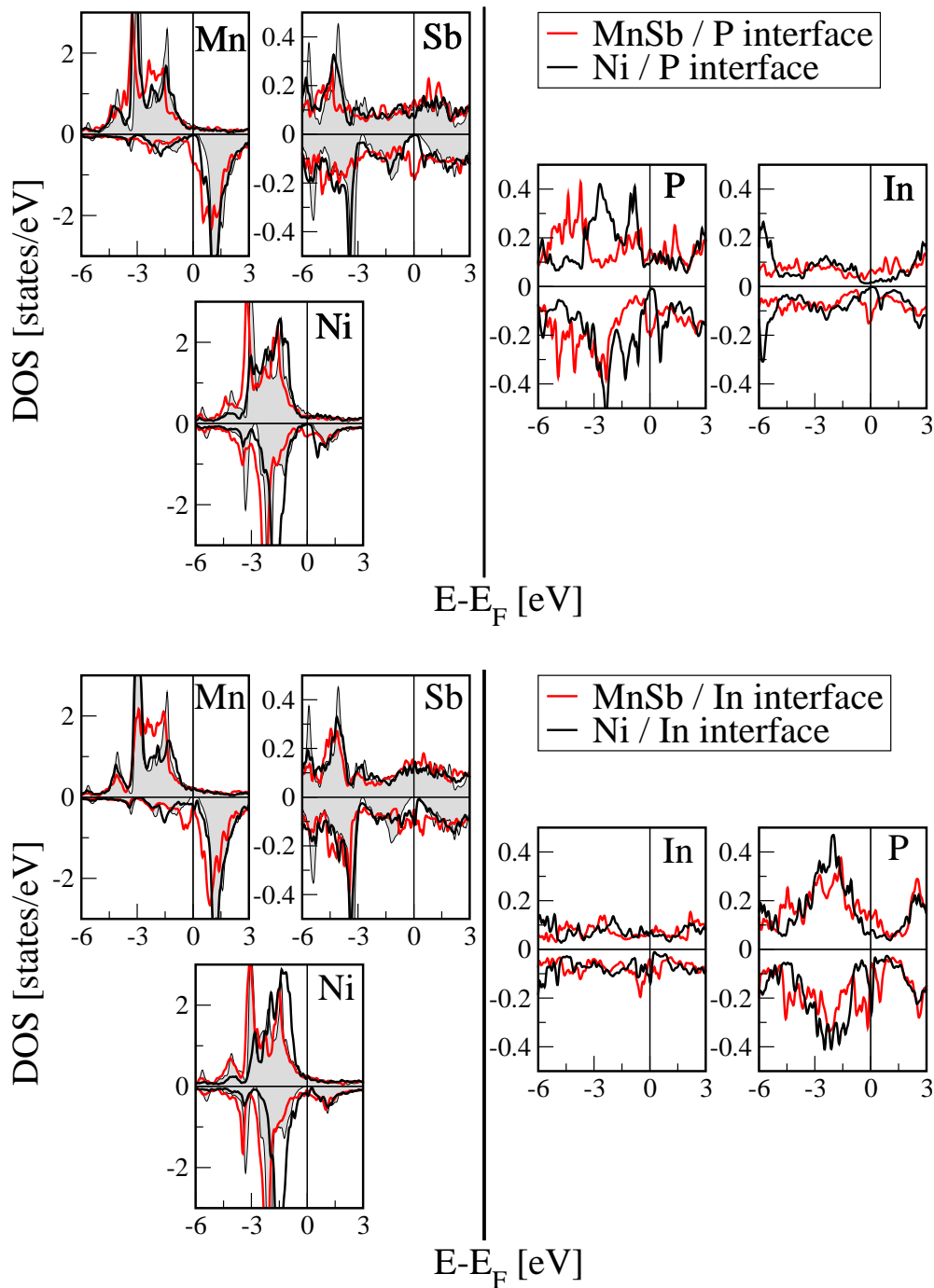
Figure 7.12: Up: Atom- and spin-resolved DOS for the case of MnSb/P (red line) and Ni/P (black line) contacts for the two interface layers and one layer deeper in the half-metal and the semiconductor. For comparison, the bulk DOS is shown as a grey background. Positive values of the DOS correspond to the majority spin and negative to the minority.
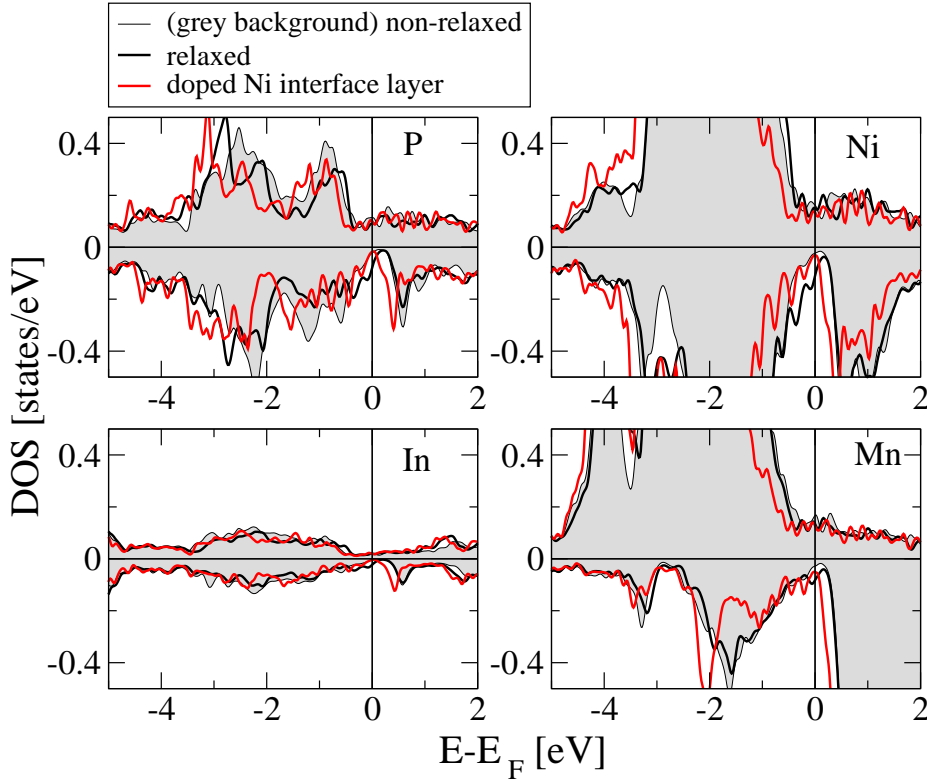Down: The same like up, but for the interfaces MnSb/In and Ni/In.

Figure 7.13: The comparison of the relaxed (black lines) and unrelaxed (grey background) Ni/P (001) interface. The red lines represent DOS for a doped interface, where 1/3 of Ni atoms was replaced by Cu atoms

pinned at the Fermi level which destroys the half-metallicity. In the Mn local DOS, this state overlaps with the unoccupied minority Mn states and it is not easily distinguished but its existence is obvious if one examines the Ni and Sb DOS. The situation is similar for the MnSb/In contact.

In the case of Ni terminated NiMnSb films, DOS at $E_F$ is more bulk-like than the case of the MnSb films. Already Ni interface atom has a spin moment of 0.27 $\mu_B$ in the case of an interface with In and 0.36 $\mu_B$ for an interface with P compared to the bulk value of 0.26 $\mu_B$. In the bulk case Ni has 4 Mn and 4 Sb atoms as first neighbors. On the Ni-terminated (001) surface the Ni atom loses half of its first neighbors. But if an interface with P is formed, the two lost Sb neighbors are replaced by two isovalent P atoms and – with the exception of the Mn neighbors – the situation is very similar to the bulk. Now the Sb $p$ bands at lower energy are not destroyed, since P has a behavior similar to Sb and still they accommodate three transition metal $d$ electrons. Thus the only change in the DOS comes from the missing

two Mn neighboring atoms. The DOS in Fig. 7.12 (up) for the Ni/P case (black lines) is clearly very close to the bulk case. In the case of the Ni/In interface (Fig. 7.12 down), there is an interface state pinned at the Fermi level which completely suppresses the spin polarization, $P$ (if we take into account the first two interface layers, $P \approx 0$). In the case of the Ni/P interface the intensity of these interface states is strongly reduced and the spin polarization for the first two interface layers is 40%, i.e. about 70% of the electrons at the Fermi level are of majority spin character.

It should be noted here, that all given data up to here refers to unrelaxed interfaces. Relaxation effects modify these values: Increased hybridization and charge-transfer can lead to pronouncedly reduced spin polarizations at the interface. The Ni-P interlayer distance is reduced by 18%, while the neighboring interlayer distances are expanded by 5-7% as compared to the ideal bulk values. Thereby, the spin polarization at the interface is decreased to only 17%. Nevertheless, these effects do not destroy the gap completely, they just lead to a shift of the local DOS and can be compensated by a doping of the interface. We found that substituting one third of the Ni atoms by Cu increases the spin polarization at the interface again to 55% (Fig. 7.13).

## Band offsets and partial DOS for NiMnSb/InP contacts

The (minority states) valence-band offset is the energy difference between the maximum of the valence band (VBM) of the semiconductor and the maximum of the minority valence band of the Heusler alloy. To calculate it, we referenced the binding energies of the core states in the interface calculation to their corresponding bulk values as described in Ref. [129]. We found that the VBM of the semiconductor is 0.83 eV lower than the one of the half-metal for the In/MnSb contact. For the other interfaces the valence band offsets are: 0.69 eV for the In/Ni, 0.69 eV for the P/Ni and 0.80 eV for the P/MnSb contact. In the bulk InP semiconductor the experimental gap is 1.6 eV, thus the Fermi level, which is 0.07 eV above the maximum of the minority NiMnSb valence band falls in the middle of the semiconductor bulk bandgap. This is similar to what is happening also in the case of the $Co_2MnGe$/GaAs (001) interfaces [125] and these junctions can be used to inject spin-polarized electrons in the semiconductor.

To make the results more clear, in Fig. 7.14 the layer-resolved partial densities of states at the Fermi level for all the (001) interfaces are gathered. As it was mentioned earlier, in the calculations a repeated slab made up from eight NiMnSb and eight InP layers was used. Thus if one interface is MnSb/In (shown in the middle of the upper figure) then the other interface is Ni/P, and it consists of the two layers shown at the edges of this figure (the
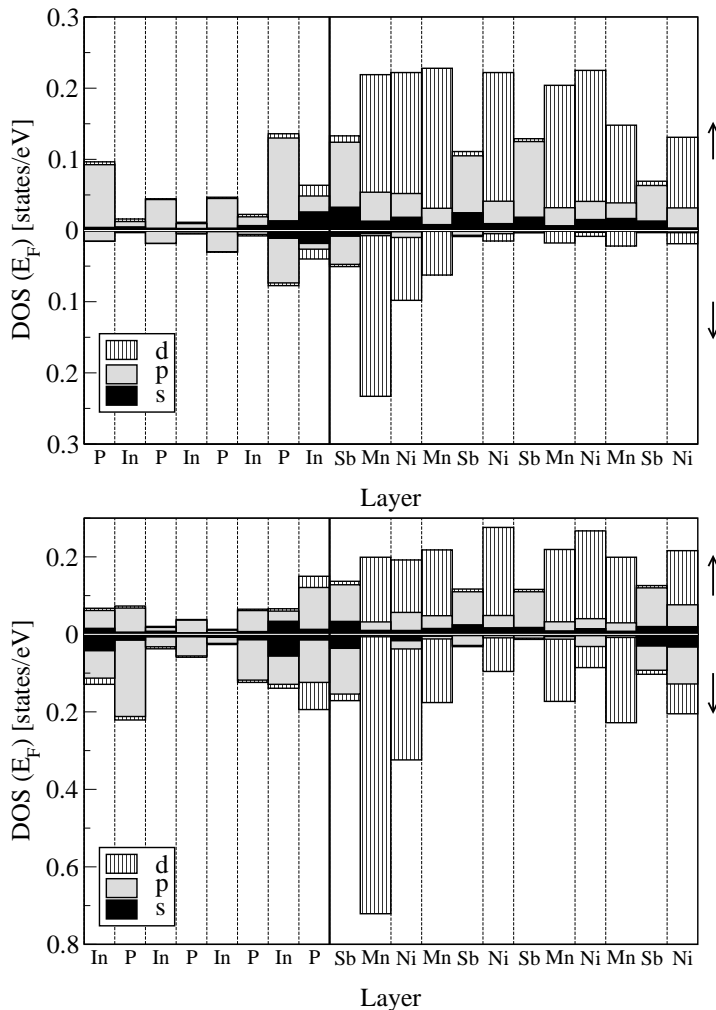
Figure 7.14: Layer-resolved DOS at the Fermi level for the (001) NiMnSb/InP contacts. Up: MnSb/In and Ni/P interfaces, down: MnSb/P and Ni/In interfaces.

slab is periodically repeated along the axis perpendicular to the interface). Similarly, the lower graph contains the results for the MnSb/P and Ni/In interfaces. The layers at the middle of the semiconductor spacer show a small DOS due to both the induced states from the half-metal and bulk NiMnSb states which decay slowly outside the half-metallic spacer and travel throughout the semiconductor. It is clearly seen that none of the interfaces is in reality half-metallic. For the MnSb/In interface the Mn atom at the interface shows an almost zero net spin polarization, while the Mn atom at

the MnSb/P interface shows a quite large minority DOS, as it was already discussed. In the case of the Ni/In interface shown in the lower panel of Fig. 7.14, the net spin polarization is also almost zero. The Ni/P interface shows a spin polarization $P$ around 40% due to the high polarization of the Ni atom at the interface which polarizes the P atom at the interface (also presenting a high majority DOS at the Fermi level).

### 7.3.3 NiMnSb(111)/InP(111) contacts

As it was mentioned, for the calculations of (111) interfaces 16 layers of NiMnSb and 12 layers of InP were used. Along the [111] direction the semiconductor is composed by pure alternating In and P layers and, thus, the semiconducting spacer is ending in P on the one side and In on the other side. The half-metallic spacer on the two sides has two inequivalent terminations. For the Mn termination, as we proceed from the interface deeper into the half-metallic spacer, the succession of the layers can be either Mn-Ni-Sb-Mn-... or Mn-Sb-Ni-Mn-... . Similarly for the Sb terminated interface we can have either Mn or Ni as subinterface layer and for the Ni termination we can have either Sb or Mn at the subinterface layer.

In Fig. 7.15 the layer-resolved partial DOS for the Ni-terminated interfaces are shown. In the top panel are the ...-In-P/Ni-Sb-Mn-... and ...-P-In/Ni-Mn-Sb-... contacts and in the bottom panel the ...-In-P/Ni-Mn-Sb-... and ...-P-In/Ni-Sb-Mn-... ones. As it was shown in the previous section, in the case of Ni- and Mn-terminated (111) surfaces there are strong surface states pinned at the Fermi level which also penetrate deeply into the subsurface layers. These surface states are present also in the case of the interfaces studied here, although their intensity decreases slightly due to the hybridization with the $sp$ atoms of the semiconductor. In all cases the net spin polarization of the Ni atom at the interface is very small with the exception of the ...-In-P/Ni-Mn-Sb-... interface (middle of the bottom panel). For this case the simultaneous presence of the P atom from the one side and of the Mn atoms at the subinterface layer create an atomic environment for Ni similar to the case of the Ni/P(001) contact and the spin polarization, taking into account the two semiconductor layers at the interface and three first NiMnSb layers, is as high as ~53% and thus more than 76% of the electrons at the Fermi level are of majority character. In the case of the Mn-terminated NiMnSb-films (not shown here) the interface states are even stronger than for the Ni-terminated spacers and the spin polarization at the interface vanishes.

In the last part of this study, we will concentrate on the Sb-terminated (111) interfaces. Firstly, we should note that contrary to the Mn and Ni
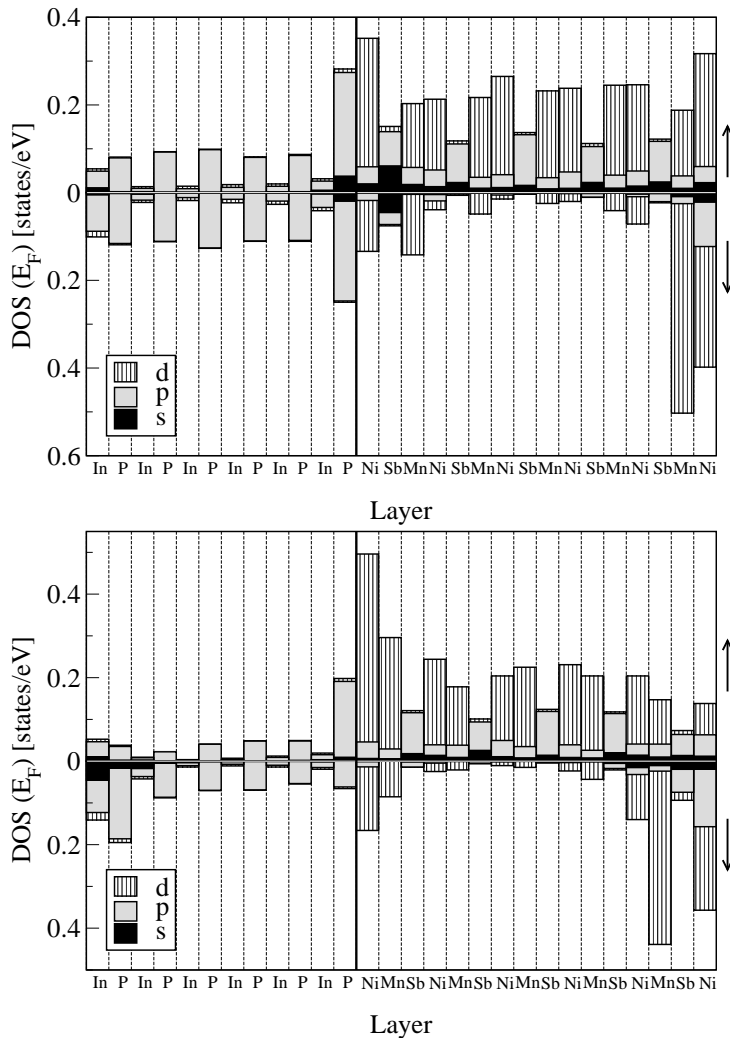
Figure 7.15: Layer-resolved DOS at the Fermi level for the Ni-terminated NiMnSb/InP(111) contacts. In the middle of the figures a Ni/P interface is shown with Sb (top) or Mn (bottom) in the subinterface layer, while at the borders of the figures the layers of a Ni/In interface can be seen with Mn (top) or Sb (bottom) in the subinterface layer.

terminated, in the case of the Sb- terminated NiMnSb(111) surfaces, the surface state was not pined exactly at the Fermi level but slightly below it and the spin polarization in the case of the Sb surfaces was still high. In the case of the interfaces between In and Sb, half-metallicity is completely destroyed and the spin polarization is even negative, i.e. there are more
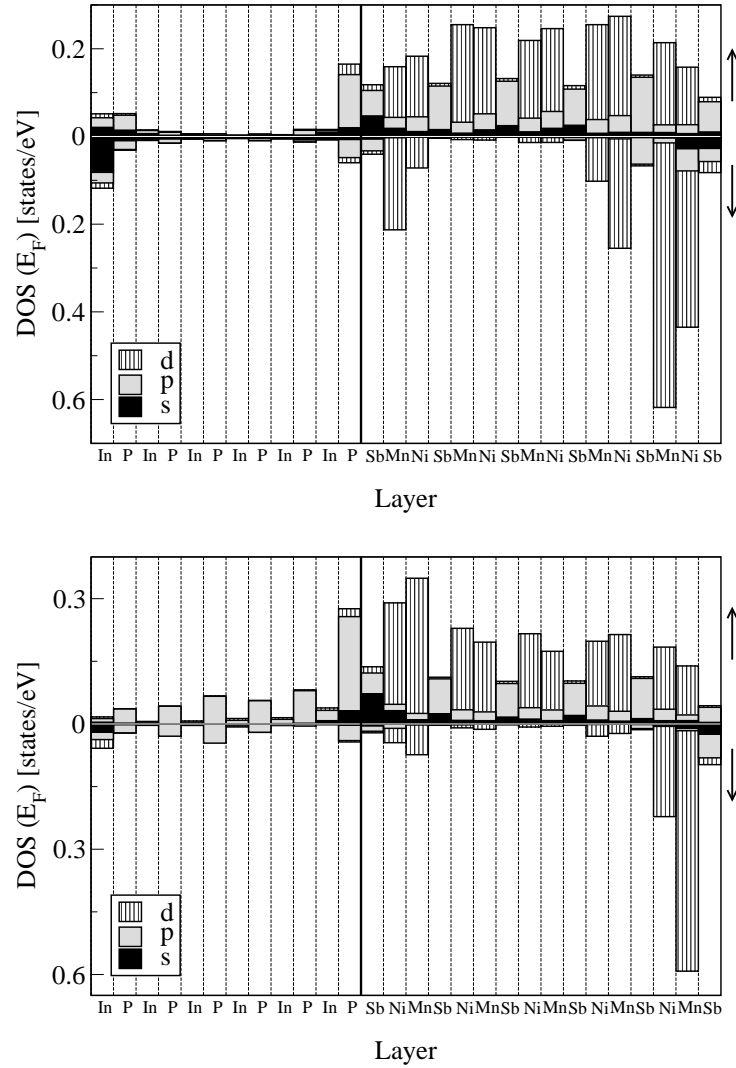
Figure 7.16: Layer-resolved DOS at the Fermi level for the Sb-terminated NiMnSb/InP(111) contacts. In the middle of the figures a Sb/P interface is shown with Mn (top) or Ni (bottom) in the subinterface layer, while at the borders of the figures the layers of a Sn/In interface can be seen with Ni (top) or Mn (bottom) in the subinterface layer.

minority-spin electrons at the Fermi level than majority ones as can be seen from the DOS at the boundaries of the pictures in Fig. 7.16.

In Fig. 7.16, also two different P/Sb-terminated interfaces are shown: in the top panel the one with Mn as subinterface layer is not of particular interest since the Mn atom shows a practically zero net spin polarization
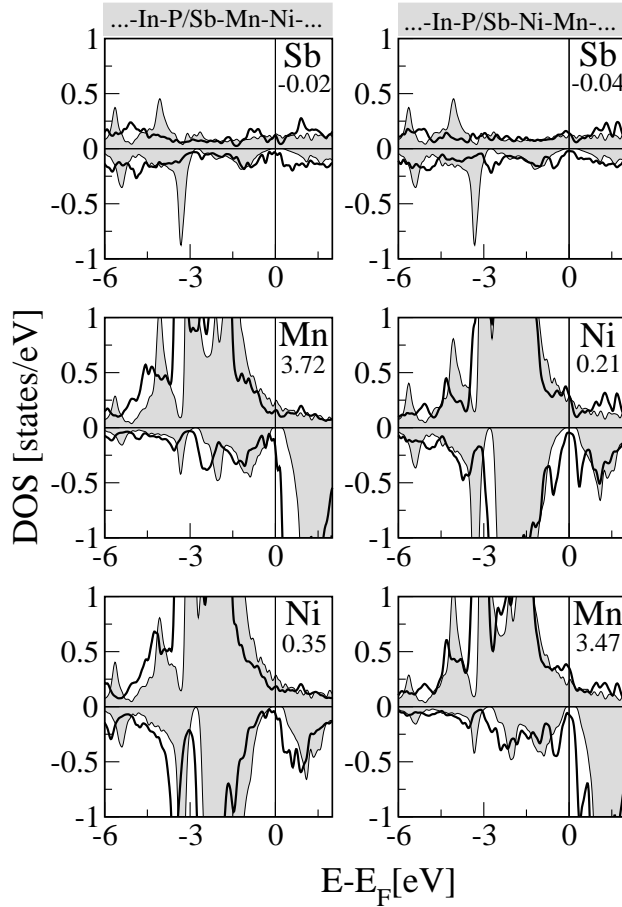
Figure 7.17: Atom- and spin-resolved DOS for the ...-In-P/Sb-Mn-Ni-... interface (left panels) and the ...-In-P/Sb-Ni-Mn-... interface (right panels). The values in the figures are the spin moments of the atoms at the interface in $\mu_B$. The thin solid line indicates the bulk results.

decreasing considerably the overall spin polarization at the interface. On the other hand, when the subinterface layer is Ni as in the middle of the bottom panel, all atoms at the interface show a very high majority DOS at the Fermi level and the resulting spin polarization, $P$, is $\sim$74% and thus $\sim$86% of the electrons at the Fermi level are of majority character. Although the induced majority DOS at the Fermi level for the P atom at the interface seems very large (it is of the same order of magnitude with the Ni one), when we move away from the Fermi level it becomes very small compared to the majority DOS of the transition-metal atoms.

The main question needed still to be answered is why the two different

P/Sb interfaces show such large differences. It is mainly the Mn atom whose spin polarization at the Fermi level is very different depending of its distance from the interface. To answer this question, in Fig. 7.17 the layer-resolved DOS for the two different P/Sb interfaces are shown. In the figure, also the atomic spin moments are included. The Sb spin moments are $-0.02\mu_B$ for the ...-In-P/Sb-Mn-Ni-... interface and $-0.04\mu_B$ for the ...-In-P/Sb-Ni-Mn-... interface. In both cases this is smaller than the bulk value of $-0.06\mu_B$. The Mn spin moment for the ...-In-P/Sb-Mn-Ni-... case is 3.72 $\mu_B$, close to the bulk value of 3.70 $\mu_B$, considerably larger than the Mn moment of 3.47 $\mu_B$ for the ...-In-P/Sb-Ni-Mn-... case. One would expect that in the first case the exchange splitting should be larger and the unoccupied minority states would be higher in energy but, as can be seen in Fig. 7.17, the contrary effect occurs. In the second case the Mn is deeper in the interface and its environment is more bulk-like and the minority states are pinned at their position. Thus the Fermi level falls within a minority local minimum resulting in a very high spin polarization. At the ...-In-P/Sb-Mn-Ni-... contact the Mn atom is closer to the interface. Here, the larger hybridization of the Mn minority states (not only with the $p$-orbitals of Sb but also with the ones of $P$, since the last ones are closer now) obliges the minority states to move slightly lower in energy. Thus, the Fermi level does not fall in the local minimum but shifts into the peak of the unoccupied minority states and the net spin polarization vanishes. The Ni states are strongly polarized by the Mn ones and also in the case of the Ni atom which is deeper than the Mn one, the Fermi level does not fall anymore within the local minimum.

Wijs and de Groot predicted that the interfaces between the Sb-terminated NiMnSb(111) film and a S-terminated CdS(111) film should keep the half-metallicity or at least show an almost 100% spin polarization at the Fermi level.[40] They considered the case of an interface where the S atoms sit exactly on top of the Sb atoms. As noticed by these authors, a similar structure can also be realized with InP instead of CdS. Therefore, we calculated also a ...-In-P/Sb-Ni-Mn-... (111) interface, where the P atoms sit exactly on top of Sb. The P-In bond at the interface has the shorter one of the two possible bond-lengths in the zb [111] stacking, and the In atoms closest to the interface at the InP side are at the positions above the closest to the interface Mn atoms on the NiMnSb side. The calculations for this particular interface were done in a film geometry. The slab contained 9 layers of NiMnSb and 6 layers of InP. The surfaces of the slab were terminated with the ...-Sb-Ni-Mn sequence from one side and with the ...-P-In on the other. The positions of the first four atoms on NiMnSb and the first two atoms of InP at the interface were allowed to relax, while the rest of the layers of the slab were allowed to make a rigid shift together. In this case a long (2.61Å) Sb-P bond
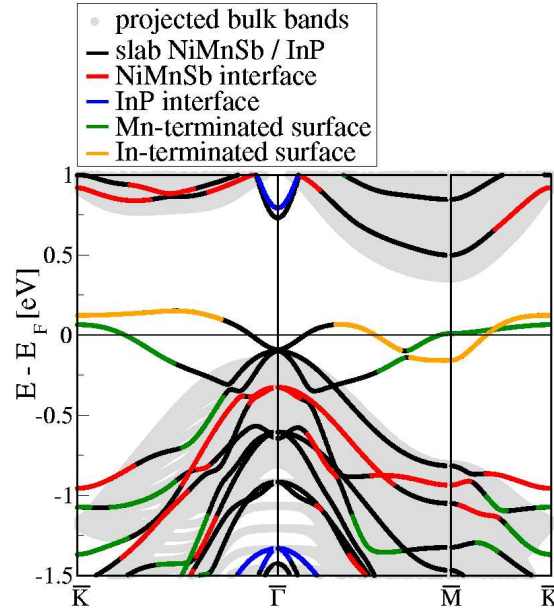
Figure 7.18: Two-dimensional bandstructure of the ...-In-P/Sb-Ni-Mn-... (111) interface, where the P atoms sit on top of the Sb ones, at the distance of 2.61Å. Note that the states at the Fermi level are the surface states located either on the Mn-, or on the In-terminated surface of the slab, and that there are no interface states at this energy

is formed, which, like in the case of CdS, is stable and the half-metallicity at the interface is preserved. The surface-bandstructure of the slab is shown in the Fig. 7.18 with the black lines, compared to the bulk (grey background). The states which have more than 50% of their weight in:

1. the three surface layers of NiMnSb are plotted in green lines;

2. the two surface layers of InP are shown in orange lines;

3. the three interface layers of NiMnSb are presented in red lines;

4. the two interface layers of InP we see in orange lines.

We see that the interface states of NiMnSb and InP are far away from the Fermi level. Thus, this interface is half-metallic. Although CdS and InP have the same number of valence electrons, this is a remarkable result, since S and P have one electron difference and the electrostatics for the two interfaces are slightly different resulting in a small displacement of the Fermi level. Our total energy calculations show that this geometry (on-top stacking) is stable with respect to other stacking variants. Yet, it is not clear which of the

possible stackings will be formed under experimental growth conditions, i.e. layer-by-layer growth.

Like in the case of (001) interfaces, for the case of the (111) interfaces the band-offset was calculated. It ranges from 0.36 eV in the case of the ...-In-P/Mn-Sb-Ni-... contact up to $\approx$1 eV for the ...-In-P/Sb-Ni-Mn-... configuration. Thus, the conclusions of the previous subsection are valid also for these interfaces. We should note here that there is a certain ambiguity in the evaluation of the band-offsets, caused by the fact that the inequivalency of the two interfaces induces an electric field in both the bulk sides of the junction which will show up as a finite slope in the core-level binding energies as a function of the distance from the interface. While this effect is small in the half-metal, due to the poor screening in the semiconductor we observe a pronounced bending on top of this slope in this side of the junction. Nevertheless, the middle of the semiconductor provides a reasonable reference point for the evaluation of the band-offsets.

Although half-metallicity at the interfaces is in general lost, there are few contacts in which a high spin polarization remains, which makes them attractive for realistic applications. Interface states are important because the interaction with defects makes them conducting and lowers the efficiency of devices based on spin-injection. Thus, building up interfaces with the highest spin polarization possible like the ones proposed here is a perquisite but not a guarantee to achieve highly efficient spin-injection.

# Chapter 8

# Finite Temperature Effects

The calculations described in previous chapters were dealing with the zero-temperature properties of half-metals. We have seen that the gap at the Fermi level in the minority spin band of these materials is in fact a fragile feature which can be more easily destroyed than preserved. To start with, there is the spin-orbit coupling which cannot be avoided, but as we have seen (Sec. 7.1), a proper choice of the compound (meaning, not using compounds which contain heavy elements) can make this problem negligible. This is, unfortunately, not the solution to all our problems. We are still left with the point defects, that can destroy the gap even in bulk, but also with the interface states, which make one's life very difficult when, for instance, trying to achieve spin-injection. These are the problems whose influence can be diminished by a careful growth of the samples and by an appropriate choice of the interfaces.

In this chapter, we will say more about the finite temperature effects, namely, we will get some estimations of the critical temperature (or Curie temperature, $T_C$) above which the spontaneous magnetization remains zero, while it is finite under it. To simulate the effect of the finite temperature, spin waves are used. At zero temperature, the system is in its ground state (ferromagnetic for the compounds studied here) and, as the temperature rises, more and more magnons (spin-wave excitations, Sec. 4.2) are excited. The difference in energies of such an excited state and the ground state, the so-called *magnon energy*, is the measure of easiness with which the temperature destroys the magnetization of the system. This means that from such differences, for some set of different magnons, one should in principle be able to extract information about the $T_C$. There are several prescriptions to do this, but since all of them involve calculations in which one determines differences of the total energies of the excited system and the system in the ground state (typically of the order of several mRy), it is recommendable

to use Andersen's magnetic force theorem (see Subsec. 2.2.2) to reduce the calculational cost. So, let us check first if this theorem can be applied for the magnon energy calculations.

## 8.1   A Check of the Applicability of the Force Theorem

The magnon energy is calculated as the difference between the total energy of the system in which a magnon (defined with the spin cone angle $\theta$ and the wave-vector $\boldsymbol{q}$, Sec. 4.2) is propagating (this is an excited state), and the ground state, which is in the systems under study here ferromagnetic. Applying Andersen's force theorem (Subsec. 2.2.2) for this case means that instead of calculating self-consistently the total energy for the excited state, it is enough to do only one self-consistent calculation for the ground state, and then consider the introduced magnons as small perturbations, run only one iteration for a specific magnon, and obtain the magnon energy as the difference of the sums of eigenvalues of the excited and the ground state. The only thing that is left to be done is to check how large the cone angle can be and what is the shortest wavelength of the magnon for which this perturbation can still be considered small enough and the approximation valid.

In the left panel of Figure 8.1, a magnon dispersion curve is shown for a magnon in NiMnSb, defined with a cone angle $\theta = 30°$, and a spin-wave vector along [001] direction, taking different values in the first Brillouin zone of the crystal. With the black line the self-consistent calculations are shown (as well as in the other two panels of the same figure) and with the red line the corresponding results obtained from the force theorem. The two curves agree pretty well. The middle and the right panel of the Figure 8.1 show the dependence of the magnon energy on the squared sinus of the cone angle ($\sin^2 \theta$), for two fixed spin-spiral vectors, $\boldsymbol{q}$=(0, 0, 0.15)$2\pi/a$ (middle) and $\boldsymbol{q}$=(0, 0, 1)$2\pi/a$ (right). In both of these panels the force theorem results are shown with blue lines. The middle panel shows that if the magnon has a long wavelength, the force theorem can be used within the full range of the cone angles ($\theta = 0° - 90°$). On the other hand, for a short-wavelength magnon (right panel), the application of the force theorem is not recommendable for the cone angles larger than $\theta_{max} \sim 50°$.

A general conclusion is that if one wants to use the force theorem to obtain the magnon dispersion within the whole first Brillouin zone of the crystal, cone angle $\theta = 30°$ seems to be a reasonable choice, since the energy
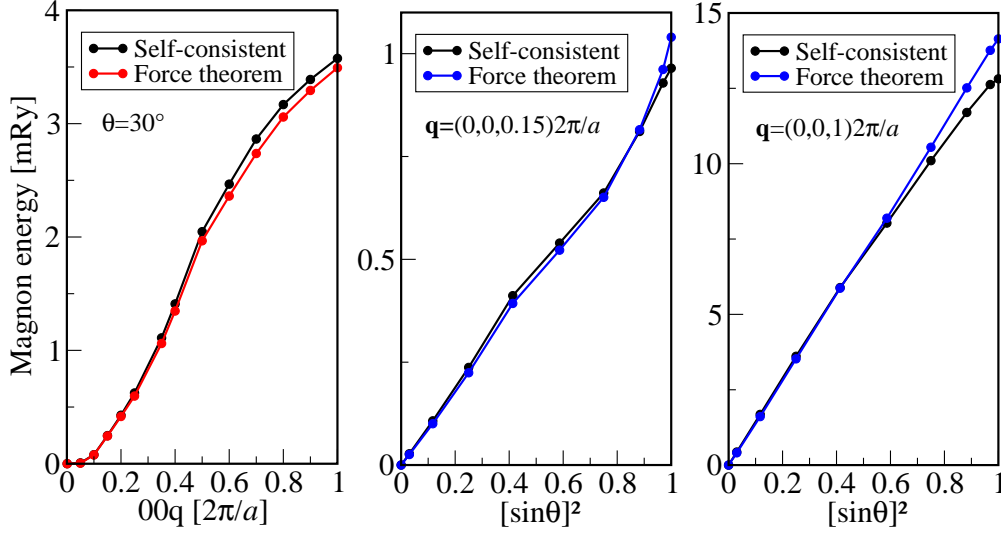
Figure 8.1: Comparison of the force theorem with self-consistent calculations for NiMnSb. Left: a dispersion curve of a magnon propagating along the [001] direction, for a cone angle $\theta = 30°$; middle, right: magnon energy vs. squared sinus of the cone angle for a long-wavelength (middle) and a short-wavelength (right) magnon propagating along the [001] direction.

differences are not too large for the magnon to stop being a small perturbation, but are also not too small so that one would have to employ a very large basis, or **k**-points set. This cone angle was used in the calculation of the Heisenberg interaction constants $J_{ij}$ presented in Section 8.3.

## 8.2   Curie Temperature of NiMnSb

In this section, a way to estimate the Curie temperature of the half-Heusler alloy NiMnSb will be presented. In Fig. 8.2, a self-consistent calculation of the energy of a flat ($\theta = 90°$) spin-spiral in NiMnSb, along the [001] direction of the crystal is shown with black dots. The knowledge of the dispersion relation allows the estimation of magnon-related properties, such as spin stiffness and Curie temperature. The total energy of a planar spin-spiral is related to the magnon energy $\omega_q$ as [130, 47]

$$\omega_q = \frac{4\mu_B}{M}E(\mathbf{q}), \qquad (8.1)$$

where M is the magnetic moment per unit cell. In the long wavelength limit, the magnon dispersion is quadratic with the prefactor $D$, also called *the*
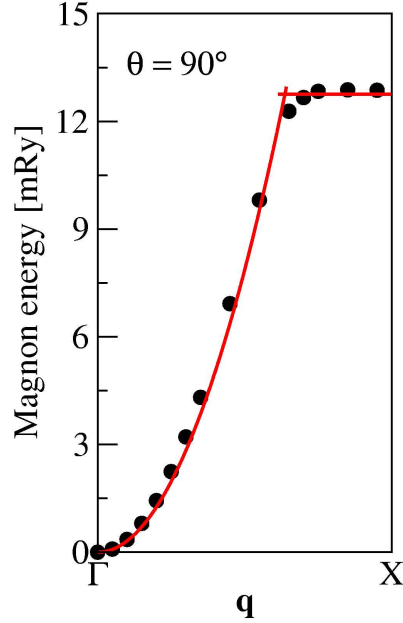
Figure 8.2: Magnon dispersion along [001] direction in NiMnSb, for a flat spiral ($\theta = 90°$). Black dots show the self-consistent calculation, while the red line is a parabolic fit up to a cutoff value $q_c = 0.65 q_D$, and a constant $\omega_c = 12,75$ mRy after it.

*spin-stiffness constant*:

$$\omega_q = Dq^2. \tag{8.2}$$

Obviously, the spin-stiffness constant is a measure of the "resistance" the spins give to the thermal excitations, i.e. a higher spin-stiffness promises a higher $T_C$. From the parabolic fit in the Fig. 8.2, we obtain the value $D = 380 \text{meV\AA}^2$, which is in a good agreement with the experimental value of $D = 305 \pm 40 \text{meV\AA}^2$ [43]. The Curie temperature, $T_C$, can be estimated on the basis of the Heisenberg model. By mapping the first-principles results to the Heisenberg model, the Curie temperature in the random phase approximation is given by [131, 132]

$$\frac{1}{k_B T_C} = \frac{6\mu_B}{M} \frac{\Omega}{(2\pi)^3} \int d^3q \frac{1}{\omega_q}, \tag{8.3}$$

where $k_B$ is the Boltzman factor and $\Omega$ is the unit cell volume. The integration should in principle be conducted over the whole Brillouin zone, but a rough estimate can be made even from the dispersion curve in the Figure. 8.2, given that there is no strong anisotropy, so that the calculated spin stiffness

is valid also for the spin waves propagating in different directions [133]. Since this is the case for NiMnSb, we can substitute the expression 8.2 into Eqn. 8.3. We work in the spirit of Debye approximation, replacing the Brillouin zone with a sphere of the radius $q_D = (6\pi^2/\Omega)^{1/3}$ and finally obtain

$$\frac{1}{k_B T_C} = \frac{3\Omega q_D \mu_B}{M\pi^2 D}.$$
(8.4)

The Curie temperature calculated from this expression with the use of the previously obtained spin-stiffness $D$ is $T_C$=1068 K, which is, compared to the experimental value of 730 K [42], too high. The dispersion curve in Fig. 8.2 for the short wavelengths deviates significantly from a parabola. An improvement to the obtained value of $T_C$ can be made if one considers the dispersion curve parabolic up to a cutoff wave vector $\boldsymbol{q}$=(0, 0, 0.65$q_D$) and constant, $\omega_c$=12.75 mRy, thereafter. The Curie temperature is then calculated from the expression

$$\frac{1}{k_B T_C} = \frac{3\Omega \mu_B}{M\pi^2} \left( \frac{3q_c}{D} + \frac{q_D^3 - q_c^3}{\omega_c} \right).$$
(8.5)

This procedure improves the result considerably, and the obtained value is now $T_C = 870K$, much closer to the experimental value.

## 8.3 Exchange Interaction Parameters

Following the prescription of Sec. 5.3, we calculated Heisenberg exchange interaction parameters ($J_{ij}$) of NiMnSb and CrTe and used the Monte Carlo method (Sec. 8.4) to obtain an estimate of the Curie temperatures for these compounds. The calculations for both compounds were performed on a $16 \times 16 \times 16$ **k**-point mesh with 2745 **q**-points in the full Brillouin zone. The planewave cutoff was $k_{\mathrm{max}} = 3.8$ au$^{-1}$. The convergence was checked with respect to the above parameters.

In CrTe, only Cr was considered as a magnetic atom and the exchange parameters for the Cr-Cr interaction were calculated (Fig. 8.3, left). In NiMnSb, though the magnetic moment of Ni is small (see Table 6.1) and actually induced by the Mn surrounding atoms, both Ni and Mn were treated as magnetic atoms and the parameters of Mn-Mn, Ni-Ni, and Mn-Ni interaction were calculated (shown with red, green and blue circles, respectively, in the right panel of Fig. 8.3).

For a weak ferromagnet, the interaction constants $J_{ij}$ follow the character-
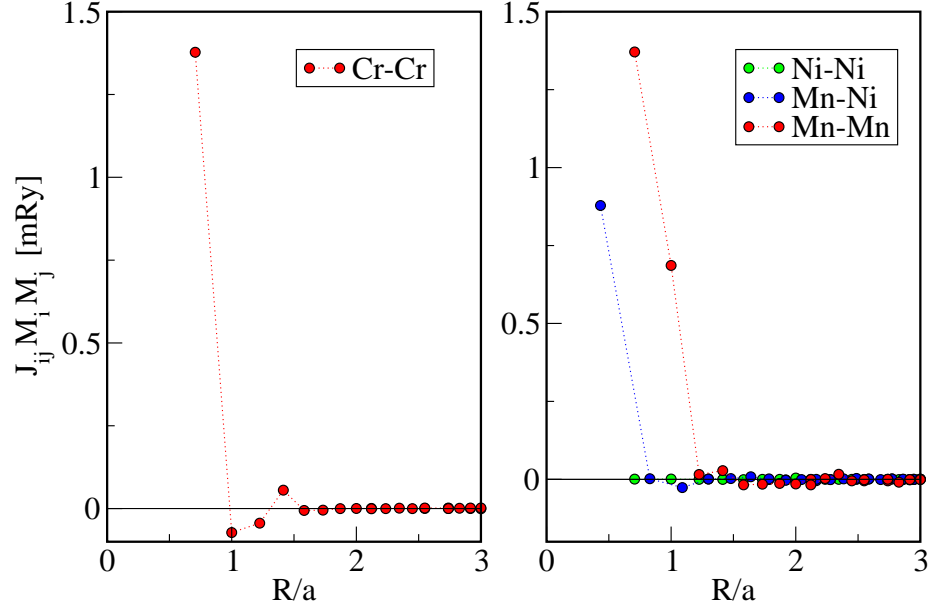
Figure 8.3: Heisenberg exchange interaction parameters of CrTe (left) and NiMnSb (right) as a function of the distance R between the atoms (in units of the lattice constant a).

istic Ruderman-Kittel-Kasuya-Yoshida (RKKY) asymptotic behavior [131],

$$J_{ij} \propto \frac{\sin\left[(\mathbf{k}_F^\uparrow + \mathbf{k}_F^\downarrow) \cdot (\mathbf{R}_i - \mathbf{R}_j) + \Phi\right]}{|\mathbf{R}_i - \mathbf{R}_j|^3}, \tag{8.6}$$

where $\mathbf{k}_F^\sigma$ is a Fermi wave vector direction such that the associated group velocity is parallel to $\mathbf{R}_i - \mathbf{R}_j$ and $\Phi$ denotes a phase factor. The exchange interaction according to Eqn.8.6 has an oscillatory character with an envelope decaying as $|\mathbf{R}_i - \mathbf{R}_j|^3$. On the other hand, in a half-metal there are no states at the Fermi level in the minority band, thus the relevant Fermi wave vector is imaginary, i.e., $\mathbf{k}_F^\downarrow = i\mathbf{K}_F^\downarrow$, corresponding to decaying states. Hence, one obtains an exponentially damped RKKY behavior [134],

$$J_{ij} \propto \frac{\sin\left[\mathbf{k}_F^\uparrow \cdot (\mathbf{R}_i - \mathbf{R}_j) + \Phi\right] \exp\left[-\mathbf{K}_F^\downarrow \cdot (\mathbf{R}_i - \mathbf{R}_j)\right]}{|\mathbf{R}_i - \mathbf{R}_j|^3}. \tag{8.7}$$

In both cases shown in Fig. 8.3, we notice this very fast decay of the interaction parameters with the distance between the atoms. For a comparison, in the left panel of Fig. 8.4, the exchange interaction parameters of bcc Fe
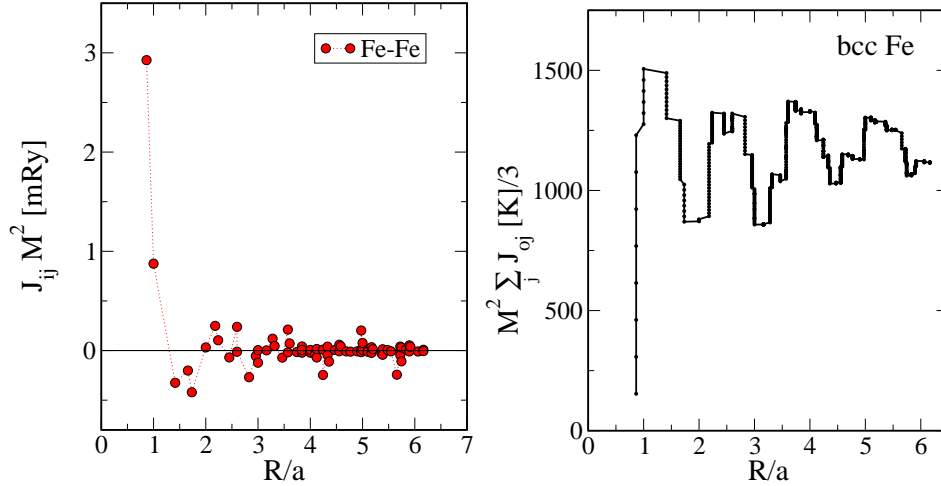
Figure 8.4: Left: Heisenberg exchange interaction parameters of bcc Fe as a function of the distance R between the atoms (in units of the lattice constant a); Right: The mean-field Curie temperature (Eqn. 8.9), as a function of the distance from the neighboring atoms taken into account in the sum 8.8.

are shown.[1] Obviously, the decay here is much slower. This can be also seen from the sum of the exchange parameters which describe the interactions of one atom with all the other atoms in the crystal,

$$J_0 = \sum_i J_{0i}, \tag{8.8}$$

where we denote the particular atom with 0 and $J_{0i}$ describes the interaction of this atom with the atom $i$. In the mean field (MF) approximation, the Curie temperature can be calculated from this sum as [59]

$$k_B T_C^{MF} = \frac{1}{3} M^2 J_0. \tag{8.9}$$

The sum $J_0$ converges rapidly for half-metals as the exchange parameters of more distant neighbors fall off exponentially. To see this, $T_C^{MF}$ was calculated according to Eqn. 8.9 as a function of the maximum distance of the neighbors entering the sum. The results are presented in Fig. 8.5 for Cr-Cr interactions in CrTe (left) and Mn-Mn interactions in NiMnSb (right). For comparison,

---

[1]The calculation was performed at experimental lattice constant $a = 2.87$ Å, using GGA, on a $16 \times 16 \times 16$ **k**-points mesh on 27001 **q**-points in the full Brillouin zone. The planewave cutoff was set to $k_{max} = 3.8$ au$^{-1}$.
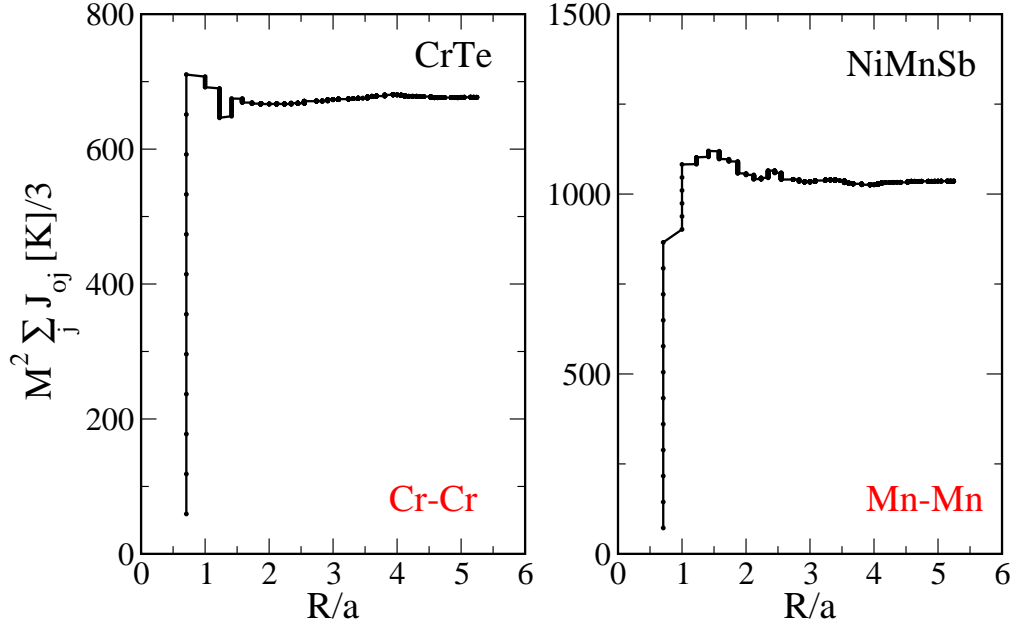
Figure 8.5: The mean-field Curie temperature (Eqn. 8.9), as a function of the distance (in units of the lattice parameter a) from the neighboring atoms taken into account in the sum 8.8, for Cr-Cr interactions in CrTe (left) and Mn-Mn interactions in NiMnSb (right).

the sum of Fe-Fe interactions is shown in the right panel of Fig. 8.4. Each dot represents one additional contribution $J_{0i}$ to the sum. The atoms that are at the same distance from the central atom (atom 0) belong to the same *shell*. Therefore, each vertical line in these graphs represents one shell. We see that the sum 8.8 converges to one constant value already at the distance of three lattice parameters in the half-metallic compounds, but needs to be calculated for much larger distances in bcc Fe to obtain a converged value.

From the Fig. 8.4 (right) we estimate $T_C^{MF} \sim 1200$ K for iron (the experimental value is 1043 K [59]) and, from the Fig. 8.5 (left), $T_C^{MF} \sim 690$ K for CrTe. Although in Fig. 8.5 (right) the sum $J_0$ was calculated using only the Mn-Mn interaction parameters, one can estimate a $T_C^{MF} \sim 1050$ K calculated at the equilibrium lattice constant of 5.9Å (experimental value being 730 K [42]) for NiMnSb, under the assumption that the atoms of Ni are not contributing significantly to the $T_C$. This assumption can be justified by the fact that the magnetic moments of Ni are induced by the Mn surrounding as well as from the fact that, as we see from the Fig. 8.3 (right), the Ni-Ni interaction is negligible compared to the Mn-Mn one, while the Ni-Mn inter-

action is important only for Nickel's first Mn neighboring shell, containing only 4 Mn atoms.

## 8.4   Monte Carlo Simulations

**Monte Carlo single-spin-flip algorithm**

In the classical limit, the spins are treated as simple three-dimensional vectors, and a good numerical approach to calculate thermal equilibrium properties is the *Monte Carlo method.* Here we discuss the method only briefly; for further information we refer to the textbook of Landau and Binder [135]. Within a Monte Carlo approach, trajectories in phase space are calculated following a master equation [136] for the time development of the probability distribution $P_S(t)$ in phase space,

$$\frac{\mathrm{d}P_S}{\mathrm{d}t} = \sum_{S'} \left( P_{S'} w_{S' \to S} - P_S w_{S \to S'} \right), \tag{8.10}$$

where $S$ and $S'$ denote different states of the system, and $w$ stands for the transition rate from one state to another. The transition rates have to fulfill *the detailed balance condition* [136],

$$\frac{w_{S \to S'}}{w_{S' \to S}} = \exp \left( \frac{E(S) - E(S')}{k_B T} \right). \tag{8.11}$$

The master equation describes the coupling of the system to the heat bath [136]. Within the Monte Carlo method, trajectories in phase space following Eqn. 8.10 are calculated usually using single-spin-flip dynamics (Fig. 8.6) within a large but finite supercell (usually with periodic boundary conditions) representing the whole crystal. A single-spin-flip algorithm goes as follows:

- At the beginning one single spin from the lattice is chosen either randomly, or in some systematic order, and a trial step of this selected spin is made (in the Fig. 8.6, the trial step is a small tilt from the initial state).

- The change of the energy of the system with respect to the initial state is calculated, according to the Hamiltonian of the system.

- The trial step is accepted with a given probability, defined, for instance, with the Metropolis criterion:

$$w_{S \to S'} = \begin{cases} 1, & \text{if} \quad E(S') < E(S) \\ \exp \left[ \frac{E(S) - E(S')}{k_B T} \right], & \text{if} \quad E(S) < E(S') \end{cases} \tag{8.12}$$
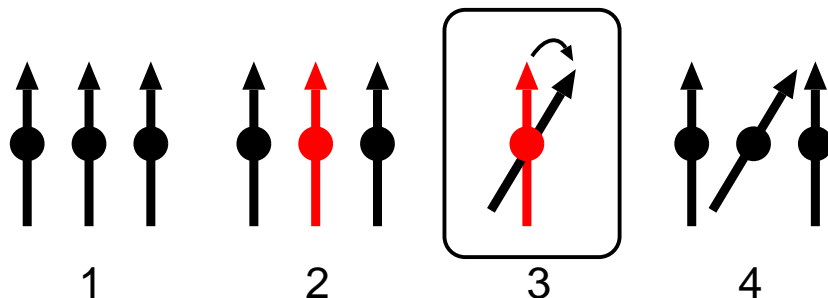
Figure 8.6: Illustration of a Monte Carlo single-spin-flip algorithm in a three-spin system: (1) an initial condition; (2) one spin is selected; (3) a trial step is made; (4) if the trial step is accepted, this is a new starting point.

(with $T$ the temperature and $k_B$ Boltzmann's constant), which is one possible choice among many satisfying the condition 8.11.

Scanning the lattice and performing the described procedure once per spin is referred to as *one Monte Carlo step*. After the Monte Carlo step, the quantities of interest, *e.g.*, average magnetization per atom, are calculated for the resulting state (this is the so-called *sampling*). Then another Monte Carlo step is taken. In this way the whole phase space is eventually sampled, giving the proper weight to the most probable states; in the end, a simple arithmetic average over many sampling steps yields the thermodynamically averaged quantities for the given temperature.

After each Monte Carlo step, the resulting state might be correlated to the previous one; therefore one takes several Monte Carlo steps between each two sampling steps, in order to decorrelate the states. Moreover, the initial state might be far from equilibrium (for instance, when the initial state is the ferromagnetic one, but one examines the system close to the Curie point). Thus an initial number of steps is needed (the *relaxation time*) in order to bring the system to equilibrium, before the sampling starts.

The Curie temperature $T_C$ can be found by inspection of the average magnetization curve $M(T)$; however, due to the finite size of the supercell, $M(T)$ does not drop to zero above $T_C$, but decays rather smoothly to low values. Instead, the peak of the susceptibility

$$\chi = \frac{1}{k_B T} \langle (\mathbf{M} - \langle \mathbf{M} \rangle)^2 \rangle, \tag{8.13}$$

is more relevant. The susceptibility is the measure of fluctuations of the magnetic moment and at the critical temperature, $T_C$, becomes infinite (although, due to the finite size of the system used in the calculations, its value appears to be finite but peaked).
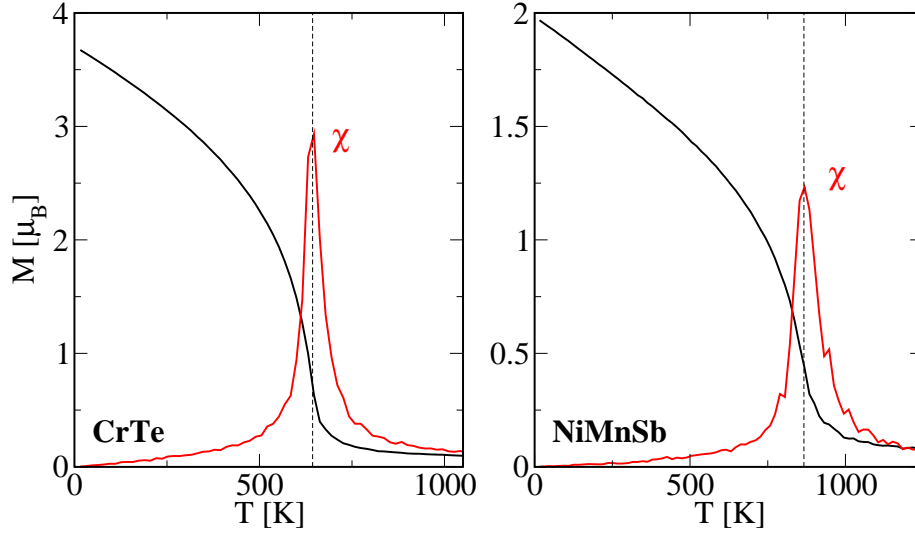
Figure 8.7: Magnetic moment per magnetic atom (black lines), and the susceptibility $\chi$ (red lines) as functions of the temperature. The peak of the susceptibility points at the Curie temperature. It is found to be 640 K for CrTe (left) and 875 K for NiMnSb (right). Note that the susceptibilities are much smaller quantities than shown, and they were in both figures scaled by appropriate factors to make them visible.

Alternatively, one can examine the intersection point of fourth-order cumulants for finite supercells of different sizes. One possible definition of the fourth-order cumulant is:

$$U_4 = \frac{5}{3} - \frac{\langle M^4 \rangle}{\langle M^2 \rangle^2} \tag{8.14}$$

Scaling arguments [135] lead to the conclusion that, for large enough supercell sizes, the curves for $U_4$ cross at $T_C$.

## $T_C$ of CrTe and NiMnSb from the Monte Carlo Method

We applied the Monte Carlo method on CrTe and NiMnSb in order to obtain the Curie temperatures of these compounds. The classical Heisenberg Hamiltonian,

$$H = -\frac{1}{2} \sum_{\substack{i,j \\ i \neq j}} J_{ij} \mathbf{M}_i \mathbf{M}_j, \tag{8.15}$$

was used to model the systems, assuming that the magnetic moments $\mathbf{M}_i$ can change their orientation, but not their length. The results of these cal-
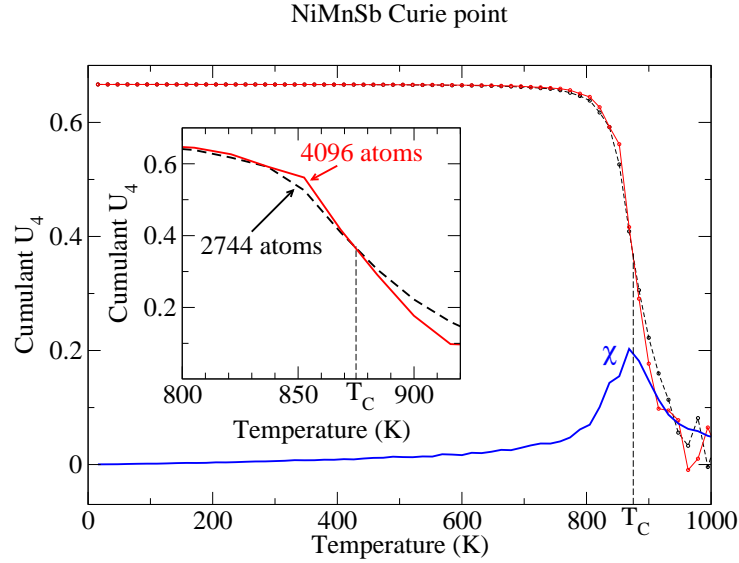
Figure 8.8: Fourth order cumulant $U_4$ for a 4096-atom supercell (red full line) and a 2744-atom supercell (black dashed line). The two lines cross at the Curie point $T_C = 875$ K (seen better in the inset). A peak of the susceptibility $\chi$ (blue line, shown for the 4096-atom supercell) at $T_C$ is also present.

culations are shown in Fig. 8.7, where the magnetic moment (per magnetic atom) is shown with the black line, and the susceptibility, $\chi$, with the red line (both as functions of temperature).

In the calculations a supercell of 4096 atoms was used for NiMnSb and one of 4000 atoms for CrTe; interactions to neighbors up to a distance of three lattice constants for NiMnSb and two lattice constants for CrTe were taken. For each temperature the total number of Monte Carlo steps was 20000, allowing an initial relaxation time of 2000 steps and then sampling every 20 steps.

The magnetization curves (black lines in Fig. 8.7) do not go to a sharp zero at $T_C$, but rather have a tail, as a result of the finite supercell. The peak of the susceptibility is, on the other hand, pretty sharp and its position can be used to determine the Curie temperature. From the positions of these peaks, we estimated for CrTe (Fig. 8.7, left) $T_C$=640 K, and for NiMnSb (right) $T_C$=875 K (experimental value being 730 K). Note that, for NiMnSb, the Ni moment was also taken into account within the Heisenberg model.

For NiMnSb, we also calculated the cumulants $U_4$ for a 2744-atom and a 4096-atom supercell (Fig. 8.8). Their intersection point agrees with the

susceptibility maximum at $T_C$.

## 8.5   One Step Beyond: Longitudinal fluctuations in NiMnSb

In NiMnSb, the local Ni moment is rather induced by the *d-d* hybridization with the Mn neighbors. As a consequence, it is not independent (even approximately) of the short-range spin configuration. For instance, on forcing the atoms of the Mn sublattice to an antiferromagnetic state, the Ni moment $\mathbf{M}_{\mathrm{Ni}}$ disappears; and on forcing the moments of the Ni sublattice to have an angle $\theta$ with respect to the moment $\mathbf{M}_{\mathrm{Mn}}$ of the ferromagnetic Mn sublattice (by constrained density functional calculations), $|\mathbf{M}_{\mathrm{Ni}}|$ becomes smaller and is completely suppressed already at $\theta = 90°$.

In view of this observation, it seems that the Heisenberg model, which explicitly assumes rigid (in magnitude) spins, is inadequate to describe the Ni sublattice magnetization. In order to gain information on the Ni magnetization, one has to allow for longitudinal as well as transverse fluctuations of $\mathbf{M}_{\mathrm{Ni}}$. One way of doing this is the following.

At each Ni site $i$ we assume that the spin-polarization energy $E(\mathbf{M}_i)$ can be expanded in powers of the local Ni moment $\mathbf{M}_i$. In the absence of a polarization due to the surrounding atoms (mainly the first Mn neighbors), the inversion symmetry $E(\mathbf{M}) = E(-\mathbf{M})$ suggests that only even powers of $\mathbf{M}_{\mathrm{Ni}}$ should enter in the expansion. Whenever there is a net magnetization of the surroundings, this acts as an effective magnetic field $\mathbf{H}_i$, polarizing also the Ni site $i$. Thus we arrive at the following energy functional for the moment at site $i$:

$$E[\mathbf{H}_i, \mathbf{M}_i] = -\mathbf{H}_i \cdot \mathbf{M}_i + AM_i^2 + BM_i^4 \qquad (8.16)$$

with

$$\mathbf{H}_i = \sum_{j \neq i} J_{ij}\mathbf{M}_j + \mathbf{H}_{\mathrm{ext}}, \qquad (8.17)$$

allowing also for an external constraining field $\mathbf{H}_{\mathrm{ext}}$. Although the expression reminds of a Landau expansion of the free energy, it should be kept in mind that it refers to the *local* moment, and not to the thermodynamically averaged one.

In case of spontaneous magnetization, $A$ would be negative and $B$ positive, giving an energy minimum at some $\mathbf{M}_0 \neq 0$ in the absence of a field $\mathbf{H}_i$. This corresponds to, *e.g.*, the Mn atoms. For the Ni atoms, we have $A > 0$ and $B > 0$, giving $\mathbf{M}_0 = 0$. Under the influence of a polarizing field $\mathbf{H}_i \neq 0$,

expression (8.16) gives an energy minimum at a nonzero spin moment $\mathbf{M}_H$ in the direction of $\mathbf{H}_i$, its magnitude being given by the condition

$$0 = \frac{\partial E[\mathbf{H}_i, \mathbf{M}_i]}{\partial M_i} = -H_i + 2AM_H + 4BM_H^3 \qquad (8.18)$$

The idea is summarized in figure 8.9.

The parameters $A$ and $B$ entering expression 8.16 can be found by first-principles calculations of the magnetic moment fitted to Equation 8.18. Two equations are needed to specify the two parameters. Firstly the fully ferromagnetic state was chosen, where $M_H = M_{\text{Ni}} = 0.258 \ \mu_B$, and $H = \sum_{j \neq i} J_{ij}\mathbf{M}_j$ and $H_{\text{ext}} = 0$. Secondly, the constrained density functional solution was considered, with $\mathbf{M}_{\text{Ni}}$ rotated by $\theta = 60°$ with respect to $\mathbf{M}_{\text{Mn}}$, as forced by an external field $\mathbf{H}_{\text{ext}}$. In practice, $\mathbf{H}_{\text{ext}}$ is always chosen to be perpendicular to $\mathbf{M}_{\text{Ni}}$, so that $\mathbf{H}_{\text{ext}} \cdot \mathbf{M}_{\text{Ni}} = 0$, and it does not affect the energy expression explicitly. But the rotation reduces $|\mathbf{M}_{\text{Ni}}|$ to $0.138\mu_B$, and in Equation (8.18) one has to put $H = |\sum_{j \neq i} J_{ij}\mathbf{M}_j| \cos 60°$.[2]

After determining the values of $A$ and $B$, the Heisenberg model can be extended to include the longitudinal change of $\mathbf{M}_{\text{Ni}}$ in the total energy expression. This reads now:

$$E = -\frac{1}{2} \sum_{i,j} J_{ij}\mathbf{M}_i \cdot \mathbf{M}_j + \sum_{\text{Ni atoms } i} \left( AM_i^2 + BM_i^4 \right) \qquad (8.19)$$

This expression can be used together with a Monte Carlo algorithm to find the statistical mechanical quantities (average magnetization, susceptibility, etc.) for $T > 0$. Within the Monte Carlo algorithm, the moment of the Mn atoms is modified only by direction, while the Ni moment is modified by direction *and* magnitude. Since longitudinal fluctuations of $M_{\text{Ni}}$ are taken into account, its value should be allowed to increase above the equilibrium Ni moment of the ferromagnetic state $M_{\text{Ni}}^0 = 0.258\mu_B$.

In the calculations, the magnitude was selected within the range $0 < M_{\text{Ni}} < 1.5M_{\text{Ni}}^0$. The cutoff of $1.5M_{\text{Ni}}^0$ was chosen after tests with different cutoffs; it was found that a further increase of the cutoff to $2M_{\text{Ni}}^0$ brought no change to the results. Considering that each value of $\mathbf{M}_{\text{Ni}}$ corresponds to a possible state, the number of possible states of a given magnitude $M_{\text{Ni}}$ is determined by the surface area of a sphere of radius $M_{\text{Ni}}$; thus it increases quadratically with $M_{\text{Ni}}$. This was taken into account in the Monte Carlo algorithm, by using a quadratic probability distribution for choosing $M_{\text{Ni}}$.

---

[2]If the sum in Eqn. (8.17) goes beyond first neighbors, then the tilting of the moments of the other Ni atoms in the crystal must be also accounted for, whence one has 61.06° instead of 60°.
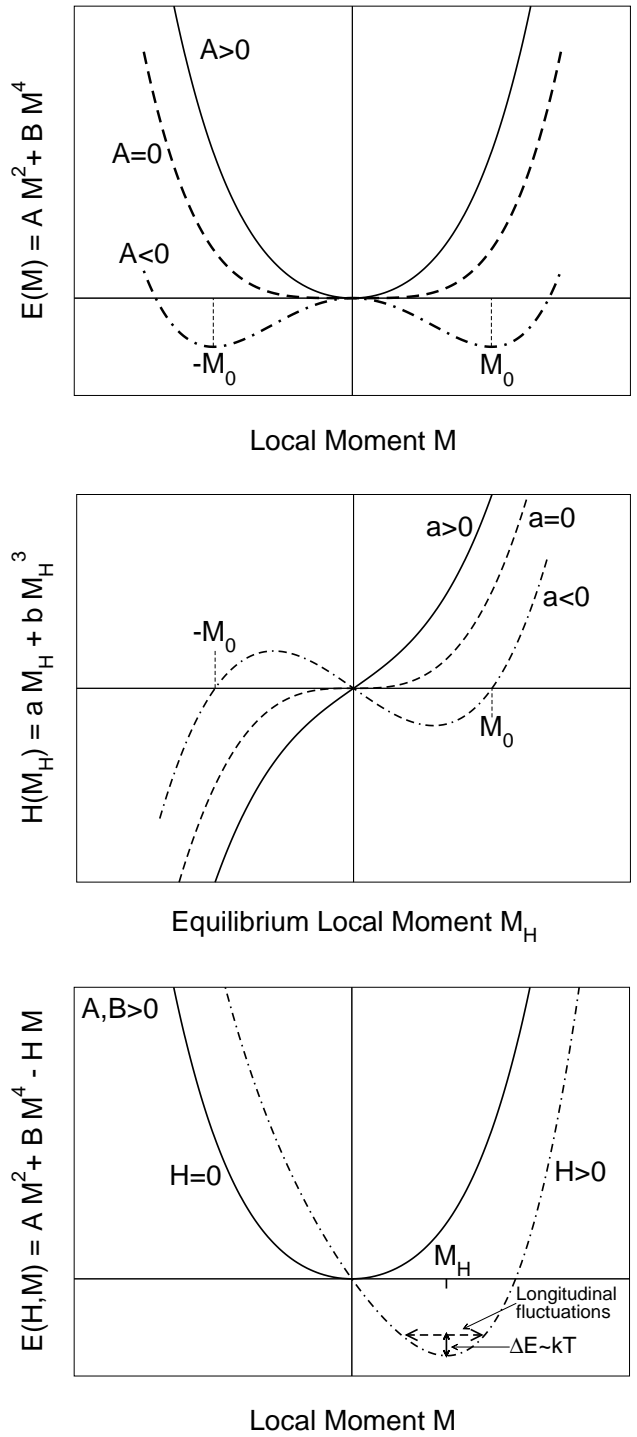
Figure 8.9: Top: Energy functional without a polarizing field $H$; Middle: magnetic moment curve, with $a = 2A$ and $b = 3B$; and Bottom: Energy in the presence of a polarizing field $H$, and longitudinal fluctuations. For details see text.

Note also that, compared to the Heisenberg model case, many more Monte Carlo steps (factor of 100) are needed now in order to arrive at averaged quantities, since the longitudinal fluctuation brings into play many more possible states.

The Monte Carlo result for the extended Heisenberg model is shown in figure 8.10, together with the result of the original Heisenberg model (which considers the Ni moments as rigid in magnitude). In both cases, it can be seen that the average Ni moment drops very fast at already low temperatures. However, when allowing for longitudinal fluctuations, the drop is even more rapid. A peak in the sublattice susceptibility shows the characteristic (though not critical) transition temperature; above this, the sublattice magnetic order is strongly reduced. In these calculations, a supercell of 1372 lattice sites (2744 atoms) was used for the Heisenberg model calculations, while only 256 lattice sites (512 atoms) were used for the extended Heisenberg model calculations due to the higher numerical effort involved.

These results for the low temperature behavior of the Ni moment should be considered with caution. It is well-known that, although the classical Heisenberg model can give a decent estimate of $T_C$, it fails to reproduce the magnetization curve at low temperatures. In particular, Bloch's law

$$M(T) = M(0)\left(1 - \text{const} \cdot T^{3/2}\right) \tag{8.20}$$

for the magnetization at low temperatures is not reproduced, since the classical Heisenberg model does not account for the discrete magnon spectrum, but rather allows for excitations with infinitesimal change of the magnetic moment. As a consequence the magnetization here falls off linearly with $T$ instead of the correct behavior of Eqn. (8.20).

Nevertheless, the low-$T$ results indicate a clear tendency: the Ni moment is weak, and even at low temperatures, far from the phase transition, fluctuations can quickly suppress it. Moreover, longitudinal fluctuations are also relevant at an energy scale far below $T_C$; thus even a quantum Heisenberg model, which can prove successful in other cases, is inadequate. A correct quantitative modeling of the low-$T$ magnetism in half-Heusler compounds is thus an open challenging question for the future.

The release of the Ni magnetic degrees of freedom at temperatures so much lower than $T_C$, and the corresponding loss of short-range order in the Ni sublattice, makes us suspect, at first sight, that the half-metallic property is easily lost. This would follow from the argument that the spin-up DOS of each Ni atom, with randomly oriented spin moment, is partly projected into the spin-down DOS of its neighbors, and vice-versa. However, in this case this picture is not completely correct. Since in NiMnSb the origin of the half-metallic gap is the $d$-$d$ hybridization between Ni and Mn spin-down states,
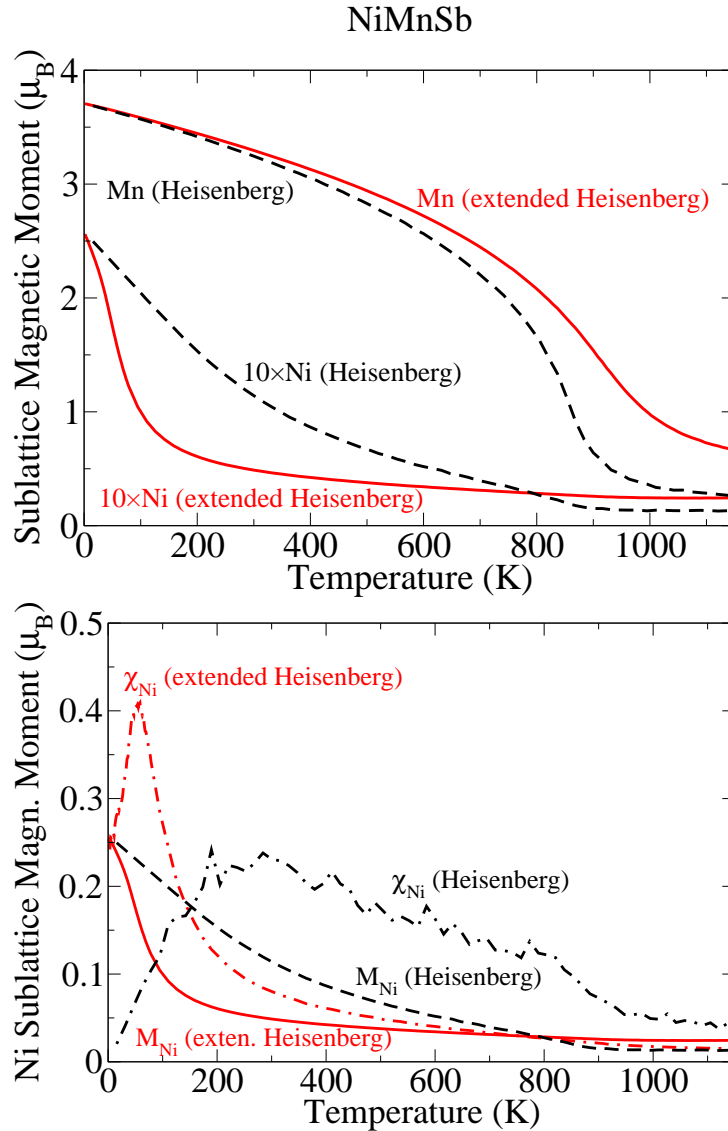
Figure 8.10: Top: Mn- and Ni-sublattice magnetic moment in the cases of the traditional Heisenberg model and the extended Heisenberg model (including longitudinal fluctuations of the Ni moment), calculated by the Monte Carlo Metropolis method. In both cases the Ni moment drops faster than the Mn moment. In the case of the extended Heisenberg model, the longitudinal fluctuations cause an even faster decrease of the Ni moment. Note that the Ni moment has been scaled up by a factor of 10. Bottom: Ni-sublattice magnetic moment and susceptibility for the same cases as before. The sublattice susceptibility has a peak much below $T_C$ (even more so in the extended Heisenberg model), indicating the early loss of magnetic order in the sublattice.

and since the Ni $d$ states exist under $E_F$ for both spin directions, a rotation of the Ni moment causes a hybridization of the Mn $d$ spin-down states partly with the Ni spin-up states and partly with the Ni spin-down states. As a result, the $d$-$d$ hybridization is still there, and the gap remains. However, the gap width is reduced. The relevant DOS can be seen in Fig. 8.11, which concerns the case of the Mn moments remaining in a ferromagnetic configuration, while the Ni moments are constrained to several different angles (at an 90° angle, the magnetic moment of Ni vanishes in the self-consistent calculation). The reduction of the gap width can be understood as a reduction of the hybridization strength: as the Ni moment is reduced, its spin-down states move lower in energy and hybridize less with the Mn spin-down states.
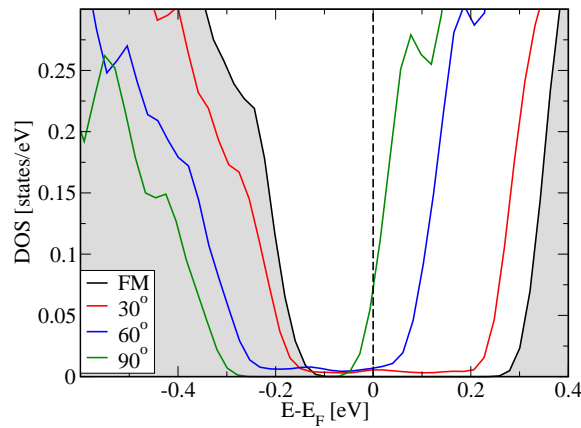


Figure 8.11: Minority DOS of NiMnSb in the gap region: ground state (black curve with the gray background) and the states when the Ni moment has been constrained to the angles of 30° (red), 60° (blue) and 90° (green) with respect to the Mn moment; the DOS is presented in the global frame, which coincides with the local frame of Mn atoms.

It is important to mention that this simple picture does not account for the fluctuating Mn moment. In reality, the fluctuations on Mn site will also create a projection of a part of Mn spin-up DOS into the spin-down DOS of its neighbours (and vice-versa), which will then lead to further hybridizations. This will necessarily affect the arrangement of the minority DOS features and the gap. As a conclusion for application purposes, a high $T_C$ is not enough to guarantee that a half-metal will be applicable at room temperature; in each case, further investigation of the sublattice magnetization is needed.

# Chapter 9

# Half-metallic Spin Valves

## 9.1 Half-metals in junctions: GMR or TMR

Half-metallic ferromagnets are, in principle, ideal spin injectors and detectors, because under moderate voltage they can carry current of only one spin direction. Therefore, they also constitute ideal components for Giant Magnetoresistant (GMR) and Tunneling Magnetoresistant (TMR) devices, with two half-metallic leads sandwiching a non-magnetic normal metal spacer (in GMR) or a semiconductor or insulator spacer (in TMR). There is, for instance, the reported experimental result of Bowen and collaborators [137] who obtained a TMR value higher than 1800% in an LSMO/STO/LSMO junction; this extreme value was attributed to the half-metallicity of LSMO.

In both the GMR and TMR cases the idea seems simple and its application straightforward: in a ferromagnetic (FM) alignment of the half-metals sandwiching the spacer, *some* current will pass, either by metallic conduction (GMR) or by tunneling (TMR) of spin-up electrons. On orienting the half-metallic leads antiferromagnetically (AF), in the one spin direction no current can enter the junction (due to the minority-spin gap of the left lead), while in the other spin no current can exit the junction (due to the minority-spin gap of the right lead); thus *no* current can pass. Hence this is the ideal spin valve.

A careful analysis of the physical processes involved in TMR and GMR junctions reveals, however, that TMR junctions are much more difficult to realize and control than GMR. The main difficulty arises from the possible presence of interface states around $E_F$ at the metal-semiconductor (or insulator) contact. Consider, for instance, the TMR junction in Fig. 9.1, where the bands are shown along the junction as shaded regions. Only one spin
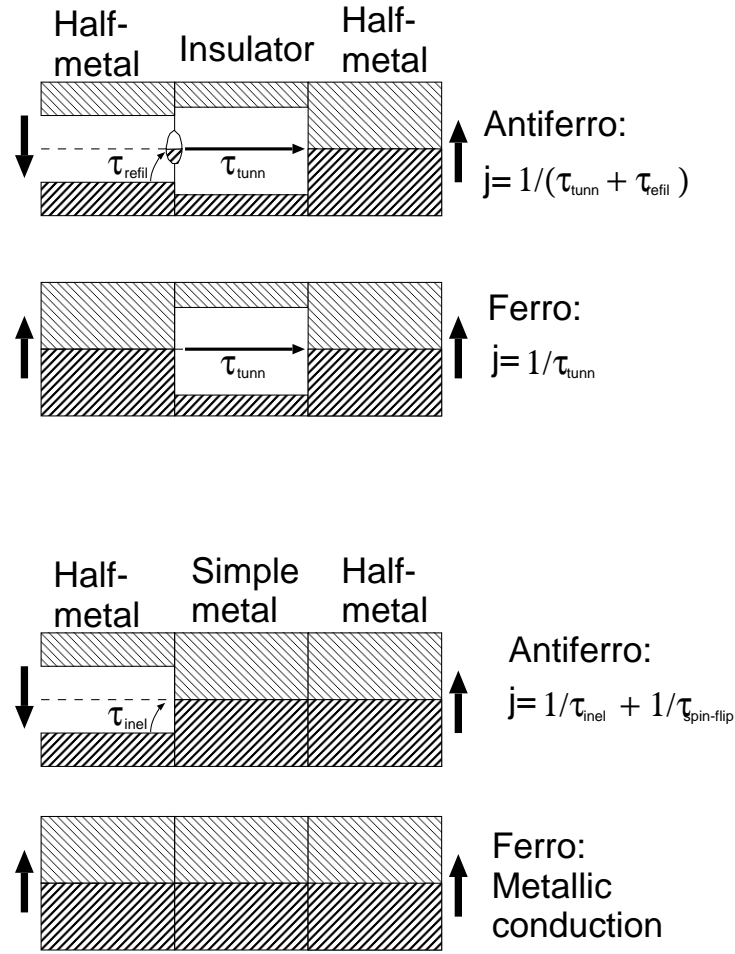
Figure 9.1: Half-metallic leads can be used in TMR (up) or GMR (down) junctions for, in principle, ideal magnetoresistance. In the case of TMR junctions, however, interface states can change the desired result.

direction is shown; in the AF case the layer-resolved DOS of the other spin direction is symmetric with respect to the center of the junction, while in the FM case the one shown is supposed to be current carrying (the opposite spin direction has only band gaps around $E_F$). The Fermi level is shown in the middle of the gaps as a dashed line. Heavily shaded regions correspond to filled bands, while lightly shaded regions indicate the empty bands (above $E_F$). At the left half-metal / insulator interface in the AF case, possible localized interface states are shown. In practice, tunneling form these into the right lead cannot be avoided. The current $j$ is then determined by the slowest of two processes: (1) The tunneling rate itself, characterized by a

time $\tau_{\text{tunn}}$, and (2) by the rate of re-filling the interface states after an electron has tunneled, with a characteristic time of $\tau_{\text{refil}}$. Then the expression for $j$ has the form

$$j_{AF} \sim \frac{1}{\tau_{\text{tunn}} + \tau_{\text{refil}}} \qquad (9.1)$$

Evidently the slowest of the two processes determines the current. If the states are immediately refilled after a tunneling event, (as in the metallic case), then $\tau_{\text{refil}} << \tau_{\text{tunn}}$ and the current is determined by the tunneling rate alone, irrespectively of the half-metallic band gap.

What determines the refill time $\tau_{\text{refil}}$? For one thing, even at low temperatures there are inelastic processes contributing with a rate $1/\tau_{\text{inel}}$. Usually these are slow, but in case that the Fermi level is in the proximity of the bands, rather than in mid-gap, they can be of significance. More importantly, there is always some spin-orbit coupling present, leading to a spin down to spin up ratio at $E_F$ of the order of 0.5% (for NiMnSb) [116]. Given this, and remembering that tunneling can be a very slow process ($\tau_{\text{tunn}}$ is long), it is very well conceivable that the interface states act practically as a reservoir of electrons just as any metallic lead would. In this case the spin up versus spin down current, determining the TMR ratio, depends only on the tunneling rates for the two spin directions and not at all on the half-metallic property of the lead!

The tunneling rates themselves depend on numerous factors, such details of the interface structure, the presence of interface disorder, the symmetry character of the states, defects in the insulating spacer, etc., just as in the case of the usual TMR with simple ferromagnetic leads. *Some* TMR value will appear, as in most junctions, but the half-metallic property is relevant only if one can eliminate the interface states.

In the case of GMR, on the other hand, the interface states play no significant role. In the FM case the conduction is metallic, while in the AF case it is confined at most to the value of the spin polarization at $E_F$ in the bulk of the half-metallic leads (plus inelastic effects); if this is determined by the spin-orbit coupling, it should lead to an effect of the order of 1%. This means that the half-metallic property is fully exploited in the case of GMR, in contrast to TMR.

We conclude that, in order to have controlled TMR by exploiting the half-metallic property, we must find half-metal / insulator interfaces without interface states. This analysis rules out the Heusler alloys as likely candidates for TMR junctions, due to the interface states formed. But there is a way out, namely by using zinc-blende compounds; and to this we now turn.

## 9.2   AF coupled half-metallic elements

In both GMR and TMR applications, it is desirable that the magnetic leads are antiferromagnetically coupled in the ground state; then with the application of a magnetic field, the leads are re-oriented ferromagnetically, and the conductance changes. Moreover, the energy difference between AF and FM, $\Delta E = E(AF) - E(FM)$, should be small enough that the switching occurs at moderate, rather than unrealistically gigantic, fields. In GMR, both the AF coupling and the coupling energy can be tuned by changing the spacer thickness $d$. The coupling strength follows a decaying, oscillating pattern, thus a convenient thickness can always be found for which $\Delta E < 0$ and small. In the case of TMR, increasing $d$ still results in a decoupling of the two leads, with $|\Delta E|$ exponentially decreasing with $d$ [138]. However, the AF coupling is not necessarily oscillating. Therefore, it is desirable to find TMR systems where the AF coupling is dictated by *a priori* known physical properties, while $|\Delta E|$ can be tuned *a posteriori* by changing the insulator spacer thickness. In addition to this, one should eliminate any interface states at $E_F$ for the reasons discussed above.

The most studied half-metallic ferromagnets are probably Heusler alloys. The bulk band structure and the origin of the gap are well understood; also their surface and interface properties have been studied by first-principles calculations. Unfortunately, almost all calculations of Heusler alloy / semiconductor interfaces are conclusive on the appearance of interface states at $E_F$. On the other hand, another class of half-metals, namely zinc-blende pnictides and chalcogenides, show no interface states at $E_F$ when brought in contact with zinc-blende (zb) semiconductors [22]. The reason is also well understood. In the half-metal, the gap originates from a bonding-antibonding splitting of the transition-metal $d$ states with the $p$ states of the $sp$ anion. This continues coherently at the interface, between the $sp$ anion and the cation of the semiconductor. No unsaturated bonds are left to produce spurious interface states.

Furthermore, the magnetic coupling in such zb compounds is rather well understood. The origin of ferromagnetism is mainly the broadening of the majority $p$-$d$ hybrid band, whenever it is partly occupied. This is the case, *e.g.*, for CrAs and MnAs, or VTe and CrTe. On the contrary, FeAs and MnTe have one electron too much: the majority $p$-$d$ band is then fully occupied, so that no energy is gained by its broadening, and the antiferromagnetic susceptibility prevails.

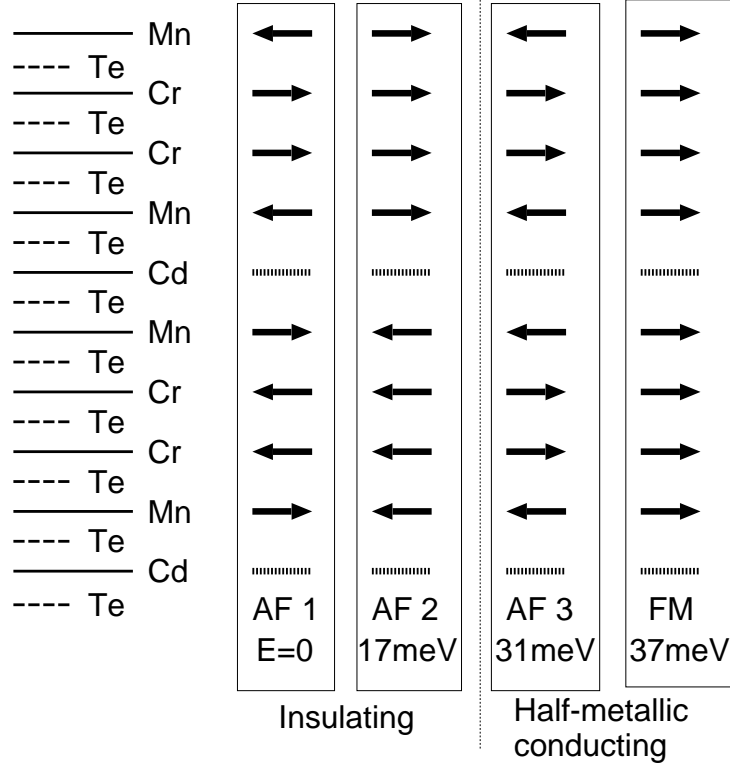Having this in mind, it is natural to ask on the coupling in a junction of

Figure 9.2: Construction of the half-metallic spin valve. The ground state (AF 1) is antiferromagnetic and completely insulating, while the ferromagnetic (FM) state is half-metallic and conducting. The energies are given in meV/junction.

the form (given layer-by-layer):

$$\cdots \mathrm{MnAsMnAsMn\underline{Te}MnAsMnAsMn} \cdots . \tag{9.2}$$

Is the Te layer in the middle enough to couple the leads antiferromagnetically? The answer is, in many cases, yes. If the interaction energy $|\Delta E|$ is too high, the layers can be further decoupled by introducing one or more semiconductor layers in-between:

$$\cdots \mathrm{MnAsMnAsMn\underline{TeCdTe}MnAsMnAsMn} \cdots . \tag{9.3}$$

A similar approach would be to change the $3d$ atom at the interface, instead of the $sp$ atom. In the junction

$$\cdots \mathrm{CrTeCrTe}\ \boxed{\mathrm{Mn}}\ \boxed{\mathrm{TeCdTe}}\ \boxed{\mathrm{Mn}}\ \mathrm{TeCrTeCr} \cdots \tag{9.4}$$
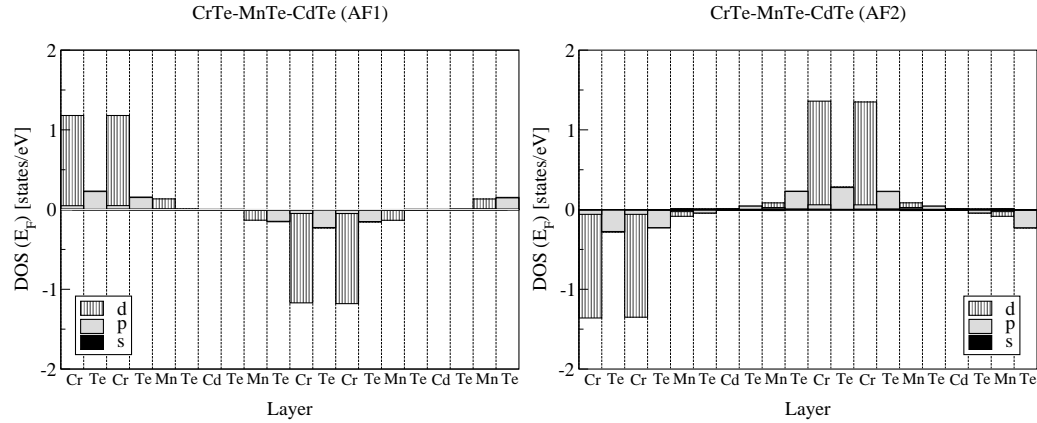
Figure 9.3: Density of states at $E_F$ for the AF 1 (left) and AF 2 (right) configurations. Evidently, the valve is insulating.

the Mn atoms at the interface can induce an antiferromagnetic coupling between the leads. The idea is always to introduce elements with higher number of valence electrons at the interface—for instance replace a group V element (As) by a group VI one (Te), or Cr by Mn, so that the majority $p$-$d$ hybrid bands are filled and the coupling turns to AF. Similar effects are observed in the case of Mn-doped II-VI semiconductors (*e.g.* (Cd,Mn)Te), which present a disordered local moment state due to an AF Mn-Mn interaction [108], in contrast to ferromagnetic Mn-doped III-V semiconductors (*e.g.* (Ga,Mn)As) [139].

A study of a (001) junction of the form 9.4 gives promising results. In Fig. 9.2 we present the calculated geometry in more detail. A supercell was used in the calculation, consisting of two "leads", each having two Cr and two Mn layers (and corresponding Te layers), and separated by a CdTe layer for decoupling. Various possible magnetic configurations were examined. The ground state (AF 1 in Fig. 9.2) is of antiferromagnetic nature, as expected. The nice feature is that, in the ground state, each lead is by itself half metallic, so that the whole system is non-conducting. This is evident also from Fig. 9.3a, where the layer-resolved density of states at $E_F$ is shown. Spin-down electrons are blocked in the first half of the junction, whereas spin up electrons are blocked in the second part.

A state with higher energy (AF 2 in Fig. 9.2, 17 meV higher than the ground state), where the Mn atoms within each lead obtain the direction of the Cr atoms, is still insulating, as shown in the layer-resolved DOS of figure 9.3b. It is important that in both cases there are no minority-spin interface states in the vicinity of $E_F$.

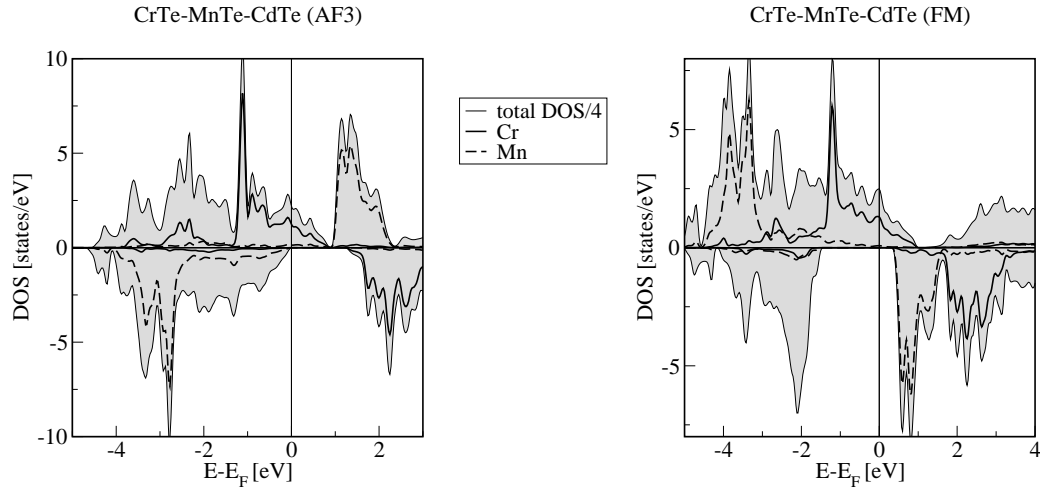CrTe-MnTe-CdTe (AF3)                                    CrTe-MnTe-CdTe (FM)



Figure 9.4: Density of states for the AF 3 (left) and FM (right) configurations. Now the junction is conducting.

Further higher in energy we find the conducting configurations, which are half-metallic throughout the junction. They are named AF 3 and FM in figure 9.2, with the latter being the fully ferromagnetic state. They are 31 meV and 37 meV, respectively, higher in energy than the AF 1 ground state. Their half-metallic character can be seen in the DOS plot of figure 9.4.

It can be argued that the energies of 30-40 meV involved for switching from the AF 1 to the AF 3 or FM states are too high to allow switching via an external field; after all, 1 meV$\sim$24.4 Tesla/$\mu_B$. However, the leads can be further decoupled by introducing more semiconducting CdTe layers in-between. Since the coupling energy falls off exponentially with spacer thickness, a desired energy difference can be quickly achieved. The decoupling can be seen by comparison to the case without a CdTe layer (the interface is then of the form Mn-Te-Mn); then the AF 1 state is higher than the FM state by 248 meV. This means that one CdTe layer lowers the energy difference by an order of magnitude. Two or three more CdTe layers should decouple the layers sufficiently.

# Chapter 10

# Conclusions

In this work, an *ab initio* study of the half-metallicity in half- and full-Heusler alloys and zinc-blende compounds was presented. The calculations were performed within the Density Functional Theory, using a Full Potential Augmented Planewave method as implemented in the `FLEUR` code.

The half-metallic ferromagnets, materials which show a metallic behavior in the majority spin band and semiconducting behavior in the minority spin band, are very interesting for applications in the field of spintronics, since, due to the 100% spin polarization that they present at Fermi level, they can maximize the efficiency of spintronic devices. For this reason they are extensively studied, in order to understand the mechanism which creates the half-metallic gap, as well as the mechanisms that might destroy it.

The full-Heusler alloys, which crystallize in $L2_1$ structure, are described by the formula $X_2YZ$, where X and Y are transition elements and Z is an *sp*-element. If the place of one of the two X-atoms remains empty, we obtain the $C1_b$ structure that characterizes the half-Heusler alloys which are described by the formula XYZ. Finally, leaving the place of Y-atom in $C1_b$ structure empty, we are left with the zinc-blende structure, which is the one adopted by the half-metallic transition-metal chalcogenides and pnictides. We have seen that the gap in half- and full-Heusler alloys is formed as a result of the hybridization of the *d*-orbitals of the two transition metals, which gives the bonding and antibonding hybrids that in the minority band have a gap in-between. In the zinc-blende compounds, the half-metallic gap is a result of the hybridization of the $t_{2g}$ *d* orbitals of the transition metal with the *p* orbitals of the *sp*-atom, giving rise to the bonding-antibonding splitting. The characteristic of all the half-metallic compounds is an integer magnetic moment whose value can be found according to the rules derived in Chapter 6.

The half-metallic gap is obtained in a perfect geometry, without spin-orbit coupling. When the spin-orbit coupling is introduced, a small density

of states appears in the gap and the spin-polarization is reduced. We find this reduction to be small, less than 1% for compounds, which do not contain heavy elements. Surfaces break the three-dimensional symmetry of the crystal and at the surface some states might appear in the gap. The same is valid for interfaces with other materials. We have investigated how this symmetry breaking influences the half-metallic gap of NiMnSb, and found that all the (001) and (111) surfaces present surface states in the gap which reduce the spin-polarization in the first several surface layers. We also investigated the (001) and (111) NiMnSb/InP contacts and found that only one of the possible (111) interfaces remains half-metallic in a somewhat unexpected geometry. Although all the other investigated interfaces lose half-metallicity, some of them remain highly spin-polarized, and thus attractive for applications.

The behavior of the half-metallic compounds at finite temperatures is one of the most important issues when the applications are considered. This behavior was investigated here by mapping the *ab initio* total energy calculations of different magnetic configurations to the Heisenberg model. Several approximations to determine the Curie temperature, $T_C$, (random phase approximation, mean field approximation and Monte Carlo method) were presented. The estimated $T_C$ of NiMnSb is in nice agreement with the experiment. The predicted $T_C$ of CrTe, and the (experimentally known) $T_C$ of NiMnSb are both much higher than room temperature and in this aspect they could both be considered good candidates in applications. However, after analyzing the results for NiMnSb at finite temperatures below $T_C$, obtained from Monte Carlo calculations, we see that this conclusion should be taken with caution. The fluctuations of the magnetic moment of the Ni atom are very large and it is vanishing at the temperatures much lower than $T_C$, and lower than the room temperature. The loss of the Ni-magnetic moment, although it doesn't destroy the the half-metallic gap, through the changes in hybridization, affects the width and the position of the gap with respect to the Fermi level. In potential applications it is necessary to make a careful choice of the half-metallic material. One solution could be to look for materials with similar strength in the exchange interaction between all components.

Finally, we propose an application of the half-metallic ferromagnets as the ideal spin-valves. Multilayers of two half-metals, which are coupled antiferromagnetically in the ground state will behave as insulator. Applying a magnetic field will align the moments of both half-metals ferromagnetically In this ferromagnetic configuration the valve is conducting (with a 100% polarization at the Fermi level). In such a construction, the interface states can play a crucial role in determining the conductance. Thus, once again we conclude that a careful choice of the material has to be made. In this thesis,

the use of zinc-blende half-metallic compounds is suggested, since these materials do not present interface states when they are brought in contact with zinc-blende semiconductors in the proposed TMR junctions.

# Bibliography

[1] S.A. Wolf, D.D. Awschalom, R.A. Buhrman, J.M. Daughton, S. von Molnár, M.L. Roukes, A.Y. Chtchelkanova, and D.M. Treger. *Science*, 294:1488, 2001.

[2] R.A. de Groot, F.M. Mueller, P.G. van Engen, and K.H.J. Buschow. *Phys. Rev. Lett.*, 50:2024, 1983.

[3] I. Žutić, J. Fabian, and S. Das Sarma. *Rev. Mod. Phys.*, 76:323, 2004.

[4] J. de Boeck, W. van Roy, J. Das, V. Motsnyi, Z. Liu, L. Lagae, H. Boeve, K. Dessein, and G. Borghs. *Semicond. Sci. Tech.*, 17:342, 2002.

[5] F. Heusler. *Verh. Dtsch. Phys. Ges.*, 5:219, 1903.

[6] P.J. Webster and K.R.A. Ziebeck. *Alloys and Compounds of d-Elements with Main Group Elements. Part 2.* Landolt-Börnstein, New Series, Group III, vol 32/c, Springer, Berlin, 2001.

[7] K.R.A. Ziebeck and K.-U. Neumann. *Magnetic Properties of Metals.* Landolt-Börnstein, New Series, Group III, vol 32/c, Springer, Berlin, 2001.

[8] J. Pierre, R.V. Skolozdra, J. Tobola, S. Kaprzyk, C. Hordequin, M.A. Kouacou, I. Karla, R. Currat, and E. Lelièvre-Berna. *J. Alloys Comp.*, 101:262, 1997.

[9] J. Tobola, J. Pierre, S. Kaprzyk, R.V. Skolozdra, and M.A. Kouacou. *J. Phys.:Condens. Mater.*, 10:1013, 1998.

[10] I. Galanakis, N. Papanikolaou, and P.H. Dederichs. *Phys. Rev. B*, 66:134428, 2002.

[11] I. Galanakis, N. Papanikolaou, and P.H. Dederichs. *Phys. Rev. B*, 66:174429, 2002.

[12] I. Galanakis. *J. Phys.: Condens. Matter*, 16:3089, 2004.

[13] M. Zhang, X. Dai, H. Hu, G. Liu, Y. Cui, Z. Liu, J. Chen, J. Wang, and G. Wu. *J. Phys.: Condens. Matter*, 15:7891, 2003.

[14] S. Datta and B. Das. *Appl. Phys. Lett.*, 56:665, 1990.

[15] K.A. Killian and R.H. Victoria. *J. Appl. Phys.*, 87:7064, 2000.

[16] C.T. Tanaka, J. Nowak, and J.S. Moodera. *J. Appl. Phys.*, 86:6239, 1999.

[17] J.A. Caballero, Y.D. Park, J.R. Childress, J. Bass, W.-C. Chiang, A.C. Reilly, W.P. Pratt Jr., and F. Petroff. *J. Vac. Sci. Technol. A*, 16:1801, 1998.

[18] R.J. Soulen Jr., J.M. Byers, M.S. Osofsky, B. Nadgorny, T. Ambrose, S.F. Cheng, P.R. Broussard, C.T. Tanaka, J. Nowak, J.S. Moodera, A. Barry, and J.M.D. Coey. *Science*, 282:85, 1998.

[19] H. Kato, T. Okuda, Y. Okimoto, Y. Tomioka, K. Oikawa, T. Kamiyama, and Y. Tokura. *Phys. Rev. B*, 69:184412, 2004.

[20] T. Shishidou, A.J. Freeman, and R. Asahi. *Phys. Rev. B*, 64:180401, 2001.

[21] I. Galanakis and Ph. Mavropoulos. *Phys. Rev. B*, 67:104417, 2003.

[22] Ph. Mavropoulos, I. Galanakis, and P.H. Dederichs. *J. Phys.: Condens. Matter*, 16:4261, 2004.

[23] W.-H. Xie, B.-G. Liu, and D.G. Pettifor. *Phys. Rev. Lett.*, 91:037204, 2003.

[24] H. Akinaga, T. Manago, and M. Shirai. *Jpn. J. Appl. Phys.*, 39:L1118, 2000.

[25] J.H. Zhao, F. Matsukura, K. Takamura, E. Abe, D. Chiba, and H. Ohno. *Appl. Phys. Lett.*, 79:2776, 2001.

[26] A. Stroppa, S. Picozzi, A. Continenza, and A.J. Freeman. *Phys. Rev. B*, 68:155203, 2003.

[27] H. Akai. *Phys. Rev. Lett.*, 81:3002, 1998.

[28] M.M. Kirillova, A.A. Makhnev, E.I. Shreder, V.P. Dyakina, and N.B. Gorina. *Phys. Stat. Sol. (b)*, 187:231, 1995.

[29] K.E.H.M. Hanssen and P.E. Mijnarends. *Phys. Rev. B*, 34:5009, 1986.

[30] P. Larson, S.D. Mahanti, and M.G. Kanatzidis. *Phys. Rev. B*, 62:12574, 2000.

[31] D. Orgassa, H. Fujiwara, T.C. Schulthess, and W.H. Butler. *Phys. Rev. B*, 60:13237, 1999.

[32] F.B. Mancoff, B.M. Clemens, E.J. Singley, and D.N. Basov. *Phys. Rev. B*, 60:R12–565, 1999.

[33] W. Zhu, B. Sinkovic, E. Vescovo, C. Tanaka, and J.S. Moodera. *Phys. Rev. B*, 64:R060403, 2001.

[34] G.L. Bona, F. Meier, M. Taborelli, E. Bucher, and P.H. Schmidt. *Sol. State. Commun.*, 56:391, 1985.

[35] S.K. Clowes, Y. Mioyoshi, Y. Bugoslavsky, W.R. Branford, C. Grigorescu, S.A. Manea, O. Monnereau, and L.F. Cohen. *Phys. Rev. B*, 69:214425, 2004.

[36] A.N. Caruso, C.N. Borca, D. Ristoiu, J.P. Nozieres, and P.A. Dowben. *Surf. Sci.*, 525:L109, 2003.

[37] S.J. Jenkins and D.A. King. *Surf. Sci.*, 494:L793, 2001.

[38] I. Galanakis. *J. Phys.: Condens. Matter*, 14:6329, 2002.

[39] S.J. Jenkins and D.A. King. *Surf. Sci.*, 501:L185, 2002.

[40] G.A. Wijs and R.A. de Groot. *Phys. Rev. B*, 64:020402, 2001.

[41] I. Galanakis, M. Ležaić, G. Bihlmayer, and S. Bl/"ugel. Unpublished [preprint: arxiv:cond-mat/0409333]. 2005.

[42] C.N. Borca, T. Komesu, H.-K. Jeong, P.A. Dowben, D. Ristoiu, C. Hordequin, J.P. Nozières, J. Pierre, Sh. Stadler, and Y.U. Idzerda. *Phys. Rev. B*, 64:052409, 2001.

[43] C. Hordequin, J. Pierre, and R. Currat. *J. Magn. Magn. Mater.*, 162:75, 1996.

[44] L.M. Sandratskii and P. Bruno. *Phys. Rev. B*, 66:134435, 2002.

148

[45] J. Kübler. *Phys. Rev. B*, 67:220403(R), 2003.

[46] J. Kübler, A.R. Williams, and C.B. Sommers. *Phys. Rev. B*, 28:1745, 1983.

[47] S.V. Halilov, H. Eschrig, A.Y. Perlov, and P.M. Oppeneer. *Phys. Rev. B*, 58:293, 1998.

[48] L.H. Thomas. *Proc. Cambridge Phil. Soc.*, 23:542, 1927.

[49] E. Fermi. *Rend. Accad. Naz.Linzei*, 6:602, 1927.

[50] J.C. Slater. *The Self-Sonsistent Field of Molecules and Solids*. McGraw-Hill, New York, 1974.

[51] P. Hohenberg and W. Kohn. *Phys. Rev. B*, 136:864, 1964.

[52] W. Kohn and L. Sham. *Phys. Rev. A*, 140:1133, 1965.

[53] Gell-Mann and K.A. Brueckner. *Phys. Rev.*, 106:369, 1957.

[54] E.P. Wiegner. *Phys. Rev.*, 46:1002, 1934.

[55] D.M. Ceperly and B.J. Alder. *Phys. Rev. Lett.*, 45:566, 1980.

[56] R.M. Dreitzler and E.K.U. Gross. *Density Functional Theory*. Springer, Berlin, 1990.

[57] G.P. Srivastava. *J. Phys. A*, 17:L317, 1984.

[58] O. Eriksson, J. Trygg, O. Hjortstam, B. Johansson, and J.M. Wills. *Surf. Sci.*, 382:93, 1997.

[59] N.W. Ashcroft and N.D. Mermin. *Solid State Physics*. Holt-Saunders Japan LTD., 1976.

[60] O. Jepsen and O.K. Andersen. *Solid. State Commun.*, 9:1763, 1971.

[61] P.E. Blöchl, O. Jepsen, and O.K. Andersen. *Phys. Rev. B*, 49:16223, 1994.

[62] M. Methfessel and T. Paxton. *Phys. Rev. B*, 40:3616, 1989.

[63] M. Methfessel and J. Kübler. *J. Phys. F: Metal Phys.*, 12:141, 1982.

[64] P.W. Atkins. *Molecular Quantum Mechanics*. Oxford University Press, Oxford, 1983.

[65] J.C. Slater. *Phys. Rev.*, 51:846, 1937.

[66] O.K. Andersen. *Phys. Rev. B*, 12:3060, 1975.

[67] D. Singh. *Planewaves, Pseudopotentials and the LAPW Method.* Kluwer Academic Publishers, Boston/Dordrecht/London, 1994.

[68] D.R. Hamann. Semiconductor charge densities with hard-core and soft-core pseudopotentials. *Phys. Rev. Lett.*, 212:662, 1979.

[69] E. Wimmer, H. Krakauer, M. Weinert, and A.J. Freeman. Full-potential self-consistent linearized-augmented-plane-wave method for calculating the electronic structure of molecules and surfaces: $O_2$ molecule. *Phys. Rev. B*, 24:864, 1981.

[70] J. Stoer. *Numerische Mathematik 1.* Springer-Verlag, Berlin, 1994.

[71] H. Krakauer, M. Posternak, and A.J. Freeman. Linearized augmented plane-wave method for the electronic band structure of thin films. *Phys. Rev. B*, 19:1706, 1979.

[72] W. Ning, C. Kailai, and W. Dingsheng. Work function of transition-metal surface with submonolayer alkali-metal coverage. *Phys. Rev. Lett.*, 56:2759, 1986.

[73] A.B. Shick, V. Drchal, J. Kudrnovský, and P. Weinberger. Electronic structure and magnetic properties of random alloys: fully relativistic spin-polarized linear muffin-tin-orbital method. *Phys. Rev. B*, 54:1610, 1996.

[74] D.D. Koelling and B.N. Harmon. A technique for relativistic spin-polarized calculations. *J. Phys. C.*, 10:3107, 1977.

[75] E.M. Rose. *Relativistic Electron Theory.* Wiley, New York, 1961.

[76] L.M. Sandratskii. Noncollinear magnetism in itinerant-electron systems: theory and application. *Advances in Physics*, 47:91, 1998.

[77] W. Brinkman and R. Elliot. *Proc. R. Soc. A*, 294:343, 1966.

[78] L.M. Sandratskii. Symmetry analysis of electronic states for crystals with spiral magnetic order. I. general properties. *JPCM*, 3:8565, 1991.

[79] Y. Tsunoda. Spin-density wave in cubic $\gamma$-Fe and $\gamma$-Fe$_{100-x}$Co$_x$ precipitates in Cu. *J. Phys.: Condens. Matter*, 1:10427, 1989.

[80] L. Nordström and A. Mavromaras. Magnetic ordering of the heavy rare earths. *Europhys. Lett.*, 49:775, 2000.

[81] O.N. Mryasov, A.N. Lichtenstein, L.M. Sandratskii, and V.A. Gubanov. Magnetic structure of fcc iron. *J. Phys. C.*, 3:7683, 1991.

[82] M. Uhl, L.M. Sandratskii, and J. Kübler. Electronic and magnetic states of $\gamma$-Fe. *J. Magn. Magn. Mater.*, 103:314, 1992.

[83] C. Herring. *Magnetism.* edited by G. Rado and H. Suhl, Academic, New York, 1966.

[84] L.M. Sandratskii. Energy band structure calculations for crystals with spiral magnetic structure. *Phys. Status Solidi B*, 136:167, 1986.

[85] L.M. Sandratskii and P.G. Guletskii. Symmetrised method for the calculation of the band structure of noncollinear magnets. *J. Phys. F: Met. Phys.*, 16:L43, 1986.

[86] L.M. Sandratskii and P.G. Guletskii. Energy band structure of bcc iron at finite temperatures. *J. Magn. Magn. Mater.*, 79:306, 1989.

[87] J. Kübler, K.H. Höck, J. Sticht, and A.R. Williams. Density functional theory of non-collinear magnetism. *J. Phys. F: Met. Phys.*, 18:469, 1988.

[88] J. Kübler, K.H. Höck, J. Sticht, and A.R. Williams. Local spin-density functional theory of noncollinear magnetism. *J. Appl. Phys.*, 63:3482, 1988.

[89] J. Sticht, K.H. Höck, and J. Kübler. Non-collinear itinerat magnetism: the case of Mn$_3$Sn. *J. Phys.: Condens. Matter*, 1:8155, 1989.

[90] O.N. Mryasov, A.I. Lichtenstein, L.M. Sandratskii, and V.A. Gubanov. Spiral-spin-density-wave states in fcc iron: Linear-muffin-tin-orbital band-structure approach. *Phys. Rev. B*, 45:12330, 1992.

[91] L. Nordström and D.J. Singh. Noncollinear intra-atomic magnetism. *Phys. Rev. Lett.*, 76:4420, 1996.

[92] S.H. Vosko and J. P. Perdew. Stoner model in dft. *Can. J. Phys.*, 53:1385, 1975.

[93] O. Gunnarsson. Exchange intergral and stoner model. *J. Phys. F: Met. Phys.*, 6:587, 1976.

[94] J.F. Janak. Exchange intergral and stoner model. *Phys. Rev. B*, 16:255, 1977.

[95] U.K. Poulsen, J. Kollár, and O.K. Andersen. Stoner model in dft. *J. Phys. F: Met. Phys.*, 6:L241, 1976.

[96] M. Takahashi. *J. Phys. C.*, 10:1289, 1977.

[97] K. Terakura, N. Hamada, T. Oguchi, and T. Asada. Local and non-local spin susceptibilities of transition metals. *J. Phys. F: Met. Phys.*, 12:1661, 1982.

[98] A.I. Liechtenstein, M.I. Katsnelson, V.P. Antropov, and V.A. Gubanov. *J. Magn. Magn. Mater.*, 67:65, 1987.

[99] J.P. Perdew, K. Burke, and M. Ernzerhof. *Phys. Rev. Lett.*, 77:3865, 1996.

[100] B.R.K. Nanda and I. Dasgupta. *J. Phys.: Condens. Matter*, 15:7307, 2003.

[101] D. Brown, M.D. Crapper, K.H. Bedwell, M.T. Butterfield, S.J. Guilfoyle, A.E.R. Malins, , and M. Petty. *Phys. Rev. B*, 57:1563, 1998.

[102] R.A. Dunlap and D.F. Jones. *Phys. Rev. B*, 26:6013, 1982.

[103] M. Mizuguchi, H. Akinaga, T. Manago, K. Ono, M. Oshima, and M. Shirai. *J. Magn. Magn. Mater.*, 239:269, 2002.

[104] J.H. Zhao, F. Matsukura, K. Takamura, E. Abe, D. Chiba, and H. Ohno. *Appl. Phys. Lett.*, 79:2776, 2001.

[105] K. Ono, J. Okabayashi, M. Mizuguchi, M. Oshima, A. Fujimori, and H. Akinaga. *J. Appl. Phys.*, 91:8088, 2002.

[106] M. Mizuguchi, H. Akinaga, T. Manago, K. Ono, M. Oshima, M. Shirai, H.J. Lin, H.H. Hsieh, and C.T. Chen. *J. Appl. Phys.*, 91:7917, 2002.

[107] A. Zunger and U. Lindefelt. *Phys. Rev. B*, 27:1191, 1983.

[108] S.-H. Wei and A. Zunger. *Phys. Rev. B*, 35:2340, 1987.

[109] S. Sanvito and N.A. Hill. *Phys. Rev. B*, 62:15553, 2000.

[110] A. Continenza, S. Picozzi, W.T. Geng, and A.J. Freeman. *Phys. Rev. B*, 64:085204, 2001.

152

[111] Y.-J. Zhao, W.T. Geng, A.J. Freeman, and B. Delley. *Phys. Rev. B*, 65:113202, 2002.

[112] Ph. Mavropoulos, O. Wunnicke, and P.H. Dederichs. *Phys. Rev. B*, 66:024416, 2002.

[113] O. Wunnicke, Ph. Mavropoulos, R. Zeller, P.H. Dederichs, and D. Gründler. *Phys. Rev. B*, 65:241306, 2002.

[114] T. Block, M.J. Carey, D.A. Gurney, and O. Jepsen. *Phys. Rev. B*, 70:205114, 2004.

[115] S. Picozzi, A. Continenza, and A.J. Freeman. *Phys. Rev. B*, 69:094423, 2004.

[116] Ph. Mavropoulos, K. Sato, R. Zeller, P.H. Dederichs, V. Popescu, and H. Ebert. *Phys. Rev. B*, 69:054424, 2004.

[117] Ph. Mavropoulos, I. Galanakis, V. Popescu, and P.H. Dederichs. *J. Phys. Condens. Matter*, 16:S5759, 2004.

[118] W. van Roy, J. de Boeck, B. Brijs, and G. Borghs. *Appl. Phys. Lett.*, 77:4190, 2000.

[119] S. Gardelis, J. Androulakis, J. Giapintzakis, O. Monnereau, and P.D Buckle. *Appl. Phys. Lett.*, 85:3178, 2004.

[120] P. Bach, A.S. Bader, C. Rüster, C. Gould, C.R. Becker, G. Schmidt, L.W. Molenkamp, W. Weigand, C. Kumpf, E. Umbach, R.Urban, G. Woltersdorf, and B. Heinrich. *Appl. Phys. Lett.*, 83:521, 2003.

[121] W. Zhu, B. Sinkovic, E. Vescovo, C. Tanaka, and J.S. Moodera. *Phys. Rev. B*, 64:R060403, 2001.

[122] J.A. Caballero, A.C. Reillyb, Y. Hao, J. Bass, W.P. Pratt, F. Petroff, and J.R. Childress. *J. Magn. Magn. Mater.*, 198-199:55, 1999.

[123] C.N. Borca, T. Komesu, and P.A. Dowben. *J. Electron Spectrosc. Relat. Phenom*, 122:259, 2002.

[124] A. Debernardi, M. Peressi, and A. Baldereschi. *Mat. Sci. Eng. C-Bio S*, 23:743, 2003.

[125] S. Picozzi, A. Continenza, and A.J. Freeman. *J. Appl. Phys.*, 94:4723, 2003.

[126] S. Picozzi, A. Continenza, and A.J. Freeman. *J. Phys. Chem. Solids*, 64:1697, 2003.

[127] I. Galanakis. *J. Phys.: Condens. Matter*, 16:8007, 2004.

[128] P. Bach, C. Rüster, C. Gould, C.R. Becker, G. Schmidt, and L.W. Molenkamp. *J. Cryst. Growth*, 251:323, 2003.

[129] S. Massidda, B.I. Min, , and A.J. Freeman. *Phys. Rev. B*, 35:9871, 1987.

[130] N.M. Rosengaard and B. Johansson. *Phys. Rev. B*, 55:14975, 1997.

[131] M. Pajda, J. Kudrnovský, I. Turek, V. Drchal, and P. Bruno. *Phys. Rev. B*, 64:174402, 2001.

[132] C.S. Wang, R.E. Prange, and V. Korenman. *Phys. Rev. B*, 25:5766, 1982.

[133] J. Enkovaara, A. Ayuela, J. Jalkanen, L. Nordström, and R.M. Nieminen. *Phys. Rev. B*, 67:054417, 2003.

[134] I. Turek, J. Kudrnovský, V. Drchal, and P. Bruno. Psi-k network: scientific highlight of the month [available at: http://psi-k.dl.ac.uk].

[135] K. Binder and D.W. Heermann. *Monte Carlo Simulation in Statistical Physics.* edited by P. Fulde, Springer-Verlag, Berlin, 1997.

[136] F. Reif. *Fundamentals of statistical and thermal physics.* McGraw-Hill Book Company, New York, 1965.

[137] M. Bowen, M. Bibes, A. Barthélémy, J.-P. Contour, A. Anane, Y. Lemaxtre, and A. Fert. *Appl. Phys. Lett.*, 83:2629, 2003.

[138] P. Bruno. *Phys. Rev. B*, 52:411, 1995.

[139] T. Dietl, H. Ohno, F. Matsukura, J. Cibert, and D. Ferrand. *Science*, 287:1019, 2000.

[140] J.S. Kouvel and J.S. Kasper. *J. Phys. Chem. Sol.*, 24:529, 1963.

[141] J.S. Kouvel and J.S. Kasper. In *Proc. Int. Conf. on Magnetism, Nottingham 1964*, page 169, London, 1965. Institute of Physics and Physical Chemistry.

154

[142] E. Krén, G. Kádár, G. Pál, and P. Szabó. *J. Appl. Phys.*, 38:1265, 1967.

[143] E. Krén, G. Kádár, G. Pál, L. Sólyom, P. Szabó, and T. Tarnoczi. *Phys. Rev.*, 140:574, 1968.

[144] Y. Endoh and Y. Ishikawa. Antiferromagnetism of $\gamma$-iron manganese alloys. *J. Phys. Soc. Japan*, 30:1614, 1971.

[145] D.J. Crockford, D.M. Bird, and M.W. Long. Band structures of non-collinear magnets in $\gamma$-Mn and $\gamma$-Fe. *J. Phys.: Condens. Matter*, 3:8665, 1991.

[146] M. Uhl, L.M. Sandratskii, and J. Kübler. Spin fluctuations in $\gamma$-Fe and in Fe$_3$Pt Invar from local-density-functional calculations. *Phys. Rev. B*, 50:291, 1994.

[147] J. Kübler. Derivation of the single-particle schrödinger equation: Density and spin-density functional theory and the magnetic susceptibility, noncollinear ground states, towards the curie temperature. 1995. Lecture Notes from: Workshop on Condensed Matter Physics.

[148] V.P. Antropov, M.I. Katsnelson, M. van Schilfgaarde, and B.N. Harmon. Ab initio spin dynamics in magnets. *Phys. Rev. Lett.*, 75:729, 1995.

[149] V.P. Antropov, M.I. Katsnelson, B.N. Harmon, M. van Schilfgaarde, and D. Kusnezov. Spin dynamics in magnets: Equation of motion and finite temperature effects. *Phys. Rev. B*, 54:1019, 1996.

[150] L.M. Sandratskii and J. Kübler. Non-collinear magnetism: effects of symmetry and relativity. *HCM newsletter*, 14:42, 1996.

[151] O.N. Mryasov, A.J. Freeman, and A.I. Lichtenstein. Theory of non-Heisenberg exchange: Results for localized and itinerant magnets. *J. Appl. Phys.*, 79:4805, 1996.

[152] M. Körling and J. Ergon. Gradient-corrected *ab initio* calculations of spin-spiral states in fcc-Fe and the effects of the atomic-spheres approximation. *Phys. Rev. B*, 54:8293, 1996.

[153] G.M. Stocks, B. Ujfalussy, Xin-Dong Wang, D.M.C. Nicholson, W.A. Shelton, Yang Wang, A. Canning, and B.L. Györffy. Towards a constrained local moment model for first principles spin dynamics. *Phil. Mag. B*, 78:665, 1998.

[154] B. Ujfalussy, Xin-Dong Wang, D.M.C. Nicholson, W.A. Shelton, G.M. Stocks, Yang Wang, and B.L. Györffy. Constrained density functional theory for first principles spin dynamics. *J. Appl. Phys.*, 85:4824, 1999.

[155] O. Grotheer and M. Fähnle. Ab initio calculations of the torques acting on localized magnetic moments including incomplete-basis-set corrections. *Phys. Rev. B*, 59:13965, 1998.

[156] O. Ivanov and V.P. Antropov. Molecular magnetism: Noncollinear ordering and spin dynamics. *J. Appl. Phys.*, 85:4821, 1999.

[157] T. Oda, A. Pasquarello, and R. Car. Fully unconstrained approach to noncollinear magnetism: Application to small Fe clusters. *Phys. Rev. Lett.*, 80:3622, 1998.

[158] D.M. Bylander and L. Kleinman. Full potential ab initio calculations of spiral spin density waves in fcc Fe. *Phys. Rev. B*, 58:9207, 1998.

[159] S. Uzdin, V. Uzdin, and C. Demangeat. Magnetic trimer on non-magnetic substrate: From frustration towards non-collinearity. *Europhys. Lett.*, 47:556, 1999.

[160] P.H. Andersson, L. Nordström, and O.Eriksson. Effect of hydrogenation on the magnetic state in cubic $Pd_3Mn$. *Phys. Rev. B*, 60:6765, 1998.

[161] D. Stoeffler and F. Gautier. Theoretical investigations of the magnetic behaviour of Cr monolayers deposited on a Fe(001) substrate: role of a mono-atomic step. *J. Magn. Magn. Mater.*, 147:260, 1995.

[162] A. Vega, D. Stoeffler, D. Dreyssé, and C. Demangeat. Magnetic-order transition in thin Fe overlayers on Cr: role of the interfacial roughness. *Europhys. Lett.*, 31:561, 1995.

[163] A. Berger and E.E. Fullerton. Phase diagram of imperfect ferromagnetic/antiferromagnetic bilayers. *J. Magn. Magn. Mater.*, 165:471, 1997.

[164] P. Bödeker, A. Hucht, J. Borchers, F. Güthoff, A. Schreyer, and H. Zabel. Reorientation of spin density waves in Cr(001) films induced by Fe(001) cap layers. *Phys. Rev. Lett.*, 81:914, 1998.

[165] Ph. Kurz, G. Bihlmayer, and S. Blügel. Noncollinear magnetism of Cr and Mn monolayers on Cu(111). *J. Appl. Phys.*, 87:6101, 2000.

[166] D. Hobbs and J. Hafner. Fully unconstrained noncollinear magnetism in triangular Cr and Mn monolayers and over-layers on Cu(111) substrates. *J. Phys.: Condens. Matter*, 12:7025, 2000.

[167] D. Hobbs, G. Kresse, and J. Hafner. Fully unconstrained noncollinear magnetism within the projector augmented wave method. submitted to Phys. Rev. B, 2000.

[168] L.M. Sandratskii and J. Kübler. Conduction electron states in gadolinium at finite temperatures. *Proceedings of Magnetism and Electronic Correlations in Local-Moment Systems: Rare-Earth Elements and Compounds*, page 271, 1998.

[169] L.M. Sandratskii and J. Kübler. Local magnetic moments of conduction electrons in gadolinium. *Europhys. Lett.*, 23(9):661, 1993.

# Acknowledgments

I had a great time in the past three years! There is something of a homey atmosphere in Forschungszentrum (the Christmas tree in the corridor is for sure a nice touch). What I like most about it are, of course, the people I was working with here.

For the relaxed and pleasant atmosphere in our group I would like to thank my supervisor, Prof. Dr. Stefan Blügel. I'm always amazed by the amount of ideas and the energy he possesses. His knowledge and guidance were very valuable for me.

For many useful discussions, I would like to say thank you to Prof. Dr. Peter H. Dederichs.

My first steps into the computational solid state physic I made at the University of Athens, under the supervision of Prof. Dr. Nikolaos Stefanou, whom I thank for a lot of help and patience.

Dr. Gustav Bihlmayer, though constantly bombed by my questions, has proved that he knows all the answers! Thanks Gustav.

For an enormous help and friendship I owe an enormous Thank you to Phivos. I'm pretty sure he deserves a Nobel prize (and that he will definitely get one).

Dr. Iosif Galanakis, the "Guru of Heusler alloys" helped me a lot in understanding the physics of these materials. Thank you Sifis!

I had a lot of fun in the office, Manni, Yura, thank you guys! Your presence made everything easier and nicer.

I would like to thank my colleagues, Markus, Daniel and Jussi – helpful and incredibly funny guys! Jussi had a lot of patience and a strong will, read my thesis very carefully and gave me useful suggestions. Thanks a lot for that!

I thank Jutta and Ute, warm smiling people, able and willing to solve any tricky problem.

My parents and my brother have given me a lot of support, love and trust during my education. I thank them with all my heart!

# Curriculum Vitae

**Personal data**

| | |
|---|---|
| Name: | Marjana Ležaić |
| Date of birth: | Feb. 18, 1971 |
| Place of birth: | Bor, Yugoslavia |
| Nationality: | Serbian |
| Address: | IFF, Forschungszentrum Jülich, 52425 Jülich, Germany |
| E-mail: | m.lezaic@fz-juelich.de |

**Education**

| | |
|---|---|
| 1978–1990 | Elementary and high school, Bor, Yugoslavia |
| 1990–1997 | Studies of physics, University of Belgrade, Yugoslavia<br>Diploma thesis: "Josephson Plasmons in High Tc Superconductors" |
| 1998–2001 | Postgraduate studies in solid state physics, University of Athens, Greece<br>Master thesis: "Metallodielectric Photonic Crystals: Porous Metals" |
| since 2002 | Ph.D studies in solid state physics, IFF, Forschungszentrum Jülich |

**Employment**

| | |
|---|---|
| 2002–2003 | Ph.D. student, Universität Osnabrück |
| 2003–2005 | Ph.D. student, Forschungszentrum Jülich |